

**Synthesis, Processing and Dynamic Fracture Behavior  
of Particulate Epoxy Composites  
with Conventional and Hierarchical Micro-/Nano-fillers**

by

Vinod Kushvaha

A dissertation submitted to the Graduate Faculty of  
Auburn University  
in partial fulfillment of the  
requirements for the Degree of  
Doctor of Philosophy

Auburn, Alabama  
December 10, 2016

Keywords: Particulate polymer composite, shape effect, loading rate, hierarchical fillers, mixed-mode fracture, XFEM

Approved by

Hareesh V Tippur, Chair, McWane Professor of Mechanical Engineering  
Jeffrey C Suhling, Quina Distinguished Professor of Mechanical Engineering  
James S Davidson, Professor of Civil Engineering  
Xinyu Zhang, Associate Professor of Chemical Engineering

## ABSTRACT

Polymer-based particulate composites have a wide range of engineering applications due to their mechanical, chemical, dielectric, and lightweight characteristics as well as simplicity of processing. The mechanical performance of these composites in general, and fracture behavior in particular, are strongly affected by the filler phase characteristics such as filler shape, size, volume fraction and filler-matrix interfacial strength. However, these composites could fail differently in different loading configurations (e.g. symmetric vs. antisymmetric) or loading rates. This dissertation addresses a few of these issues.

In the first part of the dissertation the effect of filler shape (sphere, flake and rod) and filler volume fraction (5%, 10% and 15%  $V_f$ ) on the dynamic fracture behavior of particulate polymer composites was investigated. The Digital Image Correlation (DIC) technique was utilized to map displacement fields around the crack-tip and extract stress intensity factors. The results showed a pronounced improvement in the crack initiation toughness for rod-shaped fillers, ~145% increase over unfilled epoxy at 15%  $V_f$  with flakes and spherical fillers showing ~97% and ~67% improvement, respectively, at the same  $V_f$ . For the three different volume fractions – 5%, 10%, and 15% - considered, the rod-shaped fillers produced the highest crack growth resistance followed by flakes and spheres, in that order. In addition, for 10%  $V_f$  rod-shaped filler ~113% and ~50% increase in

crack initiation toughness for the lowest ( $dK_I/dt = 53 \times 10^3 \text{ MPa}\sqrt{\text{m/s}}$ ) and the highest ( $dK_I/dt = 182 \times 10^3 \text{ MPa}\sqrt{\text{m/s}}$ ) loading rate cases, respectively, were seen compared to that of neat epoxy.

In the second part, mixed-mode dynamic fracture behavior of 10%  $V_f$  rod-shaped glass-filled epoxy composites was studied, and compared with the mode-I counterparts. In mode-I, the 10%  $V_f$  glass-filled epoxy produced ~128% increase in effective crack initiation fracture toughness compared to the neat counterpart, whereas, in the mixed-mode case, the 10%  $V_f$  glass-filled epoxy produced a ~98%-119% increase in the effective crack initiation fracture toughness, relative to the respective neat epoxy cases. Using the crack initiation toughness and mode-mixity measurements, a fracture envelope using Maximum Tensile Stress (MTS) criteria is developed for the 10%  $V_f$  composites. A modified fracture envelope equation that fits the measurements better is also demonstrated.

In the third part, the Finite Element Method (FEM) was employed to model the stress-strain behavior of 5%  $V_f$  carbon fiber modified epoxy composite under uniaxial tension. The stress-strain response from a Representative Area Element (RAE) of the composite was shown to be in agreement with the experimentally measured stress-strain response for 5%  $V_f$  carbon fiber-filled epoxy. Also, the so-called Extended FEM (XFEM) was employed to model crack propagation in this composite and to understand the underlying fracture mechanism by varying the fiber-interface strength. The computations showed that the crack tends to propagate through the fibers when the filler was perfectly bonded to the matrix. However, the crack path circumvented the fiber when it was weakly bonded to the matrix suggesting the potential crack path tortuosity.

In the last part, an ultrafast poptube approach was utilized to grow Carbon Nanotubes (CNTs) on various engineering substrates (hollow glass-microballoons, solid glass spheres, solid

glass fibers and carbon fibers) using a microwave. Subsequently, CNT-grown substrates were used as the filler to process a micro-nano hierarchical composite. The hierarchical epoxy composite made of CNT-grown microballoons enhanced the critical fracture toughness by ~17% relative to conventional syntactic foam in quasi-static fracture tests. On the other hand, the critical fracture toughness for CNT-grown carbon fiber-filled epoxy decreased by ~15% relative to the traditional counterparts. Fractography revealed that improvements due to CNTs were compromised by the agglomeration of micro-fillers with CNTs grown on them.



## ACKNOWLEDGMENTS

I thank my advisor, Dr. Hareesh V. Tippur, for his academic guidance throughout the research work for this dissertation. I thank my other committee members Dr. Jeffrey Suhling, Dr. James Davidson and Dr. Xinyu Zhang for reviewing this dissertation and their support and counsel. Partial financial support for this research through a grant from National Science Foundation (CMMI-1100700) is gratefully acknowledged.

I would like to acknowledge my labmates Rahul Jhaver, Chandru Periasamy, Kailash Jajam, Allen Craven, Robert Bedsole, Austin Branch, Amith Jain, Balamurgan Meenakshi, and Oscar Sotomayor with whom I learned a lot and spent memorable time. I would also like to acknowledge my research collaborators from Dr. Zhang's group including James Smith, Zhen Liu, and Selcuk Poyraz for their time and support during the research.

I would like to acknowledge my parents, brothers, sisters, and my wife for their immense love, inspiration and support. Particularly I want to acknowledge, my sister Poonam, my brothers Ashok and Rajesh; and my wife Priyanka for their sheer faith in me and my abilities to overcome any hurdle in my path and their support which has enabled me to reach this point. I dedicate my work most especially to them. Finally, I am thankful for the many others in my life who have helped me along the way.

## TABLE OF CONTENTS

<b>ABSTRACT</b> .....	<b>ii</b>
<b>ACKNOWLEDGMENTS</b> .....	<b>v</b>
<b>TABLE OF CONTENTS</b> .....	<b>vi</b>
<b>LIST OF FIGURES</b> .....	<b>xi</b>
<b>LIST OF TABLES</b> .....	<b>xviii</b>
<b>CHAPTER 1</b> .....	<b>1</b>
<b>INTRODUCTION</b> .....	<b>1</b>
1.1 Motivation and literature review .....	5
1.1.1 Glass-filled epoxy composite: shape, volume fraction and loading rate effects	6
1.1.2 Carbon nanotube (CNT) based conventional/hierarchical epoxy composite....	7
1.2 Objectives .....	11
1.3 Organization of dissertation.....	12
<b>CHAPTER 2</b> .....	<b>15</b>
<b>EXPERIMENTAL TECHNIQUES</b> .....	<b>15</b>
2.1 Quasi-static tension and fracture setup.....	15

2.2	Dynamic fracture setup.....	16
2.3	Digital Image Correlation.....	19
2.4	Facet (sub-image) size study .....	23
2.5	Estimation of scale factor .....	25
<b>CHAPTER 3 .....</b>		<b>26</b>
<b>EFFECT OF FILLER SHAPE, VOLUME FRACTION AND LOADING RATE ON DYNAMIC FRACTURE BEHAVIOR OF GLASS-FILLED EPOXY .....</b>		<b>26</b>
3.1	Material preparation .....	26
3.2	Physical and elastic properties.....	29
3.3	Experimental Details .....	30
3.4	Optical Data Analysis.....	32
3.5	Experimental repeatability and comparison with finite element simulations.....	37
3.6	Results and discussion.....	39
3.6.1	Effect of filler shape.....	39
3.6.2	Effect of filler volume fraction .....	46
3.6.3	Quantification of shape effects on crack initiation toughness .....	48
3.6.4	Effect of loading rate.....	50
<b>CHAPTER 4 .....</b>		<b>55</b>
<b>MIXED-MODE DYNAMIC FRACTURE .....</b>		<b>55</b>

4.1	Material preparation .....	57
4.2	Optical data analysis .....	59
4.3	Experimental repeatability and finite element simulations .....	62
4.4	Results and discussion .....	67
4.4.1	Fractography .....	70
4.5	Fracture envelope .....	72
4.6	Mixed-mode crack growth direction .....	75
<b>CHAPTER 5 .....</b>		<b>79</b>
<b>FINITE ELEMENT MODELING .....</b>		<b>79</b>
5.1	Material preparation .....	79
5.2	Quasi-static tension tests .....	80
5.3	Finite element modeling of tension tests .....	81
5.3.1	Constituent properties .....	81
5.4	Modeling approach .....	83
5.5	Boundary conditions .....	86
5.5.1	Element type .....	86
5.6	Mesh convergence .....	87
5.7	Results and discussion .....	88
5.7.1	Horizontal vs. vertical loading of RAE .....	92

5.8	Quasi-static crack propagation .....	93
5.8.1	Constituent material properties .....	95
5.8.2	Modeling approach .....	95
5.8.3	Results and discussion .....	100
<b>CHAPTER 6 .....</b>		<b>101</b>
<b>SYNTHESIS, PROCESSING AND FRACTURE BEHAVIOR OF MICRO-/NANO-HIERARCHICAL COMPOSITE .....</b>		<b>101</b>
6.1	Conventional techniques to grow carbon nanotubes .....	102
6.1.1	Arc discharge .....	102
6.1.2	Laser ablation .....	103
6.1.3	Chemical vapor deposition (CVD) .....	104
6.2	Ultrafast carbon nanotube growth - A Poptube approach .....	105
6.2.1	Step 1: Coating with conducting polymer.....	106
6.2.2	Step 2: Coating with microwave precursor.....	107
6.2.3	Step 3: Microwaving in a glass vial .....	107
6.3	Carbon nanotube growth on engineering substrates using Poptube approach .....	107
6.3.1	Carbon nanotube growth on glass microballoons .....	108
6.3.2	Quasi-static fracture test.....	110
6.3.3	Dynamic mechanic analysis (DMA).....	112

6.3.4	Carbon nanotube growth on spherical solid glass particles .....	115
6.3.5	Carbon nanotube growth on carbon fibers .....	117
<b>CHAPTER 7</b>	.....	<b>123</b>
<b>SUMMARY AND CONCLUSIONS</b>	.....	<b>123</b>
7.1	Future directions .....	130
<b>REFERENCES</b>	.....	<b>132</b>
<b>APPENDIX A</b>	.....	<b>143</b>

## LIST OF FIGURES

FIGURES	PAGES
Figure 1.1: Photograph of marine exploration device shown to explore the Titanic wreckage (top) ( <a href="http://ultimatetitanic.com/the-wreckage/#.U0cDgvldXTo">ref:http://ultimatetitanic.com/the-wreckage/#.U0cDgvldXTo</a> ). Photograph of similar marine exploration device “Perseo GTV” made of syntactic foam (bottom) ( <a href="http://www.diabgroup.com/en-GB/About-us/This-is-DIAB">ref:http://www.diabgroup.com/en-GB/About-us/This-is-DIAB</a> ) .....	2
Figure 1.2: Photograph of buoy made up of syntactic foam ( <a href="http://www.marinelink.com/news/trelleborg-compliant341500.aspx">ref:http://www.marinelink.com/news/trelleborg-compliant341500.aspx</a> ).....	3
Figure 1.3: Schematic of particle-filled underfill material in electronic package (top) and underfill material failure (bottom) ([8]).....	4
Figure 1.4 (a): Predator Tail Spar UAV cross section made up of carbon fiber composite ( <a href="http://www.fiberdynamics.net/view-other-projects.html">ref:http://www.fiberdynamics.net/view-other-projects.html</a> ); (b): Ariete main battle tank made up of composite armor ( <a href="http://www.army-technology.com/projects/ariete/ariete1.html">ref:http://www.army-technology.com/projects/ariete/ariete1.html</a> ); (c): Sports car body made up of carbon fiber composite ( <a href="http://www.fiberdynamics.net/view-other-projects.html">ref:http://www.fiberdynamics.net/view-other-projects.html</a> ); (d): Sporting skates made up of glass and carbon composite ( <a href="http://depts.washington.edu/amtas/events/amtas_08spring/K2_Composites_in_Sporting_Goods.pdf">ref:http://depts.washington.edu/amtas/events/amtas_08spring/K2_Composites_in_Sporting_Goods.pdf</a> ) .....	5
Figure 2.1: Experimental setups involving (a) Instron 4465 used for quasi-static (b) tension and (c) fracture experiments ([13]) .....	15
Figure 2.2: Schematic of dynamic fracture setup under impact loading .....	17
Figure 2.3: Experimental setup used for dynamic fracture experiments (top). Close-up of the long-bar and the specimen (bottom) ([38]) .....	18
Figure 2.4: Schematic of ultra-high speed Cordin camera: M <sub>1</sub> - M <sub>5</sub> are mirrors; R <sub>1</sub> and R <sub>2</sub> are relay lenses; r <sub>1</sub> -r <sub>32</sub> are relay lenses for CCDs; S <sub>1</sub> -S <sub>32</sub> are CCD sensors.....	19
Figure 2.5: Schematic to explain Digital Image Correlation (DIC) technique .....	20

Figure 2.6: Crack opening ( $u_y$ ) and crack sliding ( $u_x$ ) displacement contours in steps of 10 $\mu\text{m}$ , respectively (units on the displacement contour on $x$ - and $y$ -axis are in mm). First row: 10 x 10 pixel facet size (Fig. (a)), middle row: 15 x 15 pixel facet size (Fig. 2.6(b)), and last row: 20 x 20 pixel facet size (Fig. 2.6(c)); Scale factor: 1 pixel = 33 $\mu\text{m}$ ....	23
Figure 2.7: Variation of $K_I^d$ with facet size .....	25
Figure 3.1: SEM micrographs of sphere-, flake- and rod-shaped glass fillers used in present study (left to right respectively; scale bar: 50 $\mu\text{m}$ ) .....	27
Figure 3.2 (a): Schematic of test specimen, (b): Typical fractographs at four different locations for 15% $V_f$ rod-shaped glass-filled epoxy (micrograph scale bar = 100 $\mu\text{m}$ ); Note the uniformity of filler dispersion. ....	28
Figure 3.3: Displacement data collection on $[0.5 < r/B < 1.5]$ and $[-147^\circ < \theta < -90^\circ]$ & $[90^\circ < \theta < 147^\circ]$ to extract stress intensity factors. ....	35
Figure 3.4: Acquired speckle images for glass-filled epoxy with 10% $V_f$ of spheres for the ‘Al-PS’ pulse-shaper case with crack opening ( $u_y$ ) and crack sliding ( $u_x$ ) displacement contours in steps of 5 $\mu\text{m}$ , respectively (units on the displacement contour on $x$ - and $y$ -axis are in mm). First row: pre-crack initiation ( $t = -9.99 \mu\text{s}$ ), middle row: crack initiation ( $t = 0 \mu\text{s}$ ), and last row: post-crack initiation ( $t = 19.98 \mu\text{s}$ ) time instants; Scale factor: 1 pixel = 34 $\mu\text{m}$ . ....	36
Figure 3.5: Experimental repeatability of SIF histories for 15% rod-shaped glass-filled epoxy for the ‘Al-PS’ case and comparison with FE simulation. (Histories for $K_{II}$ are also provided for completeness. Being a symmetric loading experiment, $K_{II}$ histories are relatively small but useful to estimate errors in the least-squares analysis scheme) .	37
Figure 3.6: Finite element mesh used for elasto-dynamic simulation of mode-I fracture experiments using ABAQUS/explicit (left); strain history recorded on the long-bar for the ‘Al-PS’ case (right). ....	38
Figure 3.7: $K_I$ histories (a) for 5% $V_f$ , (b) 10% $V_f$ , (c) 15% $V_f$ glass-filled epoxy for the Aluminum 1100 pulse shaper (‘Al-PS’) case with different filler particle shape. ....	42
Figure 3.8: Fractographs of 10% $V_f$ sphere, flake, rod-shaped glass-filled epoxy (top to bottom respectively) for the ‘Al-PS’ pulse shaper case; scale bar = 100 $\mu\text{m}$ .....	43
Figure 3.9: Typical fracture surface profile of neat epoxy for the ‘Al-PS’ pulse shaper case ( $R_a = 6.3 \mu\text{m}$ ).....	44
Figure 3.10: Typical pseudo-colored fracture surfaces of glass-filled epoxy (10% $V_f$ ) for the ‘Al-PS’ pulse shaper case. Fillers contribute less than $\sim 1\%$ to the overall surface roughness ( $R_a$ ). ....	45



Figure 3.11: $K_I$ histories for glass-filled epoxy with (a) spherical filler, (b) flakes, (c) rods for the ‘Al-PS’ pulse shaper case with different volume fractions.....	47
Figure 3.12: Effect of aspect ratio on crack initiation toughness for the ‘Al-PS’ pulse shaper case. Error bars indicate one standard deviation relative to the average toughness value. The crack initiation toughness follows a linear relationship of the form $K_I = C_1 \cdot \log(AR) + C_2$ , where $C_1$ and $C_2$ are constants (for 5% $V_f$ : $C_1 = 0.49$ MPa $\sqrt{m}$ and $C_2 = 1.69$ MPa $\sqrt{m}$ ; for 10% $V_f$ : $C_1 = 0.59$ MPa $\sqrt{m}$ and $C_2 = 1.97$ MPa $\sqrt{m}$ and for 15% $V_f$ : $C_1 = 0.58$ MPa $\sqrt{m}$ and $C_2 = 2.37$ MPa $\sqrt{m}$ ). .....	49
Figure 3.13: Crack growth history plots for neat epoxy and 10% $V_f$ rod-filled epoxy at different loading rates. ....	52
Figure 3.14: SIF histories at different loading rates: (a) For neat epoxy (Before crack initiation, $dK_I/dt$ were $\sim 149 \times 10^3$ , $61 \times 10^3$ and $40 \times 10^3$ MPa $\sqrt{m/s}$ for ‘No-PS’, ‘Al-PS’ and ‘PC-PS’ cases, respectively, compared to $dK_I/dt$ of $\sim 6 \times 10^{-2}$ MPa $\sqrt{m/s}$ in quasi-static loading case.), (b) For glass-filled epoxy (10% $V_f$ ) (Before crack initiation, $dK_I/dt$ were $\sim 182 \times 10^3$ , $132 \times 10^3$ and $53 \times 10^3$ MPa $\sqrt{m/s}$ for ‘No-PS’, ‘Al-PS’ and ‘PC-PS’ cases, respectively, compared to $dK_I/dt$ of $\sim 1 \times 10^{-1}$ MPa $\sqrt{m/s}$ in quasi-static loading case. ....	53
Figure 3.15: Fractographs of glass-filled epoxy (10% $V_f$ ) for the highest (‘No-PS’ case (left)) and the lowest (‘PC-PS’ case (right)), respectively; scale bar=100 $\mu$ m .....	54
Figure 4.1: Schematics illustrating pure mode-I and mode-II fractures [55] .....	55
Figure 4.2: Schematics of mode-I specimen with eccentricity $e = 0$ mm (top) and mixed-mode specimen with eccentricity $e = 20$ mm (bottom).....	58
Figure 4.3: Schematic showing crack propagation at an angle $\alpha$ in mixed-mode loading configuration. Angle $\alpha$ was measured by joining initial notch tip to the current crack tip. ....	59
Figure 4.4: Acquired speckle images for glass-filled epoxy for $e = 20$ mm, $a = 10$ mm case with crack opening ( $u_y$ ) and crack sliding ( $u_x$ ) displacement contours in steps of 10 $\mu$ m, respectively (units on the displacement contour on $x$ - and $y$ -axis are in mm). First row: crack opening ( $u_y$ ) and crack sliding ( $u_x$ ) displacement, respectively, at crack initiation ( $t = 0$ $\mu$ s), middle row: crack opening ( $u_y$ ) and crack sliding ( $u_x$ ) displacement, respectively, at a post-crack initiation instant ( $t = 30$ $\mu$ s), and last row: transformed crack opening ( $u_{y'}$ ) and sliding ( $u_{x'}$ ) displacement, respectively, at post-crack initiation instant ( $t = 30$ $\mu$ s); Scale factor: 1 pixel = 49 $\mu$ m.....	60
Figure 4.5: Acquired speckle images for glass-filled epoxy for $e = 20$ mm, $a = 20$ mm case with crack opening ( $u_y$ ) and crack sliding ( $u_x$ ) displacement contours in steps of 10 $\mu$ m, respectively (units on the displacement contour on $x$ - and $y$ -axis are in mm). First row: crack opening ( $u_y$ ) and crack sliding ( $u_x$ ) displacement, respectively, at crack initiation ( $t = 0$ $\mu$ s), middle row: crack opening $u_y$ and crack sliding $u_x$ , respectively, at a post-	

crack initiation instant ( $t = 30 \mu\text{s}$ ), and last row: transformed crack opening ( $u_y'$ ) and sliding ( $u_x'$ ) displacement, respectively, at post-crack initiation instant ( $t = 30 \mu\text{s}$ ); Scale factor: 1 pixel = $45 \mu\text{m}$ .....	61
Figure 4.6: Experimental repeatability and comparison with FE simulation of (a): effective SIF histories ( $K_{\text{eff}}$ ), (b): mode-I SIF histories ( $K_I$ ), (c): mode-II SIF histories ( $K_{II}$ ) for glass-filled epoxy ( $e = 20, a = 10$ ) case.....	63
Figure 4.7: The crack opening (upper left) and crack sliding (upper right) displacement (in m) contours, respectively, obtained from 3D elasto-dynamic FEA; and the corresponding crack opening (bottom left) and crack sliding (bottom right) displacement (in $\mu\text{m}$ ), respectively, obtained from the mixed-mode dynamic fracture experiment using DIC at $t = 0$ for glass-filled epoxy ( $e = 20, a = 10$ ) case .....	64
Figure 4.8: At $t = 0$ , evaluation of mode-I (top) and mode-II (bottom) stress intensity factor using crack opening and crack sliding displacements obtained from FEA, respectively, for glass-filled epoxy ( $e = 20, a = 10$ ) case. ....	66
Figure 4.9: Fracture parameter histories of $K_I, K_{II}, K_{\text{eff}}$ and $\psi$ for neat epoxy from (a)-(d), respectively. ....	69
Figure 4.10: Fracture parameter histories of $K_I, K_{II}, K_{\text{eff}}$ and $\psi$ for 10% $V_f$ glass-filled epoxy from (a)-(d), respectively.....	70
Figure 4.11: Fractographs of glass-filled epoxy (10% $V_f$ ) for the mode-I ( $e = 0, a = 10$ ) (top left) and the mixed-mode ( $e = 20, a = 10$ ; top right) and ( $e = 20, a = 20$ ; bottom), respectively; scale bar = $100 \mu\text{m}$ .....	71
Figure 4.12: Dynamic crack initiation envelope for neat and 10% $V_f$ glass-filled epoxy ( $e$ is eccentricity in mm and $a$ is crack length in mm) using Eq. (4.5) .....	73
Figure 4.13: Dynamic crack initiation envelope for neat and 10% $V_f$ glass-filled epoxy ( $e$ is eccentricity in mm and $a$ is crack length in mm) using Eq. 4.6 for $\lambda, \mu = 1.4$ and $\lambda, \mu = 1.3$ , respectively. ....	74
Figure 4.14: Mode-I crack propagation in neat epoxy (top) and 10% $V_f$ glass-filled epoxy (bottom). The crack propagated along the initial notch direction for both neat and glass-filled epoxy.....	75
Figure 4.15: Crack propagation in neat epoxy (top) and 10% $V_f$ glass-filled epoxy (bottom) in mixed-mode loading configuration ( $e = 20, a = 10$ ). The crack propagated at $\sim 30^\circ$ and $\sim 32^\circ$ from the initial notch direction for neat and glass-filled epoxy, respectively. ..	76
Figure 4.16: Crack propagation in neat epoxy (top) and 10% $V_f$ glass-filled epoxy (bottom) in mixed-mode loading configuration ( $e = 20, a = 20$ ). The crack propagated at $\sim 52^\circ$ and $\sim 46^\circ$ from the initial notch direction for neat and glass-filled epoxy, respectively. ..	76

Figure 4.17: Crack propagation in neat epoxy (top) and 10% $V_f$ glass-filled epoxy (bottom) in mixed-mode loading configuration ( $e = 20$ , $a = 25$ ). The crack propagated at $\sim 60^\circ$ and $\sim 54^\circ$ from the initial notch direction for neat and glass-filled epoxy, respectively. ..	77
Figure 5.1: The dogbone-shaped specimens used for tension tests (thickness 4.3 mm) .....	80
Figure 5.2: True stress versus true strain response for 5% $V_f$ carbon fiber modified epoxy and neat epoxy obtained from quasi-static tension tests .....	81
Figure 5.3: Stress-strain response for carbon fiber .....	82
Figure 5.4: Random points generation using 2D Poisson homogeneous process for 5% $A_f$ carbon fiber modified epoxy composite (left: $s = 31 \mu\text{m}$ , $\delta = 0.30$ ; right: $s = 85 \mu\text{m}$ , $\delta = 0.81$ ) .....	84
Figure 5.5: Random fibers were drawn using 2D Poisson homogeneous process for 5% $A_f$ carbon fiber modified epoxy composite for $\delta = 0.81$ case.....	85
Figure 5.6: Discretized FE meshes used for convergence study (coarse (top), finer (bottom left) and the finest (bottom right)) .....	86
Figure 5.7: Comparison of FEA with experimental result for 5% $V_f$ carbon fiber modified epoxy composite of $600 \times 600 \mu\text{m}^2$ RAE case loaded in the vertical direction.....	89
Figure 5.8: Stress ( $\sigma_{yy}$ ) for 5% $V_f$ carbon fiber modified epoxy composite for plane stress case loaded in the vertical direction.....	90
Figure 5.9: Mises stresses for 5% $V_f$ carbon fiber modified epoxy composite for plane stress case loaded in the vertical direction.....	90
Figure 5.10: Normal strain ( $\varepsilon_{yy}$ ) for 5% $V_f$ carbon fiber modified epoxy composite for plane stress case loaded in the vertical direction.....	91
Figure 5.11: Maximum principal strain distribution for 5% $V_f$ carbon fiber modified epoxy composite for plane stress case loaded in the vertical direction .....	91
Figure 5.12: Stress-strain response comparison of vertical vs. horizontal loading cases for 5% $V_f$ carbon fiber modified epoxy composite.....	92
Figure 5.13: A mesh of four elements with (left) and without (right) a double node [72] .....	94
Figure 5.14: Random fibers were drawn for mimicking 5% $A_f$ carbon fiber modified epoxy composite and a $144 \mu\text{m}$ long crack ( $a/W=0.2$ ) was introduced at the left mid-span to model crack propagation using XFEM .....	96
Figure 5.15: Fiber ( $60 \mu\text{m}$ long and $8 \mu\text{m}$ wide) placed in front of the crack-tip. On the left strongly bonded case. On the right, weakly bonded case with an interface layer ( $1 \mu\text{m}$ thick) between the fiber and the epoxy matrix .....	97

Figure 5.16: Strongly bonded fiber case: Normal stress ( $\sigma_{yy}$ ) (top) and maximum principal strain contour for 5% $V_f$ carbon fiber modified epoxy composite (bottom) show that crack propagates through the fiber .....	98
Figure 5.17: Weakly bonded fiber case: Normal stress ( $\sigma_{yy}$ ) (top) and maximum principal strain contour for 5% $V_f$ carbon fiber modified epoxy composite (bottom) show that crack path circumvents the fiber.....	99
Figure 6.1: Schematic of an arc discharge setup (ref: <a href="http://upload.wikimedia.org/wikipedia/commons/a/af/Arc_discharge_nanotube.png">http://upload.wikimedia.org/wikipedia/commons/a/af/Arc_discharge_nanotube.png</a> ) .....	103
Figure 6.2: Schematic of a laser ablation furnace [87] .....	104
Figure 6.3: Schematic of a CVD furnace [87] .....	105
Figure 6.4: Steps involved in poptube approach to grow CNTs on engineering materials (ref:[88]) .....	107
Figure 6.5: Silane treated XLD3000 used for CNT growth.....	109
Figure 6.6: CNT-grown glass microballoons using poptube approach (top-left), CNT grown microballoons shown at higher magnification (top-right and bottom) .....	109
Figure 6.7: HRTEM of individual CNT with trapped Fe catalyst particle (scale bar: 5 nm) (ref:[87]) .....	110
Figure 6.8: Load-displacement response for conventional SF and nano-SF. Inset: SEM image of the CNT grown glass microballoon, scale bar: 10 $\mu$ m.....	111
Figure 6.9: Storage modulus comparison between SF and Nano-SF .....	113
Figure 6.10: $\tan(\delta)$ comparison between SF and Nano-SF.....	113
Figure 6.11: Fractograph of 15% $V_f$ syntactic foam.....	114
Figure 6.12: Fractograph of 15% $V_f$ nano-syntactic foam showing agglomeration of CNT-grown microballoons.....	115
Figure 6.13: CNT Synthesis on solid spherical glass particles. The top micrograph shows the poor CNT coverage and the bottom shows the large fused clump of solid glass particles .....	116
Figure 6.14: CNT growth on carbon fibers (top-left); excellent CNT coverage on a few carbon fibers (top-right); almost no CNT coverage on some carbon fibers (bottom) .....	117
Figure 6.15: Load-displacement response for carbon fiber modified (CF modified) epoxy and CNT grown carbon fiber modified (CNT CF modified) epoxy.....	119

Figure 6.16: Fractograph of 5% $V_f$ carbon fiber modified epoxy .....	120
Figure 6.17: Fractograph of 5% $V_f$ CNT grown carbon fiber modified epoxy (top), center spot at high resolution showing material pull out during crack propagation (bottom) .....	120
Figure 6.18: Storage modulus comparison between CF and CNT CF modified epoxy .....	122
Figure 6.19: $\tan(\delta)$ comparison between CF and CNT CF modified epoxy.....	122

## LIST OF TABLES

<b>TABLES</b>	<b>PAGES</b>
Table 3.1: Glass Filler Characteristics .....	27
Table 3.2: Material properties of glass-filled epoxy composite .....	29
Table 3.3.: Crack initiation toughness (in $\text{MPa}\sqrt{\text{m}}$ ) comparison for different filler shapes at different $V_f$ using an aluminum pulse shaper ('Al-PS') during impact (% improvement is relative to neat epoxy) .....	48
Table 3.4.: Critical energy release rate (in $\text{kPa}\cdot\text{m}$ ) comparison for different filler shapes at different $V_f$ using an aluminum pulse shaper ('Al-PS') during impact (% improvement is relative to neat epoxy).....	48
Table 3.5.: Crack initiation toughness (in $\text{MPa}\sqrt{\text{m}}$ ) comparison (% improvement is relative to the neat epoxy of the respective pulse shaper used during loading).....	52
Table 3.6.: Critical energy release rate (in $\text{kPa}\cdot\text{m}$ ) comparison (% improvement is relative to the neat epoxy of the respective pulse shaper used during loading).....	52
Table 3.7: Crack initiation time and crack speed comparison for neat epoxy and 10% $V_f$ rod-filled epoxy .....	53
Table 4.1: Material properties of neat epoxy and glass-filled epoxy composite .....	59
Table 4.2: Effective crack initiation toughness (in $\text{MPa}\sqrt{\text{m}}$ ) comparison between neat and glass-filled epoxy (% improvement is relative to neat epoxy) .....	68
Table 4.3: Critical energy release rate (in $\text{kPa}\cdot\text{m}$ ) comparison between neat and glass-filled epoxy (% improvement is relative to neat epoxy) .....	68
Table 4.4: Crack kink angle comparison for neat epoxy and glass-filled epoxy .....	77
Table 5.1: Carbon fiber characteristics .....	80
Table 5.2: Measured material properties from uniaxial tension tests .....	81

Table 5.3: Elastic properties used for neat epoxy and carbon fibers .....	82
Table 5.4: Elastic modulus comparison for coarse vs. fine mesh.....	88
Table 5.5: Elastic Modulus comparison between FE simulation and experiment.....	89
Table 5.6: Modulus comparison for horizontal vs. vertical loading cases.....	93
Table 5.7: Elastic properties used for neat epoxy, carbon fibers and interface .....	95
Table 5.8: Crack initiation and propagation parameters used for neat epoxy, carbon fibers, and interface.....	100
Table 6.1: Quasi-static fracture toughness and critical energy release rate comparison .....	112
Table 6.2: Quasi-static fracture toughness and critical energy release rate comparison .....	121

## CHAPTER 1

### INTRODUCTION

Particulate polymer composites contain two or more constituents and are normally made by modifying the polymer using inorganic-particulate fillers such as alumina, mica or silica etc. Particulate polymer composites have been widely used in various engineering applications due to their lightweight characteristics combined with their excellent mechanical properties, chemical resistance, dielectric and adhesion properties. More importantly, they are also relatively easy to process at low costs and the overall properties can be tailored by choosing the filler size and shape, filler-matrix interfacial strength and/or the volume fraction in the composite. Unlike traditional fiber-reinforced composites, simplicity of particulate polymer composite in terms of macroscopic isotropy is another aspect which often makes them quite desirable for mechanical design. Therefore, understanding the role of filler concentration, filler size and shape, and filler interfacial strength with the polymer matrix on macromechanical properties such as stiffness, strength and toughness of the resulting particulate polymer composite is critical for proper engineering applications.

In the following examples, a few polymer composite applications are discussed to demonstrate their superiority over other engineering materials, which explain the researcher's keen interest in this research area. One class of particulate polymer composite where filler particles are micron-sized hollow spherical glass particles (microballoons) dispersed into epoxy matrix is called syntactic foams. They are often used in naval and marine applications including submersibles (Figure 1.1), buoys and marine platforms (Figure 1.2) due to their excellent mechanical properties



combined with their lightweight and corrosion resistance. They are also used in civil and industrial engineering as imitation wood and in building construction materials for their high shear stiffness and specific strength [1].



Figure 1.1: Photograph of marine exploration device shown to explore the Titanic wreckage (top) (ref:<http://ultimatetitanic.com/the-wreckage/#.U0cDgvldXTo>). Photograph of similar marine exploration device “Perseo GTV” made of syntactic foam (bottom) (ref:<http://www.diabgroup.com/en-GB/About-us/This-is-DIAB>)

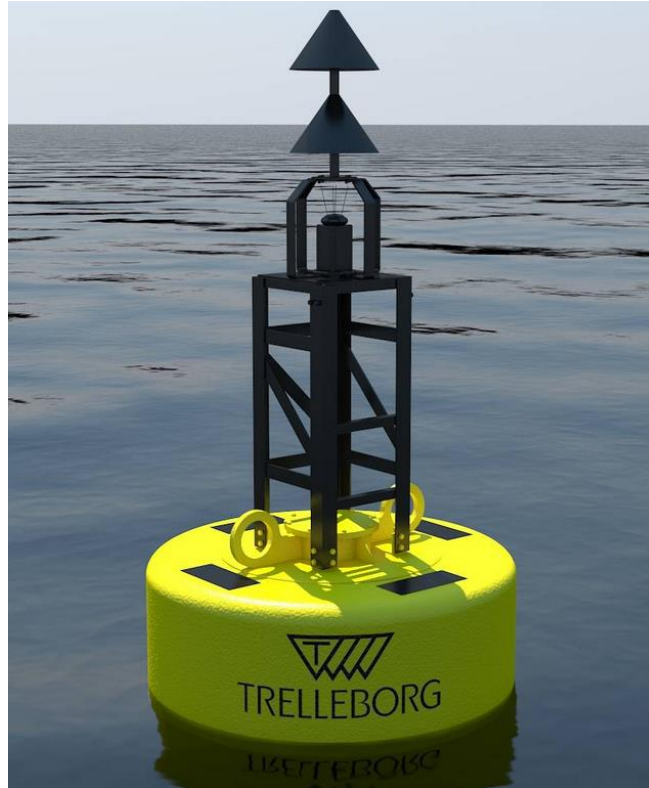


Figure 1.2: Photograph of buoy made up of syntactic foam (ref:<http://www.marinelink.com/news/trelleborg-compliant341500.aspx>)

The electronic packaging industry often makes use of particle-filled polymer composites as underfill materials to minimize thermal expansion. As shown in Figure 1.3, ball grid arrays, chip scale packages, and flip chip on board assemblies use epoxies filled with fillers to improve reliability by enhancing mechanical and thermal load carrying capacity as well as by providing environmental protection to solder joints.

In real life applications, structural members and their material constituents are subjected to a wide range of mechanical loading. Specifically, the mechanical loading can vary from being virtually static to highly transient. Researchers have demonstrated that material response is fundamentally linked to the rate at which the material is loaded and can significantly impact its critical material properties such as stiffness, yield strength, ultimate strength, failure stress and failure

strain [2][3][4][5][6][7]. Figure 1.4 shows examples of manufactured items where structural members and their material constituents encounter elevated rates of loading. Since the same material behaves differently under different loading conditions it is crucial to study their mechanical behavior under different loading rate regimes.

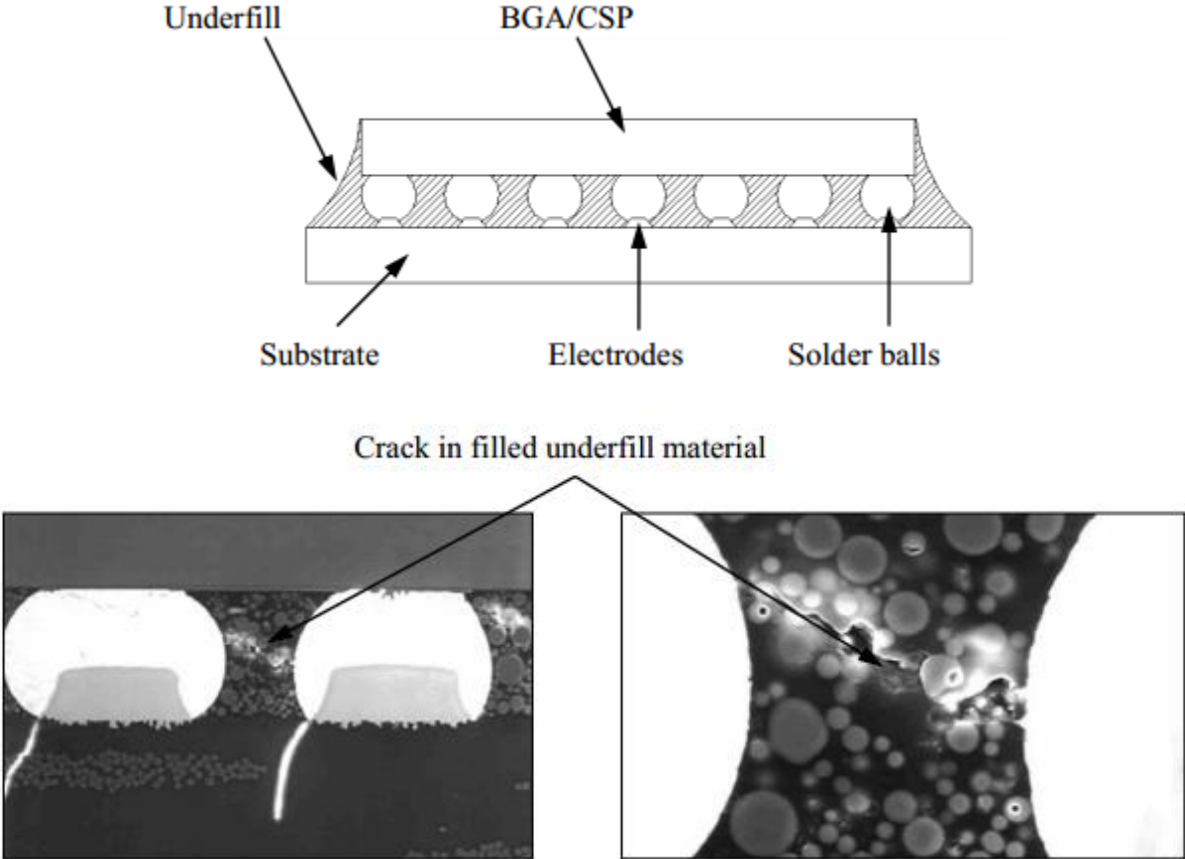


Figure 1.3: Schematic of particle-filled underfill material in electronic package (top) and underfill material failure (bottom) ([8])

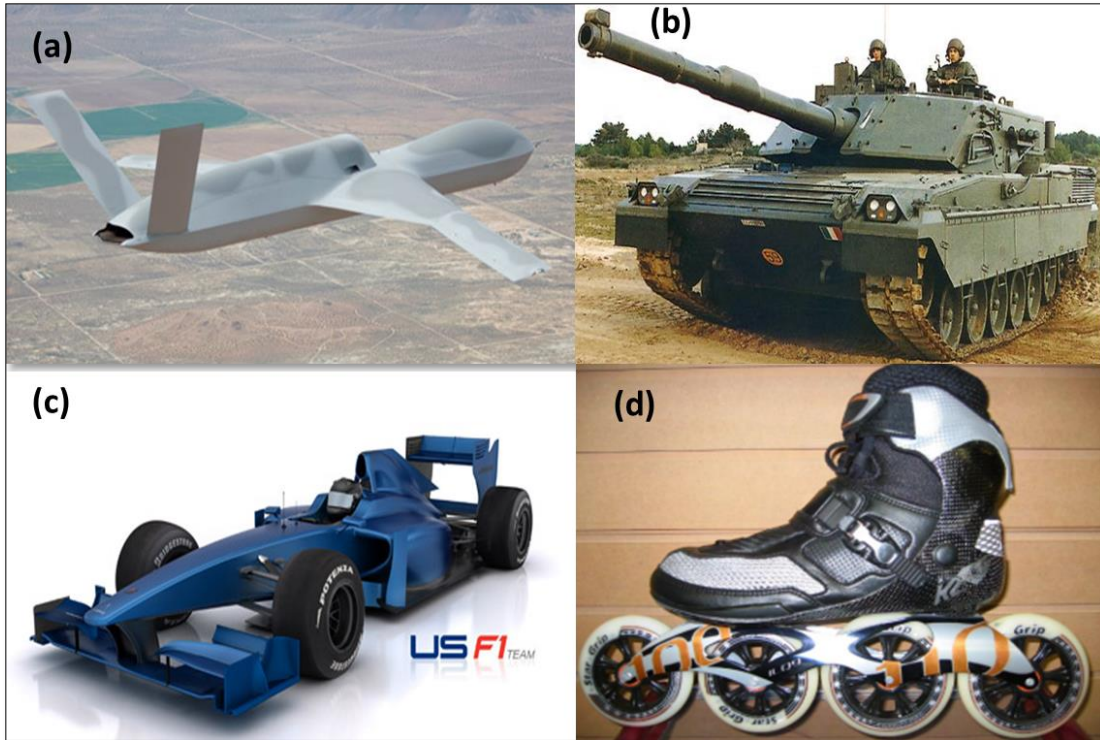


Figure 1.4 (a): Predator Tail Spar UAV cross section made up of carbon fiber composite (ref:<http://www.fiberdynamics.net/view-other-projects.html>); (b): Ariete main battle tank made up of composite armor (ref:<http://www.army-technology.com/projects/ariete/ariete1.html>); (c): Sports car body made up of carbon fiber composite (ref:<http://www.fiberdynamics.net/view-other-projects.html>); (d): Sporting skates made up of glass and carbon composite (ref:[http://depts.washington.edu/amtas/events/amtas\\_08spring/K2\\_Composites\\_in\\_Sporting\\_Goods.pdf](http://depts.washington.edu/amtas/events/amtas_08spring/K2_Composites_in_Sporting_Goods.pdf))

## 1.1 Motivation and literature review

In most particulate polymer composites, matrix materials are thermosets due to their higher stiffness, ultimate strength and glass transition temperature relative to the thermoplastics. The most common class of thermosets for structural applications are epoxies, as they are fairly easy to process and relatively inexpensive. However, their relative brittleness often leads to catastrophic structural damage due to poor crack growth resistance. The most common and cost effective approach to improve damage tolerance is to introduce secondary reinforcement phases by filling polymers with particles of different size, shape, stiffness, and filler-matrix interfacial strength.

### 1.1.1 Glass-filled epoxy composite: shape, volume fraction and loading rate effects

As said earlier, polymers are normally modified by adding inorganic-particulate fillers such as alumina, mica or silica, to name a few [5][9][10][11][12][13][14][15][16]. Song et al. studied the particle shape effects on the fracture and ductility of spherical and an irregularly shaped particle-reinforced Al-6061 composite containing 20%  $\text{Al}_2\text{O}_3$  by volume under quasi-static tensile loading [17]. The spherical particles produced a slightly lower yield strength and work hardening rate but considerably higher ductility than the irregular particle counterpart. Their finite element analysis results indicate that the distinction between the failure modes for these two composites can be attributed to the differences in the development of internal stresses and strains within the composite due to particle shape. Nakamura et al. examined the effect of particle size on the static fracture behavior of epoxy filled with different size (ranging from 6 to 42  $\mu\text{m}$ ) spherical silica particles [18]. They observed an increase in both energy release rate and fracture toughness with varying particle size. Fractography showed a relatively smooth fracture surface with small particles (6  $\mu\text{m}$ ) and a rough surface with large particles (caused by crack deflections around large particles). Wu analytically studied the effect of inclusion shape on the elastic modulus of two phase solids [19]. Their disk-shaped inclusions showed the maximum enhancement in elastic modulus compared to needles and spheres. The effect of particle size (4.5–62  $\mu\text{m}$ ) on the elastic modulus of epoxy/spherical glass particle composites was examined by Spanoudakis et al.[20]. At lower volume fractions ( $V_f$ ) (10–18%), the modulus was nearly independent of particle size. For higher  $V_f$  (30–46%), there was a slight decrease in the elastic modulus with increasing particle size. In a similar study, the effect of particle size on the modulus of epoxy/spherical and irregularly-shaped silica composites have been explored [21] for a size range of 2-30  $\mu\text{m}$  and the modulus was observed to remain constant with particle size. Kitey and Tippur studied the role of particle size on

the dynamic fracture behavior of glass-filled epoxy using optical interferometry and high-speed photography [22]. Spherical particles (ranging from 7-200  $\mu\text{m}$ ) were used in their work to reinforce epoxy at a constant 10%  $V_f$ . The elastic characteristics were unaffected by the filler size, whereas fracture toughness increased with size from 7-35  $\mu\text{m}$  and then decreased from 35-200  $\mu\text{m}$ .

The existing literature in this area suggests that the particle shape effect on fracture toughness for particulate composites is largely unexplored. Therefore, a focus of the current research is to understand the effect of filler shape and their volume fraction on fracture behavior of glass-filled epoxy composites, particularly under *dynamic* loading conditions. However, the failure of the Particulate Polymer Composite (PPC) could initiate differently under different loading rates [2][3][4][6][10][23][24]. Hence, to bridge this gap, the loading rate effects, characterized by the rate of change of stress intensity factor on dynamic fracture behavior of epoxy filled with 10%  $V_f$  rod-shaped filler, were also studied since this filler shape produced a large improvement in fracture toughness.

### **1.1.2 Carbon nanotube (CNT) based conventional/hierarchical epoxy composite**

Since the discovery of CNTs in 1991 by Iijima of the NEC fundamental research laboratory in Japan, extensive research has occurred in this area to understand their physical and mechanical properties and their use in diverse engineering disciplines [25]. From exceptional mechanical properties where the strength and resilience combined with low density exceeds any current existing material to unique electronic properties and a thermal conductivity higher than that of a diamond, CNTs offer tremendous opportunities for the development of multi-functional material systems [26]. Due to potential enhancement in material properties, the development of nanoscale reinforced composites is presently seen as one of the most promising approaches in the field of engineering

applications. In particular, the extraordinary high strength property combined with its lightweight makes nanotube-reinforced composites a potential candidate for naval and aerospace applications.

Several researchers have investigated the mechanical properties of nanocomposites with the addition of carbon nanotubes as the filler material. Gojny et al. studied the mechanical properties of double-walled carbon nanotube-reinforced epoxy composite [27]. They observed that the introduction of only 0.1% of CNTs by weight led to an increase of strength, Young's modulus and strain to failure. Particularly, they found significant advancement in fracture toughness compared to other enhancements. In another study, Schadler et al. investigated the mechanical behavior of 0.5% by weight multi-walled carbon nanotube-reinforced epoxy composite in both compression and tension [28]. They noticed a significant increase in compression as well as in tensile modulus. It has been found that during the load transfer to multi-walled nanotubes that only the outer layers are stressed in tension whereas all the layers participated in compression. Therefore, the load transfer to the nanotubes in the composite is much higher in compression, which leads to a higher elastic modulus in compression than in tension. To understand the dynamic behavior of nanocomposites, Jindal et al. analyzed CNT-reinforced polycarbonate composite using the Split Hopkinson Pressure Bar (SHPB) [29]. It has been observed that a CNT concentration of 0.5% by weight is capable of enhancing the impact strength of the composite by about 10% at a true strain of 25%.

However, due to inhomogeneous dispersion of nanotubes, a large scatter in the experimental data in case of CNT-reinforced composites has been observed. Therefore, the primary issue of homogeneous dispersion of the CNTs into a polymer matrix has to be resolved to effectively transfer the excellent properties of CNTs to the nanocomposites [26]. Due to their unique atomic structure and morphology CNTs possess enormous surface area. This surface area acts as interface for stress transfer, but is also responsible for agglomeration and entanglement of CNTs during

material processing. In the past, various techniques such as stirring, kneading and sonication etc. have been used to disperse the CNTs homogeneously into the polymer matrix. Although these techniques showed respective advantages, detrimental effect on mechanical properties was also noticed due to the CNT damage into the polymer matrix [30].

Failure to achieve superior material properties from CNT-reinforced composites due to inhomogeneous dispersion has led researchers to grow CNT directly on the surface of various types of substrates, such as carbon fibers, graphite foil and glass fibers. Therefore, CNT grown substrates which acts as CNT carrier can be dispersed homogeneously into the polymer matrix without affecting the nanotube properties. Hung et al. characterized the tensile response of nanotube-grown carbon fiber-reinforced epoxy composite [31]. The Chemical Vapor Deposition (CVD) method was used to grow the carbon nanotubes on micron-size carbon fibers. A bundle of CNT-grown carbon fiber was impregnated with an epoxy resin to form a unidirectional composite. When compared with the conventional fiber composites, the present composite adds two new material properties: the CNT-matrix interface strength, and the CNT tensile strength. The importance of these strengths depends on the aspect ratio (length to diameter ratio of nanotubes) and quality of nanotubes. Tensile tests were carried out on the composite and different failure modes were studied. It was found that CNT/fiber interface fracture was the most dominant failure mode. The other modes were debonding and sliding of CNTs. The capability of energy dissipation can be improved if the debonding and the sliding of CNTs become more prevalent. Mathur et al. examined the flexural properties of nanotube-grown multi-directional carbon fiber-reinforced phenolic resin composite [32]. The mechanical properties were found to increase with the increasing amount of Chemical Vapor Deposition (CVD) grown CNTs on carbon fibers. The flexural modulus improved



by 28% for unidirectional, 54% for bi-directional and 46% for tri-directional composite as compared with neat carbon fiber-reinforced composite. The flexural strength also improved by 20%, 75% and 66%, respectively. However, all existing CNT growing techniques require fairly complex setups, and high cost involved in their production has been the major challenge for producing them in large quantity.

To reinforce the nanocomposite homogeneously, another way is to impregnate the CNT-grown micro and nano sized spherical fillers directly into the polymer matrix. The resulting “sea urchin configuration” helps the filler to anchor firmly into the polymer matrix, which potentially enhances the mechanical response of nanocomposites. To explore this feasibility, Nguyen et al. analyzed mechanical characteristics of CNT-grown stainless steel-reinforced polyurethane composite [33]. Multi-walled CNTs were directly grown on spherical stainless steel particles average diameter of 100 nm using the CVD method to produce a sea urchin-like filler. The impregnation of these particles into the polyurethane matrix resulted in a high tensile strength composite due to their effective dispersion and better interfacial bonding with the polymer matrix.

In addition to mechanical strengthening, nanoscale fillers also facilitate thermal and electrical conductivity improvements in polymer composite. In the past, carbon black has been commonly used to enhance the conductivity of polymer composites. However, a high concentration of carbon black in the polymer matrix often deteriorates the mechanical properties of the composite. Therefore, highly conducting material such as CNT is viewed as a more appropriate filler in this regard, since it can enhance electrical and thermal transport even at very low concentration without compromising its mechanical characteristics. Zhan et al. investigated the electrical properties of nano ceramics reinforced with Single-Walled Nanotubes (SWNTs) and reported a several fold

increase in its electrical conductivity [34]. Moisala et al. studied the thermal and electrical conductivity of 0.005-0.5 weight % of CNT-infused epoxy composite [35]. They found that multi-walled nanotube composites had an electrical percolation threshold of <0.005 weight %, whereas the thermal conductivity of the same sample increased modestly as a function of the filler content. The effect of functionalization on thermo-mechanical properties of MWNTs/epoxy composite was studied by Gojny et al. [36]. They observed that an increase in the amount of nanotubes led to an increase in glass transition temperature. Also, samples containing functionalized nanotubes showed a stronger influence on glass transition temperature when compared to composites containing the same amount of non-functionalized nanotubes, demonstrating the influence of a functionalization of CNTs on the interfacial interactions between CNT and polymer.

The existing literature suggests that a simple and cost effective technique is required to produce CNTs in large quantity. Also, to address the poor dispersion, CNTs should be directly grown on a filler surface and then dispersed into the polymer matrix to achieve superior mechanical, thermal and electrical properties in the resulting composite.

## **1.2 Objectives**

Based on the literature review presented in the previous section the primary objectives of this dissertation are as follows:

- Investigate the effect of filler-shape and volume fraction on dynamic fracture behavior of glass-filled epoxy composite.
- Investigate the role of loading rate on dynamic fracture behavior of glass-filled epoxy composite.

- Investigate mixed-mode fracture behavior of glass-filled epoxy composite under impact loading.
- Model of carbon fiber modified epoxy composite using the 2D finite element method and the RAE approach to capture some salient features observed experimentally.
- Grow carbon nanotubes on engineering substrates using a novel Poptube approach which is both fast and inexpensive, and uses a readily available kitchen microwave.
- Develop micro-nano hierarchical epoxy composites using CNT-grown engineering substrates and study their fracture characterization.

### **1.3 Organization of dissertation**

The dissertation is organized into seven chapters. This first introduction chapter describes the topics of interest along with the motivation for the present research and also the literature which provides an overview of previous research in this area.

Chapter 2 presents the major experimental testing techniques used for mechanical characterization of materials developed/processed during this research. Quasi-static and dynamic fracture test setups used along with high speed photography and digital image correlation are discussed.

Chapter 3 describes material preparation of glass-filled epoxy particulate composites with three different filler shapes and volume fractions. It includes the effect of filler shape, volume fraction and loading rate studied using digital image correlation and high-speed photography under impact loading. Fractographic evaluation of glass-filled epoxy composite and the various mechanisms associated with crack-growth are explained.

In Chapter 4 the mixed-mode fracture behavior of glass-filled particulate composite is studied using digital image correlation and high-speed photography under impact loading and the results are compared with the corresponding neat epoxy. Fracture envelope is drawn for both neat and glass-filled epoxy using experimentally measured crack initiation fracture toughness. The crack kink angles are measured and examined relative to existing theories for brittle materials. Fractographic evaluation explained the failure mechanisms associated with the mixed-mode versus mode-I loading of glass-filled epoxy composite.

Chapter 5 discusses the finite element modeling of carbon fiber modified epoxy composite under quasi-static tension. The quasi-static tension tests are performed on neat epoxy and carbon fiber modified epoxy. The material property obtained from the quasi-static tension test of neat epoxy and the material property of carbon fiber obtained from the manufacturer are used as input in finite element simulations. The modeling process of a 3D carbon fiber modified specimen was simplified using 2D models based on a representative area element (RAE). The analysis was carried out in plane stress and plane strain conditions to obtain the upper and lower bounds of mechanical response. The simulations were limited to recovering the stress-strain response of carbon fiber modified epoxy composite and comparing with it the experimental results. Also, XFEM was employed to model the crack propagation in carbon fiber modified epoxy composite using Abaqus.

In Chapter 6 a particularly novel technique called Poptube Approach is presented to grow carbon nanotubes on various engineering substrates using a kitchen microwave in just a few seconds. Using this novel poptube approach, carbon nanotubes are grown on hollow glass-microballoons, solid glass spheres and carbon fibers and then used as filler phase in the synthesis of micro-nano hierarchical composites. This chapter also discusses the quasi-static fracture behavior of these hierarchical composites.

Finally, Chapter 7 presents the summary and conclusions of the present research and potential topics for future research.

## CHAPTER 2

### EXPERIMENTAL TECHNIQUES

This chapter details the experimental techniques employed in this research to study the mechanical behavior of particulate polymer composites under quasi-static and dynamic (impact) loading. The dynamic fracture behavior of particulate composite is studied using digital image correlation and high-speed photography under impact loading.

#### 2.1 Quasi-static tension and fracture setup

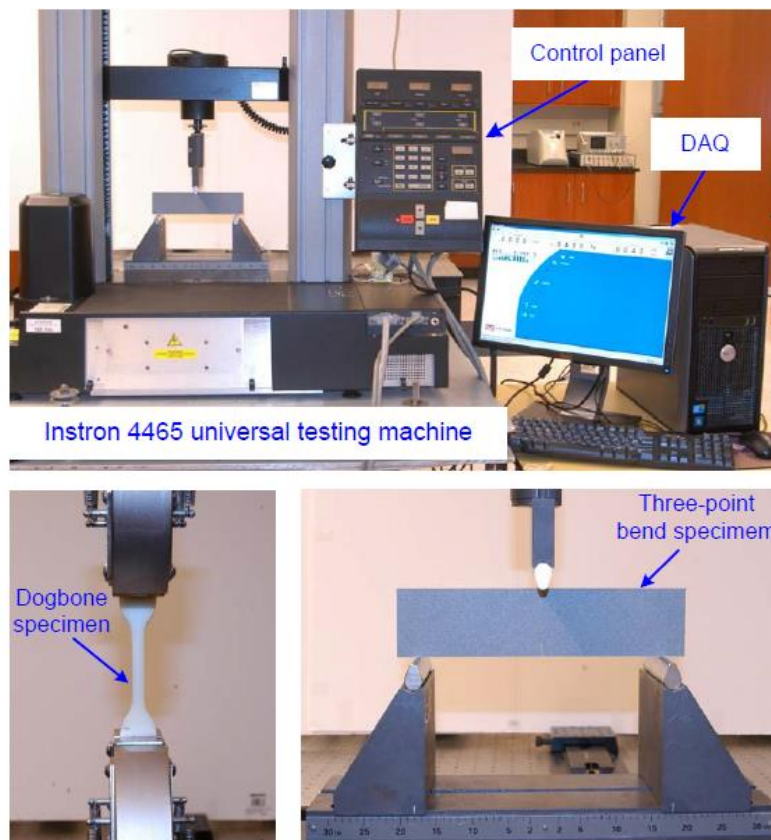


Figure 2.1: Experimental setups involving (a) Instron 4465 used for quasi-static (b) tension and (c) fracture experiments ([13])

The quasi-static crack initiation toughness,  $K_{IC}$ , measurements were performed using Instron 4465 universal testing machine. Fracture tests were carried out in symmetric three-point bending configuration and displacement control mode using a cross-head speed of 1.27 mm/min. Typically, the load-displacement response was linear up to crack initiation followed by an abrupt fracture of the specimen (Figure 2.1). The quasi-static fracture toughness was calculated using Equation (2.1).

$$K_{IC} = \frac{\left(\frac{P_{max}}{B\sqrt{W}}\right)\left(3\frac{S}{W}\sqrt{\frac{a}{W}}\right)}{2\left(1+2\frac{a}{W}\right)\left(1-\frac{a}{W}\right)^{1.5}} \left[1.99 - \frac{a}{W}\left(1 - \frac{a}{W}\right)\left\{2.15 - 3.93\left(\frac{a}{W}\right) + 2.7\left(\frac{a}{W}\right)^2\right\}\right] \dots\dots\dots (2.1)$$

where  $P_{max}$  is the maximum load prior to fracture,  $a$  is the crack length,  $B$  is the thickness,  $W$  is the width and,  $S$  is the span.

The uniaxial quasi-static tensile tests were performed on dogbone-shaped particulate polymer composite using Instron 4465. Tension tests were carried out for measuring elastic modulus, ultimate tensile strength, and strain at break in displacement control mode with a cross-head speed of 2 mm/min.

## 2.2 Dynamic fracture setup

In this research, the dynamic fracture behavior of particulate polymer composite was studied using a long-bar impactor. A schematic of the experimental setup used for dynamic fracture tests is shown in Figure 2.2. The setup included a 1.83 m long, 25.4 mm diameter long-bar with a 6.35 mm diameter bull-nose tip registered against an unconstrained specimen and a 304.8 mm long, 25.4 mm diameter striker held inside the barrel of a gas-gun (Figure 2.3). Both the long-bar and the striker were of the same diameter and made of aluminum 7075-T6. This eliminated the impedance mismatch between the long-bar and the striker. Three different dynamic loading rates

were achieved by using different pulse shapers between the striker and the long-bar. The role of the pulse shaper was to ramp up the stress amplitude in a controlled fashion in the long-bar during impact [37]. The striker was launched towards the long-bar using the gas-gun at a velocity of  $\sim 16$  m/s. When the striker contacted the long-bar, a compressive stress wave was initiated and propagated through the bar before its transmission into the specimen.

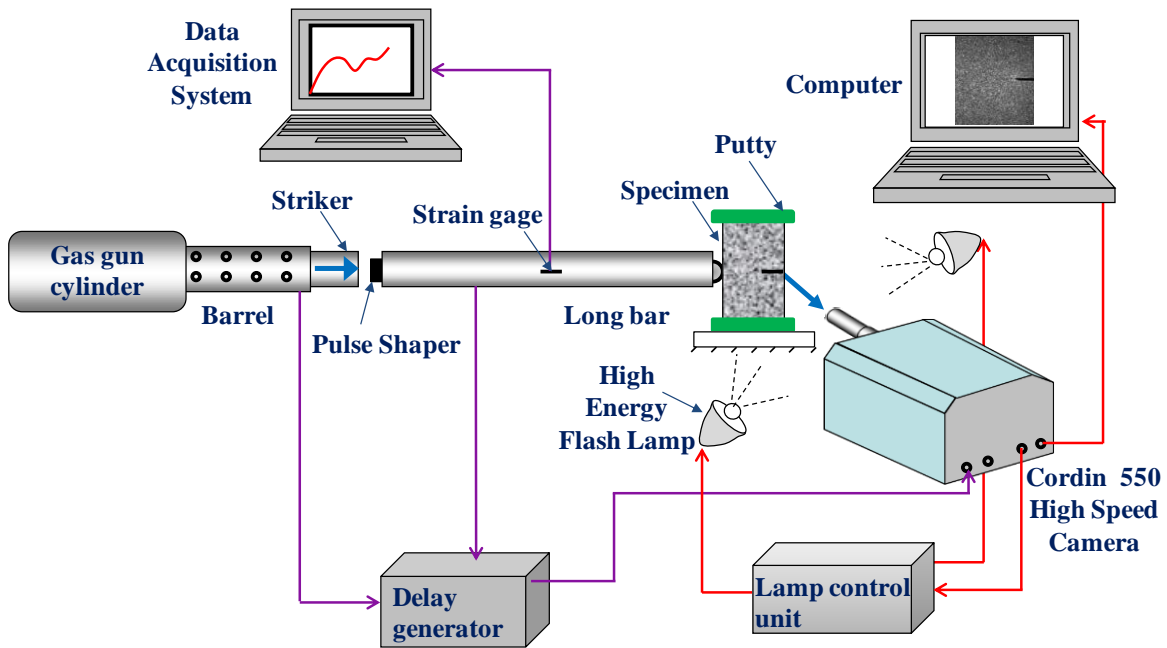


Figure 2.2: Schematic of dynamic fracture setup under impact loading

A stochastic black and white speckle pattern was sprayed onto the specimen surface for performing in-plane deformation measurement using the 2D Digital Image Correlation (DIC) method (DIC details are explained in the next section). The pattern was photographed using a Cordin-550 ultrahigh-speed digital camera (Cordin Scientific Imaging, Salt Lake City, UT, USA). Figure 2.4 shows the internal optical arrangement of the Cordin 550 camera. It is capable of recording images at rates of up to 2 million frames per second on 32 individual  $1000 \times 1000$  pixel CCD sensor arrays positioned circumferentially around a five-facet rotating mirror which reflects and sweeps light over these sensors. Prior to loading, a set of 32 images corresponding to the



undeformed state of the specimen were recorded at a rate of  $\sim 300,000$  frames per second. To record a second set of 32 images corresponding to the deformed state of the specimen, the striker was launched towards the long-bar by discharging the gas-gun. When the striker contacted the long-bar it completed an electrical circuit, signaling a delay generator to trigger the camera. The camera in turn triggered a pair of high energy flash lamps and initiated image capture at the same framing rate. Thus, each image in the undeformed (reference) set had a corresponding image in the deformed set. The recorded sets of deformed and undeformed images were then correlated to obtain in-plane displacement components.

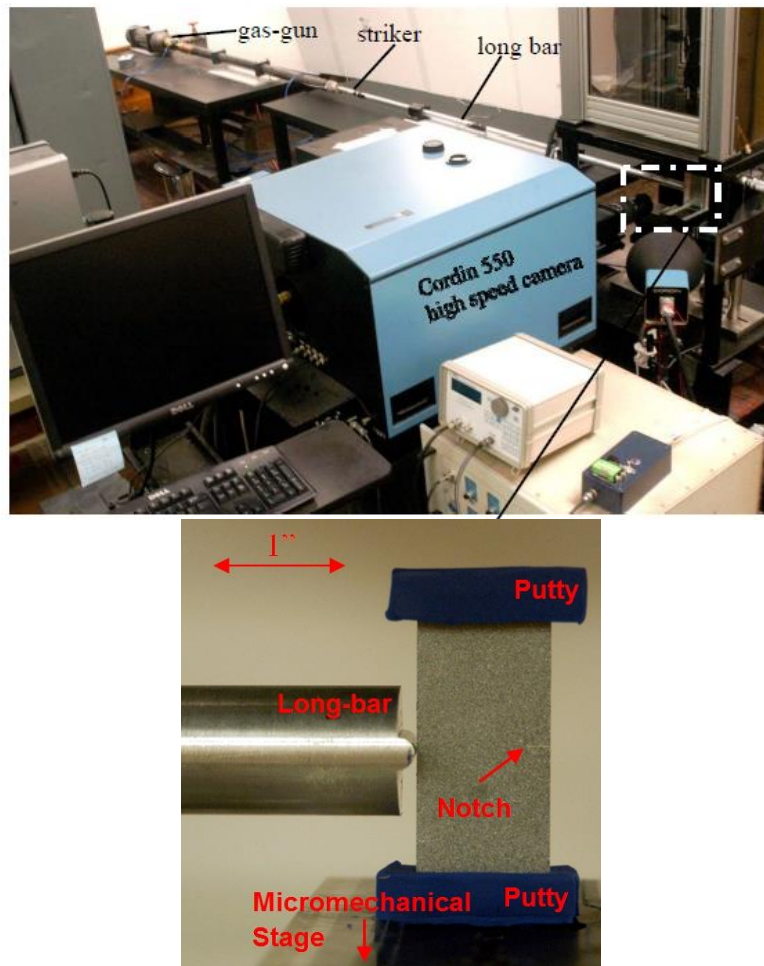


Figure 2.3: Experimental setup used for dynamic fracture experiments (top). Close-up of the long-bar and the specimen (bottom) (ref:[38])

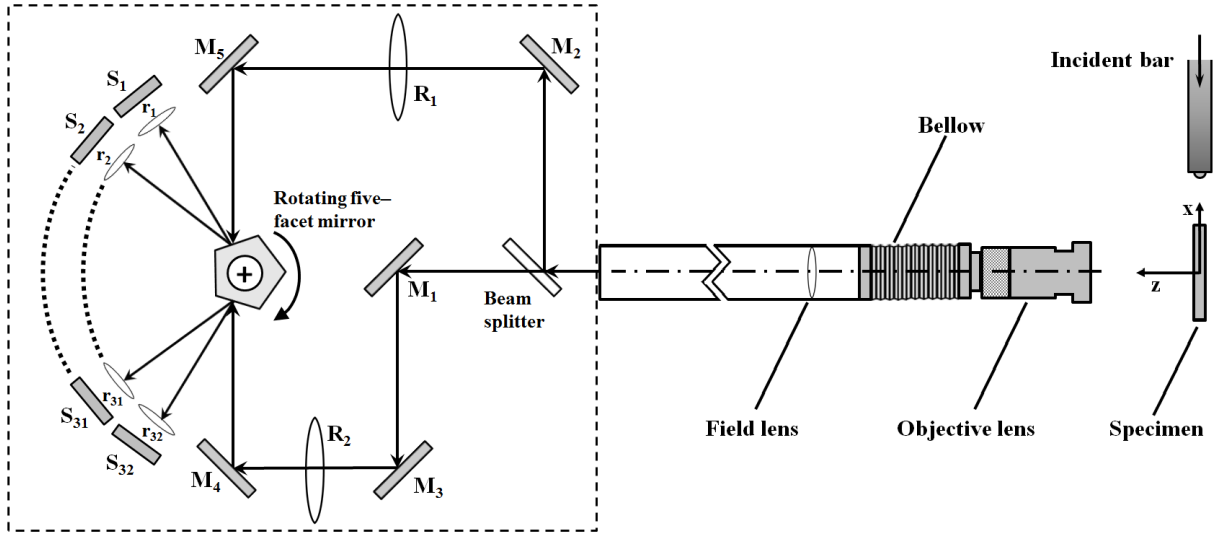


Figure 2.4: Schematic of ultra-high speed Cordin camera:  $M_1$ -  $M_5$  are mirrors;  $R_1$  and  $R_2$  are relay lenses;  $r_1$ - $r_{32}$  are relay lenses for CCDs;  $S_1$ - $S_{32}$  are CCD sensors

### 2.3 Digital Image Correlation

Digital Image Correlation (DIC) was first developed and applied in experimental stress analysis in the 1980's [39][40][41]. A major advantage of DIC is that it can be applied to structures having irregular geometries [42][43]. DIC is superior to strain gauges due to its non-contact and quantitative full-field surface deformation measurement capability, and less cumbersome to implement, making it an ideal candidate for performing full field deformation measurements in engineering applications. Generally, 2D DIC method can be implemented using the four steps as follows:

- **Specimen preparation:** This involves covering the specimen surface with stochastic black and white pattern to perform in-plane deformation measurement. The stochastic pattern can be the natural texture of the specimen surface or an artificial decoration.
- **Region of interest (ROI) selection:** The ROI is a selected sub-image of the specimen surface identified for a particular purpose (i.e., crack propagation or critical stress region confined

within the ROI). DIC provides full-field information only in the ROI. Therefore, selection of the ROI is the most critical step in the DIC process.

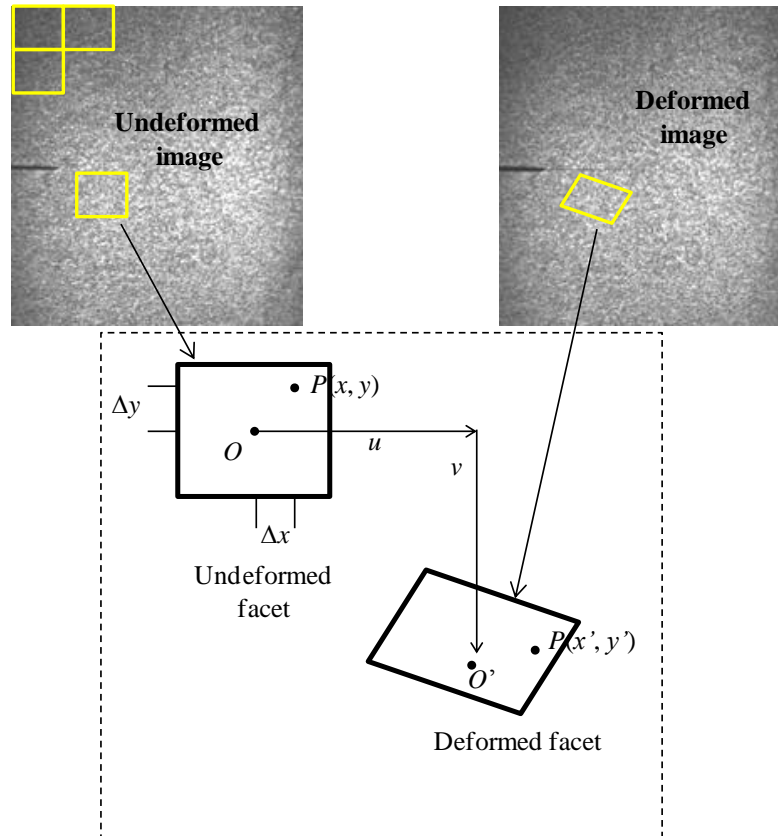


Figure 2.5: Schematic to explain Digital Image Correlation (DIC) technique

- **Image acquisition of ROI before and after loading the specimen:** In 2D DIC, the image of ROI is captured using a digital camera before and after loading the specimen. In this process, the ROI must be flat and parallel to the charged coupled device (CCD) sensor of the digital camera.
- **Processing the acquired images using a computer program:** The basis of DIC is the mapping of a particular point (or pixel) between two images in the same ROI before and after loading. To achieve this, the ROI surface is illuminated using incoherent light (typically a white light) source to produce a diffusely reflected light from the ROI surface. The CCD sensor

captures an analog intensity field  $I(x, y)$  over the ROI. Then, analog intensity field  $I(x, y)$  is converted into a discrete gray scale field  $D(x, y)$ . The gray scale intensity of the ROI is used in the pattern matching process. In a common DIC process, the ROI is divided into facets (sub-images). Then, for each facet in the undeformed image its location was searched in the deformed image as shown in Figure 2.5. For a facet centered at point  $O$  in the undeformed state, the discretely sampled intensity variations can be represented using interpolation functions at  $O$  and its neighborhood including point  $P$  by Equations (2.2) and (2.3), respectively.

$$D(O) = D(x, y) \dots\dots\dots (2.2)$$

$$D(P) = D(x + dx, y + dy) \dots\dots\dots (2.3)$$

where, the neighboring point  $P$  is located at an incremental distance from the origin  $O$ . After deformation, the discretely sampled intensity variations at new locations (denoted by the primed symbols) are given by, Equations (2.4) and (2.5).

$$D'(O') = D(x', y') \dots\dots\dots (2.4)$$

$$D'(P') = D(x' + dx', y' + dy') \dots\dots\dots (2.5)$$

where  $x' = x + u(x, y)$ ,  $y' = y + v(x, y)$ . For small deformations, the above equations can be represented by Equations (2.6) and (2.7).

$$D'(x', y') = D[x + u(x, y), y + v(x, y)] \dots\dots\dots (2.6)$$

$$D'(x' + dx', y' + dy') = D[x + dx + u(x + dx, y + dy), y + dy + v(x + dx, y + dy)] \dots\dots\dots (2.7)$$

Alternatively, using Equation (2.8)

$$D(x'+dx', y'+dy') = D\left[x+u(x, y) + \left(1 + \frac{\partial u}{\partial x}\right)dx + \frac{\partial u}{\partial y}dy, y+v(x, y) + \frac{\partial v}{\partial x}dx + \left(1 + \frac{\partial v}{\partial y}\right)dy\right] \dots \quad (2.8)$$

If the facet is sufficiently small then displacement gradients are nearly constant within the facet, then  $u, v, \partial u/\partial x, \partial v/\partial x, \partial u/\partial y, \partial v/\partial y$  can be evaluated. This is generally correlation criterion. Although different correlation criteria can be found in the literature, these can be divided into two categories, namely cross correlation (CC) and sum of squared differences (SSD) [44][45]:

(1) Cross-correlation (CC):

$$C_{CC} = \sum_i [D'(O')D(O)] \dots \dots \dots \quad (2.9)$$

(2) Normalized cross-correlation (NCC):

$$C_{NCC} = \frac{\sum_i D'(O')D(O)}{\sqrt{\sum_i D'(O')^2} \sqrt{\sum_i D(O)^2}} \dots \dots \dots \quad (2.10)$$

(3) Sum of squared differences (SSD):

$$C_{SSD} = \sum_i [D'(O') - D(O)]^2 \dots \dots \dots \quad (2.11)$$

(4) Normalized sum of squared differences (NSSD):

$$C_{NSSD} = \sum_i \left[ \frac{D'(O')}{\sqrt{\sum_i D'(O')^2}} - \frac{D(O)}{\sqrt{\sum_i D(O)^2}} \right]^2 \dots \dots \dots \quad (2.12)$$

Maximizing Equations (2.9) and (2.10), or minimizing Equations (2.11) and (2.12) in the above will provide estimates of all displacement and displacement gradients.

## 2.4 Facet (sub-image) size study

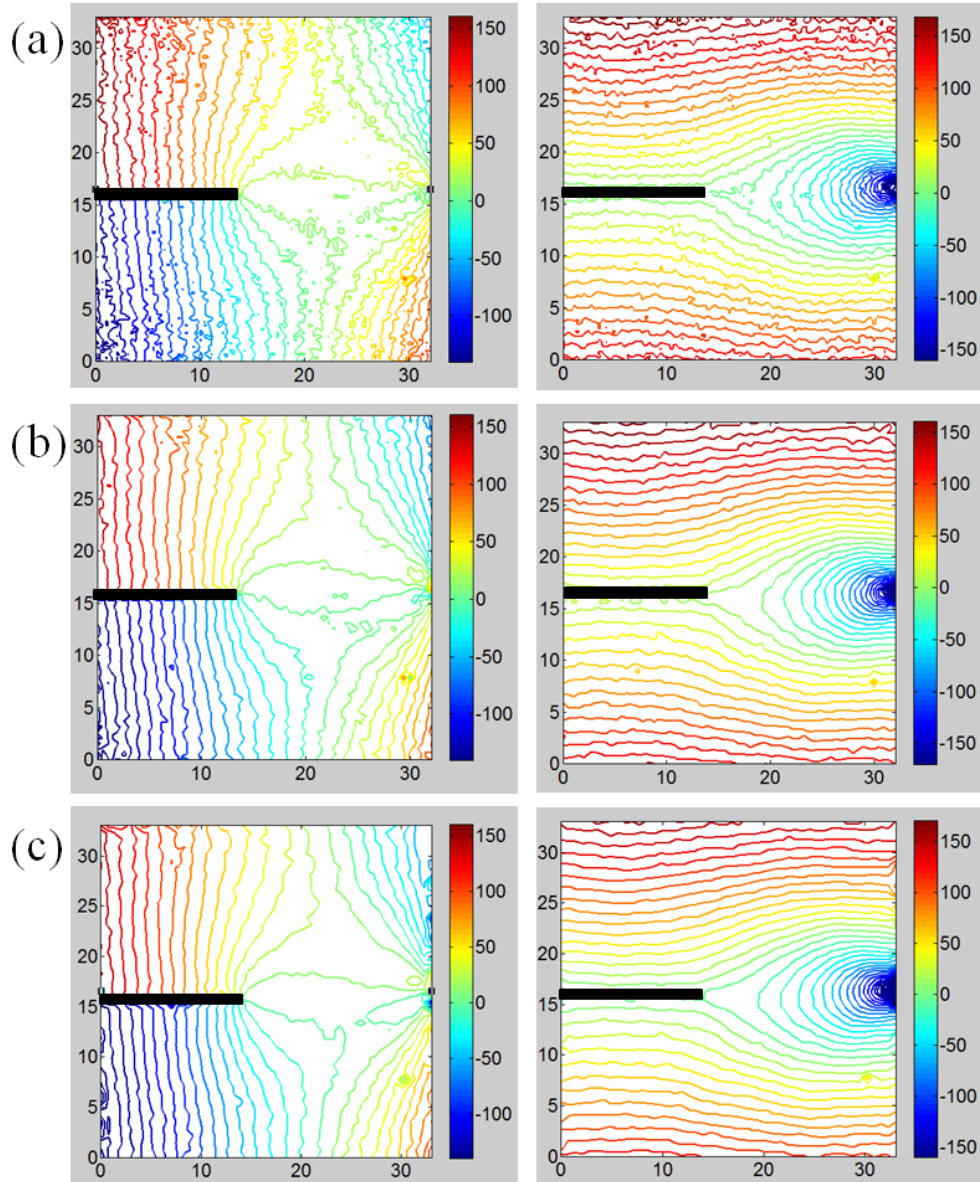


Figure 2.6: Crack opening ( $u_y$ ) and crack sliding ( $u_x$ ) displacement contours in steps of  $10\ \mu\text{m}$ , respectively (units on the displacement contour on  $x$ - and  $y$ -axis are in mm). First row:  $10 \times 10$  pixel facet size (Fig. (a)), middle row:  $15 \times 15$  pixel facet size (Fig. 2.6(b)), and last row:  $20 \times 20$  pixel facet size (Fig. 2.6(c)); Scale factor:  $1\ \text{pixel} = 33\ \mu\text{m}$ .

In order to determine an appropriate facet size for DIC, a pair of images from a dynamic fracture test of 10% glass-filled epoxy was correlated over a range of possible sizes. Figure 2.6 shows the crack opening ( $u_y$ ) and crack sliding ( $u_x$ ) displacement contours in steps of  $10\ \mu\text{m}$ , (units

on the displacement contour on  $x$ - and  $y$ -axis are in mm) for three different  $10 \times 10$  (Figure 2.6 (a)),  $15 \times 15$  (Figure 2.6 (b)) and  $20 \times 20$  (Figure 2.6 (c)) pixel facet sizes, respectively. For smaller facet size, DIC algorithm averages the gray scale intensity over a smaller facet area which results in relatively noisy displacement contours. It can be seen in Figure 2.6 as the facet size increases from  $10 \times 10$  to  $20 \times 20$  pixels the displacement contours get smoother due to the averaging effect. This facet size comparison study explains that if the facet size is too small it produces fairly noisy displacement contours on the other hand if the facet size is too big it produces overly smoothed displacement contours resulting in a relatively poor spatial resolution. Hence, the selected facet size was  $15 \times 15$  pixels throughout this research due to the inherent trade-off between noise and spatial resolution resulting from averaging effects over the facet size.

Figure 2.7 shows the variation in dynamic SIFs  $K_I^d$  with facet size of  $10 \times 10$ ,  $15 \times 15$  and  $20 \times 20$  pixels. The different facet sizes lead to different displacement matrix sizes, e.g., for  $1000 \times 1000$  pixel image;  $10 \times 10$ ,  $15 \times 15$  and  $20 \times 20$  pixels size facet would have  $100 \times 100$ ,  $66 \times 66$  and  $50 \times 50$  size displacement matrix, respectively. It should be noted that to determine  $K_I^d$ , the crack tip location could not be identified exactly for different facet sizes using the crack opening displacement matrix. The crack tip was identified as the location in the crack opening displacement matrix where the difference between the top and bottom crack lip displacements decreases to less than  $4\text{-}6 \mu\text{m}$ . Therefore, the crack tip location is likely to be different for different facet sizes for different spatial resolutions caused by the facet size variation. However, there are small changes in  $K_I^d$  for different facet sizes. The  $K_I^d$  for facet size of  $15 \times 15$  pixels is  $\sim 6\%$  higher and  $\sim 2\%$  lower than  $K_I^d$  of facet size  $10 \times 10$  and  $20 \times 20$  pixels, respectively.

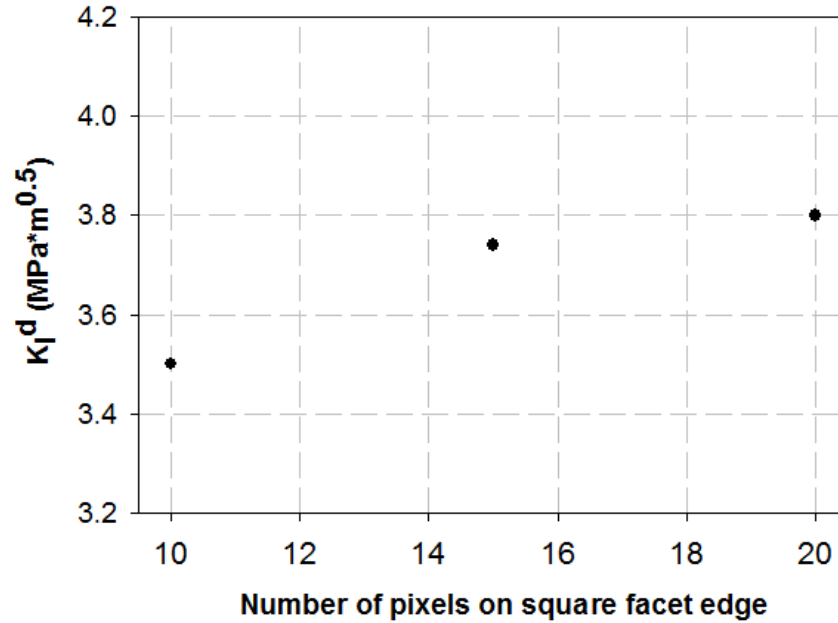


Figure 2.7: Variation of  $K_I^d$  with facet size

## 2.5 Estimation of scale factor

Scale factor is calculated to resize the DIC contours to the actual ROI scale. It is calculated by estimating the size of one pixel in micron. That is if 100 pixels are distributed over 20 mm length of ROI, the size of one pixel would be  $(20 \times 1000)/100 = 200 \mu\text{m}$ . The product of total number of pixels along a dimension and the scale factor (size of one pixel) determines the size of ROI along that dimension.



## CHAPTER 3

### **EFFECT OF FILLER SHAPE, VOLUME FRACTION AND LOADING RATE ON DYNAMIC FRACTURE BEHAVIOR OF GLASS-FILLED EPOXY**

This chapter presents the effect of filler shape, volume fraction and loading rate of glass-filled epoxy composite on its fracture behavior under impact loading. The first two sections discuss the specimen preparation and their material property measurement, respectively. The next two sections deal with experimental measurement using digital image correlation and high speed photography, and optical data analysis procedure to extract stress intensity factors, respectively. The section after that shows experimental repeatability and experimental results validation using the finite element method. The last section presents the detailed experimental results supported by existing failure modes in these composites responsible for increase in dynamic fracture toughness with filler shape, volume fraction and loading rate variations.

#### **3.1 Material preparation**

Glass fillers of similar density (intrinsic property) and size, but differing aspect ratios (flakes, rods, and spheres; see Table 3.1) were chosen to study their relative shape effects on the dynamic fracture mechanisms of Particulate Polymer Composites (PPC) (Figure 3.1). None of the fillers used had their surface modified by wetting agents and this was guided by the earlier work by Kitey and Tippur [46] showing uncoated fillers produce better fracture characteristics under dynamic loading conditions.

Table 3.1: Glass Filler Characteristics

Shape	Source	Average Dimensions	Aspect Ratio*(AR)	Density (kg/m <sup>3</sup> )
Flake	ACF-300: Isorca Inc., USA	30 μm wide, 5 μm thick	30/5 = 6	2,500
Rod	Milled Fiber: Fiberglass Supply, USA	800 μm long, 10 μm diameter	800/10 = 80	2,500
Sphere	A300: Potters Industries, USA	35 μm diameter	35/35 = 1	2,500

\*Aspect Ratio was determined by dividing the largest average dimension by the shortest average for each filler type, provided by the manufacturer.

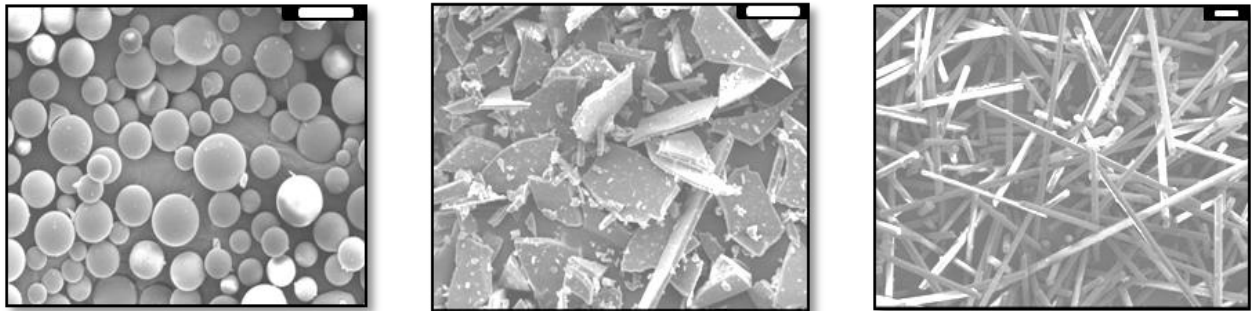


Figure 3.1: SEM micrographs of sphere-, flake- and rod-shaped glass fillers used in present study (left to right respectively; scale bar: 50 μm)

The glass fillers were dispersed into a low-viscosity epoxy (Epo-Thin, from Beuhler Inc., USA; Bisphenol-A resin and Amine based hardener; densities 1130 kg/m<sup>3</sup> and 961 kg/m<sup>3</sup>, respectively). To carry out the dynamic fracture study, glass-filled epoxy (containing 0% (neat epoxy), 5%, 10% and 15% glass filler by volume, respectively) sheets were cast. To ensure uniform dispersion, fillers were added into the epoxy resin and stirred and then degassed until the mixture appeared to be free from trapped air bubbles. Subsequently, stoichiometric proportion of hardener was added to the mixture and stirred until it gelled to avoid settlement of filler particles before pouring into the mold. Upon curing for a minimum of 7 days, the sheets were demolded and machined into rectangular specimens of dimensions 60 mm × 30 mm × 9 mm (Figure 3.2 (a)). An

edge notch of 6 mm length was introduced at the mid-span of each specimen using a diamond-impregnated circular saw and the notch tip was sharpened using a sharp razor blade. The uniformity of filler dispersion was confirmed subsequently using Scanning Electron Microscopy (SEM) images of fractured specimen surfaces. Fractographs at four different locations for 15%  $V_f$  rod-shaped glass-filled epoxy are shown in Figure 3.2(b). The 15%  $V_f$  rod-shaped filler example is presented here as they tend to be most prone to agglomeration. However, as evident from the micrographs, agglomeration is largely absent.

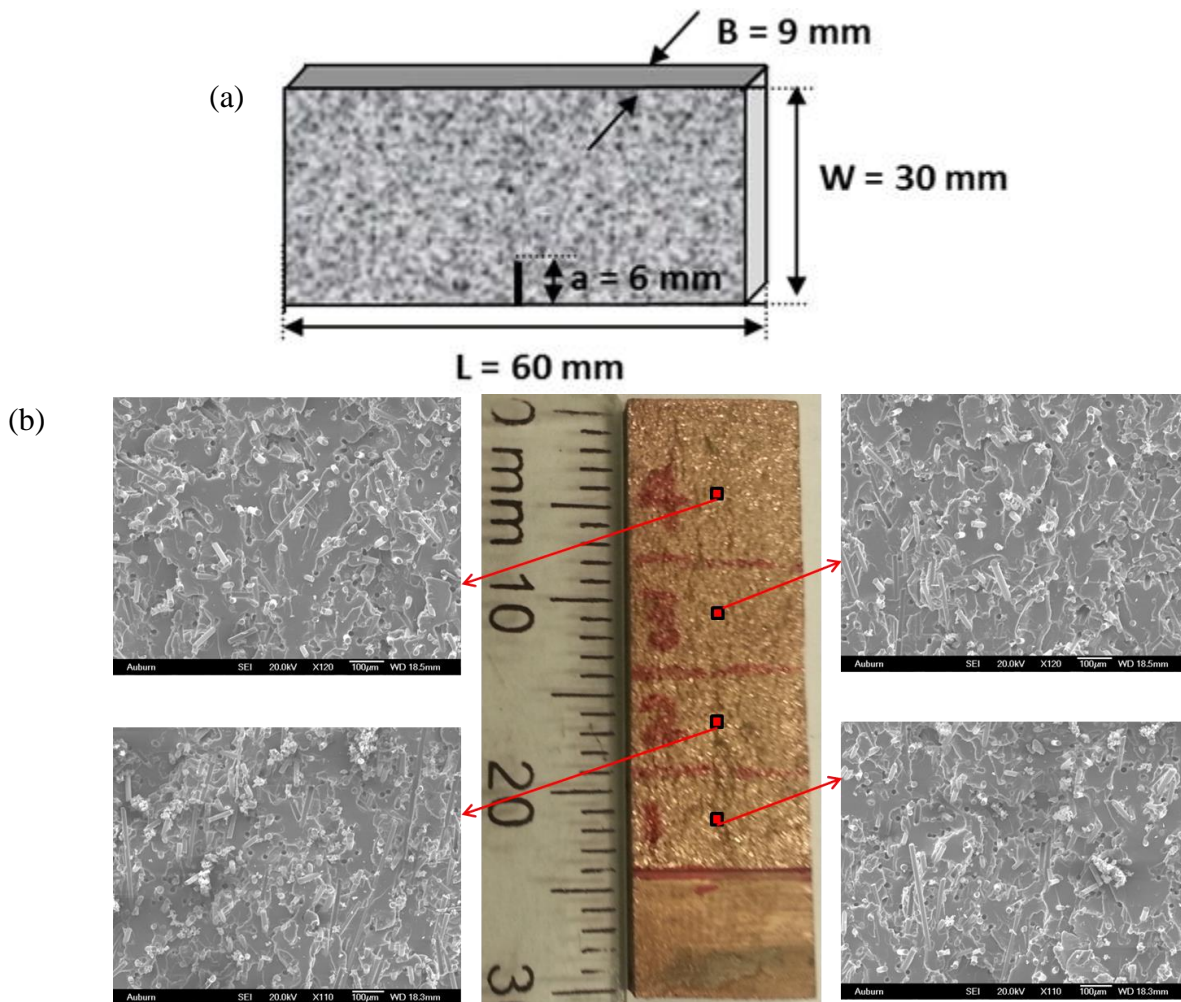


Figure 3.2 (a): Schematic of test specimen, (b): Typical fractographs at four different locations for 15%  $V_f$  rod-shaped glass-filled epoxy (micrograph scale bar = 100  $\mu\text{m}$ ); Note the uniformity of filler dispersion.

### 3.2 Physical and elastic properties

Physical and elastic properties were measured for all PPC and are tabulated in Table 3.2. Ultrasonic transducers (for longitudinal wave: Panametrics #V129 RM, 10 MHz; for shear wave: Panametrics #V156 RM, 5 MHz) coupled with a signal analyzer and an oscilloscope were used to perform pulse-echo measurements to determine the longitudinal ( $C_l$ ) and shear wave ( $C_s$ ) speeds at discrete locations of the cast sheet. After measuring the material density ( $\rho$ ), dynamic elastic modulus ( $E_d$ ) and Poisson's ratio ( $\nu_d$ ) were calculated from expression for  $C_l$  and  $C_s$ ,

$$C_l = \sqrt{\frac{E_d(1-\nu_d)}{\rho(1+\nu_d)(1-2\nu_d)}}, \quad C_s = \sqrt{\frac{E_d}{2\rho(1+\nu_d)}}.$$

Thus measured physical and elastic properties are

shown in Table 3.2. It should be noted that relative to neat epoxy,  $\rho$ ,  $C_l$ ,  $C_s$  and  $E_d$  of the composites with 5%, 10% and 15%  $V_f$  of fillers show a monotonic increase whereas the shape of the filler seems to produce negligible variation at a constant  $V_f$ .

Table 3.2: Material properties of glass-filled epoxy composite

a)  $V_f = 5\%$  (for density, no. of measurements = 3; for wave speeds, no. of measurements = 10)

<b>Particle type</b>	<b>Density <math>\rho</math>(kg/m<sup>3</sup>)</b>	<b>Longitudinal wave speed <math>C_l</math> (m/s)</b>	<b>Shear wave speed <math>C_s</math> (m/s)</b>	<b>Elastic modulus <math>E_d</math> (GPa)</b>	<b>Poisson's ratio <math>\nu_d</math></b>
<b>Epoxy</b>	1146±10	2481±12	1128±3	3.99	0.37
<b>Sphere</b>	1222±12	2534±8	1177±3	4.62	0.36
<b>Flake</b>	1225±11	2526±6	1187±6	4.69	0.36
<b>Rod</b>	1226±12	2534±22	1188±7	4.68	0.36

b)  $V_f = 10\%$  (for density, no. of measurements = 3; for wave speeds, no. of measurements = 10)

<b>Particle type</b>	<b>Density <math>\rho</math>(kg/m<sup>3</sup>)</b>	<b>Longitudinal wave speed <math>C_l</math> (m/s)</b>	<b>Shear wave speed <math>C_s</math> (m/s)</b>	<b>Elastic modulus <math>E_d</math> (GPa)</b>	<b>Poisson's ratio <math>\nu_d</math></b>
<b>Sphere</b>	1286±9	2553±6	1207±4	5.08	0.36
<b>Flake</b>	1288±8	2571±9	1248±11	5.40	0.35
<b>Rod</b>	1285±11	2534±6	1243±7	5.33	0.34

c)  $V_f = 15\%$  (for density, no. of measurements = 3; for wave speeds, no. of measurements = 10)

<b>Particle type</b>	<b>Density <math>\rho</math>(kg/m<sup>3</sup>)</b>	<b>Longitudinal wave speed <math>C_l</math> (m/s)</b>	<b>Shear wave speed <math>C_s</math> (m/s)</b>	<b>Elastic modulus <math>E_d</math> (GPa)</b>	<b>Poisson's ratio <math>\nu_d</math></b>
<b>Sphere</b>	1358±9	2600±6	1243±5	5.67	0.35
<b>Flake</b>	1361±7	2630±6	1300±6	6.16	0.34
<b>Rod</b>	1375±8	2598±12	1286±9	6.08	0.34

### 3.3 Experimental Details

A schematic of the experimental setup used for dynamic fracture tests is shown in Figure 2.2. The setup included a 1.83 m long, 25.4 mm diameter long-bar with a 6.35 mm diameter bull-nose tip registered against an unconstrained specimen and a 304.8 mm long, 25.4 mm diameter striker held inside the barrel of a gas-gun. Both the long-bar and the striker were of the same diameter and made of aluminum 7075-T6. This eliminated the impedance mismatch between the long-bar and the striker. Three different dynamic loading rates were achieved by using different pulse shapers between the striker and the long-bar shown in Figure 2.2 [47]. A soft aluminum 1100 disc (hereon designated as 'Al-PS') of diameter 8 mm and thickness 0.9 mm produced a *strain-*

rate of 10.7 /sec, measured on the long-bar by a strain gage during impact. A combined polycarbonate washer (outer diameter 6.3 mm, inner diameter 2.2 mm and thickness 0.7 mm) and Al 1100 disc sandwich pulse shaper (hereon designated as ‘PC-PS’) produced a lower strain rate of 3.7 /sec relative to Al-PS. The highest strain rate of 42.0 /sec was attained when no pulse shaper (hereon designated as ‘No-PS’) was used. The role of the pulse shaper was to ramp up the stress wave in a controlled fashion in the long-bar during impact [37]. The striker was launched towards the long-bar using the gas-gun at a velocity of ~16 m/s. When the striker contacted the long-bar, a compressive stress wave was initiated and propagated through the bar before transmission into the specimen.

A stochastic black and white speckle pattern was sprayed onto the specimen surface for performing in-plane deformation measurement using 2D DIC method. The pattern was photographed using a Cordin-550 ultrahigh-speed digital camera (Cordin Scientific Imaging, Salt Lake City, UT, USA) equipped with 32 independent CCD image sensors (1000 x 1000 pixels) positioned circumferentially around a rotating mirror which sweeps light over the sensors. Prior to loading, a set of 32 images corresponding to the undeformed state of the specimen were recorded at a rate of ~300,000 frames per second. To record a second set of 32 images corresponding to the deformed state of the specimen, the striker was launched towards the long-bar by discharging the gas-gun. When the striker contacted the long-bar, it completed an electrical circuit, signaling a delay generator to trigger the camera. The camera in turn triggered a pair of high energy flash lamps and initiated image capture at the same framing rate. Thus, each image in the undeformed (reference) set had a corresponding image in the deformed set. The recorded sets of deformed and undeformed images were then correlated to obtain in-plane displacement components.

### 3.4 Optical Data Analysis

The recorded undeformed and deformed sets of images were correlated using a digital image correlation tool ARAMIS™ (GOM mbH, Germany) and the in-plane crack-opening ( $u_y$ ) and crack-sliding ( $u_x$ ) displacement fields were estimated near the crack-tip vicinity. Knowing the asymptotic expressions presented in Equations (3.1) and (3.2) for a dynamically loaded stationary crack,

$$\begin{aligned}
 u_x = & \sum_{n=1}^N \frac{(K_I)_n}{2\mu} \frac{r^{n/2}}{\sqrt{2\pi}} \left\{ \kappa \cos \frac{n}{2} \theta - \frac{n}{2} \cos \left( \frac{n}{2} - 2 \right) \theta + \left\{ \frac{n}{2} + (-1)^n \right\} \cos \frac{n}{2} \theta \right\} + \\
 & \sum_{n=1}^N \frac{(K_{II})_n}{2\mu} \frac{r^{n/2}}{\sqrt{2\pi}} \left\{ \kappa \sin \frac{n}{2} \theta - \frac{n}{2} \sin \left( \frac{n}{2} - 2 \right) \theta + \left\{ \frac{n}{2} - (-1)^n \right\} \sin \frac{n}{2} \theta \right\} + \dots \quad (3.1) \\
 & Pr \cos \theta + Qr \sin \theta + u_{0x}
 \end{aligned}$$

$$\begin{aligned}
 u_y = & \sum_{n=1}^N \frac{(K_I)_n}{2\mu} \frac{r^{n/2}}{\sqrt{2\pi}} \left\{ \kappa \sin \frac{n}{2} \theta + \frac{n}{2} \sin \left( \frac{n}{2} - 2 \right) \theta - \left\{ \frac{n}{2} + (-1)^n \right\} \sin \frac{n}{2} \theta \right\} + \\
 & \sum_{n=1}^N \frac{(K_{II})_n}{2\mu} \frac{r^{n/2}}{\sqrt{2\pi}} \left\{ -\kappa \cos \frac{n}{2} \theta - \frac{n}{2} \cos \left( \frac{n}{2} - 2 \right) \theta + \left\{ \frac{n}{2} - (-1)^n \right\} \cos \frac{n}{2} \theta \right\} + \dots \quad (3.2) \\
 & Pr \cos \theta + Qr \sin \theta + u_{0y}
 \end{aligned}$$

where,  $u_x$  and  $u_y$  represent crack sliding and opening displacements,  $(r, \theta)$  are crack-tip polar coordinates,  $\kappa$  is  $(3-\nu)/(1+\nu)$  for plane stress where  $\mu$  and  $\nu$  are shear modulus and Poisson's ratio, respectively;  $P$  and  $Q$  account for any rigid body rotation [48], and  $u_{0x}$  and  $u_{0y}$  represent rigid body translation along the  $x$ - and  $y$ - directions, respectively. The coefficients  $(K_I)_n$  and  $(K_{II})_n$  of the leading terms (when  $n=1$ ) are the mode-I and mode-II dynamic stress intensity factors (SIF), respectively.

Once the crack started propagating, the asymptotic expressions for sliding and opening displacements for a steadily growing crack [49] were evaluated using Equations

(3.3) and

(3.4),

$$\begin{aligned}
 u_x = & \sum_{n=1}^N \frac{(K_I)_n B_I(C)}{2\mu} \sqrt{\frac{2}{\pi}} (n+1) \left\{ r_1^{n/2} \cos \frac{n}{2} \theta_1 - h(n) r_2^{n/2} \cos \frac{n}{2} \theta_2 \right\} + \\
 & \sum_{n=1}^N \frac{(K_{II})_n B_{II}(C)}{2\mu} \sqrt{\frac{2}{\pi}} (n+1) \left\{ r_1^{n/2} \sin \frac{n}{2} \theta_1 - h(\bar{n}) r_2^{n/2} \sin \frac{n}{2} \theta_2 \right\} + \dots \quad (3.3) \\
 & Pr \cos \theta + Qr \sin \theta + u_{0x}
 \end{aligned}$$

$$\begin{aligned}
 u_y = & \sum_{n=1}^N \frac{(K_I)_n B_I(C)}{2\mu} \sqrt{\frac{2}{\pi}} (n+1) \left\{ -\beta_1 r_1^{n/2} \sin \frac{n}{2} \theta_1 + \frac{h(n)}{\beta_2} r_2^{n/2} \sin \frac{n}{2} \theta_2 \right\} + \\
 & \sum_{n=1}^N \frac{(K_{II})_n B_{II}(C)}{2\mu} \sqrt{\frac{2}{\pi}} (n+1) \left\{ \beta_1 r_1^{n/2} \cos \frac{n}{2} \theta_1 + \frac{h(\bar{n})}{\beta_2} r_2^{n/2} \cos \frac{n}{2} \theta_2 \right\} + \dots \quad (3.4) \\
 & Pr \cos \theta + Qr \sin \theta + u_{0y}
 \end{aligned}$$

$$r_m = \sqrt{X^2 + \beta_m^2 Y^2}, \quad \theta_m = \tan^{-1} \left( \frac{\beta_m Y}{X} \right), m=1,2$$

$$\beta_1 = \sqrt{1 - \left( \frac{c}{C_L} \right)^2}, \quad \beta_2 = \sqrt{1 - \left( \frac{c}{C_S} \right)^2}$$

$$C_L = \sqrt{\frac{(\kappa+1)\mu}{(\kappa-1)\rho}}, \quad C_S = \sqrt{\frac{\mu}{\rho}}, \quad \kappa = \frac{3-\nu}{1+\nu}$$

$$\text{where, } B_I(C) = \frac{(1+\beta_2^2)}{D}, \quad B_{II}(C) = \frac{2\beta_2}{D}, \quad D = 4\beta_1\beta_2 - (1+\beta_2^2)^2 \dots \quad (3.5)$$

$$h(n) = \begin{cases} \frac{2\beta_1\beta_2}{1+\beta_2^2} & \text{for odd } n \\ \frac{1+\beta_2^2}{2} & \text{for even } n \end{cases}$$

and

$$h(\bar{n}) = h(n+1)$$



Here  $(r, \theta)$  and  $(x, y)$  are the polar and Cartesian coordinates, respectively,  $c$  is the instantaneous crack speed,  $C_L$  and  $C_S$  are the longitudinal and shear wave speeds for the material, and  $\mu$  and  $\nu$  are shear modulus and Poisson's ratio, respectively;  $P$  and  $Q$  define rigid body rotation [48], and  $u_{0x}$  and  $u_{0y}$  represent rigid body translation along the  $x$ - and  $y$ - directions, respectively as in Equations (3.1) and (3.2). Again, coefficients  $(K_I)_n$  and  $(K_{II})_n$  of the leading terms are the mode-I and mode-II dynamics stress intensity factors, respectively.

In order to extract the Stress Intensity Factor (SIF) history from fracture events,  $(u_y, u_x)$  displacement fields were digitized by identifying the current crack-tip location and subsequently establishing the Cartesian and polar coordinates at the crack-tip. About four hundred data points were collected in the vicinity of the current crack-tip over radial and angular extents of  $0.5 < r/B < 1.5$  (where  $B$  is sample thickness) and  $[(-147^\circ < \theta < -90^\circ) \text{ and } (90^\circ < \theta < 147^\circ)]$  to avoid regions of dominant 3D deformations and far-field effects shown in Figure 3.3 [50]. At each data point the two displacement components  $(u_y, u_x)$  as well as the location of these points were stored. For time instants before crack initiation, the asymptotic expressions for a dynamically loaded stationary crack were used to extract mode-I and –II stress intensity factors using an over-deterministic least-squares analysis of the data. For time instants after crack initiation, the asymptotic expressions for sliding and opening displacements for a steadily growing crack were used.

For a mode-I problem, the crack-opening displacements  $(u_y)$  are rich in mode-I information whereas crack sliding displacements  $(u_x)$  are rich in mode-II information. Thus,  $u_y$  and  $u_x$  were used to extract mode-I and –II stress intensity factors  $K_I$  and  $K_{II}$ , respectively. The acquired speckle images for glass-filled epoxy with 10%  $V_f$  of spheres for the ‘Al-PS’ pulse-shaper case with crack opening  $(u_y)$  and crack sliding  $(u_x)$  displacement, respectively, are shown in Figure 3.4. The crack-tip is shown using the arrow in each speckle image. The  $u_y$  and  $u_x$  fields show that contour lines

(in  $5\mu\text{m}$  increments) and magnitude of displacement (in  $\mu\text{m}$  shown by color-bars) are nearly symmetric relative to the crack, consistent with mode-I fracture behavior. The  $u_x$ -field plot shows a dense set of isolines emerging from the right-hand side of the contour plots due to impact loading on the edge of the specimen ahead of the initial crack-tip.

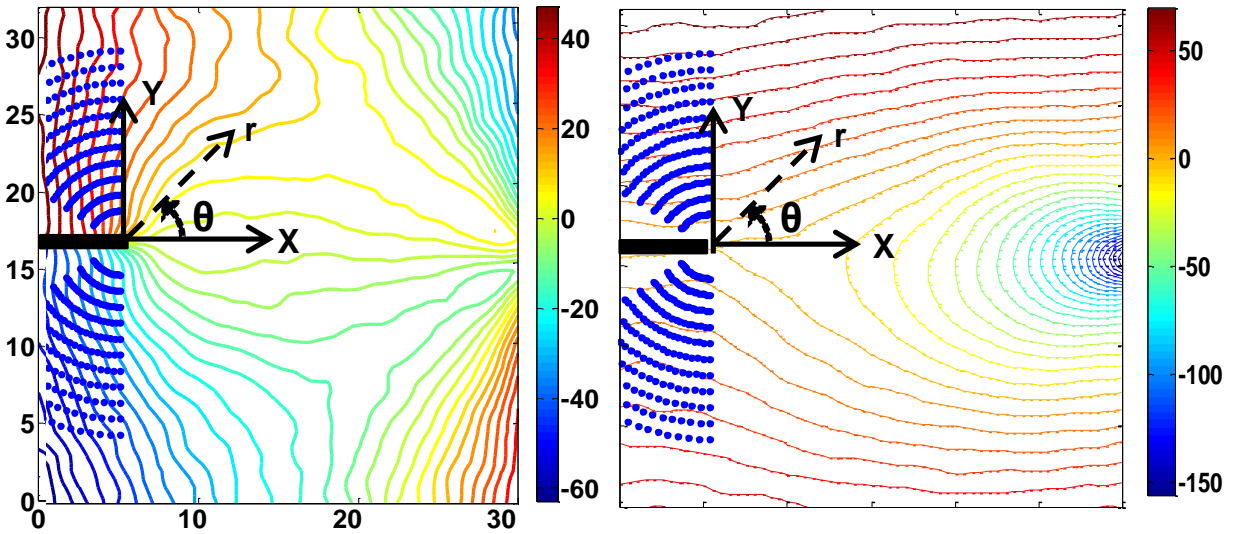


Figure 3.3: Displacement data collection on  $[0.5 < r/B < 1.5]$  and  $[-147^\circ < \theta < -90^\circ]$  and  $[90^\circ < \theta < 147^\circ]$  to extract stress intensity factors.

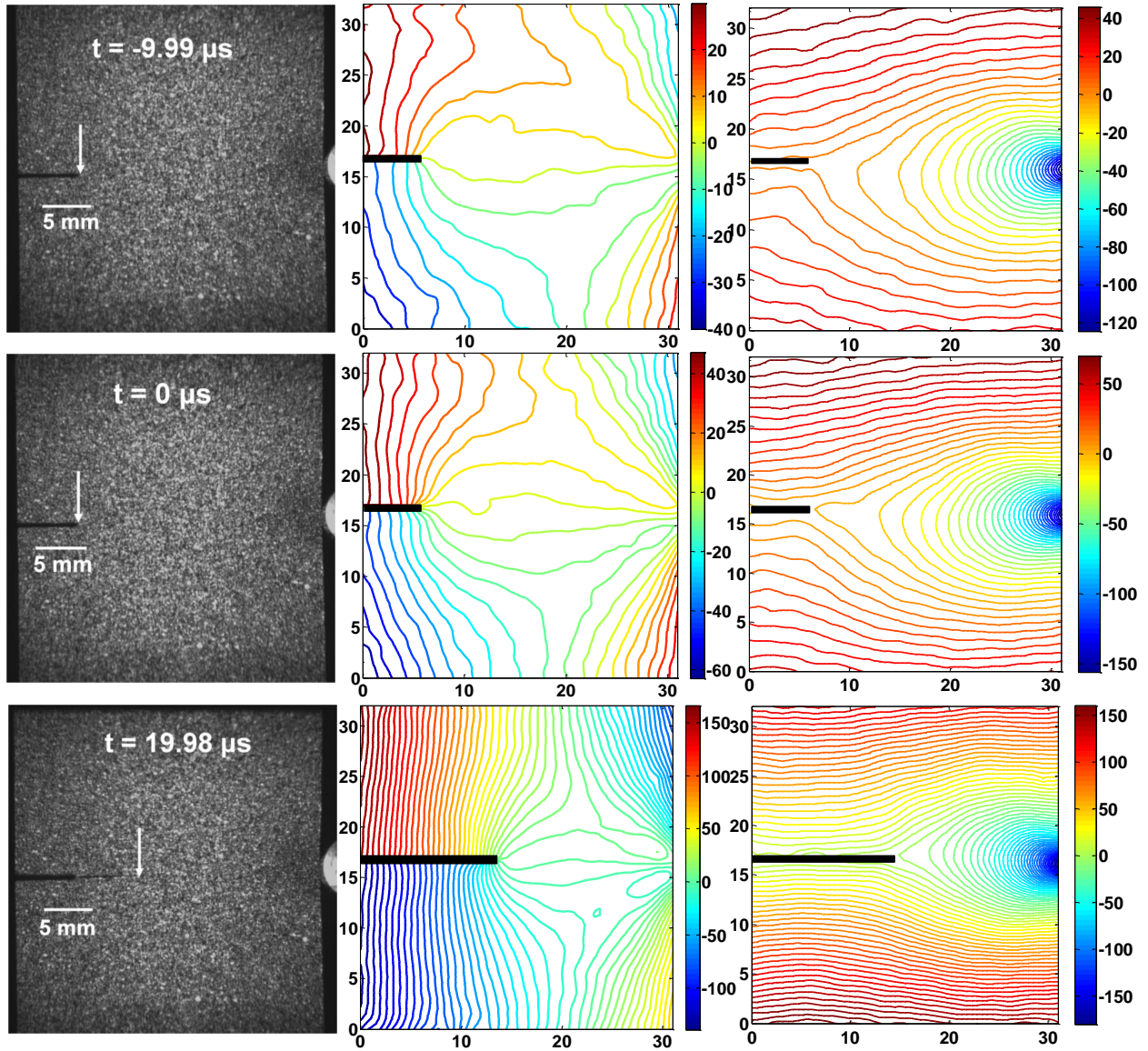


Figure 3.4: Acquired speckle images for glass-filled epoxy with 10%  $V_f$  of spheres for the ‘ALPS’ pulse-shaper case with crack opening ( $u_y$ ) and crack sliding ( $u_x$ ) displacement contours in steps of  $5 \mu\text{m}$ , respectively (units on the displacement contour on  $x$ - and  $y$ -axis are in mm). First row: pre-crack initiation ( $t = -9.99 \mu\text{s}$ ), middle row: crack initiation ( $t = 0 \mu\text{s}$ ), and last row: post-crack initiation ( $t = 19.98 \mu\text{s}$ ) time instants; Scale factor: 1 pixel =  $34 \mu\text{m}$ .

### 3.5 Experimental repeatability and comparison with finite element simulations

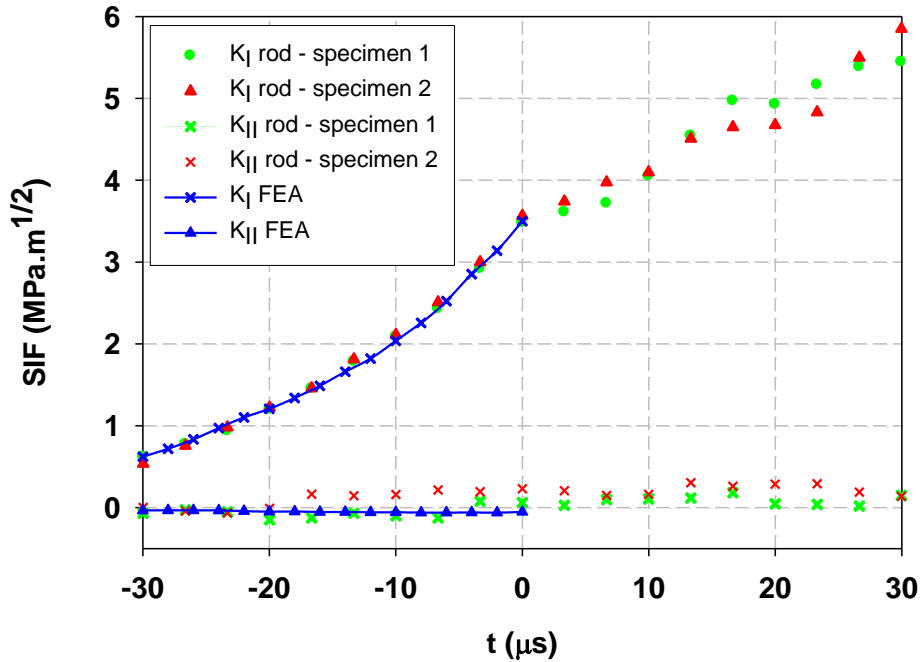


Figure 3.5: Experimental repeatability of SIF histories for 15% rod-shaped glass-filled epoxy for the ‘Al-PS’ case and comparison with FE simulation. (Histories for  $K_{II}$  are also provided for completeness. Being a symmetric loading experiment,  $K_{II}$  histories are relatively small but useful to estimate errors in the least-squares analysis scheme)

Multiple experiments were conducted for each specimen filled with particles of different shape at different volume fractions (5%, 10% and 15%) to assure experimental repeatability. Figure 3.5 shows the SIF histories for two 15%  $V_f$  rod-shaped glass-filled epoxy specimens and the ‘Al-PS’ case. For both specimens,  $K_I$  values increases monotonically and nearly overlap on each other up to crack initiation (marked as  $t = 0 \mu\text{s}$ ). The crack initiation is associated with a noticeable drop in the rate of increase of  $K_I$ . Subsequent  $K_I$  history shows an increasing trend with an oscillatory behavior due to the random distribution of fillers in the crack path as well as a finite specimen size causing stress wave reflections from the free boundaries. The crack being loaded symmetrically, the extracted values of  $K_{II}$  histories are negligible within the measurement errors, which

further confirms a mode-I event. The mode-II histories can be used here as a guide to estimate errors associated with the SIF extraction method employed.

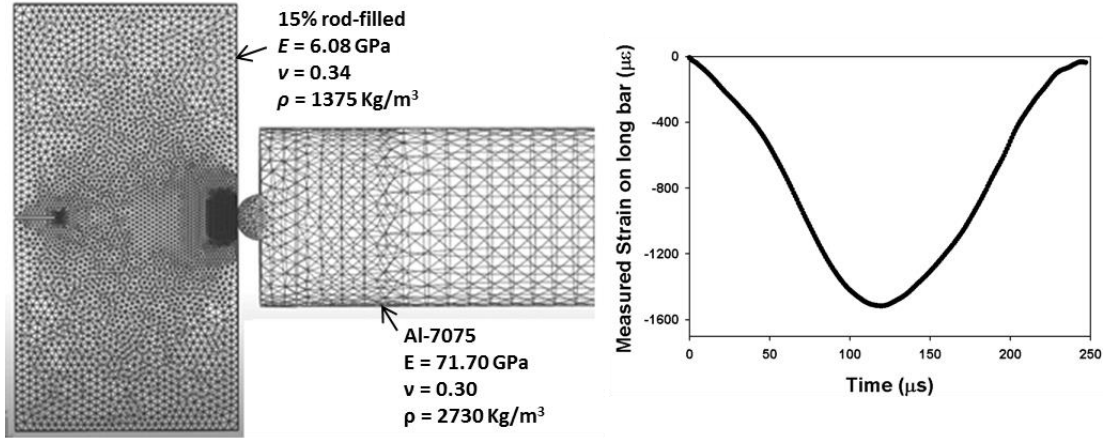


Figure 3.6: Finite element mesh used for elasto-dynamic simulation of mode-I fracture experiments using ABAQUS/explicit (left); strain history recorded on the long-bar for the ‘Al-PS’ case (right).

The strain history on the long-bar was recorded by a strain gage affixed to it. The strain history for the case of ‘Al-PS’ pulse shaper is shown in Figure 3.6. Subsequently, the particle velocity in the long-bar was calculated [51] using the measured strain history as boundary condition for a companion finite element (FE) simulation. A 3D elasto-dynamic simulation was carried out in ABAQUS/explicit up-to-crack initiation. Four-node tetrahedron elements were used to simulate 15% glass-filled epoxy specimen with rod-shaped fillers. The long-bar impacting the notched specimen was included in the numerical model. The mesh and material properties used in the FE analysis are shown in Figure 3.6. The crack-tip and contact region of the long-bar with the specimen were finely discretized (element size 0.05 mm) [47]. Both the specimen and long-bar were unconstrained and were butted against each other with a frictionless contact. The cross-sectional area of the long-bar was loaded at the other far-end with particle velocity input recorded during the test. The instantaneous crack-opening and crack-sliding displacements were obtained from the

FE simulation. Subsequently, the SIF histories were generated using regression analyses of crack face opening and sliding displacements up to crack initiation [52]. The SIF history obtained from FE analysis shows a good agreement with the experimental results (Figure 3.5).

## 3.6 Results and discussion

### 3.6.1 Effect of filler shape

The filler shape effect on the dynamic fracture behavior was studied by comparing the SIF histories and energy release rate for different glass fillers at 5%, 10% and 15%  $V_f$  in epoxy for the ‘Al-PS’ case (Table 3.3 and Table 3.4, respectively). Plots of  $K_I$  histories are shown in Figure 3.7 (a)-(c) for 5%, 10% and 15%  $V_f$ , respectively. The data from both pre- and post-crack initiation periods are included. It should be noted that the measured histories of each sample have been shifted along the time axis to make crack initiation time (identified as  $t = 0$ ) of each experiment coincide. For all volume fractions, the  $K_I$  histories show a monotonic increase until and after crack initiation. A modest kink in the history is noticeable in some cases at crack initiation depending on when the crack initiated during the inter-frame period. Among all the three volume fractions, the rod-shaped fillers produced the highest crack initiation toughness as well post-initiation  $K_I$  values. The histories for flakes and spheres, respectively, follow successively. Also, for all the three volume fractions, the rate of increase of  $K_I$  followed a similar trend up to pre-crack initiation. The rate of increase of  $K_I$  was approximately constant for all shapes of fillers, once the crack starts propagating. For 5%  $V_f$  (Figure 3.7 (a)), rod, flake and spherical filler cases showed 82%, 47% and 18% improvement in crack initiation toughness, respectively, and 184%, 84% and 21% improvement in energy release rate, respectively, relative to that for neat epoxy. The 10%  $V_f$  (Figure 3.7 (b)) rod, flake and spherical filler cases showed 118%, 71% and 39% improvement in crack

initiation toughness, respectively, and 257%, 116% and 51% improvement in energy release rate, respectively, compared to neat epoxy. Furthermore, as expected, for 10%  $V_f$ , the SIF histories of each type of filler showed a higher value when compared to the 5%  $V_f$  composites. For 15%  $V_f$  (Figure 3.7 (c)) rod, flake and spherical filler cases showed 145%, 97% and 68% improvement in crack initiation toughness, respectively, and 294%, 152% and 98% improvement in critical energy release rate, respectively, compared to neat epoxy. Again, as expected, 15%  $V_f$  SIF histories of each type of the filler showed a higher value when compared to both 5% and 10%  $V_f$  counterparts.

A fractographic study was carried out to understand the underlying toughening mechanisms for the dramatic improvement in fracture responses due to filler shape change. It should be first noted that fracture surface micrographs (Figure 3.8) show no agglomeration of filler particles in all cases and filler distribution is uniform. As the stress waves propagate through the specimen, the crack front is driven forward until it encounters filler particles. A careful observation of fractographs suggests that interaction of the crack front with filler phase leads to the following potential failure modes: (a) matrix cracking, (b) filler-matrix interface separation, (c) filler pullout, and/or (d) filler breakage. During crack growth each active failure mode contributes to energy dissipation which adds to the overall increase in fracture toughness of the composite. In case of spherical fillers, matrix cracking and inclusion-matrix debonding were found to be the dominant modes. A few spherical fillers were pulled out but none of them were found fractured. Therefore due to a low aspect ratio ( $= 1$  in this case), crack bridging can be assumed inactive (or minimum) and the crack circumvented the inclusion by crack deflection and/or debonding of the interface causing momentary crack front arrest and reinitiation. In case of flakes, fracture surface is dominated by matrix cracking, inclusion-matrix debonding and filler breakage. The breakage of flakes contributes to extra energy dissipation besides crack deflection and trapping mechanisms. All these

contribute to an increase in fracture toughness when compared to spherical filler counterpart. For rod-shaped filler, the failure modes were matrix cracking, inclusion-matrix debonding and filler breakage with evidence of filler pullout. On the fracture surface, several broken short fibers were identified. Since the average fiber length was  $\sim 800 \mu\text{m}$ , it is likely fiber bridges across the crack front resisted crack growth, before eventually getting pulled out of the matrix or fractured as the crack grew. The tensile strength of the fibers being  $\sim 3 \text{ GPa}$  (compared to that of neat epoxy of  $\sim 70 \text{ MPa}$ ), even a few fiber breakages could result in a rather high apparent fracture toughness of the composite.

The fracture surface features such as roughness and tortuosity scale with energy dissipation during crack propagation [53]. Hence, fracture surfaces were profiled using white light interferometry (Zygo New View 6000) at a magnification of 10x (20x Mirau lens with a 0.5x Zoom). Nine fields of view were stitched together to obtain a total sample surface of  $1.91 \times 1.43 \text{ mm}$ , with an areal resolution of  $1 \mu\text{m}$  and vertical resolution better than  $10 \text{ nm}$ . To determine the effect of filler particles on surface roughness measurements, surfaces were analyzed for surface roughness both before and after employing a masking procedure to remove regions containing filler particles in the images.



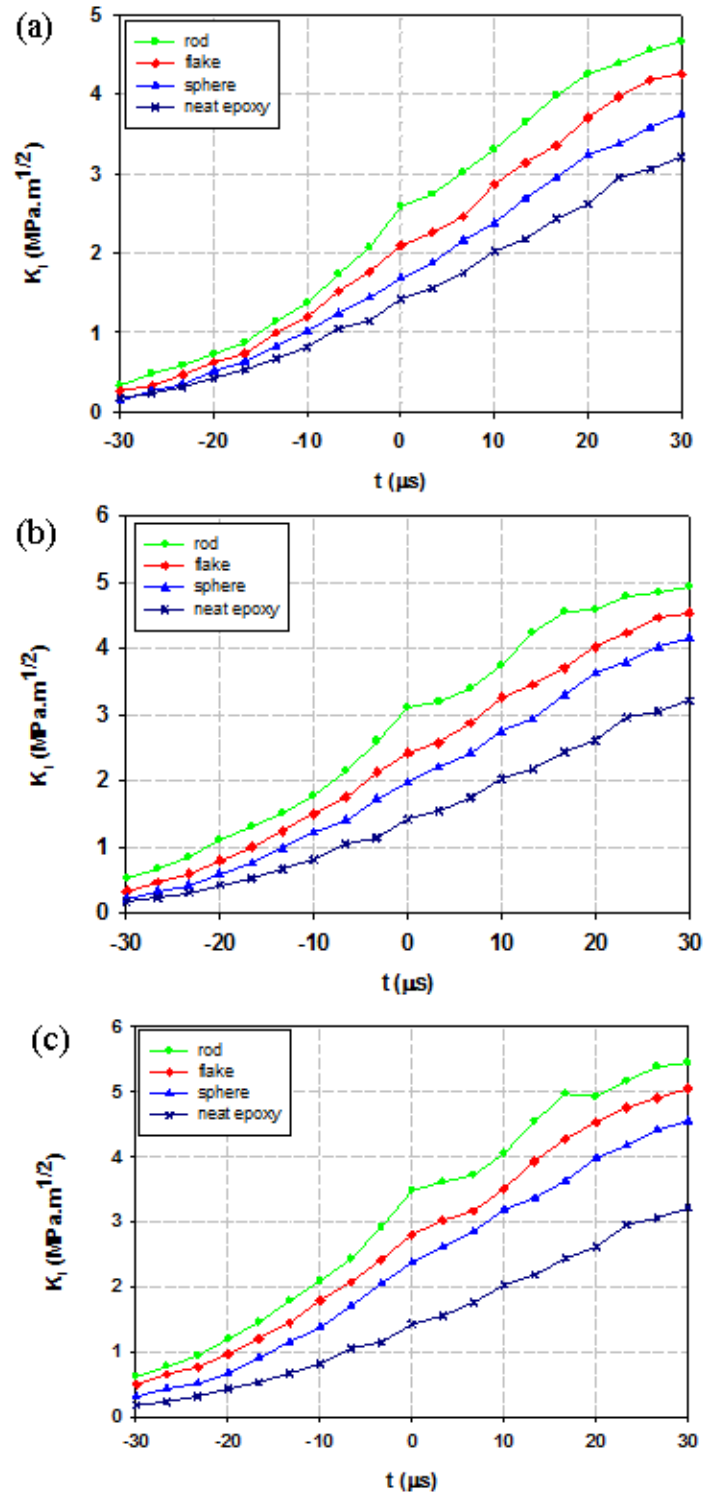


Figure 3.7:  $K_I$  histories (a) for 5%  $V_f$ , (b) 10%  $V_f$ , (c) 15%  $V_f$  glass-filled epoxy for the Aluminum 1100 pulse shaper ('Al-PS') case with different filler particle shape.

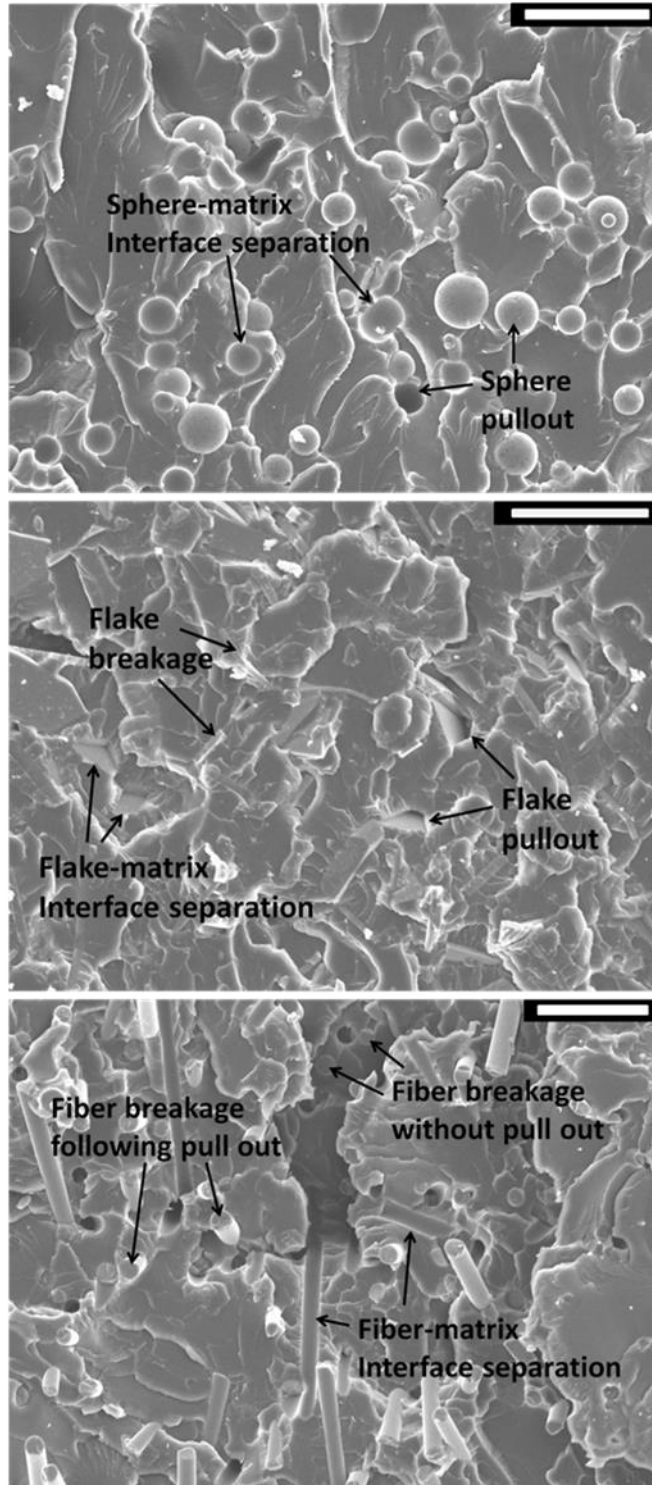


Figure 3.8: Fractographs of 10%  $V_f$  sphere, flake, rod-shaped glass-filled epoxy (top to bottom respectively) for the 'Al-PS' pulse shaper case; scale bar = 100 $\mu$ m

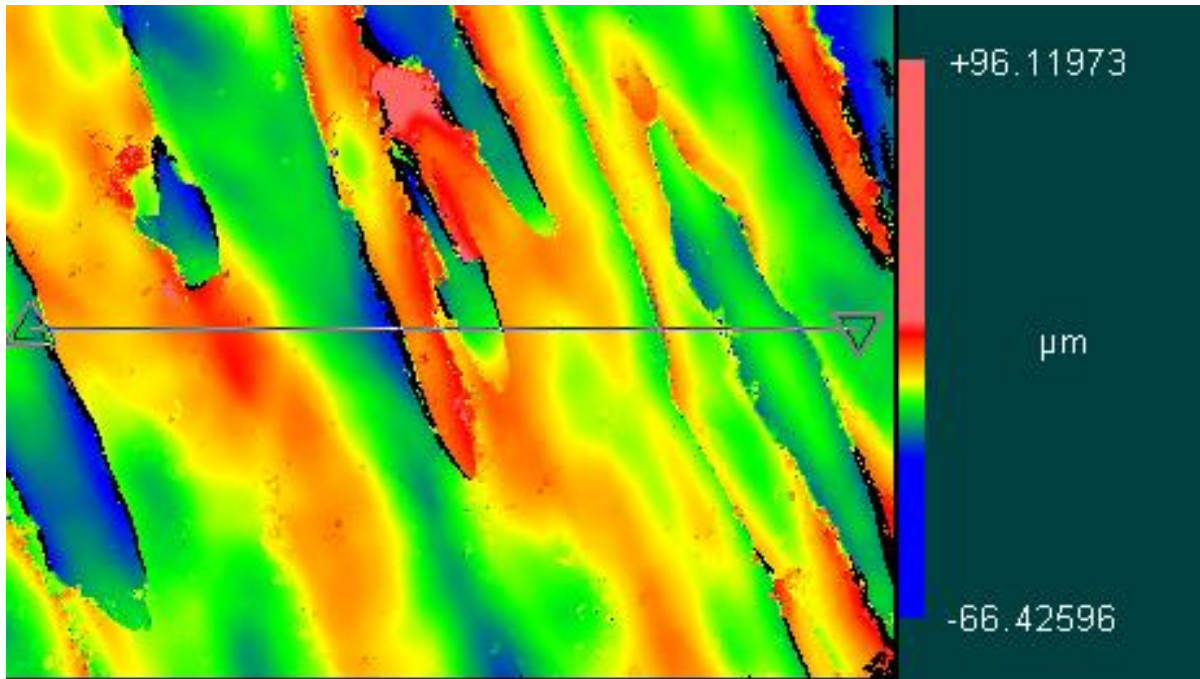


Figure 3.9: Typical fracture surface profile of neat epoxy for the ‘Al-PS’ pulse shaper case ( $R_a = 6.3 \mu\text{m}$ ).

Figure 3.9 shows a typical false-color image of the fracture surface of neat epoxy. It appears relatively smooth with a measured roughness ( $R_a$ ) of  $6.3 \mu\text{m}$ . Figure 3.10 shows typical fracture surfaces of samples with different fillers at  $10\% V_f$ . All samples have a higher surface roughness than neat epoxy, ranging from  $R_a = 15.5 \mu\text{m}$  for flakes, to  $R_a = 24.9 \mu\text{m}$  for rods. To test the effect of the filler on the overall surface roughness, masks were created in the Zygo Metro-Pro analysis software. Each mask was developed to remove data points/regions representing the fillers. Typical data sets showing before and after the masking operation are shown in Figure 3.10. The filler materials have very little effect on the overall surface roughness, in all cases contributing  $< 1\%$  to the  $R_a$  value. Thus, while fillers might contribute to the overall roughness at smaller scales, the roughness at larger scales is primarily due to crack propagation behavior.

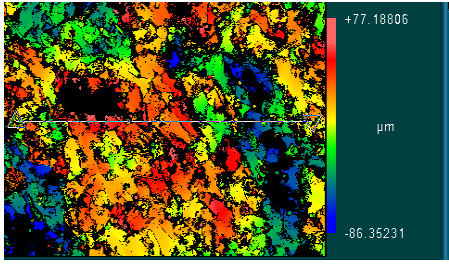
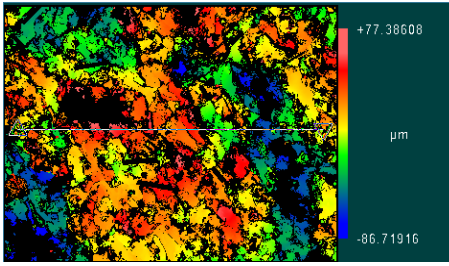
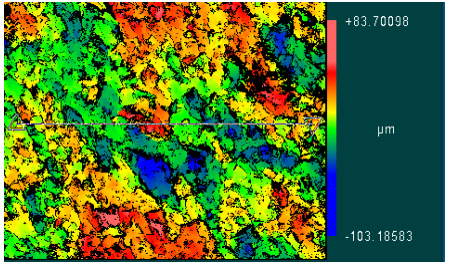
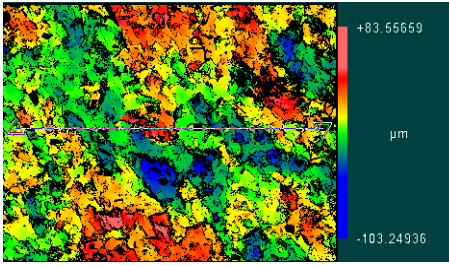
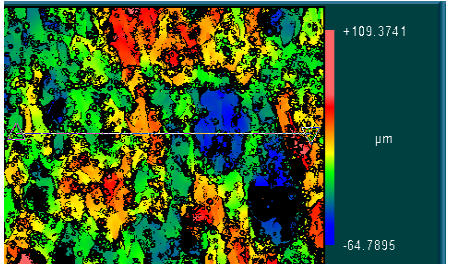
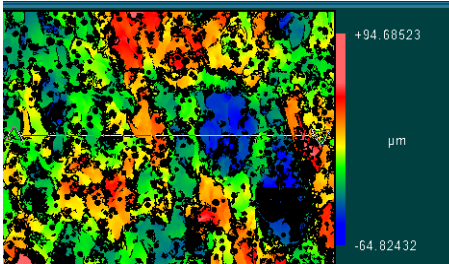
	Before Masking	After Masking	$K_I$ (MPa $\sqrt{m}$ )
<b>Rods</b>	 $R_a = 24.9 \mu\text{m}$	 $R_a = 24.8 \mu\text{m}$	3.10
<b>Flakes</b>	 $R_a = 15.5 \mu\text{m}$	 $R_a = 15.4 \mu\text{m}$	2.43
<b>Spheres</b>	 $R_a = 19.2 \mu\text{m}$	 $R_a = 19.1 \mu\text{m}$	1.97

Figure 3.10: Typical pseudo-colored fracture surfaces of glass-filled epoxy (10%  $V_f$ ) for the ‘Al-PS’ pulse shaper case. Fillers contribute less than ~1% to the overall surface roughness ( $R_a$ ).

The surface roughness measurements indicate higher  $R_a$  for spherical fillers than flakes although macromer measurements show higher stress intensity factors for the sample with flakes. The fractographic evaluation explains this apparent inconsistency for this. During crack growth, each failure mechanism contributes to energy dissipation which adds to the overall increase in fracture toughness of the PPC. In case of spheres, only filler pull out and filler-matrix interface separations besides matrix cracking were found. None of the spheres were found broken whereas in the case

of flakes an extra failure mode namely filler breakage was found. This additional failure mode provides more energy absorption due to higher tensile strength of glass flakes.

### **3.6.2 Effect of filler volume fraction**

For each filler shape, dynamic  $K_I$  histories were compared for 0%, 5%, 10% and 15% filler  $V_f$ , respectively, when an aluminum pulse shaper ('Al-PS') was used. In each case,  $K_I$  showed an increasing trend with volume fraction of the filler during the entire fracture event. The rate of increase of  $K_I$  followed the above volume fractions trend up to crack initiation. The rate of increase of  $K_I$  was approximately constant for all volume fractions, once the crack started propagation. For spherical-fillers (Figure 3.11 (a)), 5%, 10% and 15%  $V_f$  showed 18%, 39% and 68% improvement in crack initiation toughness compared to neat epoxy, respectively. For flakes (Figure 3.11 (b)), 5%, 10% and 15%  $V_f$  showed 47%, 71% and 97%, improvement in crack initiation toughness compared to neat epoxy, respectively.

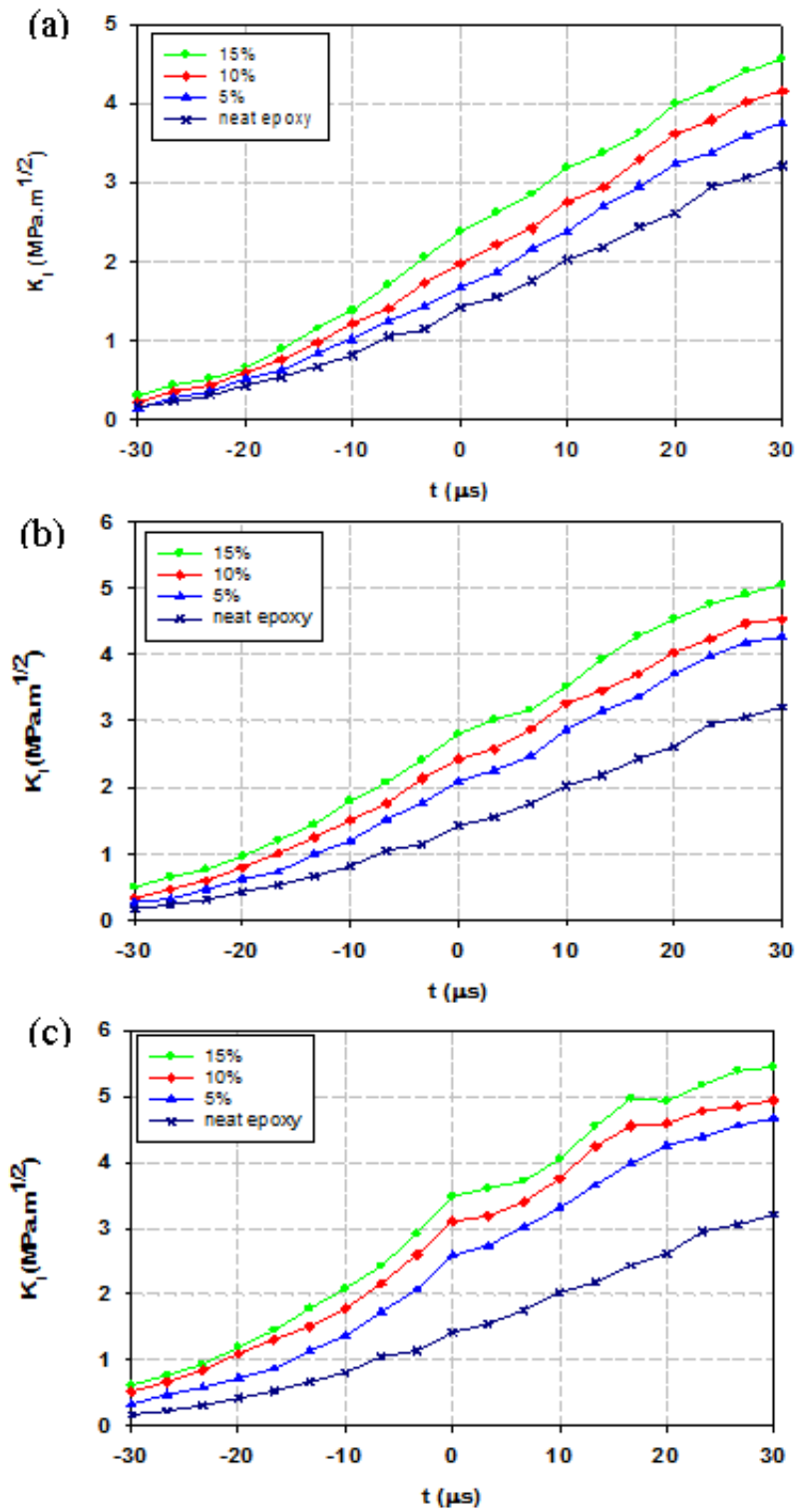


Figure 3.11:  $K_I$  histories for glass-filled epoxy with (a) spherical filler, (b) flakes, (c) rods for the ‘Al-PS’ pulse shaper case with different volume fractions.

Table 3.3.: Crack initiation toughness (in  $\text{MPa}\sqrt{\text{m}}$ ) comparison for different filler shapes at different  $V_f$  using an aluminum pulse shaper ('Al-PS') during impact (% improvement is relative to neat epoxy), no. of measurements = 3

Volume fraction		Crack initiation toughness		
0% (Neat Epoxy)		1.42±0.06		
		<b>Sphere</b>	<b>Flakes</b>	<b>Rods</b>
5%		1.68±0.07	2.09±0.09	2.59±0.11
	improvement in $K_I$	18%	47%	82%
10%		1.97±0.14	2.43±0.11	3.10±0.16
	improvement in $K_I$	39%	71%	118%
15%		2.38±0.13	2.80±0.16	3.48±0.16
	improvement in $K_I$	68%	97%	145%

Table 3.4.: Critical energy release rate (in  $\text{kPa}\cdot\text{m}$ ) comparison for different filler shapes at different  $V_f$  using an aluminum pulse shaper ('Al-PS') during impact (% improvement is relative to neat epoxy), no. of measurements = 3

Volume fraction		Critical energy release rate		
0% (Neat Epoxy)		0.51±0.04		
		<b>Sphere</b>	<b>Flakes</b>	<b>Rods</b>
5%		0.61±0.05	0.93±0.08	1.44±0.12
	improvement in $G_I$	21%	84%	184%
10%		0.77±0.11	1.09±0.10	1.81±0.19
	improvement in $G_I$	51%	116%	257%
15%		1.00±0.11	1.28±0.15	1.99±0.18
	improvement in $G_I$	98%	152%	294%

For rods (Figure 3.11 (c)), on the other hand, showed 82%, 118% and 145% improvement, respectively, for 5%, 10% and 15% filler  $V_f$  compared to neat epoxy. It should also be noted that a noticeable slope change in  $K_I$  histories are evident when the crack initiates at 15% filler  $V_f$ . A summary of crack initiation toughness and energy release rate values and the corresponding enhancements for all the different cases are provided in Table 3.3 and Table 3.4, respectively.

### 3.6.3 Quantification of shape effects on crack initiation toughness

To obtain the functional form of dependence of dynamic crack initiation toughness on the filler aspect ratio, the measured values were plotted as a function of the log of aspect ratio ( $AR$ ) (see, Table 3.1) for each filler shape at 5%, 10% and 15%  $V_f$  (Figure 3.12) for the 'Al-PS' case.

For all the three volume fractions,  $K_I$  vs  $\log(AR)$  plots were essentially linear. Further, crack initiation toughness increases with aspect ratio and follows a linear relationship of the form  $K_I = C_1 \cdot \log(AR) + C_2$ , where  $C_1$  and  $C_2$  are constants (for 5%  $V_f$ :  $C_1 = 0.49 \text{ MPa}\sqrt{\text{m}}$  and  $C_2 = 1.69 \text{ MPa}\sqrt{\text{m}}$ , for 10%  $V_f$ :  $C_1 = 0.59 \text{ MPa}\sqrt{\text{m}}$  and  $C_2 = 1.97 \text{ MPa}\sqrt{\text{m}}$  and for 15%  $V_f$ :  $C_1 = 0.58 \text{ MPa}\sqrt{\text{m}}$  and  $C_2 = 2.37 \text{ MPa}\sqrt{\text{m}}$ ). For all the three  $V_f$  considered here,  $C_1$  is nearly independent of  $V_f$ . Fractography previously revealed that interaction between the crack front and the rod-shaped filler with maximum aspect ratio contributed to various crack bridging mechanisms during crack propagation which in turn contributed to energy dissipation during crack growth. This resulted in higher fracture toughness whereas in the case of flakes and sphere due to their relatively lower aspect ratio crack front generally avoided the filler typically by circumventing it.

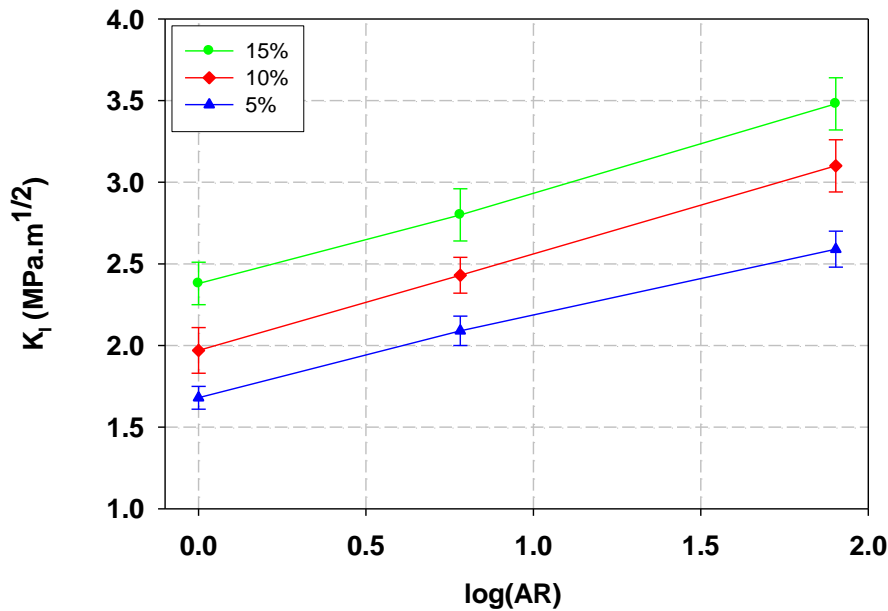


Figure 3.12: Effect of aspect ratio on crack initiation toughness for the ‘Al-PS’ pulse shaper case. Error bars indicate one standard deviation relative to the average toughness value. The crack initiation toughness follows a linear relationship of the form  $K_I = C_1 \cdot \log(AR) + C_2$ , where  $C_1$  and  $C_2$  are constants (for 5%  $V_f$ :  $C_1 = 0.49 \text{ MPa}\sqrt{\text{m}}$  and  $C_2 = 1.69 \text{ MPa}\sqrt{\text{m}}$ ; for 10%  $V_f$ :  $C_1 = 0.59 \text{ MPa}\sqrt{\text{m}}$  and  $C_2 = 1.97 \text{ MPa}\sqrt{\text{m}}$  and for 15%  $V_f$ :  $C_1 = 0.58 \text{ MPa}\sqrt{\text{m}}$  and  $C_2 = 2.37 \text{ MPa}\sqrt{\text{m}}$ ).



### 3.6.4 Effect of loading rate

Previous sections show that filled-epoxy with rod-shaped fillers produce the highest enhancement in crack initiation and post-initiation toughness among the three different fillers shapes considered. Accordingly, the loading rate effects were examined for this particular case using composites containing 10%  $V_f$  of the filler. The rate effects were studied by comparing the crack growth histories and stress intensity factor produced by the three different pulse shapers (Table 3.5 and Table 3.6). The crack length histories are plotted for both the neat epoxy and the 10%  $V_f$  glass-filled epoxy in Figure 3.13. Crack initiation time instants and crack speeds are tabulated in Table 3.5. Time  $t = 0$  is the time instant when the long-bar impacts the specimen. Due to the reinforcement, PPCs with rod-shaped filler resisted crack initiation for a longer duration when compared to the neat epoxy counterpart studied using the same pulse shaper. The crack propagation was also faster in neat epoxy compared to filled epoxy for each pulse shaper case. Plots of  $K_I$  histories are shown in Figure 3.14 (a) and Figure 3.14 (b) for the neat epoxy and the 10%  $V_f$  filled-epoxies, respectively. The  $K_I$  histories show a monotonic increase until and after crack initiation for all the three pulse shapers for both the filled and neat epoxy cases. In each case, the loading rate was characterized by  $dK_I/dt$  [54] by measuring the slope of the  $K_I$  history in the linearly increasing region up to crack initiation. For neat epoxy, before crack initiation,  $K_I$  histories show higher slope for the ‘No-PS’ ( $dK_I/dt = 149 \pm 12 \times 10^3 \text{ MPa}\sqrt{\text{m/s}}$ ) case followed by the ‘Al-PS’ ( $dK_I/dt = 61 \pm 8 \times 10^3 \text{ MPa}\sqrt{\text{m/s}}$ ) and ‘PC-PS’ ( $dK_I/dt = 40 \pm 7 \times 10^3 \text{ MPa}\sqrt{\text{m/s}}$ ) cases, respectively and for 10% filled-epoxy,  $K_I$  histories show slightly higher slopes for the ‘No-PS’ ( $dK_I/dt = 182 \pm 11 \times 10^3 \text{ MPa}\sqrt{\text{m/s}}$ ) case followed by the ‘Al-PS’ ( $dK_I/dt = 132 \pm 16 \times 10^3 \text{ MPa}\sqrt{\text{m/s}}$ ) and ‘PC-PS’ ( $dK_I/dt = 53 \pm 4 \times 10^3 \text{ MPa}\sqrt{\text{m/s}}$ ) cases, respectively. For neat epoxy,  $K_I$  history showed a drop at crack initiation for the ‘No-PS’ case corresponding to the highest loading rate. For 10% filled epoxy in ‘No-PS’ and ‘Al-

PS' cases, a small kink in the histories are noticeable. The 'No-PS' case produces the highest crack initiation toughness as well as post-initiation  $K_I$  values and 'Al-PS' and 'PC-PS' cases, respectively, follow for both the neat epoxy and filled-epoxy. For neat epoxy, the rate of increase of  $K_I$  was approximately constant for the 'Al-PS' and 'PC-PS' cases but lower than the 'No-PS' case, whereas for filled-epoxy, the rate of increase of  $K_I$  was approximately constant for the 'No-PS' and 'Al-PS' cases but greater than the 'PC-PS' case, once the crack initiated. The filled epoxies show 113%, 118% and 50% increase in crack initiation toughness and 239%, 257% and 68% in energy release rate for the 'PC-PS', 'Al-PS' and 'No-PS' cases, respectively, compared to the neat epoxy studied using the respective pulse shaper. This comparison, though not strictly rigorous due to different  $dK_I/dt$  between filled and neat samples, does provide a good estimation of loading rate effects.

The fractographic study was carried out on filled epoxy for different pulse shaper cases to understand the underlying toughening mechanisms on crack initiation toughness due to loading rate differences. In Figure 3.15, micrographs of 10%  $V_f$  glass-filled epoxy with rod-shaped filler for the 'No-PS' case (left) and the 'PC-PS' case (right) are shown, respectively. It is evident that the surface ruggedness is noticeably higher for the 'No-PS' case compared to the 'PC-PS' case. Also, for higher loading rate, filler-matrix interface separation mode is substantially higher for the 'No-PS' case than the 'PC-PS' case. The fibers bridging the crack faces result in an overall stiffer response at the higher loading rate and they likely break before being pulled out of the matrix during crack growth. The reported tensile strength of the fibers being  $\sim 3$  GPa, the process contributes to a rather high apparent crack initiation and propagation SIF values for the PPC.

Table 3.5.: Crack initiation toughness (in  $\text{MPa}\sqrt{\text{m}}$ ) comparison (% improvement is relative to the neat epoxy of the respective pulse shaper used during loading), no. of measurements = 3

Pulse shaper	Crack initiation	Neat Epoxy	Rods (10% $V_f$ )
‘Quasi-static’	$K_{I}$	1.92 [13]	$2.48\pm 0.02$
	improvement in $K_{I}$	-	29%
‘PC-PS’	$K_{I}$	$1.22\pm 0.07$	$2.60\pm 0.08$
	improvement in $K_{I}$	-	113%
‘Al-PS’	$K_{I}$	$1.42\pm 0.05$	$3.10\pm 0.16$
	improvement in $K_{I}$	-	118%
‘No-PS’	$K_{I}$	$2.28\pm 0.15$	$3.42\pm 0.17$
	improvement in $K_{I}$	-	50%

Table 3.6.: Critical energy release rate (in  $\text{kPa}\cdot\text{m}$ ) comparison (% improvement is relative to the neat epoxy of the respective pulse shaper used during loading), no. of measurements = 3

Pulse shaper	Critical energy release rate	Neat	Rods (10% $V_f$ )
‘Quasi-static’	$G_I$	0.90	$1.15\pm 0.02$
	improvement in $G_I$	-	28%
‘PC-PS’	$G_I$	$0.37\pm 0.04$	$1.27\pm 0.08$
	improvement in $G_I$	-	239%
‘Al-PS’	$G_I$	$0.51\pm 0.04$	$1.81\pm 0.19$
	improvement in $G_I$	-	257%
‘No-PS’	$G_I$	$1.31\pm 0.17$	$2.20\pm 0.22$
	improvement in $G_I$	-	68%

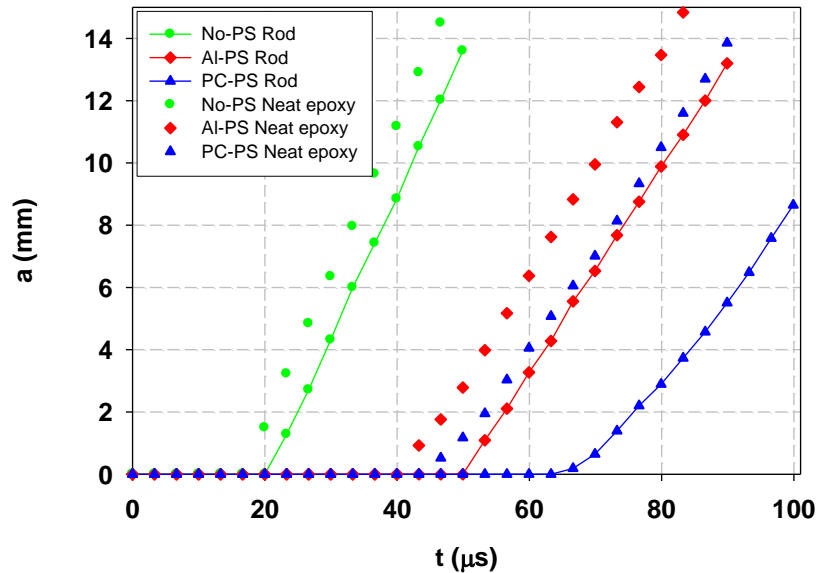


Figure 3.13: Crack growth history plots for neat epoxy and 10%  $V_f$  rod-filled epoxy at different loading rates.

Table 3.7: Crack initiation time and crack speed comparison for neat epoxy and 10%  $V_f$  rod-filled epoxy, no. of measurements = 3

Pulse shaper	Crack initiation time ( $\mu\text{s}$ )		Crack speed (m/s)	
	Neat Epoxy	Rods (10% $V_f$ )	Neat Epoxy	Rods (10% $V_f$ )
'No-PS'	$17 \pm 3$	$20 \pm 3$	$486 \pm 29$	$462 \pm 35$
'Al-PS'	$40 \pm 3$	$50 \pm 3$	$358 \pm 11$	$332 \pm 26$
'PC-PS'	$43 \pm 3$	$63 \pm 3$	$306 \pm 14$	$256 \pm 13$

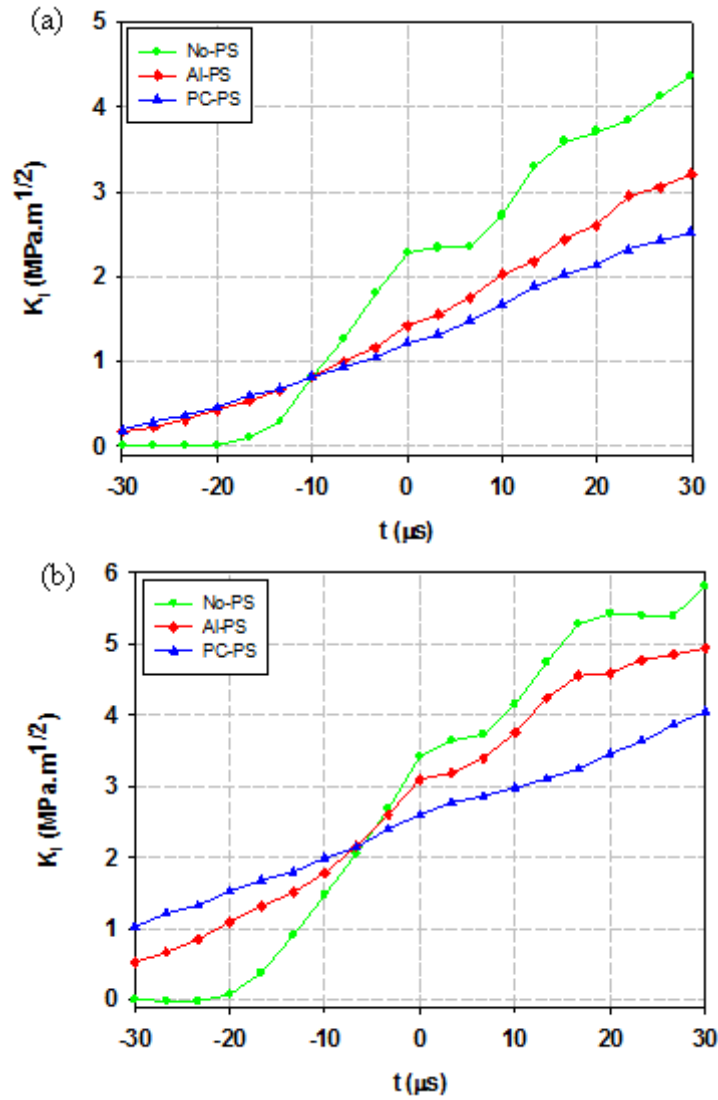


Figure 3.14: SIF histories at different loading rates: (a) For neat epoxy (Before crack initiation,  $dK_I/dt$  were  $\sim 149 \times 10^3$ ,  $61 \times 10^3$  and  $40 \times 10^3$   $\text{MPa}\sqrt{\text{m/s}}$  for 'No-PS', 'Al-PS' and 'PC-PS' cases, respectively, compared to  $dK_I/dt$  of  $\sim 6 \times 10^{-2}$   $\text{MPa}\sqrt{\text{m/s}}$  in quasi-static loading case.), (b) For glass-filled epoxy (10%  $V_f$ ) (Before crack initiation,  $dK_I/dt$  were  $\sim 182 \times 10^3$ ,  $132 \times 10^3$  and  $53 \times 10^3$   $\text{MPa}\sqrt{\text{m/s}}$  for 'No-PS', 'Al-PS' and 'PC-PS' cases, respectively, compared to  $dK_I/dt$  of  $\sim 1 \times 10^{-1}$   $\text{MPa}\sqrt{\text{m/s}}$  in quasi-static loading case.

More fiber pullouts were found in the 'PC-PS' case than the 'No-PS' case, explaining the lowest crack initiation toughness in the 'PC-PS' case among all the three pulse shapers. However, for neat epoxy, the only failure mode was matrix cracking. At a higher loading rate neat epoxy resisted crack growth via microscopic crack branches producing higher surface roughness.

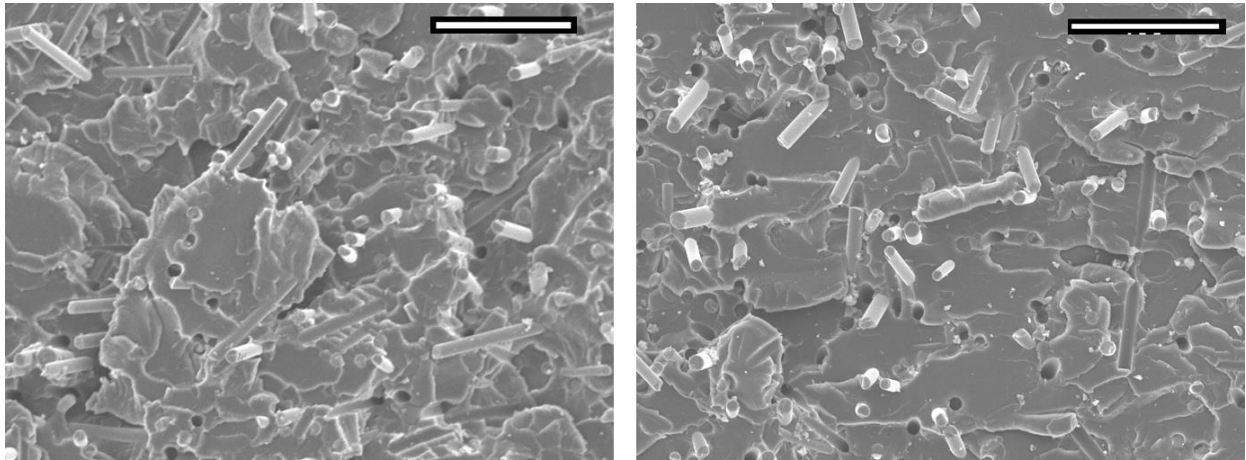


Figure 3.15: Fractographs of glass-filled epoxy (10%  $V_f$ ) for the highest ('No-PS' case (left)) and the lowest ('PC-PS' case (right)), respectively; scale bar=100 $\mu$ m

## CHAPTER 4

### MIXED-MODE DYNAMIC FRACTURE

Fracture mechanics literature has traditionally concentrated on crack growth problems under a symmetric crack opening, or mode-I, condition. However, cracks in structures are not only subjected to symmetric and to antisymmetric deformations simultaneously resulting in the crack initiation and propagation under mixed-mode conditions. This chapter deals with dynamic tension and in-plane shear loading of cracks producing a mixture of mode-I and mode-II fracture (see Figure 4.1) of glass-filled epoxy.

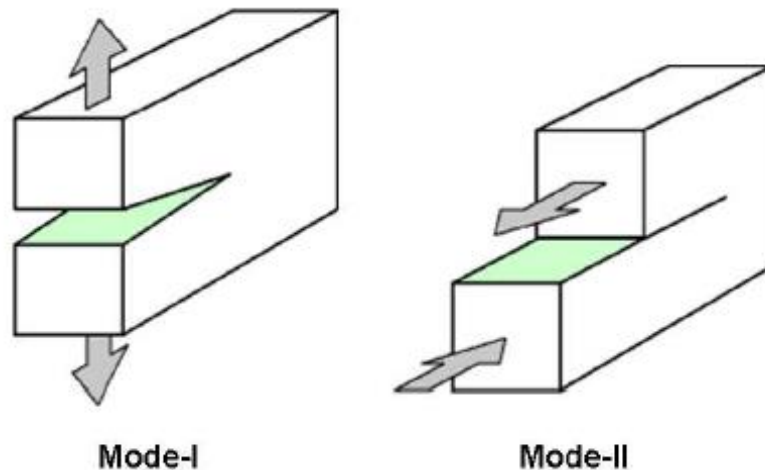


Figure 4.1: Schematics illustrating pure mode-I and mode-II fractures [55]

Qian and Fatemi conducted the literature survey on mixed-mode crack growth studies and found that the most of the experimental studies of crack growth under mixed mode-I and -II loadings have been on plate type specimens with inclined central cracks under quasi-static tension [56]. Experimental evidence suggests that the mode of crack propagation depends on material, load

magnitude and ratio of tensile and shear far-field loads. Kirugulige and Tippur studied the mixed-mode dynamic fracture behavior of functionally graded glass-filled epoxy using the optical method of coherent gradient sensing and high-speed photography [57]. The mixed-mode crack initiation and growth was found dominated by mode-I conditions. The initial crack kink angle was predicted using the Maximum Tangential Stress (MTS) criterion based on the stress intensity factors just prior to crack initiation and they found that predicted crack kink angles agreed reasonably well with the observed ones during early stages of crack growth. In another study Kirugulige and Tippur studied the mixed-mode dynamic fracture behavior of syntactic foams using DIC and high-speed photography [58]. Again, the stress intensity factor histories obtained from experiments were in good agreement with the ones from finite element computations up to crack initiation, and the crack initiation and growth in syntactic foams also occurred under dominant mode-I conditions.

In the filler shape effect investigation reported in the previous chapter, the rod-shaped glass-filled epoxy produced the largest improvement in crack initiation toughness when compared to the neat epoxy under mode-I conditions among the three different filler shapes. However, as noted earlier, it is also important to understand its fracture behavior for mixed-mode loading. To bridge this gap, dynamic fracture behavior of glass-filled epoxy was investigated under mixed-mode loading conditions. The experiments were conducted under impact loading conditions using DIC and high-speed photography for measuring instantaneous crack tip deformations at different mixities. The results were compared with the respective mode-I cases. To understand the fracture behavior, SIF histories were plotted in pre- and post-crack initiation regimes. Based on crack initiation fracture toughness values at different mode-mixities, a fracture envelope was proposed for neat and glass-filled epoxy for impact loading conditions.

## 4.1 Material preparation

The rod-shaped glass fillers were dispersed into a low-viscosity epoxy (Epo-Thin 2\*, from Beuhler Inc., USA; Bisphenol-A resin and Amine based hardener; densities  $1130 \text{ kg/m}^3$  and  $961 \text{ kg/m}^3$ , respectively). The previous chapter shows that filled-epoxy with rod-shaped fillers produce the highest enhancement in terms of crack initiation and post-initiation toughness among the three different filler shapes considered. Therefore, the rod-shaped glass-filled epoxy with a 10% filler volume fraction was chosen to study the mixed-mode loading effects. To carry out the dynamic fracture study, glass-filled epoxy (containing 0% (or the neat epoxy) and 10% glass filler by volume, respectively) sheets were cast. To ensure uniform dispersion, fillers were added into the epoxy resin, mechanically stirred and then degassed until the mixture appeared free from trapped air bubbles. Subsequently, a stoichiometric amount of hardener was added to the mixture and stirred until it gelled before pouring into the mold to avoid settlement of filler particles. Upon curing for a minimum of 7 days, the sheets were demolded and machined into rectangular specimens of dimensions  $100 \text{ mm} \times 50 \text{ mm} \times 9 \text{ mm}$  as shown in Figure 4.2. Some of the relevant physical and elastic properties of the material studied are shown in Table 4.1. An edge notch was introduced into each specimen using a diamond-impregnated circular saw and the notch tip was sharpened with a sharp razor blade.

---

\*The supplier discontinued producing Epo-thin used in the earlier part of the research; hence, this set of experiments was carried-out using their new formulation called Epo-thin 2.



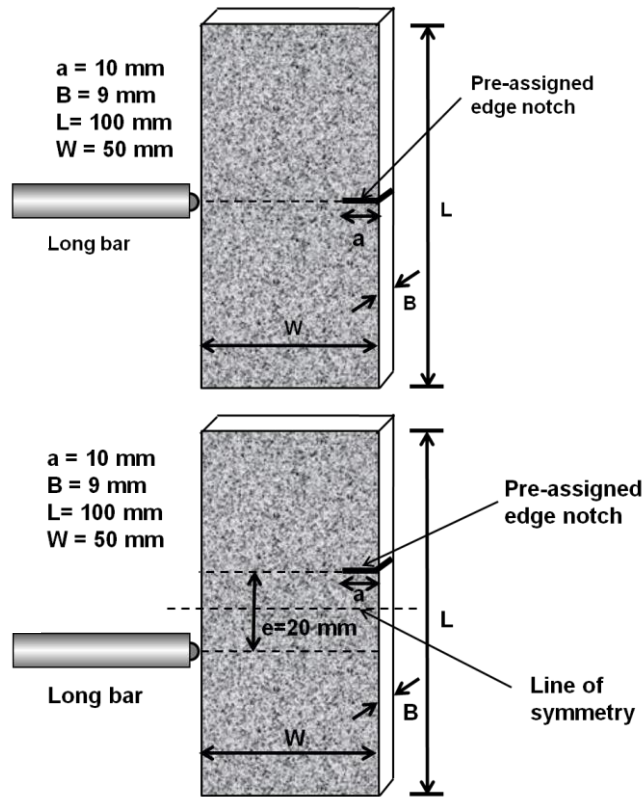


Figure 4.2: Schematics of mode-I specimen with eccentricity  $e = 0$  mm (top) and mixed-mode specimen with eccentricity  $e = 20$  mm (bottom)

In mode-I fracture experiments, the specimen having an edge notch of 10 mm length ( $a = 10$  mm) was impacted symmetrically (i.e., eccentricity  $e = 0$  mm) with respect to the pre-notch. The compressive stress wave traveled across the specimen, reached the free edge with the pre-notch, reflected back as a tensile wave, opened the pre-notch and initiated crack growth in mode-I, all while inertia was holding the specimen within the view of the high speed camera. However, in the mixed-mode case, the specimens were impacted at different eccentricities to create dynamic tension and in-plane shear loading of pre-notch producing a mixture of mode-I and mode-II fracture, respectively. The first two sets of experiments used specimens with an edge notch of 10 mm ( $a = 10$  mm) and were impacted at eccentricities  $e = 15$  and 20 mm for both neat and glass-filled epoxies. However, the mode-mixity (the ratio of mode-II to mode-I stress intensity factors) at crack

initiation could not be increased due to geometric limitations as crack initiation could not be consistently achieved. Hence, to achieve further higher mode-mixities (i.e., further higher in-plane shear compared to tensile loading at the crack-tip) at crack initiation, edge notch length was increased to 15, 20 and 25 mm ( $a = 15, 20, 25$  mm) while holding eccentricity constant at  $e = 20$  mm. Figure 4.2 shows schematics of the mode-I (top) and mixed-mode (bottom) dynamic test configurations for ( $e = 0, a = 10$ ) and ( $e = 20, a = 10$ ), respectively.

Table 4.1: Material properties of neat epoxy and glass-filled epoxy composite (for density, no. of measurements = 3; for wave speeds, no. of measurements = 10)

Particle type	Density $\rho$ (kg/m <sup>3</sup> )	Longitudinal wave speed $C_l$ (m/s)	Shear wave speed $C_s$ (m/s)	Elastic modulus $E_d$ (GPa)	Poisson's ratio $\nu_d$
Neat epoxy	1146±10	2481±12	1128±3	3.99	0.37
Glass-filled epoxy ( $V_f = 10\%$ )	1285±11	2534±6	1243±7	5.33	0.34

## 4.2 Optical data analysis

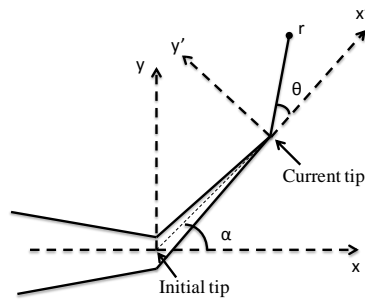


Figure 4.3: Schematic showing crack propagation at an angle  $\alpha$  in mixed-mode loading configuration. Angle  $\alpha$  was measured by joining initial notch tip to the current crack tip.

As described in the previous chapters, crack tip deformations were measured under dynamic loading conditions using 2D DIC, high-speed photography and the long-bar impactor. The method for analyzing crack tip fields has already been discussed earlier in Chapter 3 (Section 3.4). In the mixed-mode cases, until crack initiation,  $u_y$  and  $u_x$  were used to extract mode-I and –II stress

intensity factors,  $K_I$  and  $K_{II}$ , respectively. Once the crack started to propagate (as shown schematically in Figure 4.3) at a kink angle  $\alpha$  relative to the  $x$ -axis, the displacement fields were transformed to the local coordinates  $x'$  and  $y'$  using Equation (4.1).

$$\begin{pmatrix} u_{x'} \\ u_{y'} \end{pmatrix} = \begin{pmatrix} \cos \alpha & \sin \alpha \\ -\sin \alpha & \cos \alpha \end{pmatrix} \begin{pmatrix} u_x \\ u_y \end{pmatrix} \dots\dots\dots (4.1)$$

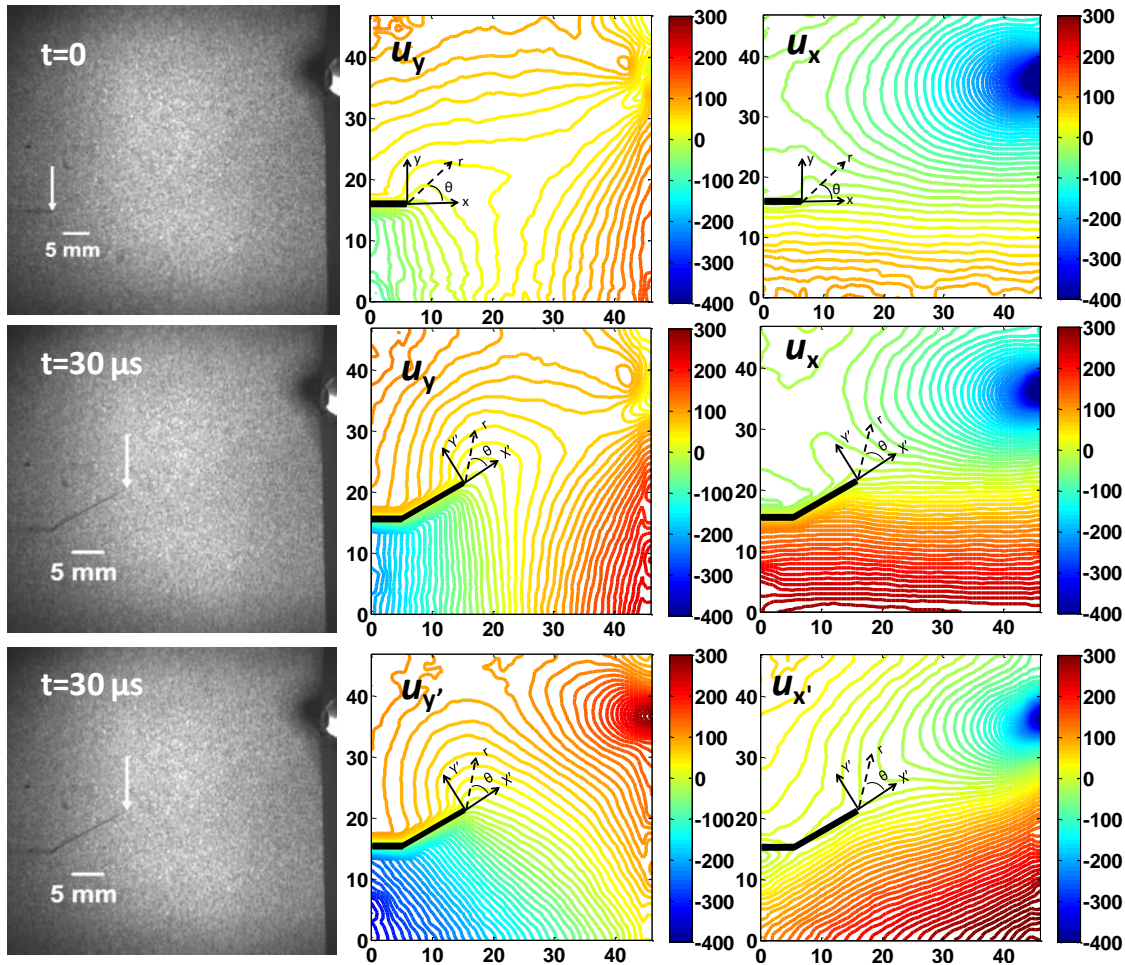


Figure 4.4: Acquired speckle images for glass-filled epoxy for  $e = 20$  mm,  $a = 10$  mm case with crack opening ( $u_y$ ) and crack sliding ( $u_x$ ) displacement contours in steps of  $10 \mu\text{m}$ , respectively (units on the displacement contour on  $x$ - and  $y$ -axis are in mm). First row: crack opening ( $u_y$ ) and crack sliding ( $u_x$ ) displacement, respectively, at crack initiation ( $t = 0 \mu\text{s}$ ), middle row: crack opening ( $u_y$ ) and crack sliding ( $u_x$ ) displacement, respectively, at a post-crack initiation instant ( $t = 30 \mu\text{s}$ ), and last row: transformed crack opening ( $u_{y'}$ ) and sliding ( $u_{x'}$ ) displacement, respectively, at post-crack initiation instant ( $t = 30 \mu\text{s}$ ); Scale factor: 1 pixel =  $49 \mu\text{m}$ .

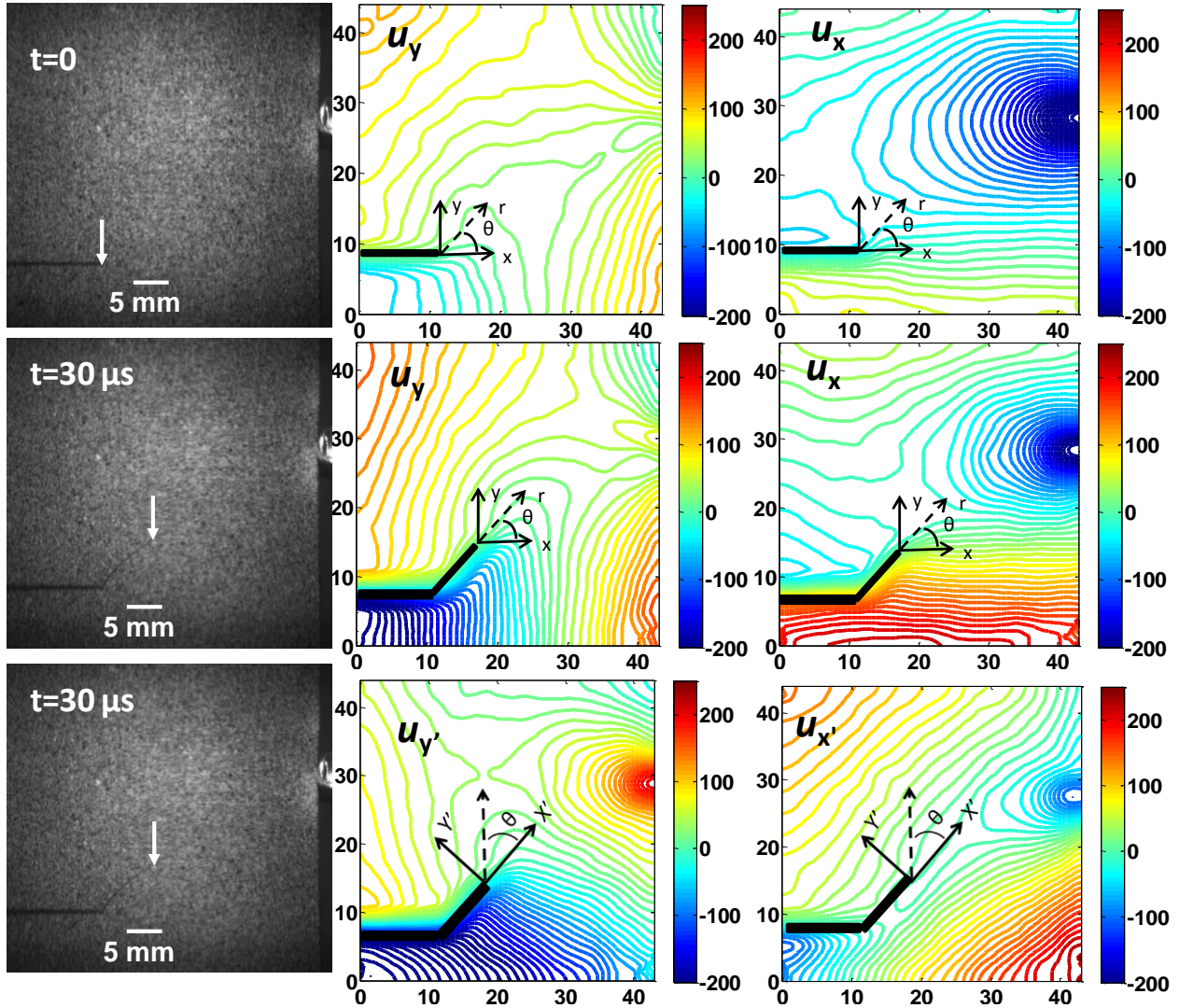


Figure 4.5: Acquired speckle images for glass-filled epoxy for  $e = 20$  mm,  $a = 20$  mm case with crack opening ( $u_y$ ) and crack sliding ( $u_x$ ) displacement contours in steps of  $10 \mu\text{m}$ , respectively (units on the displacement contour on  $x$ - and  $y$ -axis are in mm). First row: crack opening ( $u_y$ ) and crack sliding ( $u_x$ ) displacement, respectively, at crack initiation ( $t = 0 \mu\text{s}$ ), middle row: crack opening  $u_y$  and crack sliding  $u_x$ , respectively, at a post-crack initiation instant ( $t = 30 \mu\text{s}$ ), and last row: transformed crack opening ( $u_{y'}$ ) and sliding ( $u_{x'}$ ) displacement, respectively, at post-crack initiation instant ( $t = 30 \mu\text{s}$ ); Scale factor: 1 pixel =  $45 \mu\text{m}$ .

The transformed displacement fields  $u_{y'}$  and  $u_{x'}$  are the crack opening and sliding displacements, respectively, once the crack starts to propagate. Hence, following crack initiation,  $u_{y'}$  and  $u_{x'}$  were used in place of  $u_y$  and  $u_x$  to extract instantaneous mixed-mode stress intensity factors  $K_{\text{I}}$  and  $K_{\text{II}}$ , respectively. For the mixed-mode case, effective stress intensity factor  $K_{\text{eff}}$  is defined as

the vector sum of stress intensity factors in mode-I and mode-II whereas mode-mixity is defined as an angular ratio of  $K_{II}$  and  $K_I$  presented in Equation (4.2),

$$K_{eff} = \sqrt{K_I^2 + K_{II}^2}, \quad \psi = \tan^{-1}(K_{II} / K_I) \dots\dots\dots (4.2)$$

The acquired speckle images for glass-filled epoxy with  $e = 20$  mm,  $a = 10$  mm and  $e = 20$  mm,  $a = 20$  mm cases with crack opening and crack sliding displacement fields, respectively, are shown in Figure 4.4 and Figure 4.5, respectively. The crack-tip is shown using the arrow in each speckle image. The displacement fields show contour lines in 10  $\mu$ m increments and the magnitude of displacements are in micrometers shown in the color-bars. Appendix A contains the acquired speckle images with crack opening and crack sliding displacement fields for glass-filled epoxy at seven different time instants, corresponding to three for pre-, one at and three post-crack initiation instants.

### 4.3 Experimental repeatability and finite element simulations

Multiple experiments were conducted for each case to assure experimental repeatability. Figure 4.6 (a)-(c) shows the SIF histories for two cases of  $e = 20$  mm,  $a = 10$  mm glass-filled epoxy specimens. For both,  $K_{eff}$  values increase monotonically and nearly overlap up to crack initiation (marked as  $t = 0 \mu$ s). Individual SIF histories for  $K_I$  and  $K_{II}$  are shown in Figure 4.6 (b) and (c), respectively, over the same time window. In Figure 4.6 (b), for both the specimens  $K_I$  shows a similar behavior as  $K_{eff}$  because the crack initiation and propagation occur dominantly under mode-I condition in this case. However, the mode-II histories showed a monotonic increase up to the crack initiation and once crack initiated a distinct drop in magnitude due to elastic unloading near

the crack-tip as shown in Figure 4.6 (c). The distinct drop in the magnitude of  $K_{II}$  shows the preference of the crack to propagate under mode-I conditions, as evident from the response in the post-initiation regime.

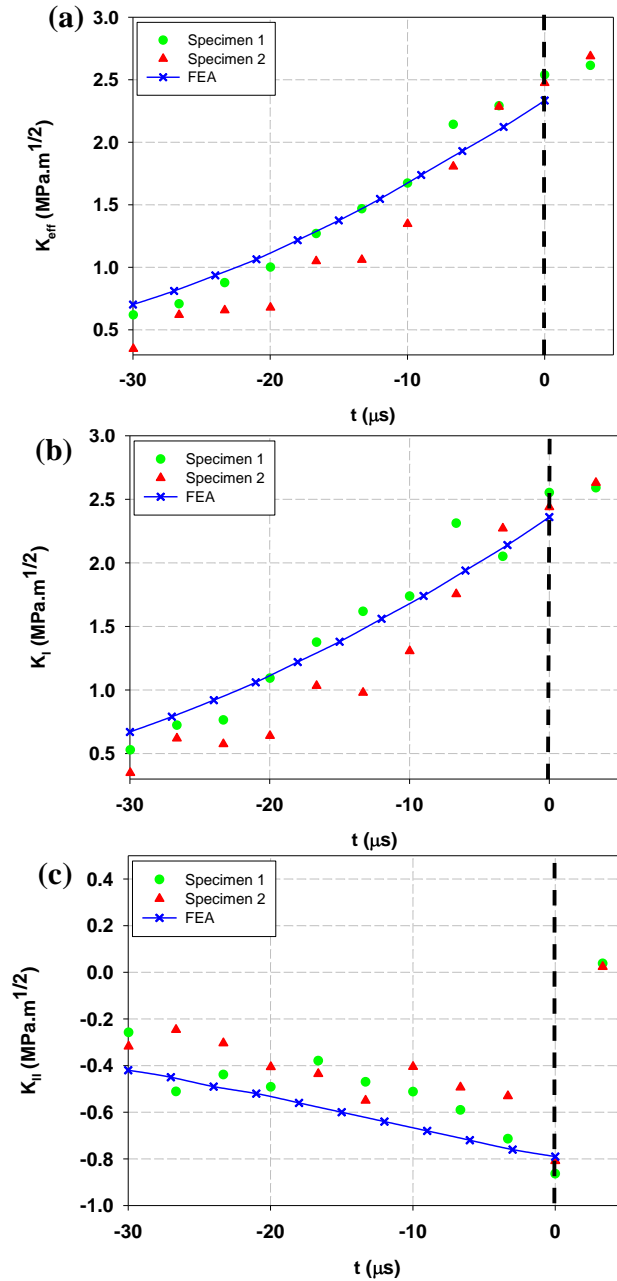


Figure 4.6: Experimental repeatability and comparison with FE simulation of (a): effective SIF histories ( $K_{\text{eff}}$ ), (b): mode-I SIF histories ( $K_I$ ), (c): mode-II SIF histories ( $K_{II}$ ) for glass-filled epoxy ( $e = 20$ ,  $a = 10$ ) case.

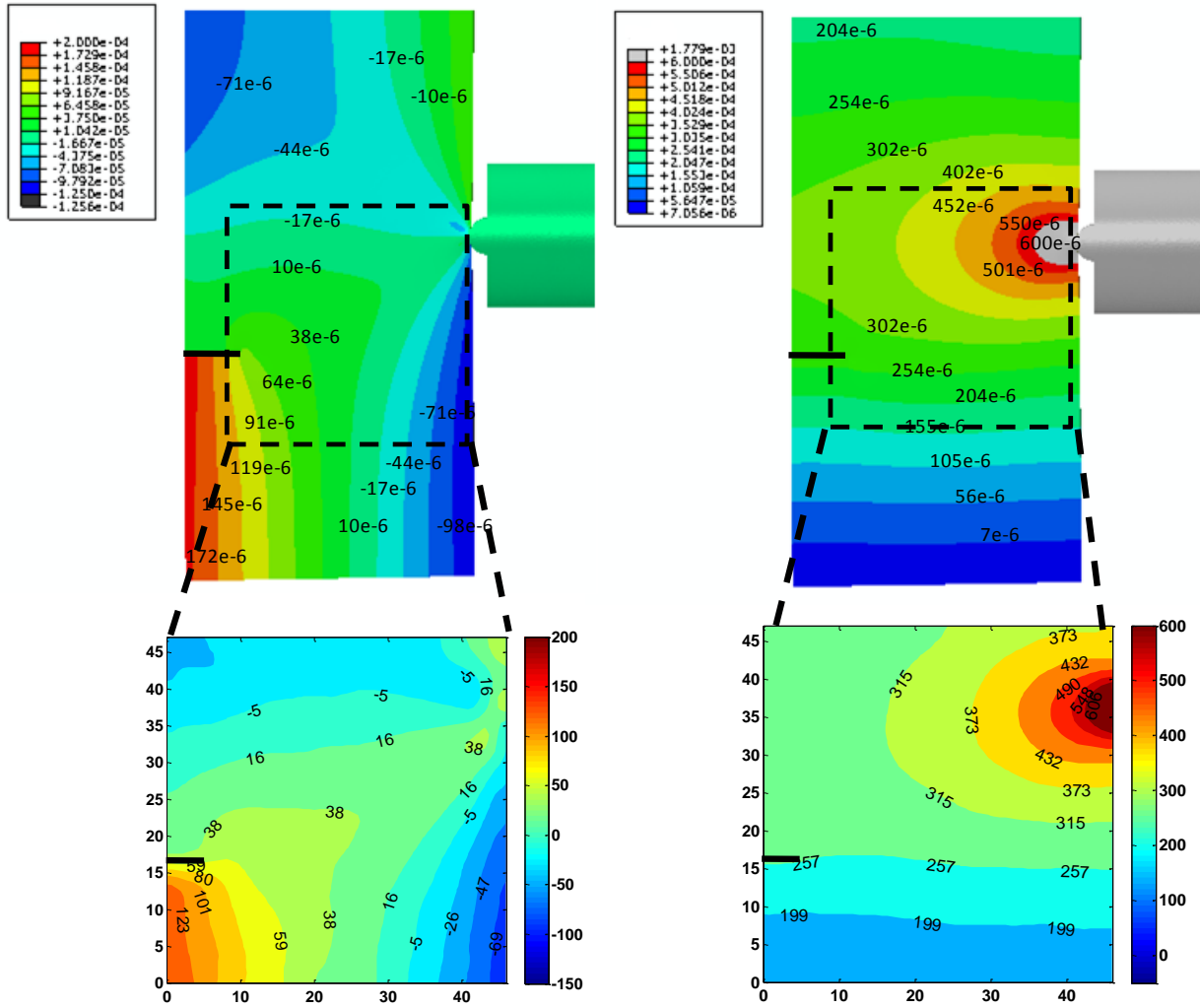


Figure 4.7: The crack opening (upper left) and crack sliding (upper right) displacement (in m) contours, respectively, obtained from 3D elasto-dynamic FEA; and the corresponding crack opening (bottom left) and crack sliding (bottom right) displacement (in  $\mu\text{m}$ ), respectively, obtained from the mixed-mode dynamic fracture experiment using DIC at  $t = 0$  for glass-filled epoxy ( $e = 20$ ,  $a = 10$ ) case

The strain history on the long-bar was recorded by a strain gauge affixed at its mid-span. Subsequently, the particle velocity in the long-bar was calculated [51] using the measured strain history to provide a boundary condition for a companion Finite Element (FE) simulation. A 3D elasto-dynamic simulation was carried out in ABAQUS/explicit up to crack initiation. Four-node tetrahedron elements were used to simulate a 10% glass-filled epoxy specimen ( $e = 20$  mm,  $a =$



10 mm case). The long-bar impacting the notched specimen was included in the numerical model. Both the specimen and long-bar were unconstrained and were butted against each other with a frictionless contact. The cross-sectional area of the long-bar was loaded at the far-end with particle velocity as input. The instantaneous crack-opening and crack-sliding displacements contours obtained from the FE simulation are shown in Figure 4.7. The corresponding crack opening and crack sliding displacement contours obtained from the mixed-mode experiment using DIC are also plotted in Figure 4.7 to compare with FE results. The FE contours match well with DIC contours and show the same displacement values around the crack tip used to extract the SIFs. Subsequently, the  $K_I$  and  $K_{II}$  were determined using regression analyses of the instantaneous crack opening and sliding displacements along the crack flanks obtained from the FE, respectively, using Equations (4.3) and (4.4),

$$\begin{aligned} (K_I)_{app} &= \frac{E\sqrt{2\pi}}{8\sqrt{r}} (u_y^{upper\ flank} - u_y^{lower\ flank}) \\ (K_I)_{app} &= K_I + C_1 \times r \end{aligned} \quad \dots \quad (4.3)$$

$$\begin{aligned} (K_{II})_{app} &= \frac{E\sqrt{2\pi}}{8\sqrt{r}} (u_x^{upper\ flank} - u_x^{lower\ flank}) \\ (K_{II})_{app} &= K_{II} + C_2 \times r \end{aligned} \quad \dots \quad (4.4)$$

where  $E$  is the elastic modulus,  $r$  is the distance from the crack tip along the  $x$ -axis,  $u_y$  is the crack opening displacement,  $u_x$  is the crack sliding displacement and  $C_1$ ,  $C_2$  are constants. The subscript 'app' in the above represents the apparent values of the stress intensity factors evaluated at locations others than the crack tip where far-field effects could be a factor. The displacements along the crack tip were exported from FE simulation and  $(K_I)_{app}$  and  $(K_{II})_{app}$  were computed using the above



expressions. Then  $(K_I)_{app}$  and  $(K_{II})_{app}$  were plotted against  $x$  and the intercept of that line gives the value of  $K_I$  and  $K_{II}$ , respectively, as shown in Figure 4.8. At crack initiation ( $t = 0$ ), the apparent stress intensity factors are extrapolated (see Figure 4.8) to obtain the actual stress intensity factors in mode-I and mode-II, respectively, using FEA. Later their vector sum was computed to obtain the instantaneous  $K_{eff}$  up to crack initiation. The SIF history obtained from FE analysis shows a good agreement with the experimental results (Figure 4.6 (a)-(c)).

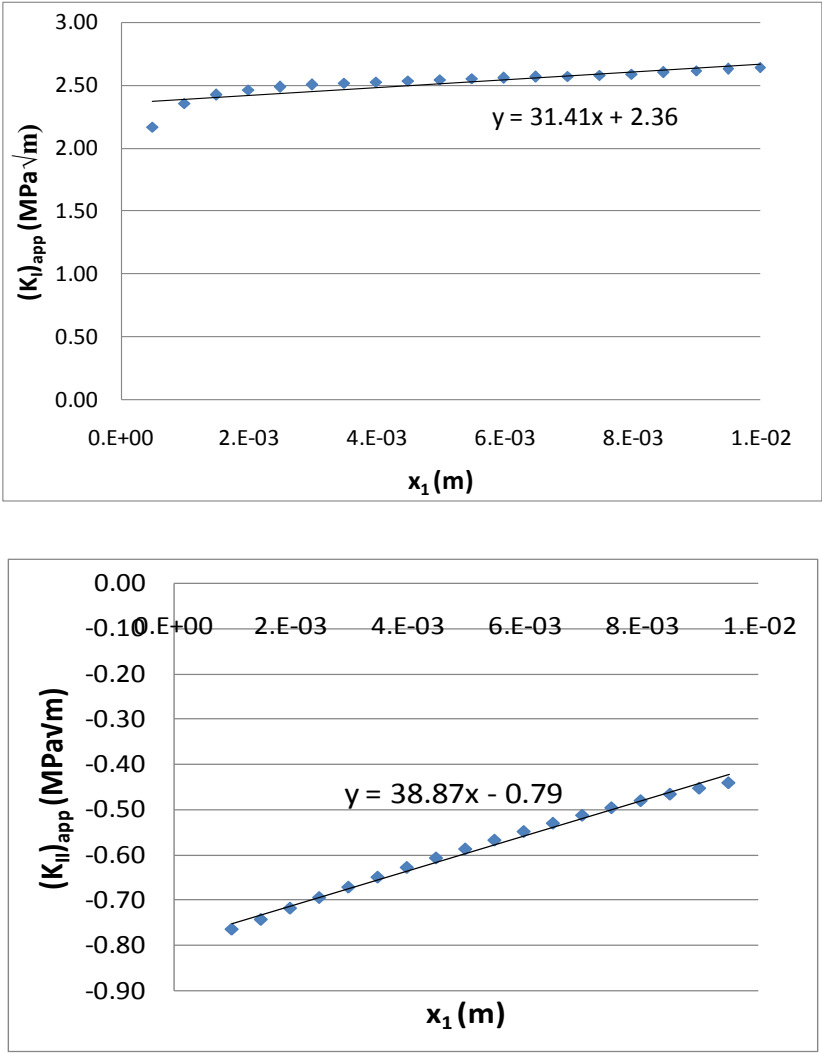


Figure 4.8: At  $t = 0$ , evaluation of mode-I (top) and mode-II (bottom) stress intensity factor using crack opening and crack sliding displacements obtained from FEA, respectively, for glass-filled epoxy ( $e = 20$ ,  $a = 10$ ) case.

#### 4.4 Results and discussion

The dynamic fracture behavior was studied by comparing the SIF histories of neat epoxy with glass-filled epoxy (Table 4.2). Plots of  $K_I$ ,  $K_{II}$ ,  $K_{\text{eff}}$  and  $\psi$  histories are shown in Figure 4.9 and Figure 4.10, respectively. The data from both the pre- and post-crack initiation periods are included. It should be noted that the measured histories of each sample have been shifted along the time axis to make crack initiation time (identified as  $t = 0$ ) of each experiment coincide. For -30 to -10  $\mu\text{s}$   $K_I$  and  $K_{II}$  are very small which makes  $\psi = \tan^{-1}(K_{II}/K_I)$  noisy, therefore  $\psi$  history is truncated up to -10  $\mu\text{s}$  for both neat and glass-filled epoxy.

In the select geometries studied, for neat epoxy, the mixed-mode crack initiation and crack propagation was found to occur dominantly in mode-I condition for ( $e = 15, a = 10$ ), ( $e = 20, a = 10$ ), and ( $e = 20, a = 15$ ) and dominantly in mode-II condition for ( $e = 20, a = 20$ ) and ( $e = 20, a = 25$ ). Similarly, for glass-filled epoxy, the mixed-mode crack initiation and crack propagation was found to occur dominantly in mode-I condition for ( $e = 15, a = 10$ ), ( $e = 20, a = 10$ ), ( $e = 20, a = 15$ ), and ( $e = 20, a = 20$ ) and dominantly in mode-II condition for and ( $e = 20, a = 25$ ). For both mode-I and mixed-mode loading, the  $K_{\text{eff}}$  and  $K_I$  histories show a monotonic increase up to the crack initiation. Further for both neat and glass-filled epoxy cases, the effective crack initiation toughness was higher for the mode-I case when compared to its respective mixed-mode counterpart. In mode-I, the glass-filled epoxy produced ~128% and ~288% improvement in effective crack initiation fracture toughness (Table 4.2) and critical energy release rate (

Table 4.3), respectively, compared to the neat epoxy. In the mixed-mode case, the glass-filled epoxy produced ~112%, ~117%, ~108%, 119% and 98% improvement in the effective crack initiation fracture toughness relative to its respective ( $e = 15, a = 10$ ), ( $e = 20, a = 10$ ), ( $e = 20, a$

= 15), ( $e = 20, a = 20$ ) and ( $e = 20, a = 25$ ) neat epoxy cases, respectively. Similarly, in the mixed-mode case, the glass-filled epoxy produced improvement in ~236%, ~266%, ~225%, ~263% and ~194% in the critical energy release rate, respectively, relative to its respective ( $e = 15, a = 10$ ), ( $e = 20, a = 10$ ), ( $e = 20, a = 15$ ), ( $e = 20, a = 20$ ) and ( $e = 20, a = 25$ ) neat epoxy cases.

Table 4.2: Effective crack initiation toughness (in  $\text{MPa}\sqrt{\text{m}}$ ) comparison between neat and glass-filled epoxy (% improvement is relative to neat epoxy), no. of measurements = 3

		<b>Effective crack initiation toughness</b>	
		<b>Neat epoxy</b>	<b>Glass-filled epoxy</b>
<b>Mode-I</b> ( $e = 0, a = 10$ )		$1.34 \pm 0.06$	$3.05 \pm 0.10$
	improvement in $K_{\text{eff}}$	-	~128%
<b>Mixed-mode</b> ( $e = 15, a = 10$ )		$1.25 \pm 0.10$	$2.65 \pm 0.18$
	improvement in $K_{\text{eff}}$	-	~112%
<b>Mixed-mode</b> ( $e = 20, a = 10$ )		$1.19 \pm 0.09$	$2.63 \pm 0.18$
	improvement in $K_{\text{eff}}$	-	~117%
<b>Mixed-mode</b> ( $e = 20, a = 15$ )		$1.21 \pm 0.12$	$2.52 \pm 0.14$
	improvement in $K_{\text{eff}}$	-	~108%
<b>Mixed-mode</b> ( $e = 20, a = 20$ )		$1.13 \pm 0.12$	$2.49 \pm 0.19$
	improvement in $K_{\text{eff}}$	-	~119%
<b>Mixed-mode</b> ( $e = 20, a = 25$ )		$1.11 \pm 0.10$	$2.20 \pm 0.16$
	improvement in $K_{\text{eff}}$	-	~98%

Table 4.3: Critical energy release rate (in  $\text{kPa}\cdot\text{m}$ ) comparison between neat and glass-filled epoxy (% improvement is relative to neat epoxy), no. of measurements = 3

		<b>Critical energy release rate</b>	
		<b>Neat epoxy</b>	<b>Glass-filled epoxy</b>
<b>Mode-I</b> ( $e = 0, a = 10$ )		$0.45 \pm 0.04$	$1.75 \pm 0.11$
	improvement in $G_{\text{cr}}$	-	~288%
<b>Mixed-mode</b> ( $e = 15, a = 10$ )		$0.39 \pm 0.06$	$1.32 \pm 0.18$
	improvement in $G_{\text{cr}}$	-	~236%
<b>Mixed-mode</b> ( $e = 20, a = 10$ )		$0.35 \pm 0.05$	$1.30 \pm 0.18$
	improvement in $G_{\text{cr}}$	-	~266%
<b>Mixed-mode</b> ( $e = 20, a = 15$ )		$0.37 \pm 0.07$	$1.19 \pm 0.13$
	improvement in $G_{\text{cr}}$	-	~225%
<b>Mixed-mode</b> ( $e = 20, a = 20$ )		$0.32 \pm 0.07$	$1.16 \pm 0.18$
	improvement in $G_{\text{cr}}$	-	~263%
<b>Mixed-mode</b> ( $e = 20, a = 25$ )		$0.31 \pm 0.06$	$0.91 \pm 0.13$
	improvement in $G_{\text{cr}}$	-	~194%

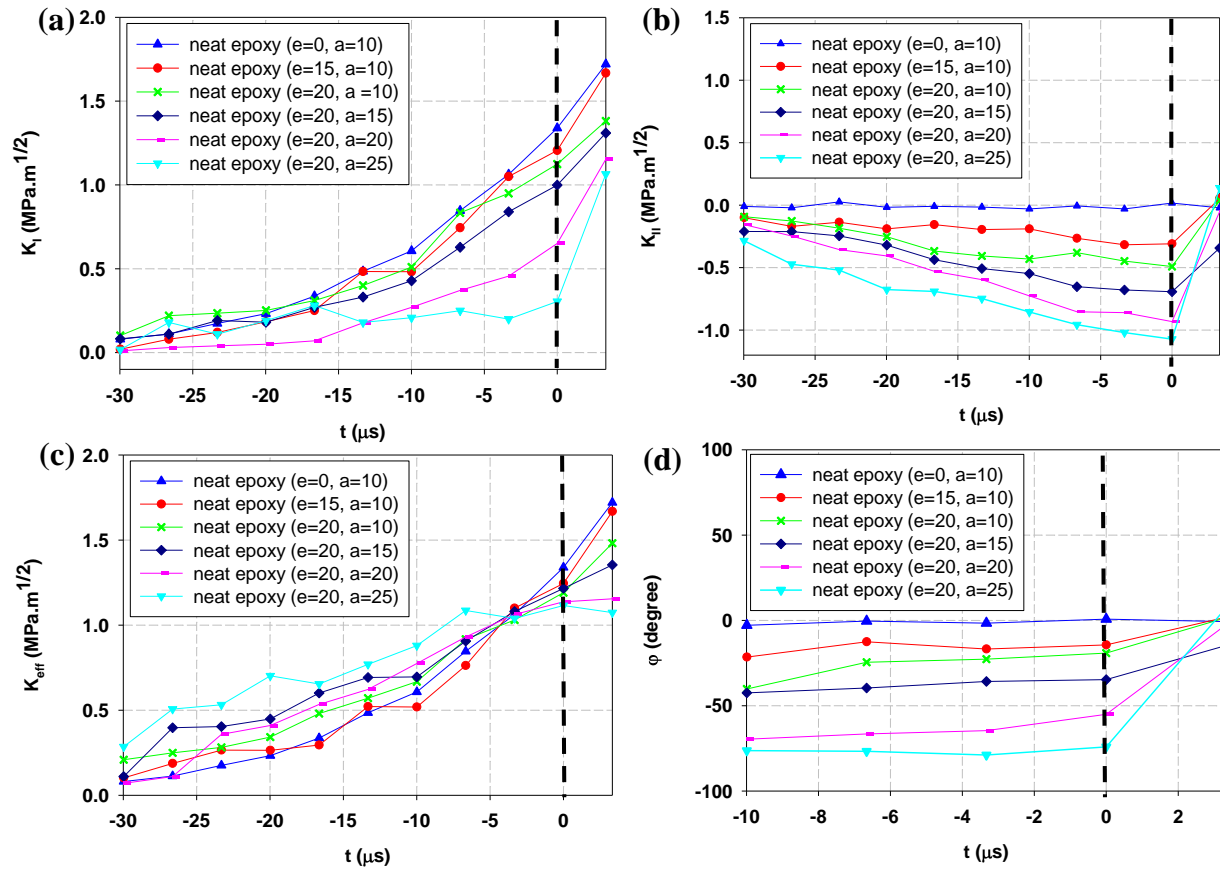


Figure 4.9: Fracture parameter histories of  $K_I$ ,  $K_{II}$ ,  $K_{eff}$  and  $\psi$  for neat epoxy from (a)-(d), respectively.

In the mode-I case, as the crack is loaded symmetrically, the extracted values of  $K_{II}$  histories show negligible values within the measurement errors. However, in the mixed-mode case, the mode-II histories showed a monotonic increase in magnitude up to crack initiation and once crack propagated a sudden drop due to unloading near the crack-tip. Interestingly, no such noticeable drop is evident in  $K_I$  histories suggesting the tendency of the crack to grow under mode-I condition. The relative amount of in-plane shear stress to normal stress amplification near the crack can be quantified by the mode-mixity parameter  $\psi = \tan^{-1}(K_{II}/K_I)$ . A higher value of mode-mixity  $\psi$

indicates the presence of a significant in-plane shear component at the crack tip up to crack initiation. Once the crack initiated, mode-mixity  $\psi$  drops nearly to zero, again suggesting a tendency to propagate under dominant mode-I conditions.

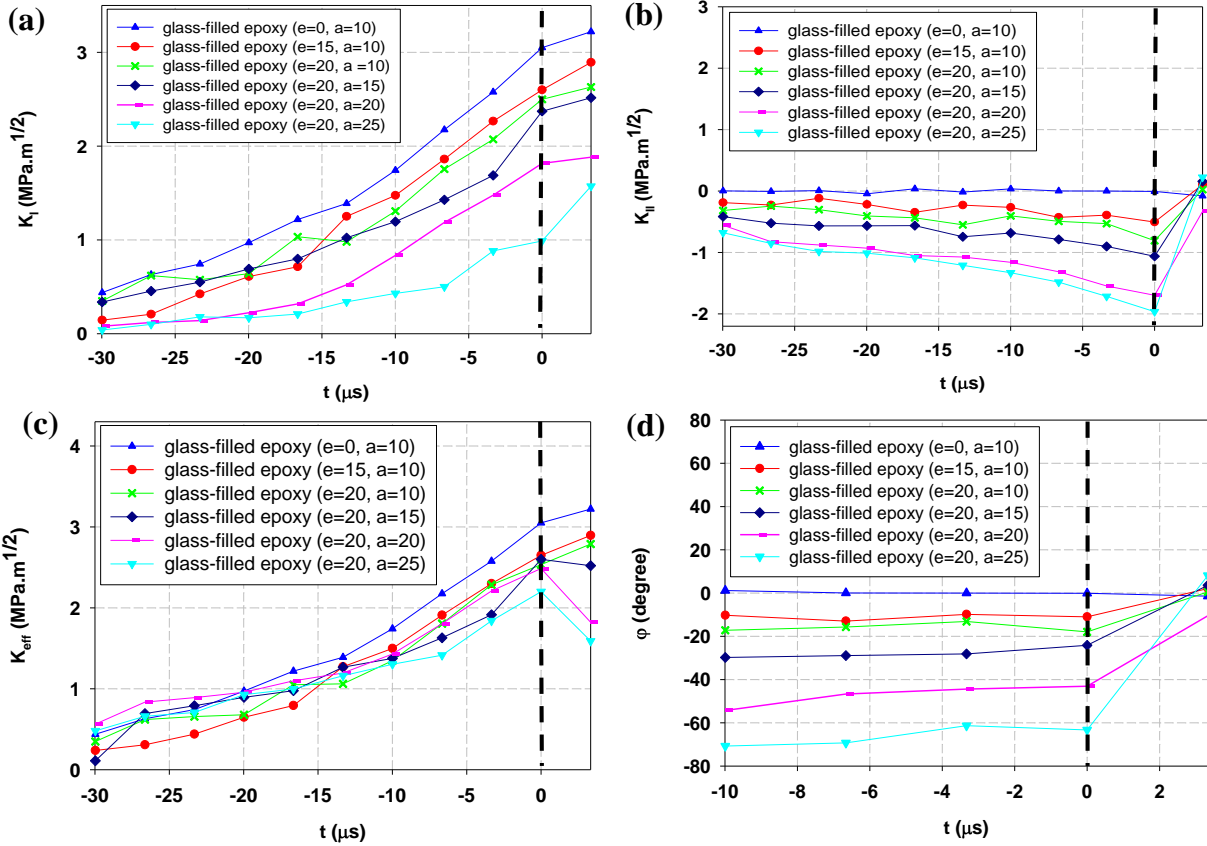


Figure 4.10: Fracture parameter histories of  $K_I$ ,  $K_{II}$ ,  $K_{eff}$  and  $\psi$  for 10%  $V_f$  glass-filled epoxy from (a)-(d), respectively.

#### 4.4.1 Fractography

A comparative fractographic study was carried out on glass-filled epoxy to understand the underlying toughening mechanisms on crack initiation toughness due to mode-I and mixed-mode loading. The fracture surface micrographs were obtained from the steady state crack growth region. It should be noted first that the micrographs (Figure 4.11) show no agglomeration of filler particles,

and the filler distribution is relatively uniform. As the stress waves propagate through the specimen, the crack front is driven forward until it encounters filler particles. As explained in Chapter 3, a careful observation of fractographs suggests that interaction of the crack front with filler phase leads to the following potential failure modes: (a) matrix cracking, (b) filler-matrix interface separation, (c) filler pullout, and/or (d) filler breakage. During crack growth each active failure mode contributes to energy dissipation which adds to the overall increase in fracture toughness of the composite.

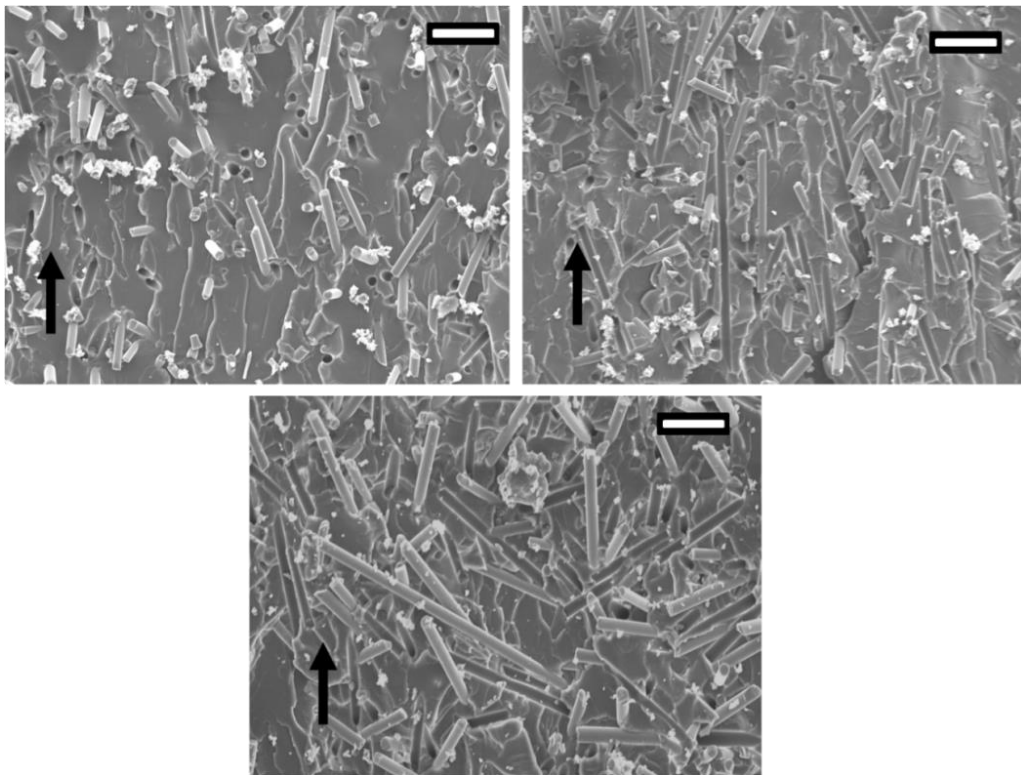


Figure 4.11: Fractographs of glass-filled epoxy (10%  $V_f$ ) for the mode-I ( $e = 0$ ,  $a = 10$ ) (top left) and the mixed-mode ( $e = 20$ ,  $a = 10$ ; top right) and ( $e = 20$ ,  $a = 20$ ; bottom), respectively; scale bar = 100  $\mu\text{m}$ .

It is evident from the micrographs that the surface ruggedness is noticeably higher for the mixed-mode ( $e = 20$ ,  $a = 10$ ; top right and  $e = 20$ ,  $a = 20$ ; bottom) case compared to the mode-I

case. The higher surface ruggedness is attributed to the fiber-matrix interface separation, a predominant failure mode under mixed-mode configuration due to the presence of a significant in-plane shear component at the crack tip. Also, energy dissipation due to interface separation is quite low compared to fiber breakage/pullout as explained in Chapter 3. However, in mode-I configuration, fiber-matrix separation was relatively small compared to the mixed-mode configuration. In mode-I, evidence of fiber breakage and fiber pullout was found to be significantly higher in number compared to the mixed-mode case. As noted in Chapter 3, the tensile strength of the fibers being ~3 GPa (compared to that of neat epoxy of ~ 70 MPa), a small number of fiber breakages could result in a rather high apparent fracture toughness of the composite. Hence, the number of broken fibers in the mode-I case contributed to the higher crack initiation fracture toughness compared to the mixed-mode case.

#### 4.5 Fracture envelope

The fracture envelope is a locus of points in  $K_I$ - $K_{II}$  space where combined action of  $K_I$  and  $K_{II}$  reaches a material dependent value. Based on energy principles, experimental results are shown to follow an elliptical fracture envelope for many conventional brittle materials under quasi-static conditions,

$$\left( \frac{K_I}{(K_I)_C} \right)^2 + \left( \frac{K_{II}}{(K_{II})_C} \right)^2 = 1 \dots\dots\dots (4.5)$$

where  $(K_I)_C$  and  $(K_{II})_C$  are the critical values in pure mode-I and pure mode-II conditions, respectively. The reasonable prediction of  $(K_{II})_C$  using Maximum Tangential Stress (MTS) criterion is  $0.866(K_I)_C$  [59]. The fracture envelope drawn using Equation (4.5) is shown in Figure 4.12 and compared with experimentally measured  $K_I$ - $K_{II}$  at crack initiation for both neat and glass-filled

epoxy. The experimentally measured critical  $K_I$ - $K_{II}$  and the fracture envelope drawn using Equation (4.5) follow the same trends but deviations of up to ~6% and ~15% between the two were observed (Figure 4.12) for neat and glass-filled epoxy, respectively.

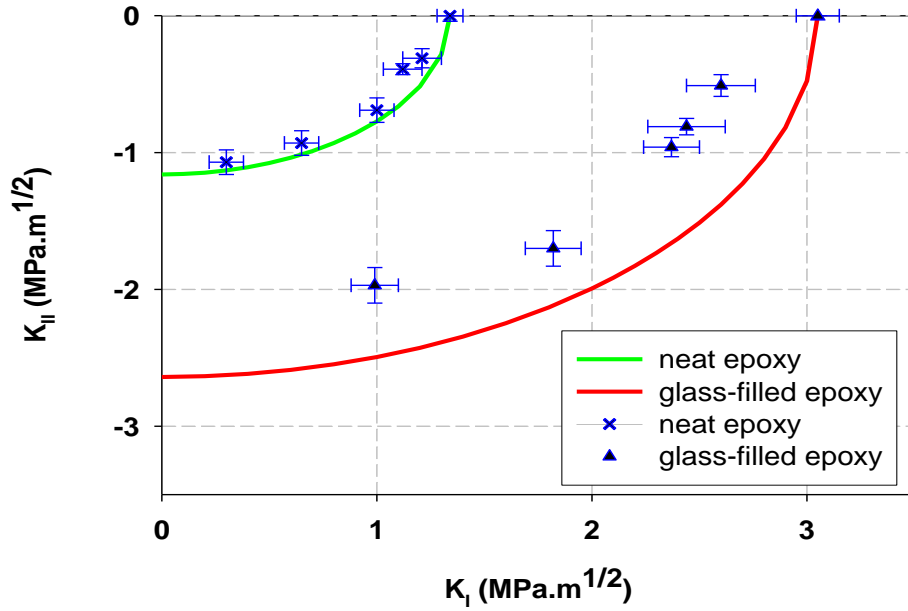


Figure 4.12: Dynamic crack initiation envelope for neat and 10%  $V_f$  glass-filled epoxy ( $e$  is eccentricity in mm and  $a$  is crack length in mm) using Eq. (4.5)

Lim et al. used an empirical criterion and suggested an equation for fitting the experimental results since the available brittle fracture criteria failed to predict the mixed-mode fracture of their rock specimens [60]. The general form of such empirical fracture criteria is described using Equation (4.6).

$$\left(\frac{K_I}{(K_I)_c}\right)^\lambda + \left(\frac{K_{II}}{(K_{II})_c}\right)^\mu = 1 \dots\dots\dots (4.6)$$

where  $\lambda$  and  $\mu$  are parameters that are assumed to depend only on the material parameters. Ayatollahi and Aliha reported that other researchers have also employed similar empirical fracture criterion by using different values of  $\lambda$  and  $\mu$  for fitting empirical curve to their mixed-mode test data



in brittle materials [60]. Lim et al. examined numerous values for  $\lambda$  and  $\mu$  and found that  $\lambda = \mu = 2.55$  provides the best fit to the test results [61]. Similarly, Richard found  $\lambda = 1, \mu = 2$  and Shah found  $\lambda = 1, \mu = 1$  gave the best fit to their test results [61]. In the literature, no one has proposed the fracture envelope for the dynamic loading condition. In the current research where inertial effects are significant, the fracture envelope was proposed by curve fitting critical values of stress intensity factors at different mode-mixities for both neat and glass-filled epoxy. It was found that the fracture envelope for  $\lambda = 1.4, \mu = 1.4$  and  $\lambda = 1.3, \mu = 1.3$  was the best fit (maximum deviation of ~6% between the experimentally measured critical  $K_I$ - $K_{II}$  and the fracture envelope drawn using Equation (4.6)) with experimental data for neat and glass-filled epoxy, respectively, as shown in Figure 4.13.

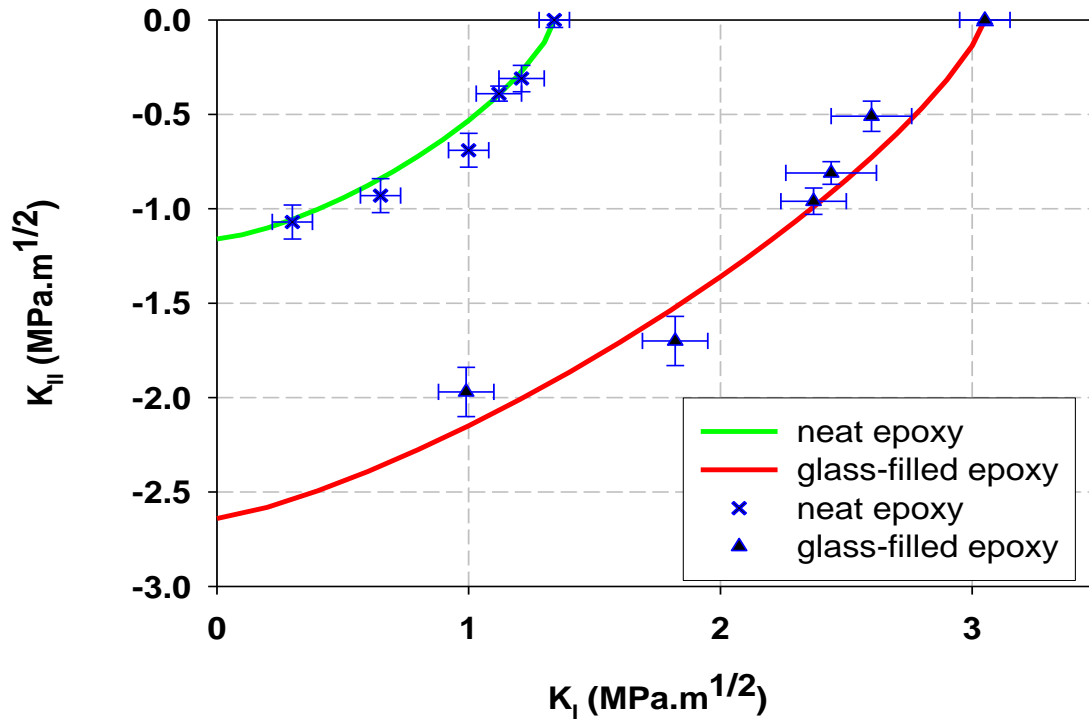


Figure 4.13: Dynamic crack initiation envelope for neat and 10%  $V_f$  glass-filled epoxy ( $e$  is eccentricity in mm and  $a$  is crack length in mm) using Eq. 4.6 for  $\lambda, \mu = 1.4$  and  $\lambda, \mu = 1.3$ , respectively.

#### 4.6 Mixed-mode crack growth direction

In this section, using the MTS criterion and based on the stress intensity factor values just before crack initiation crack kink direction was estimated using Equation (4.7).

$$\tan \frac{\theta_c}{2} = \frac{1}{4} \left( \frac{K_I}{K_{II}} \pm \sqrt{\left( \frac{K_I}{K_{II}} \right)^2 + 8} \right) \dots\dots\dots (4.7)$$

where  $\theta_c$  is the crack kink angle relative to the initial notch orientation. The crack initiation angles were measured on a fractured specimen (Figure 4.14 - Figure 4.17) manually by constructing a tangent at the notch tip in the crack initiation direction. The measured values were compared with the computed ones for both neat and glass-filled epoxy cases, respectively.

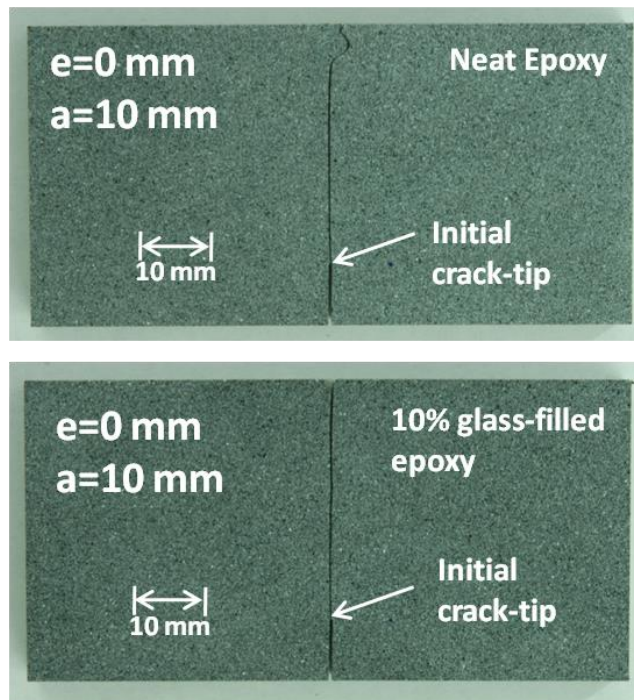


Figure 4.14: Mode-I crack propagation in neat epoxy (top) and 10%  $V_f$  glass-filled epoxy (bottom). The crack propagated along the initial notch direction for both neat and glass-filled epoxy.

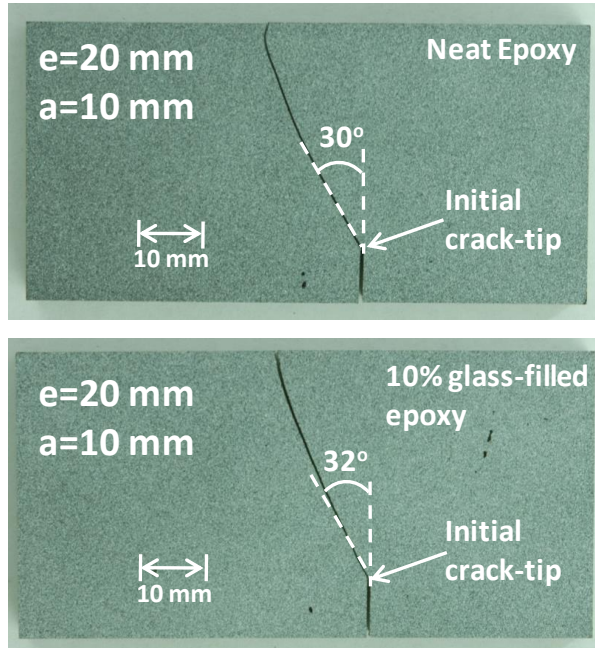


Figure 4.15: Crack propagation in neat epoxy (top) and 10%  $V_f$  glass-filled epoxy (bottom) in mixed-mode loading configuration ( $e = 20$ ,  $a = 10$ ). The crack propagated at  $\sim 30^\circ$  and  $\sim 32^\circ$  from the initial notch direction for neat and glass-filled epoxy, respectively.

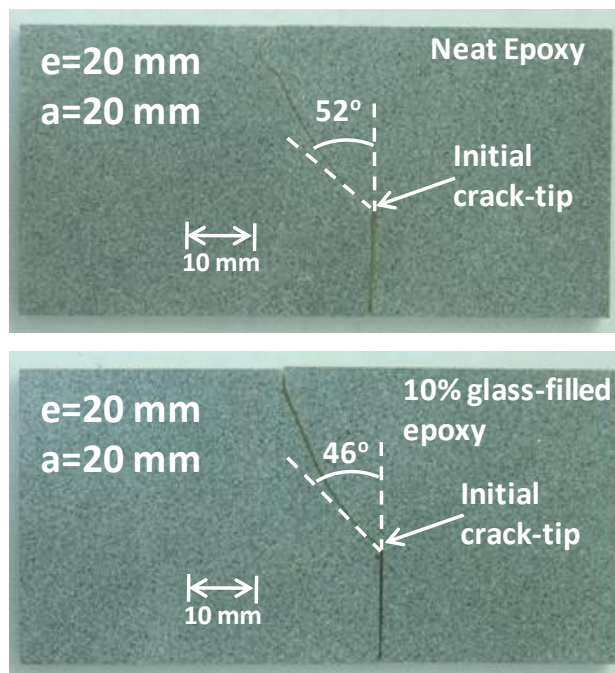


Figure 4.16: Crack propagation in neat epoxy (top) and 10%  $V_f$  glass-filled epoxy (bottom) in mixed-mode loading configuration ( $e = 20$ ,  $a = 20$ ). The crack propagated at  $\sim 52^\circ$  and  $\sim 46^\circ$  from the initial notch direction for neat and glass-filled epoxy, respectively.

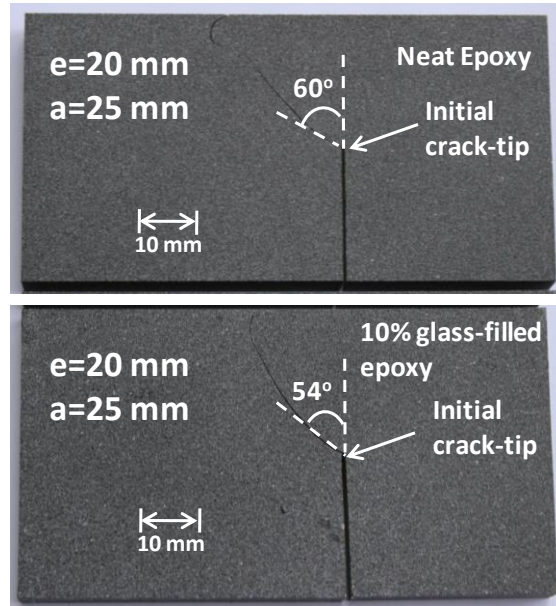


Figure 4.17: Crack propagation in neat epoxy (top) and 10%  $V_f$  glass-filled epoxy (bottom) in mixed-mode loading configuration ( $e = 20$ ,  $a = 25$ ). The crack propagated at  $\sim 60^\circ$  and  $\sim 54^\circ$  from the initial notch direction for neat and glass-filled epoxy, respectively.

Table 4.4: Crack kink angle comparison for neat epoxy and glass-filled epoxy

	Measured Angle	Using Equation (4.7)*	Difference (%)
Neat epoxy ( $e = 15$ , $a = 10$ )	$24^\circ$	$26^\circ$	$\sim 8\%$
Neat epoxy ( $e = 20$ , $a = 10$ )	$30^\circ$	$32^\circ$	$\sim 7\%$
Neat epoxy ( $e = 20$ , $a = 15$ )	$41^\circ$	$44^\circ$	$\sim 7\%$
Neat epoxy ( $e = 20$ , $a = 20$ )	$52^\circ$	$58^\circ$	$\sim 12\%$
Neat epoxy ( $e = 20$ , $a = 25$ )	$60^\circ$	$65^\circ$	$\sim 8\%$
Glass-filled epoxy ( $e = 15$ , $a = 10$ )	$21^\circ$	$23^\circ$	$\sim 10\%$
Glass-filled epoxy ( $e = 20$ , $a = 10$ )	$32^\circ$	$35^\circ$	$\sim 9\%$
Glass-filled epoxy ( $e = 20$ , $a = 15$ )	$38^\circ$	$41^\circ$	$\sim 8\%$
Glass-filled epoxy ( $e = 20$ , $a = 20$ )	$46^\circ$	$52^\circ$	$\sim 13\%$
Glass-filled epoxy ( $e = 20$ , $a = 25$ )	$54^\circ$	$61^\circ$	$\sim 13\%$

\* $K_I$  and  $K_{II}$  measured at crack initiation from mixed-mode dynamic experiments

Photographs of fractured specimens are shown in Figure 4.14 - Figure 4.17 for both the neat and glass-filled epoxy cases under mode-I and mixed-mode loading conditions. In mode-I case, the crack propagated self for both neat and glass-filled epoxy. However, in the mixed-mode cases, the crack kinked at an angle for both neat and glass-filled epoxy. The experimentally measured  $K_I$  and  $K_{II}$  just before the observed crack initiation were used in the MTS criterion to obtain the crack propagation direction and compared with the measured angles. The results are tabulated in Table 4.4. It is evident from the results that the MTS criterion predicted the crack propagation direction reasonably well (maximum error ~13%) when compared to experimentally measured angles.

## CHAPTER 5

### FINITE ELEMENT MODELING

The mechanical behavior of particulate polymer composites does not just depend on the material properties of its constituents but also on their mutual interaction including interfacial characteristics during deformation. To understand these, the finite element method was employed to model the mechanical behavior of carbon fiber modified epoxy composite using ABAQUS version 6.12 structural analysis software. The quasi-static tension tests were performed on neat and carbon fiber modified epoxy. The material response obtained from the quasi-static tension test for the neat epoxy and properties of carbon fiber provided by the manufacturer were utilized in these simulations. The simulations were limited to recovering the stress-strain response of carbon fiber modified epoxy composite and comparing with it the experimental results. It also included examining the crack growth behavior in the vicinity of a single fiber located in a representative area containing a random distribution of fibers.

#### 5.1 Material preparation

Neat epoxy and rod-shaped carbon (Table 5.1) fiber modified epoxy composite were chosen to study their quasi-static tensile behavior and modeling that behavior using the finite element method. The fillers were dispersed into the low-viscosity epoxy (Bisphenol-A resin and Amine based hardener; densities  $1130 \text{ kg/m}^3$  and  $961 \text{ kg/m}^3$ , respectively) used in the earlier part of this research. To carry out the tension test study, neat epoxy and 5% carbon fiber modified epoxy by

volume sheets were cast separately. The sheets were machined into dogbone specimens shown in Figure 5.1.

Table 5.1: Carbon fiber characteristics

Filler	Source	Average Dimensions	Aspect Ratio*(AR)	Density (kg/m <sup>3</sup> )
Carbon fiber	Toho Tenax Inc., USA	60 μm long, 8 μm diameter	60/8 = 7.5	1810

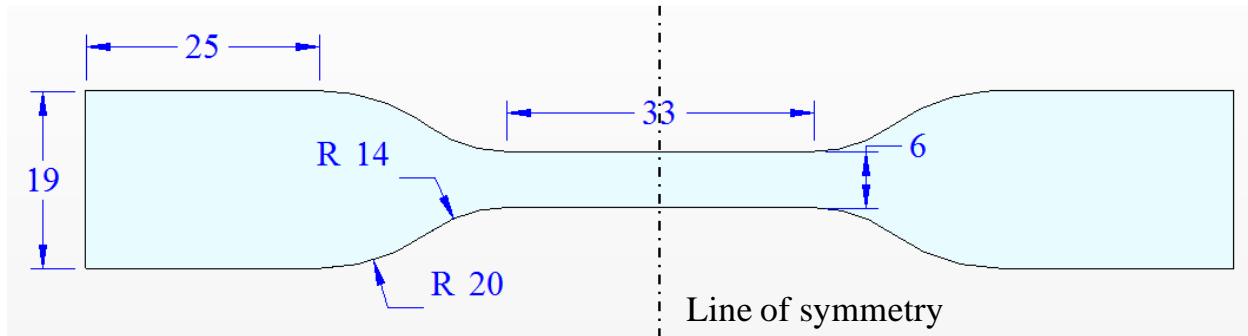


Figure 5.1: The dogbone-shaped specimens used for tension tests (thickness 4.3 mm)

## 5.2 Quasi-static tension tests

The uniaxial quasi-static tensile tests were performed on dogbone-shaped neat epoxy and carbon fiber modified epoxy composite using Instron 4465. Tension tests were carried out to record their stress-strain response in displacement control mode with a cross-head speed of 2 mm/min. The strain was measured using an extensometer. The experimental data was converted into true stress and true strain using Equations (5.1) and (5.2) [62] and plotted in Figure 5.2.

$$\varepsilon_{true} = \ln(1 + \varepsilon_{eng}) \dots\dots\dots (5.1)$$

$$\sigma_{true} = \sigma_{eng} * (1 + \varepsilon_{eng}) \dots\dots\dots (5.2)$$

Table 5.2: Measured material properties from uniaxial tension tests, no. of measurements = 2

	Elastic modulus $E$ (GPa)	Ultimate strength (MPa)
Neat epoxy	$4.00 \pm 0.10$	$64 \pm 4$
Carbon fiber modified epoxy	$5.58 \pm 0.23$	$72 \pm 5$

The measured elastic modulus and ultimate strength are tabulated in Table 5.2 for neat and carbon fiber modified epoxy.

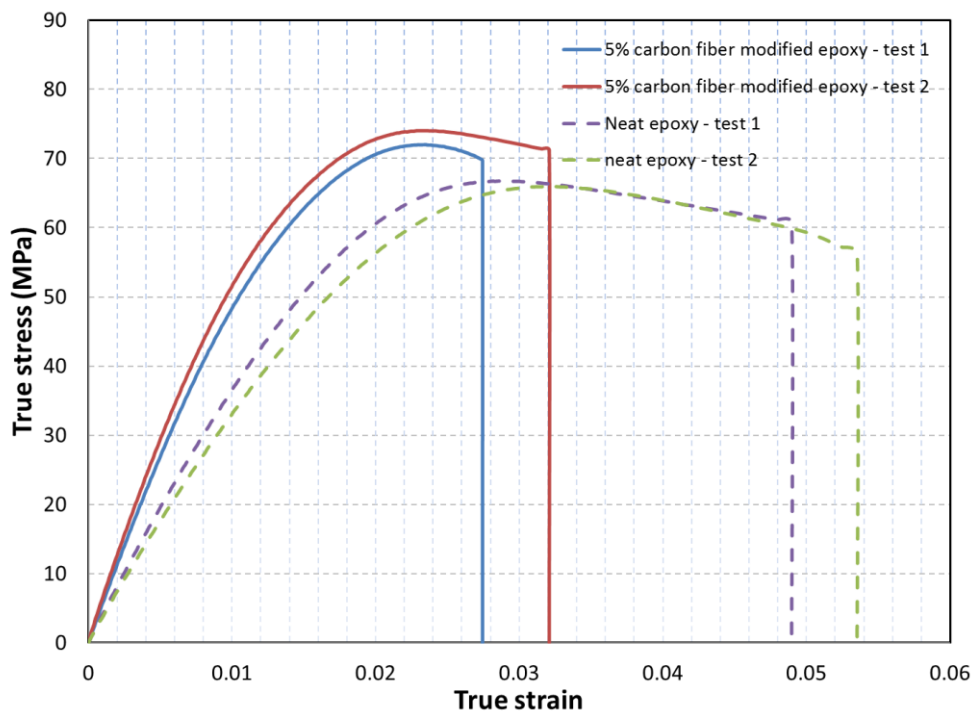


Figure 5.2: True stress versus true strain response for 5%  $V_f$  carbon fiber modified epoxy and neat epoxy obtained from quasi-static tension tests

### 5.3 Finite element modeling of tension tests

#### 5.3.1 Constituent properties

In carbon fiber epoxy composites, carbon fibers and the neat epoxy are the two material constituents. The stress-strain response for carbon fiber was provided by the manufacturer (Toho



Tenax Inc.) and is shown in Figure 5.3. For neat epoxy, true stress versus true strain response was used as material input obtained from the uniaxial tension test. The material properties for neat epoxy and carbon fibers used in finite element simulations are shown in Table 5.3.

Table 5.3: Elastic properties used for neat epoxy and carbon fibers

	Elastic modulus $E$ (GPa)	Poisson ratio $\nu$
Neat epoxy	4.0	0.3
Carbon fibers	225	0.2

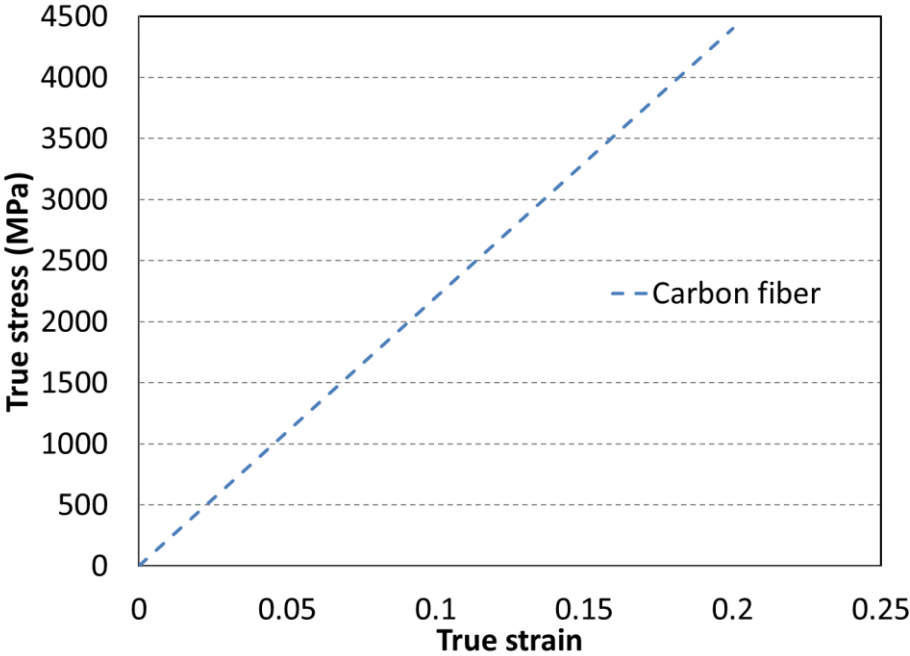


Figure 5.3: Stress-strain response for carbon fiber

In order to model the nonlinear response, ABAQUS requires that the strain be divided into elastic and plastic regimes [63]. For plastic material property input the plastic strain was computed using Equation (5.3).

$$\varepsilon_p = \varepsilon_{true} - \frac{\sigma_{true}}{E} \dots\dots\dots (5.3)$$

Isotropic hardening was used to model the plastic behavior using ABAQUS. In isotropic hardening, the yield surface changes its size uniformly in all directions such that the yields stress increases (or decreases) in all stress directions as plastic straining occurs [1].

#### 5.4 Modeling approach

The modeling process of a 3D carbon fiber modified specimen was simplified using 2D models based on a representative area element (RAE). The analysis was carried out in both plane stress and plane strain conditions to obtain the upper and lower bounds of mechanical response. The size of RAE was established as follows: On average the carbon fibers are 60  $\mu\text{m}$  long and 8  $\mu\text{m}$  in diameter. Hence, a RAE ten times larger than the largest dimension of the carbon fiber, i.e. 600 x 600  $\mu\text{m}^2$  in size was chosen [64]. Using a MATLAB code proposed by Martinez based on random generation of points and Simple Sequential Inhibition (SSI) process thirty-eight random points  $(x, y)$  (thirty-eight fibers account for 5% area ( $A_f$ ) fraction) were generated over the selected RAE [65]. The random point generation process is briefly explained as follows:

- First point was generated randomly using *rand* command in MATLAB within the RAE. The second point was randomly generated next and its distance was calculated from the first. If this distance was more than the *inhibition distance*  $s$ , the second point was kept; otherwise it was discarded, and the same process was repeated. The inhibition distance  $s$  is to generate a more regular pattern of points within the RAE.
- For the points randomly generated next, their distance was calculated from the previously generated ones. If the distance was more than  $s$ , they were kept; otherwise discarded. The process

was continued until the desired number of points (which is 38 in this particular case) were generated within the RAE.

- The maximum distance of inhibition is given by  $r = \sqrt{\frac{2 * RAE}{\sqrt{3} * n}}$

where  $n$  is the number of points to be generated in RAE [66]. Hence a ‘regularity’ parameter can be quantified as  $\delta = s/r$ . Note that for  $\delta = 1$ , the maximum inhibition distance  $s$  can be equal to  $r$  (i.e.,  $s=r$ ). To simulate homogeneous dispersion of carbon fibers into the composite, the random points should be generated with maximum regularity (i.e.,  $\delta = 1$ ). However, using SSI process the probability of achieving  $\delta = 1$  is very small even with infinite computational resources [67]. Thus,  $\delta = 0.81$  was the maximum regularity parameter achieved using SSI process with available computational resources. Figure 5.4 shows the comparison of randomly generated points at  $\delta = 0.30$  and  $\delta = 0.81$  and it should be noted that the latter produces relatively more homogenous set of points when compared to the former. Therefore, all the simulations were performed at  $\delta = 0.81$ .

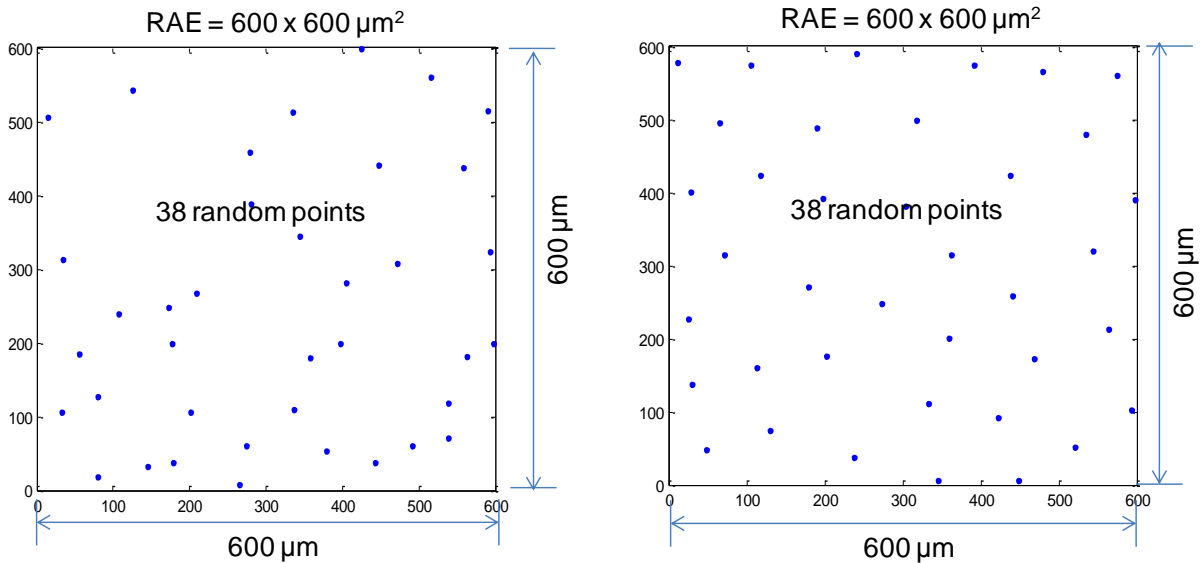


Figure 5.4: Random points generation using 2D Poisson homogeneous process for 5%  $A_f$  carbon fiber modified epoxy composite (left:  $s = 31 \mu\text{m}$ ,  $\delta = 0.30$ ; right:  $s = 85 \mu\text{m}$ ,  $\delta = 0.81$ )

The output of the MATLAB code consists of a list of points and their coordinates  $(x, y)_n$ . To account for the orientation of each fiber, 38 random angles were generated between  $-180^\circ$  to  $180^\circ$  at these locations in the RAE. Using those points and angles, 38 fibers were constructed in that RAE using AutoCAD. Then those were imported from AutoCAD into ABAQUS for further finite element modeling as shown in Figure 5.5.

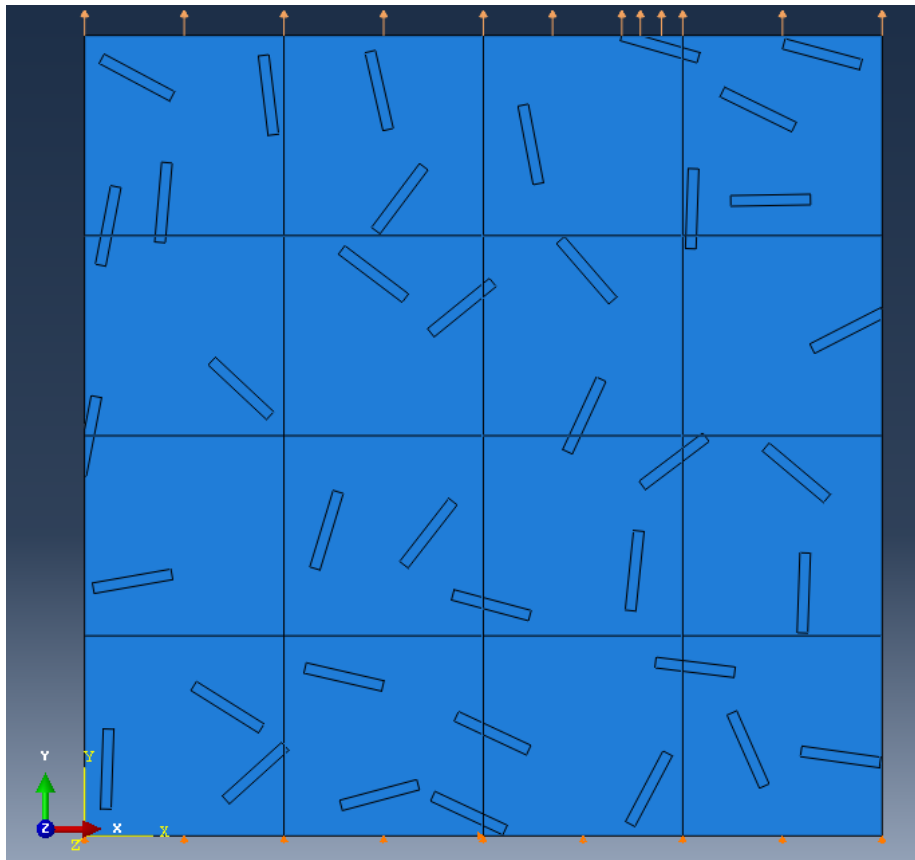


Figure 5.5: Random fibers were drawn using 2D Poisson homogeneous process for 5%  $A_f$  carbon fiber modified epoxy composite for  $\delta = 0.81$  case

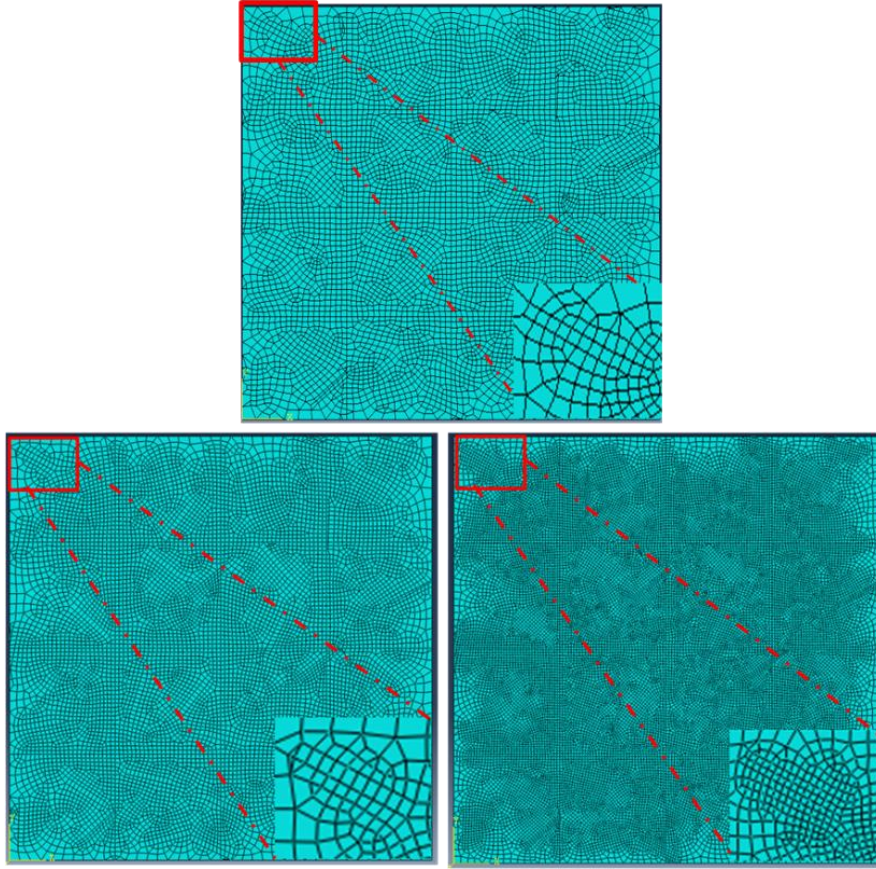


Figure 5.6: Discretized FE meshes used for convergence study (coarse (top), finer (bottom left) and the finest (bottom right))

## 5.5 Boundary conditions

The applied boundary conditions are shown in Figure 5.5. The upper edge was displaced with a velocity of 2 mm/min in the  $y$ -direction same as the cross-head speed used in the tension tests. All the nodes along the lower edge were constrained in the  $y$ -direction. The center node on the lower edge of the model was constrained in the  $x$ -direction as well.

### 5.5.1 Element type

For plane stress and plane strain cases, CPS4R and CPE4R elements were used, respectively. Both element types are 4-node bilinear quadrilateral and reduced integration elements.

## 5.6 Mesh convergence

The mesh convergence study was carried out using three different mesh sizes. Figure 5.6 shows the three different mesh sizes used. The model at the top in Figure 5.6 has a relatively coarser mesh compared to the other two at the bottom. The coarsest mesh produced the stiffer response compared to the other two mesh sizes and produced a relatively higher modulus in both plane stress as well as plane strain situations. The total number of elements in the other two finer mesh cases (10073 and 23492 elements) is more than two and four times compared to coarse mesh (6181 elements) shown in Table 5.4. To extract the stress-strain response from the FEA model, the whole geometry was divided by three equally spaced horizontal and vertical lines as shown in Figure 5.5. When the model is loaded in the vertical direction, stress and strain values are output at those three horizontal lines and then averaged to get the stress-strain response for various applied displacements. The elastic modulus is extracted from the models using plane stress and plane strain approximations, separately and tabulated in Table 5.4. The coarsest mesh produced 5.109 and 5.605 GPa elastic modulus in plane stress and plane strain case, respectively. As the mesh was refined to 10073 elements, model produced about 4% lower elastic modulus in both plane stress and plane strain cases. However, further refinement of mesh showed negligible change in the elastic modulus as shown in Table 5.4.

Table 5.4: Elastic modulus comparison for coarse vs. fine mesh

	<b>Number of elements</b>	<b><i>E</i> (GPa)</b>
<b>Coarse mesh-Plane stress</b>	6181	5.109
<b>Coarse mesh-Plane strain</b>	6181	5.605
<b>Finer mesh-Plane stress</b>	10073	4.900
<b>Finer mesh-Plane strain</b>	10073	5.368
<b>Finest mesh-Plane stress</b>	23492	4.895
<b>Finest mesh -Plane strain</b>	23492	5.361

## 5.7 Results and discussion

The 2D finite element stress-strain responses were in agreement with measurements for 5%  $V_f$  carbon fiber modified epoxy composite (Figure 5.7). The plane stress and plane strain results showed the lower and upper bounds, respectively. The modulus measured from the tension test experiments and computed from the planes stress and plane strain simulations are shown in Table 5.6. The plane stress and plane strain cases produced 12% and 4% lower elastic modulus compared to the measured value. Both plane stress and plane strain cases match well with 3D experimental response up to the elastic limit (assumed to be 0.2% strain). The match between the 2D finite element results with the measurements up to the elastic limit is attributed to perfect bonding between epoxy matrix and carbon fibers in the composite for simulations. Beyond the elastic limit, at higher strain levels 3D effects being significant experimental response deviates from 2D responses. The plane strain case produced stiffer response than the plane stress case as expected. In carbon fibers, the higher stress (Figure 5.8 and Figure 5.9) and lower strain (Figure 5.10 and Figure 5.11) magnitudes were evident in fiber modified epoxy due to significantly higher stiffness of carbon fibers compared to epoxy matrix. Another point to be noted is that the fibers aligned with

the loading direction get activated to carry higher load and hence show higher stress magnitude in them (Figure 5.8). This in turn reduces matrix stresses significantly in its neighborhood.

Table 5.5.: Elastic Modulus comparison between FE simulation and experiment

	<i>E</i> (GPa)	
<b>Experiment</b>	5.58±0.23	
<b>Simulation-Plane stress</b>	4.90	~ -12%
<b>Simulation-Plane strain</b>	5.37	~ -4%

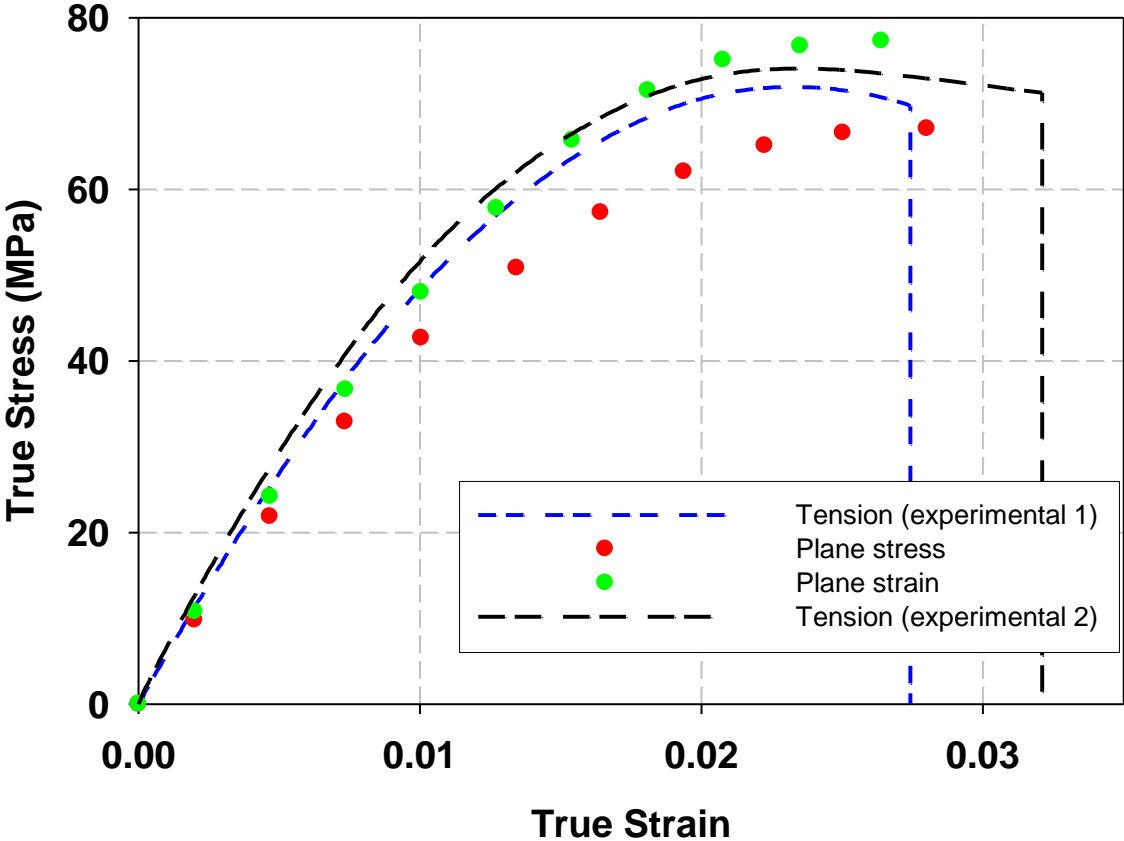


Figure 5.7: Comparison of FEA with experimental result for 5%  $V_f$  carbon fiber modified epoxy composite of  $600 \times 600 \mu\text{m}^2$  RAE case loaded in the vertical direction



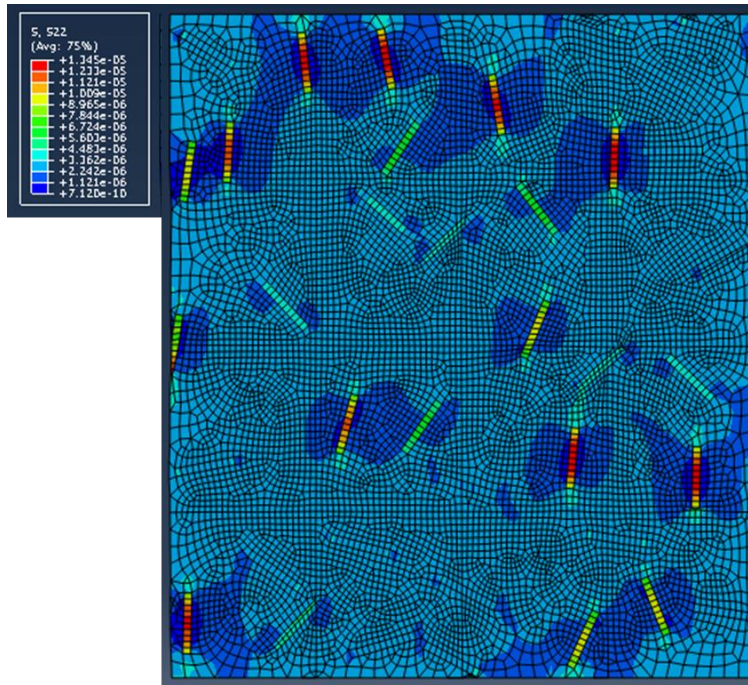


Figure 5.8: Stress ( $\sigma_{yy}$ ) for 5%  $V_f$  carbon fiber modified epoxy composite for plane stress case loaded in the vertical direction

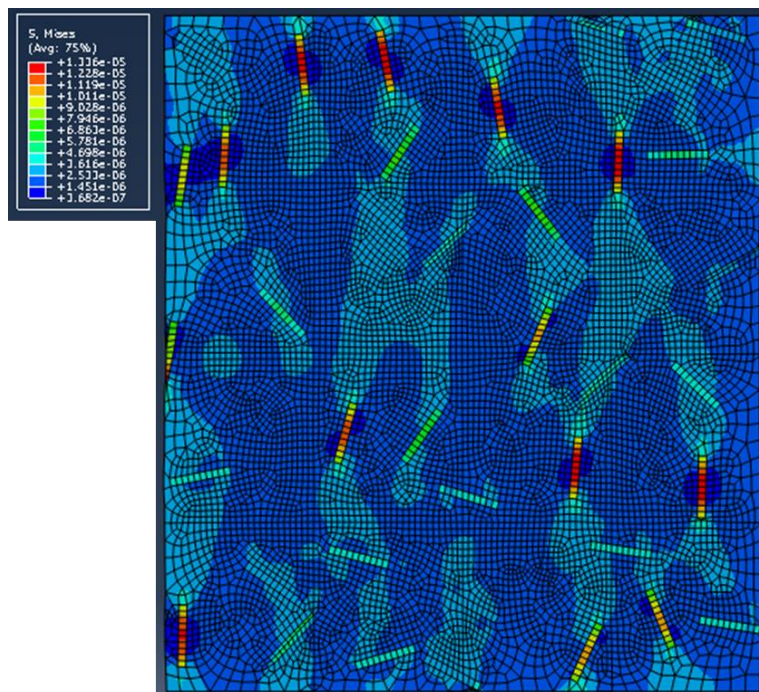


Figure 5.9: Mises stresses for 5%  $V_f$  carbon fiber modified epoxy composite for plane stress case loaded in the vertical direction

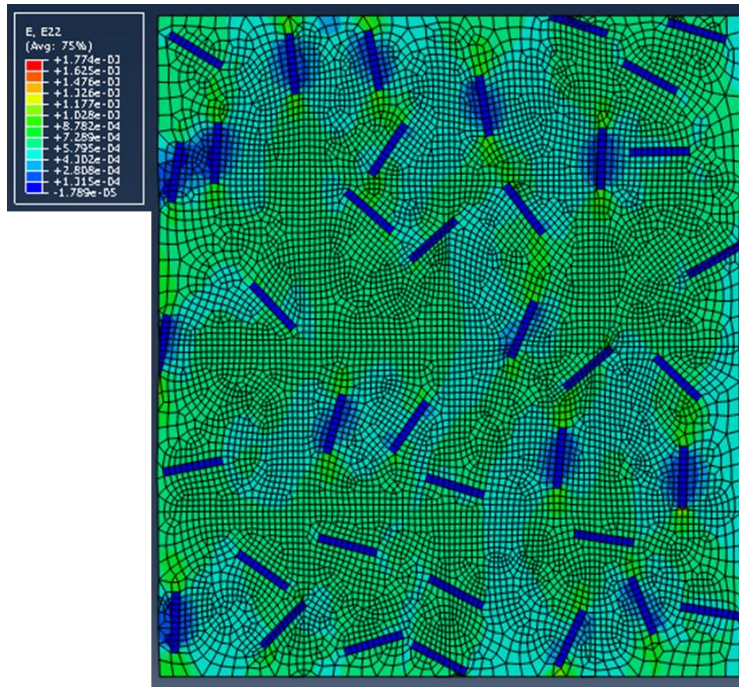


Figure 5.10: Normal strain ( $\epsilon_{yy}$ ) for 5%  $V_f$  carbon fiber modified epoxy composite for plane stress case loaded in the vertical direction

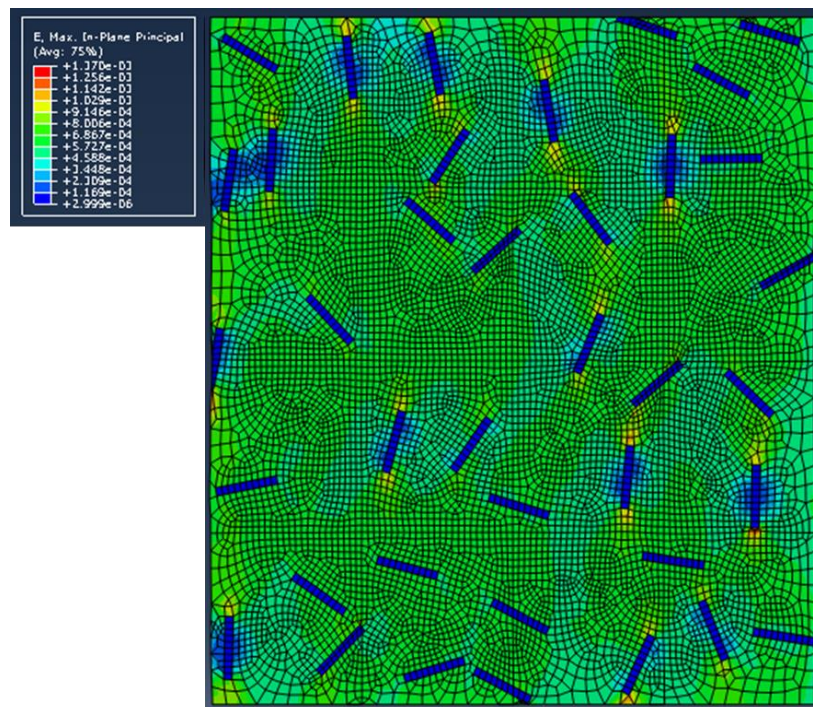


Figure 5.11: Maximum principal strain distribution for 5%  $V_f$  carbon fiber modified epoxy composite for plane stress case loaded in the vertical direction



### 5.7.1 Horizontal vs. vertical loading of RAE

To ensure the randomness of fibers in the model, the same model shown in Figure 5.5 was loaded in the horizontal direction and the stress-strain response was computed. The stress-strain responses for plane stress and plane strain conditions, obtained in the vertical and horizontal loading direction were compared with the experiment and both were found to be in agreement as shown in Figure 5.12. For the vertical loading case, the elastic modulus obtained was ~12% lower in the plane stress case and ~4% lower in the plane strain case, respectively, whereas for the horizontal loading case the elastic modulus obtained was ~7% lower in the plane stress case and ~2% higher in the plane strain case, respectively, compared to experiment as shown in Table 5.7. The overall stress-strain response also follows the trends observed earlier for the vertical loading case suggesting good reproducibility of fiber randomness. The deviations between the different cases and the experimental measurements reflect numerous simplifications (all fibers of equal length, perfect bonding) used in simulations.

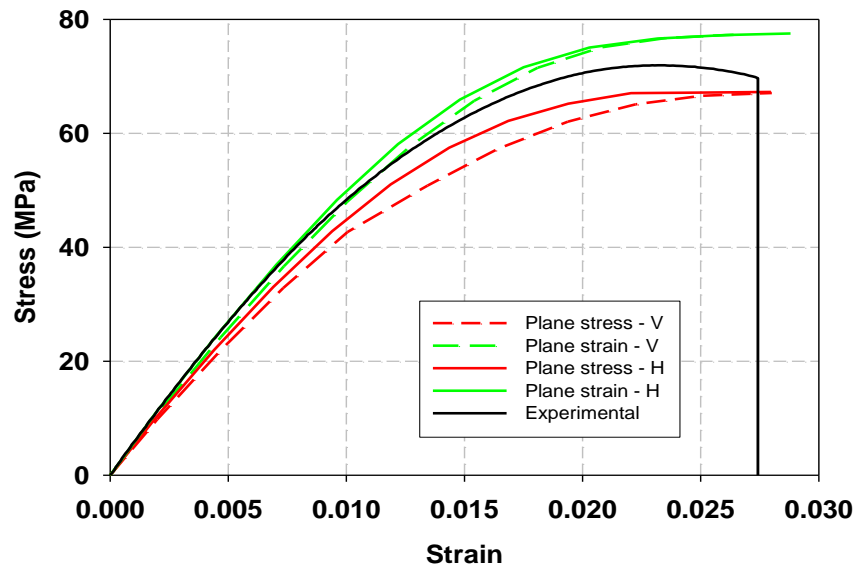


Figure 5.12: Stress-strain response comparison of vertical vs. horizontal loading cases for 5%  $V_f$  carbon fiber modified epoxy composite

Table 5.6: Modulus comparison for horizontal vs. vertical loading cases

		<b><i>E</i> (GPa)</b>	
	<b>Experiment</b>	5.58±0.23	
<b>Vertical loading simulation</b>	<b>Plane stress</b>	4.90	~ 12% lower than experiment
	<b>Plane strain</b>	5.37	~ 4% lower than experiment
<b>Horizontal loading simulation</b>	<b>Plane stress</b>	5.21	~7% lower than experiment
	<b>Plane strain</b>	5.67	~2% higher than experiment

## 5.8 Quasi-static crack propagation

This section presents crack propagation in carbon fiber modified epoxy composite under quasi-static loading using the so-called Extended Finite Element method (XFEM) [68] in ABAQUS v6.12. The researchers have used XFEM to model dynamic crack propagation by developing their customized programs [69][70]. However, ABAQUS 6.12 does not have capability to model crack propagation in dynamic implicit/explicit problems using XFEM. Hence, only the quasi-static cases were modeled. The XFEM is a numerical technique, based on the finite element method to model discontinuities such as cracks and voids. The simulation of the moving discontinuities using the standard finite element method is difficult to handle due to the need to update the mesh topology to match the geometry of the discontinuity [71], i.e., the edges of the element must conform to these geometric entities. The advantage of XFEM method is that it circumvents these issues via element enrichment. The enrichment involves the use of discontinuous basis functions in addition to the standard polynomial basis functions for nodes that belong to elements intersected by a crack [68]. In XFEM, the geometry of the discontinuity is evolved by updating the enrichment scheme and hence no remeshing is necessary [72]. The enrichment process is described as follows.

In Figure 5.13, a mesh of four elements (left) where a discontinuity has been introduced using a double node (nodes 9 and 10) is shown. The objective is to use the enrichment process to represent the left mesh using the right mesh plus the enrichment terms.

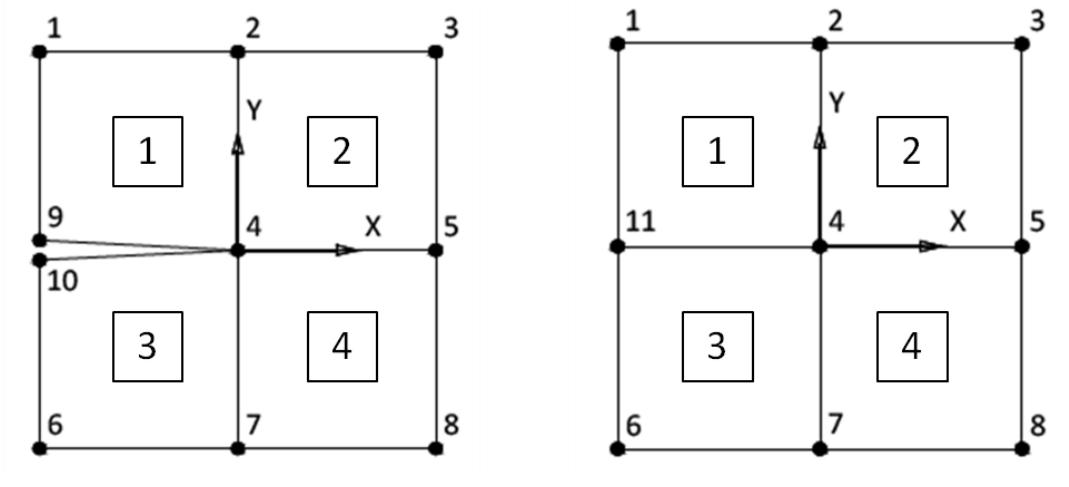


Figure 5.13: A mesh of four elements with (left) and without (right) a double node [73]

The finite element approximation of the left mesh is presented in Equation (5.4).

$$u = \sum_{i=1}^{10} u_i N_i \dots\dots\dots (5.4)$$

where  $u$  denotes displacement and  $N$  the shape functions. By defining:  $a = (u_9 + u_{10})/2$ ,  $b = (u_9 - u_{10})/2$ ,  $u_9$  and  $u_{10}$  in terms of  $a$  and  $b$ :  $u_9 = a+b$  and,  $u_{10} = a-b$ . By replacing  $u_9$  and  $u_{10}$  in the finite element expression we get the Equation (5.5).

$$u = \sum_{i=1}^8 u_i N_i + a(N_9 + N_{10}) + b(N_9 - N_{10})H(x) \dots\dots\dots (5.5)$$

where  $H(x)$  is a jump function  $H(x) = \begin{cases} 1 & \text{for } y \geq 0 \\ -1 & \text{for } y < 0 \end{cases}$

By considering the right mesh we replace  $N_9 + N_{10}$  by  $N_{11}$  in Equation (5.5), we get

$$u = \sum_{i=1}^8 u_i N_i + u_{11} N_{11} + b N_{11} H(x) \dots\dots\dots (5.6)$$

The above Equation (5.6) is equivalent to the finite element approximation of Equation (5.4) plus the discontinuous enrichment term. The third term in Equation (5.6) can be interpreted as an enrichment term of the finite element basis function by a technique of the partition of unity. The enrichment process described above can be reiterated on any one-dimensional, two-dimensional, or three-dimensional mesh containing a discontinuity modeled by double nodes.

### 5.8.1 Constituent material properties

The material properties used in XFEM simulations for neat epoxy, carbon fiber and interface are shown in Table 5.8. To simulate a weaker interface between the fibers and the epoxy matrix, the elastic modulus for interface was assumed to be one tenth of that for the epoxy matrix.

Table 5.7: Elastic properties used for neat epoxy, carbon fibers and interface

	<b>Elastic modulus <math>E</math> (GPa)</b>	<b>Poisson ratio <math>\nu</math></b>
<b>Neat epoxy</b>	4.0	0.3
<b>Carbon fiber</b>	225	0.2
<b>Interface</b>	0.4	0.3

### 5.8.2 Modeling approach

As explained in the section 5.3.2, using the SSI process, random points were generated using MATLAB in the RAE of 720 x 720  $\mu\text{m}^2$  and then fibers were drawn at those points in random directions using AutoCAD. On the left mid-span of the RAE, a 144  $\mu\text{m}$  long horizontal

crack was introduced. The crack length to sample width ratio was initially 0.2. The applied boundary conditions are shown in Figure 5.14. The upper and lower edges were pulled with a velocity of 2 mm/min in the (+) and (-) y-directions, respectively, as shown in Figure 5.14 which was same as the cross-head speed used in the tension tests. The plane stress CPS4R elements were used in these simulations which are 4-node bilinear quadrilaterals.

To study the interaction of the crack front with the fibers during crack propagation, a fiber was intentionally placed in front of the crack-tip. Two different cases were studied. In the first case, the fiber in front of the crack-tip was perfectly bonded to the epoxy matrix (Figure 5.15, left). In the second case, the fiber in front of the crack-tip was weakly bonded. That is, the fiber had a layer of elements around it as an interface between the matrix and the fiber with elastic modulus, ultimate strength and fracture energy one tenth [74] of the one for neat epoxy (Figure 5.15, right). The goal was to qualitatively study how the crack propagation would change when a weak interface layer exists between the fiber and the epoxy matrix.

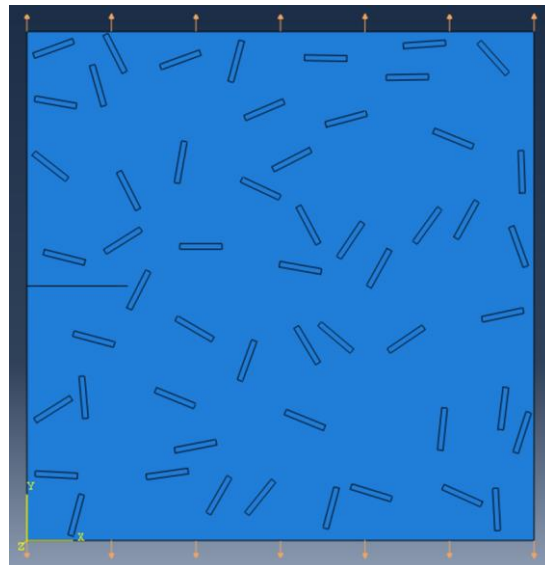


Figure 5.14: Random fibers were drawn for mimicking 5%  $A_f$  carbon fiber modified epoxy composite and a 144  $\mu\text{m}$  long crack ( $a/W=0.2$ ) was introduced at the left mid-span to model crack propagation using XFEM

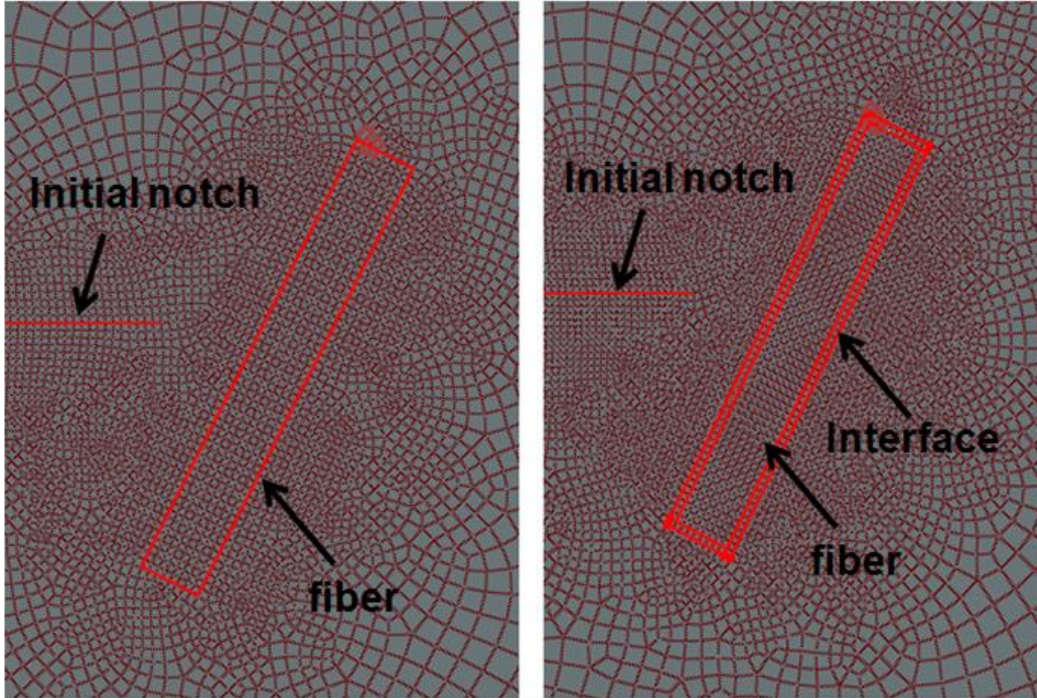


Figure 5.15: Fiber (60  $\mu\text{m}$  long and 8  $\mu\text{m}$  wide) placed in front of the crack-tip. On the left strongly bonded case. On the right, weakly bonded case with an interface layer (1  $\mu\text{m}$  thick) between the fiber and the epoxy matrix

The crack initiation and propagation parameters used for neat epoxy, carbon fiber and the interface layer between them to model crack propagation using XFEM in ABAQUS are shown in Table 5.8. The crack initiates at that point in the modeled geometry where the principal stress reaches the ultimate strength (crack initiation criterion) first, and then starts propagating from that same point when the energy reaches the fracture energy (crack propagation criterion). The quasi-static fracture toughness ( $K_{IC}$ ) for the neat epoxy and carbon fiber was 1.9  $\text{MPa}\sqrt{\text{m}}$  [7] and 1.6  $\text{MPa}\sqrt{\text{m}}$  [75], respectively. These were used to calculate the energy release rate  $G = (K_{IC})^2/E$  (for plane stress). As before, the crack initiation and propagation parameters for the interface were assumed to be one tenth of the neat epoxy values.



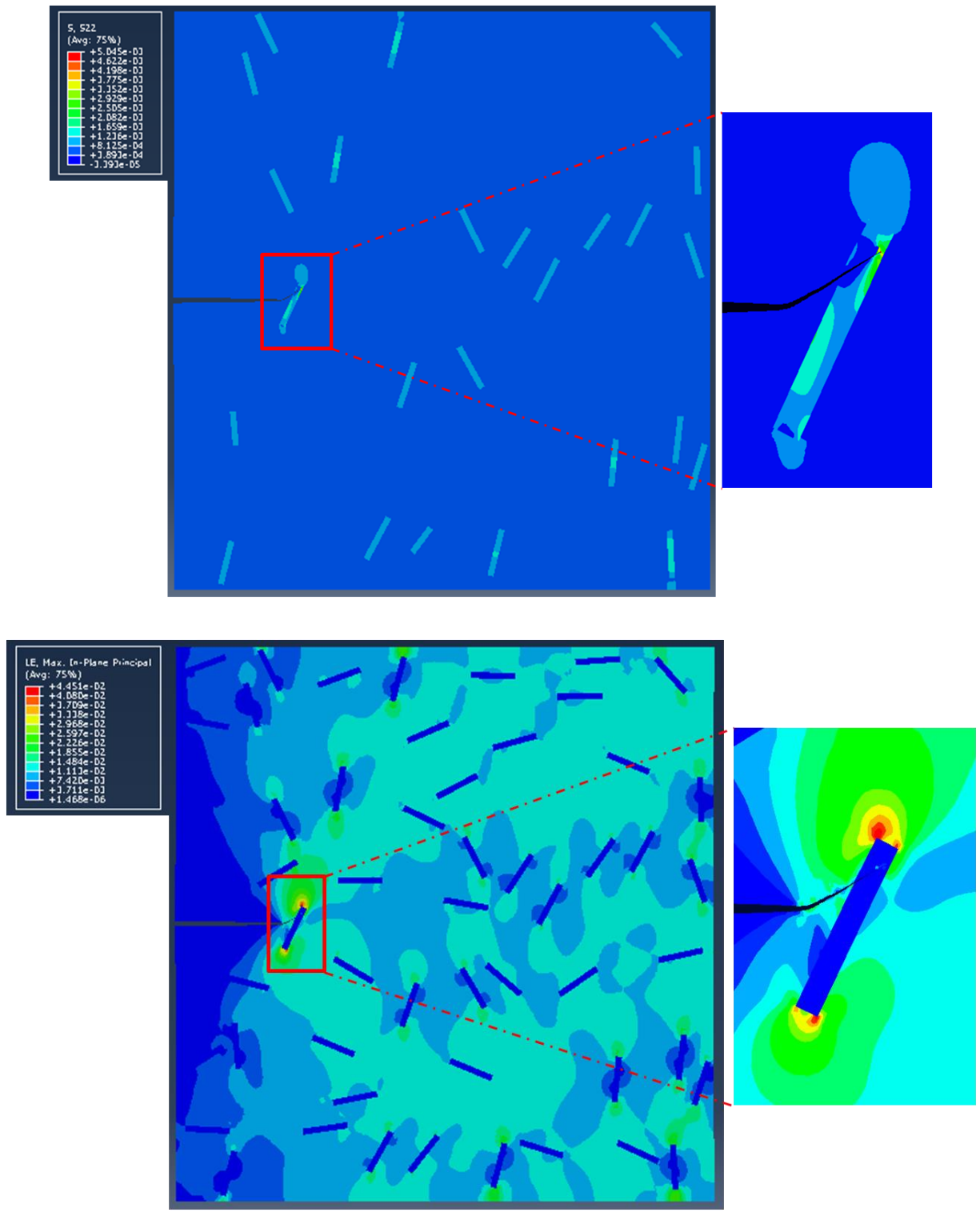


Figure 5.16: Strongly bonded fiber case: Normal stress ( $\sigma_{yy}$ ) (top) and maximum principal strain contour for 5%  $V_f$  carbon fiber modified epoxy composite (bottom) show that crack propagates through the fiber

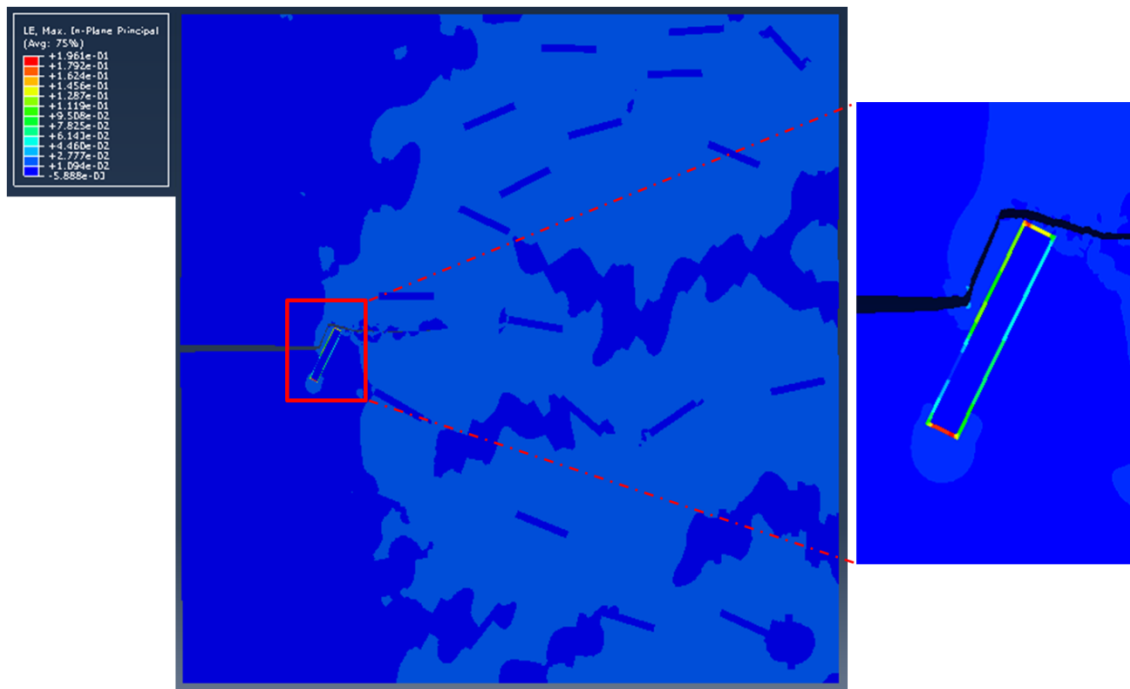
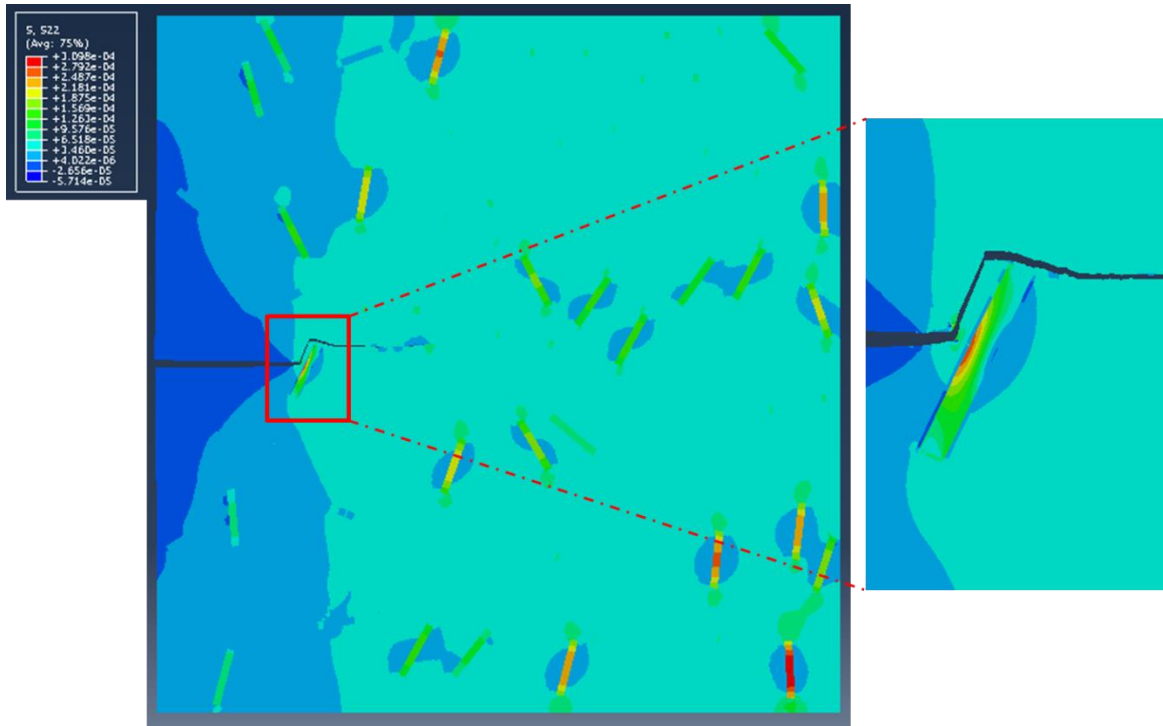


Figure 5.17: Weakly bonded fiber case: Normal stress ( $\sigma_{yy}$ ) (top) and maximum principal strain contour for 5%  $V_f$  carbon fiber modified epoxy composite (bottom) show that crack path circumvents the fiber

Table 5.8: Crack initiation and propagation parameters used for neat epoxy, carbon fibers, and interface

	<b>Crack initiation – Ultimate strength (MPa)</b>	<b>Crack propagation – Fracture energy (<math>G = (K_{IC})^2/E</math>) for plane stress</b>
<b>Neat epoxy</b>	64	0.88 kN/m
<b>Carbon fiber</b>	4000*	0.01 kN/m
<b>Interface</b>	6.4	0.09 kN/m

\*provided by the Toho-tenax Inc.

### 5.8.3 Results and discussion

The XFEM results of crack propagation in filled epoxy with perfectly and weakly bonded cases are shown in Figure 5.16 and Figure 5.17, respectively. The crack always takes the path of least resistance. In the perfectly bonded fiber case, the crack propagated through the fiber as shown in Figure 5.16. However, in the weakly bonded fiber case due to the presence of interface layer, the crack path circumvented the fiber as shown in Figure 5.17. The FE analysis explained the carbon fibers were strongly bonded with the epoxy matrix in carbon fiber modified epoxy composite and the crack propagation analysis showed that the crack propagates through the fibers in the perfectly bonded case. Thus, during crack propagation carbon fiber resisted the crack growth and eventually broke through causing higher energy dissipation and hence higher apparent fracture toughness of the composite.

## CHAPTER 6

### **SYNTHESIS, PROCESSING AND FRACTURE BEHAVIOR OF MICRO-/NANO-HIERARCHICAL COMPOSITE**

Carbon nanotubes (CNTs) have drawn a great deal of attention since Iijima discovered this new class of allotrope of carbon [25]. Due to its extraordinary mechanical, thermal and electrical properties, the CNT possesses huge application potential in composite materials [76], smart structures [77], chemical sensors [78], energy storage [79] and nano-electronic devices [80]. However, challenges remain in the high cost of CNT raw materials and the difficulty in its processing and applications. For example, vacuum or inert gas protection, high temperature and/or high energy density furnaces are always needed for the production of CNT, e.g. arc-discharge [81], laser ablation [82] and chemical vapor deposition (CVD) [83] approaches, which make the cost of mass-produced CNTs high. In addition, strong van der Waals force induced poor solubility/dispersibility is another factor that restricts the application of a CNT, especially in reinforcing composite materials [84]. As an attempt to address the challenges mentioned above, some investigations explained to grow CNT on carbon fibers through conventional thermal heating process [85], and CVD methods [86], which can partially address the dispersibility issue, but the reaction setup is still not economical, and the process is time consuming and energy inefficient due to the target-less volumetric heating. As reported by Zhang et al. conducting polymers can be heated to a very high temperature in a short time, and converted to graphitic nanocarbons [87]. Based on this finding, we can use conducting polymers as the heating source towards growth of CNT on substrates through a fairly simple kitchen microwave approach.

## **6.1 Conventional techniques to grow carbon nanotubes**

More than twenty years after the discovery of CNTs the researchers are still searching for simple, efficient and economical ways to produce well-controlled and defects-free CNTs. In 1991, Iijima reported the first observation of multi-walled CNTs in carbon-soot using the arc discharge method [25]. Since then the excellent electrical, mechanical and thermal characteristics of CNTs have captured the attention of researchers worldwide. Exploring these properties and understanding their potential benefits have been a main driving force in this area. But the full potential of CNTs for useful applications cannot be realized until the growth of the CNTs can be optimized. Real-world applications such as nanocomposites desire high quality nanotubes in bulk using growth techniques that are fast, simple and inexpensive. To address these challenges, significant work has been carried out over the past two decades. The various techniques have been developed to produce the nanotubes in sizeable quantities. Most of them take place in a vacuum or using process gases.

### **6.1.1 Arc discharge**

Arc discharge, the first recognized technique for producing CNTs, has been developed for producing both high quality multi-walled nanotubes (MWNTs) and single-walled nanotubes (SWNTs). In this method, a high current (~50 to 120 amps) at a low voltage (~12 to 25V) passes through two graphite electrodes immersed in an inert gas medium such as He or Ar. The schematic experimental setup for arc discharge is shown in Figure 6.1. The several variations in the arc discharge process has revealed that by tailoring the Ar:He gas ratio the diameter of the SWNTs can be controlled, with greater amount of Ar yielding smaller diameters. When pure graphite rods are

used, fullerenes are deposited as soot inside the chamber, and MWNTs are deposited on the cathode. When a graphite anode containing a metal catalyst (Fe or Co) is used with a pure graphite cathode SWNTs are generated in the form of soot. The distance between graphite electrodes can be changed to vary the strength of the plasma formed in between. In general, the nanotubes produced by this technique need extensive purification before use [26][88].

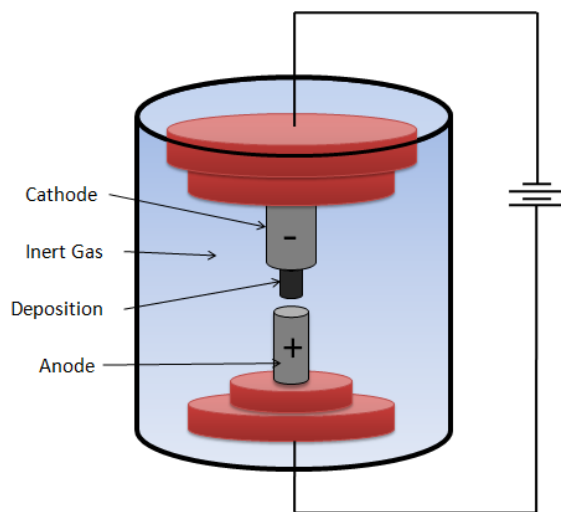


Figure 6.1: Schematic of an arc discharge setup (ref:[http://upload.wikimedia.org/wikipedia/commons/a/af/Arc\\_discharge\\_nanotube.png](http://upload.wikimedia.org/wikipedia/commons/a/af/Arc_discharge_nanotube.png))

### 6.1.2 Laser ablation

Laser ablation was the first large scale (1-10 gm) SWNTs production technique, developed by Smalley's group at Rice University in 1996. The method utilized intense laser pulses to ablate a carbon target (graphite source) containing 0.5 atomic percent of nickel and cobalt. The target was placed in a quartz tube furnace heated to 1200°C. During laser ablation, a flow of inert gas was passed through the growth chamber to carry the grown nanotubes downstream to be collected on a cold finger. The nanometer size metal catalyst particles are formed in the plume of vaporized graphite. The metal particles catalyze the growth of SWNTs in the plasma plume, but many by-

products (graphitic and amorphous carbon, concentric fulleroid spheres surrounding metal catalyst and small fullerenes, etc.) are formed at the same time. The yield collected on the cold finger varies from 20 to 80% of SWNTs by weight. The diameter distribution of SWNTs produced by this method is roughly between 1.0 and 1.6 nm [26][88]. The schematic experimental setup for laser ablation is shown in Figure 6.2.

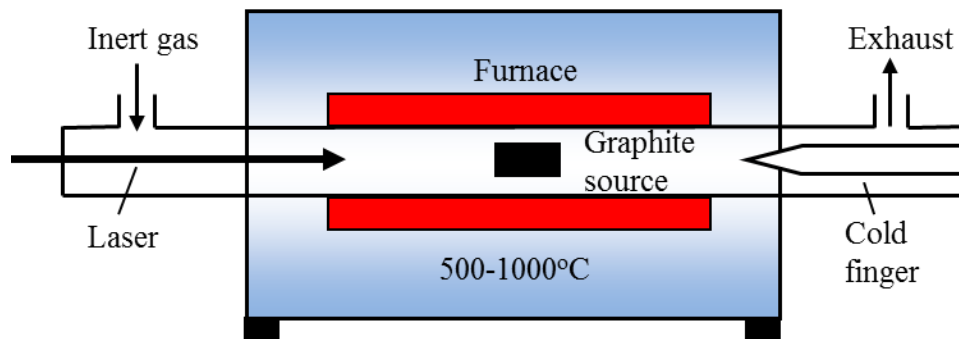


Figure 6.2: Schematic of a laser ablation furnace [87]

Conceptually, arc discharge and laser ablation are similar techniques, as both use a metal impregnated graphite target to produce SWNTs, and both produce MWNTs when pure graphite is used instead.

### 6.1.3 Chemical vapor deposition (CVD)

CVD was first reported to produce defective MWNTs in 1993. Later in 1996, Smalley's group successfully demonstrated CO-based CVD to produce SWNTs at Rice University [88]. The schematic experimental setup for CVD is shown in Figure 6.3. The growth process involves heating a catalyst material to high temperatures in a tube furnace and flowing a hydrocarbon gas through the tube reactor for a period of time. The materials grown over the catalyst are collected upon cooling the system to room temperature. The key parameters in nanotube CVD growth are the hydrocarbons, catalysts and growth temperature. The general CNT growth mechanism in a

CVD process involves the dissociation of hydrocarbon molecule catalyzed by the transition metal, and dissolution and saturation of carbon atoms in the metal nanoparticle. The precipitation of carbon from the saturated metal particle leads to the formation of tubular carbon solids in  $sp^2$  structure. A major issue for CVD-grown MWNTs has been the high defect densities in their structures. The defective nature of CVD-grown MWNTs is due to the relatively low growth temperature, which does not provide sufficient thermal energy to anneal nanotubes into perfectly crystalline structures. Growing perfect MWNTs by CVD remains a challenge to this day [26].

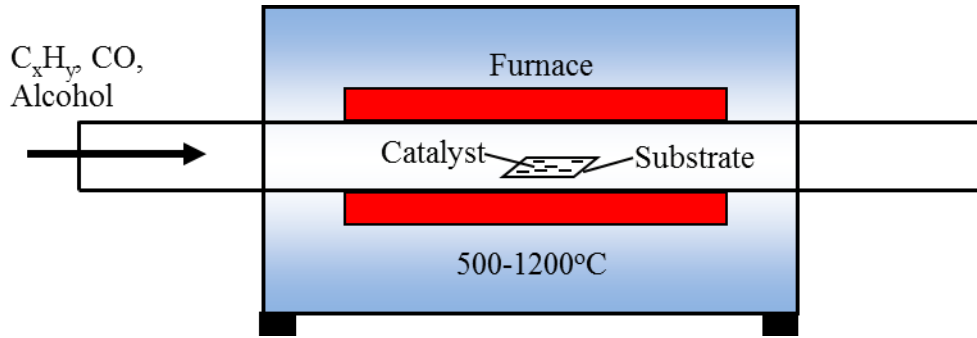


Figure 6.3: Schematic of a CVD furnace [87]

As discussed above, all existing conventional techniques are expensive, complicated and their processing is time consuming and energy inefficient. Hence a new technique called the pop-tube approach [89][90][91] was developed to grow CNTs which is relatively simple, fast, energy efficient and cost-effective compared to conventional techniques.

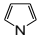
## 6.2 Ultrafast carbon nanotube growth - A Poptube approach

The growing process of carbon nanotubes in the Poptube approach on engineering materials can be divided primarily into three steps shown in Figure 6.4. The first step involves coating the engineering material with a conducting polymer. In the second step the conducting polymer-coated engineering material is coated with microwave precursor ferrocene powder. In the third



step ferrocene-coated engineering material is placed in a glass vial and microwaved for about 15-30 seconds. To the best of our knowledge, this is the fastest CNT growth in terms of the process duration, and probably the only approach that can be done in ambient condition.

### **6.2.1 Step 1: Coating with conducting polymer**

The first step can be named as coating of engineering material with a conducting polymer. Firstly the appropriate amount (explained later) of substrate (engineering material) and Hydrochloric acid (HCl) are mixed using a mechanical shaker for a few minutes to avoid agglomeration. Once the substrate looks completely dispersed into HCl, Pyrrole ( $C_4H_4NH$ )  is added into that mixture and stirred again using the same mechanical shaker for about half an hour to avoid phase separation of Pyrrole. To initiate the polymerization process, Ammonium Persulfate (APS) ( $(NH_4)_2S_2O_8$ ) is added into the mixture. The Ammonium Persulfate behaves like a radical initiator in the reaction, which begins the polymerization reaction. At that moment Ammonium Persulfate is added into the mixture, reaction starts and the mixture turns into a black color from white. It takes half an hour for complete polymerization to take place, but to make a better coating the mixture is stirred for about 4-5 hours. Following the stirring process, the polymerized substrate is separated using a filtering flask assembly. The filtering flask assembly consists of a vacuum flask, a filtering funnel covered with a filter paper and pipe connecting the side outlet of the flask to a vacuum pump. To get rid of the moisture completely, the conducting polymer-coated substrate is dried out for about 12 hours in an oven at 80°C.

### 6.2.2 Step 2: Coating with microwave precursor

In the second step, the conducting polymer-coated substrate is coated again with a powder form microwave precursor called Ferrocene ( $\text{Fe}(\text{C}_5\text{H}_5)_2$ ) which is an organometallic compound; it behaves like a spark initiator in this CNT growing process.

### 6.2.3 Step 3: Microwaving in a glass vial

In this step the ferrocene-coated substrate is placed into a glass vial with loose lid and then microwaved for about 15-30 seconds. In the first few seconds, microwave irradiation ignites the ferrocene causing a spark inside the glass vial and starts converting the carbon present into conducting polymer and finally into CNTs.

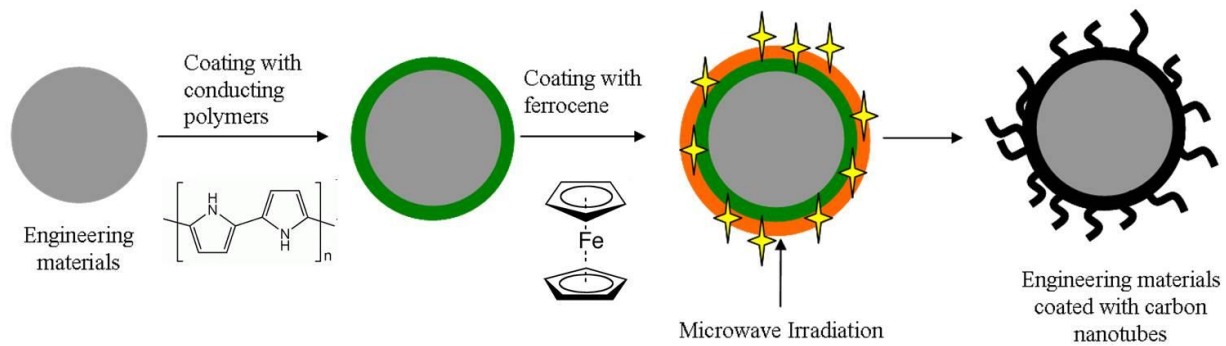


Figure 6.4: Steps involved in Poptube approach to grow CNTs on engineering materials (ref:[88])

## 6.3 Carbon nanotube growth on engineering substrates using Poptube approach

Poptube approach was employed to grow CNTs on micron-sized engineering substrates, e.g., hollow glass micro-balloons, solid glass spheres, glass fibers and carbon fibers, to use them as filler phase in the synthesis of micro-nano hierarchical composites.

### 6.3.1 Carbon nanotube growth on glass microballoons

Poptube approach was used to grow CNTs on micron-sized hollow glass microballoons 3M-XLD300 which was later used as the filler in the synthesis of hierarchical composite called nano-syntactic foam (Nano-SF). The XLD3000 glass microballoons (true density – 230 Kg/m<sup>3</sup> and effective size – 30 μm) were purchased from 3M Corporation, USA. Several trials were made to find the right proportion of microballoons and conducting polymer Pyrrole for the polymerization step. The final recipe which showed the best results involves the following steps. In the first step, 2 gm of silane-treated microballoons + 150 ml of HCl + 1 ml of Pyrrole + 1.15 gm of APS were placed in a glass bottle and stirred for four hours. In the second step, 100 mg of conducting polymer-coated microballoons were mixed with 100 mg of ferrocene and spun in a speed mixer at 3500 rpm for 5 minutes. Then in the last step 200 mg of ferrocene and conducting polymer-coated microballoons mixture was placed in a glass vial and microwaved for 15-20 seconds to grow the CNTs on the surface of the glass microballoons. Figure 6.5 and Figure 6.6 show the scanning electron microscope image of silane treated glass microballons before and after the CNT growth, respectively. Even after several trials of changing the constituents proportion still we could not achieve more than 50-60% CNT coverage in the case of glass microballoons. The CNTs produced using the poptube approach were analyzed using a High Resolution Transmission Electron Microscope (HRTEM) and it was found that these nanotubes are multi-walled in nature confirming ~20 layers of coaxially folded grapheme sheets which can be seen in Figure 6.7.

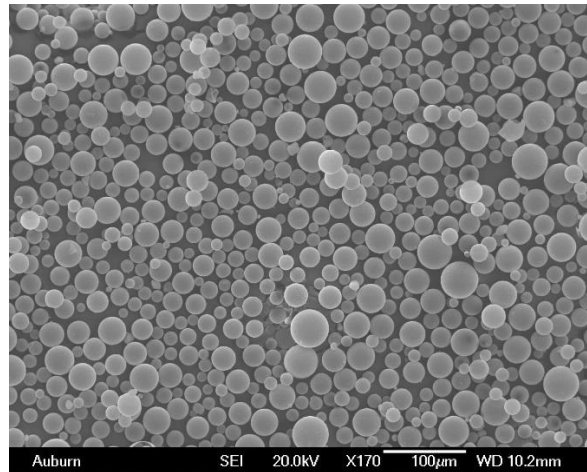


Figure 6.5: Silane treated XLD3000 used for CNT growth

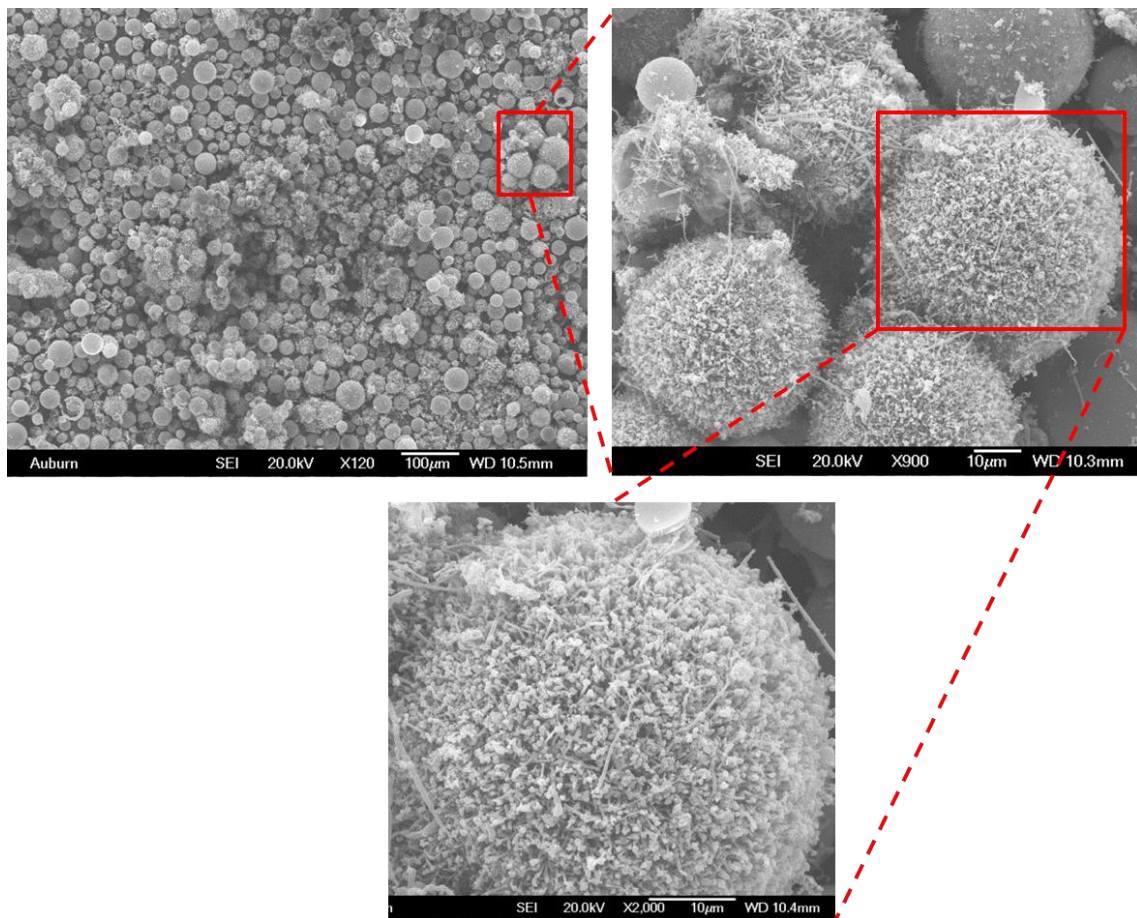


Figure 6.6: CNT-grown glass microballoons using poptube approach (top-left), CNT grown microballoons shown at higher magnification (top-right and bottom)

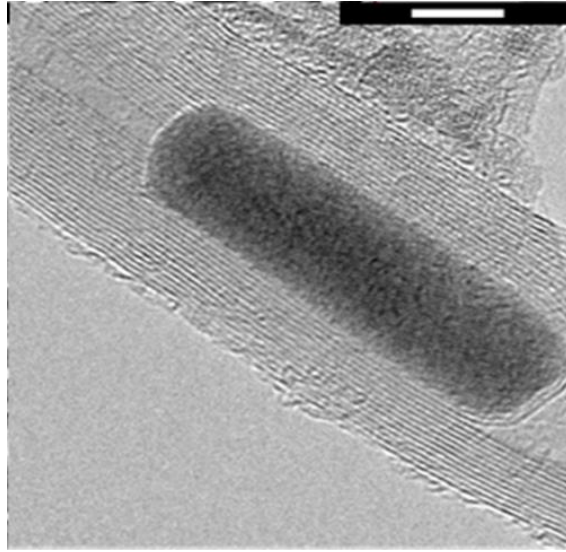


Figure 6.7: HRTEM of individual CNT with trapped Fe catalyst particle (scale bar: 5 nm) (ref:[89])

### 6.3.2 Quasi-static fracture test

To demonstrate the mechanical benefits of the above mentioned method, CNT-grown hollow glass microballoons were used as filler to strengthen the mechanical characteristics of epoxy-based conventional syntactic foam (SF). The carbon nanotube grown microballoons were dispersed in a low-viscosity epoxy (Epo-Thin, from Beuhler Inc., USA; Bisphenol-A resin and Amine based hardener; densities 1130 kg/m<sup>3</sup> and 961 kg/m<sup>3</sup>, respectively) to make a novel nanocomposite, called nano-syntactic foam (Nano-SF). To carry out the comparative static fracture study, syntactic foam (containing 15% microballoons by volume) and nano-syntactic foam (containing an equal amount of carbon nanotube grown microballoons as in the case of syntactic foam) sheets were cast separately. Cast sheets were machined into test specimens of dimensions 76 mm x 22 mm x 9 mm. An edge notch of nominal length of 4.4 mm was introduced at mid-span of each specimen using a high-speed diamond impregnated circular saw. The tip of the notch was sharpened using a razor blade.

The three-point bending tests (no. of tests = 3) were performed at room temperature using an Instron 4465 testing machine, under displacement control mode and a crosshead speed of 0.12 mm/min. The load-displacement behavior (Figure 6.8) remains linear until fracture, which suggests the failure to be brittle for syntactic as well as nano-syntactic foams. The critical fracture toughness  $(K_{I})_{cr}$  at failure was computed using the load at fracture. The  $(K_{I})_{cr}$  values for syntactic and nano-SF are  $2.00 \pm 0.01 \text{ MPa}\sqrt{\text{m}}$  (at ultimate cross head displacement of  $0.55 \pm 0.02 \text{ mm}$ ) and  $2.35 \pm 0.06 \text{ MPa}\sqrt{\text{m}}$  (at ultimate cross head displacement of  $0.60 \pm 0.03 \text{ mm}$ ), respectively, shown in Table 6.1. The introduction of carbon nanotube grown microballoons enhanced the critical fracture toughness and cross head displacement at fracture by  $\sim 17.0\%$  and  $\sim 7.5\%$ , respectively, compared to conventional SF. To assure the repeatability of experimental results, three specimens of each composite were tested under identical conditions. The results were repeatable within the error range of  $\sim 4.0\%$ .

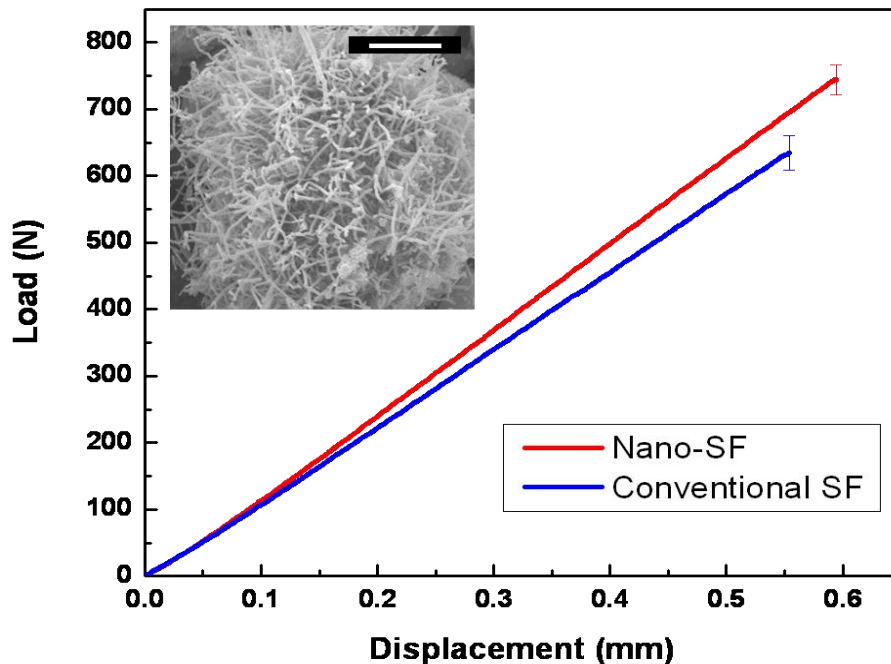


Figure 6.8: Load-displacement response for conventional SF and nano-SF. Inset: SEM image of the CNT grown glass microballoon, scale bar: 10  $\mu\text{m}$

Table 6.1: Quasi-static fracture toughness and critical energy release rate comparison

	<b>SF</b>	<b>Nano-SF</b>	<b>Improvement</b>
<b><math>(K_I)_{cr}</math> (MPa<math>\sqrt{m}</math>)</b>	2.00 $\pm$ 0.01	2.34 $\pm$ 0.06	17%
<b>*<math>(G_I)_{cr}</math> (kPa<math>\cdot</math>m)</b>	1.05 $\pm$ 0.01	1.17 $\pm$ 0.06	11%

(\*for  $(G_I)_{cr}$  calculation  $E$  was measured using ultrasonic method described in chapter 3)

### 6.3.3 Dynamic mechanic analysis (DMA)

DMA analysis was performed to assess the storage modulus and  $\tan(\delta)$  characteristics of SF and Nano-SF using RSA3 TA instruments in three-point bending configuration. Specimens were machined to 30 mm x 8 mm x 3 mm. For both SF and Nano-SF, the dynamic temperature ramp test was performed at 0.1% strain at a frequency of 1 Hz from 25°C to 100°C with a heating rate of 5°C/min. The storage modulus vs. temperature and  $\tan(\delta)$  plots are shown in Figure 6.9 and Figure 6.10, respectively. It was found that at room temperature Nano-SF showed 18% higher storage modulus compared to SF. The storage modulus showed a steep drop for both SF and Nano-SF as temperature reached to glass transition temperature ( $T_g$ ) as expected (because material enters into a rubbery phase). The  $T_g$  was found to be about 62°C for both SF and Nano-SF.

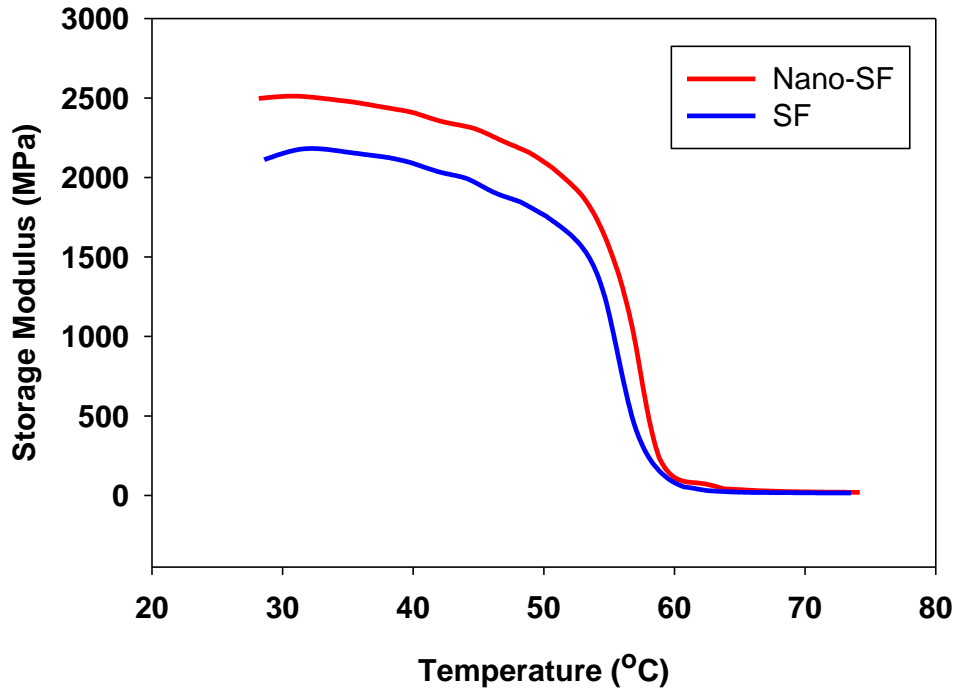


Figure 6.9: Storage modulus comparison between SF and Nano-SF

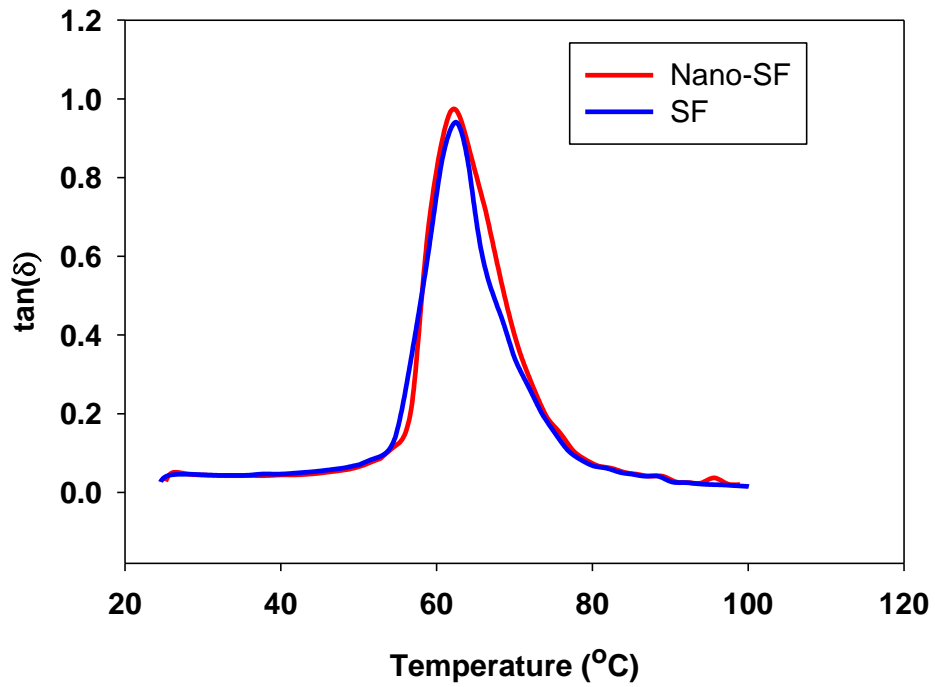


Figure 6.10: tan(δ) comparison between SF and Nano-SF



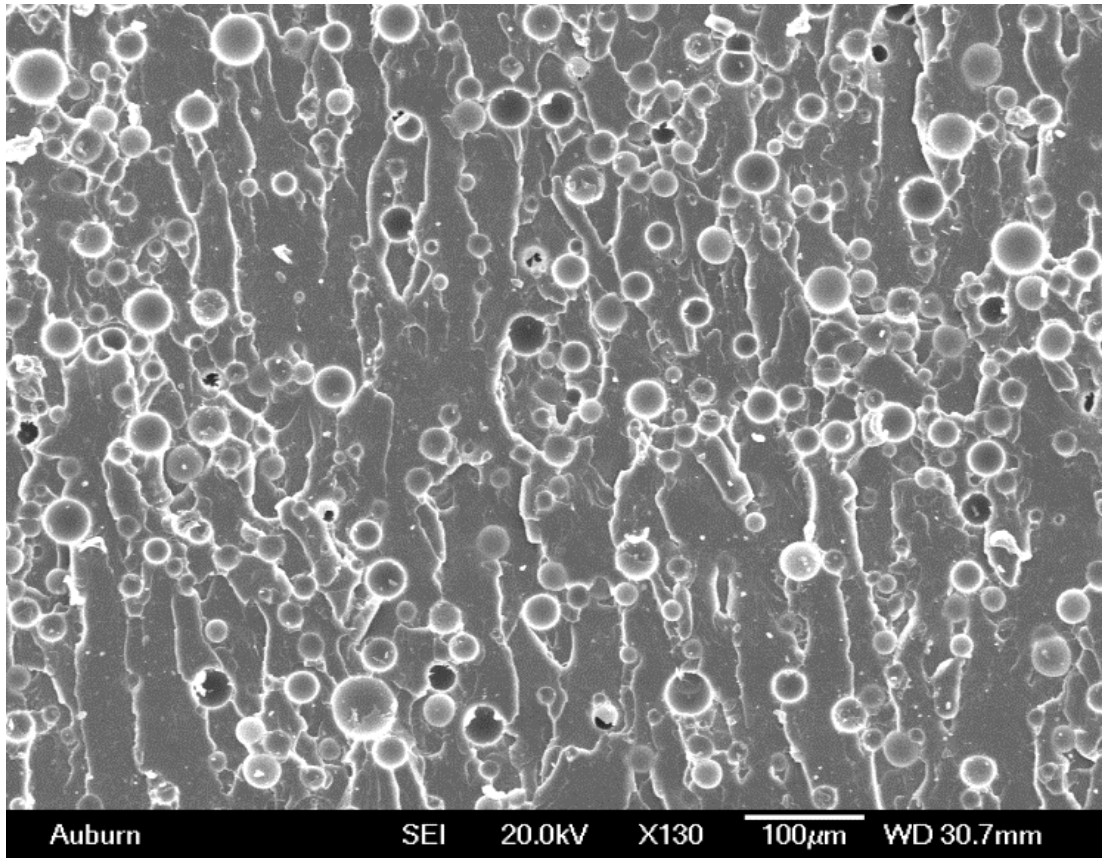


Figure 6.11: Fractograph of 15%  $V_f$  syntactic foam

Fractographs of SF and nano-SF test specimens are shown in Figure 6.11 and Figure 6.12, respectively. In the case of SF, more filler pullout were found compared to nano-SF which explains that the CNT-grown microballoons better resisted the crack growth rather than just being pulled out during the crack propagation as in the case of SF. However, in the case of nano-SF some agglomerations were found as typically expected due to strong van der waals forces among the carbon nanotubes. Hence some of the improvement was compromised in the case of nano-SF due the agglomeration of the filler phase.

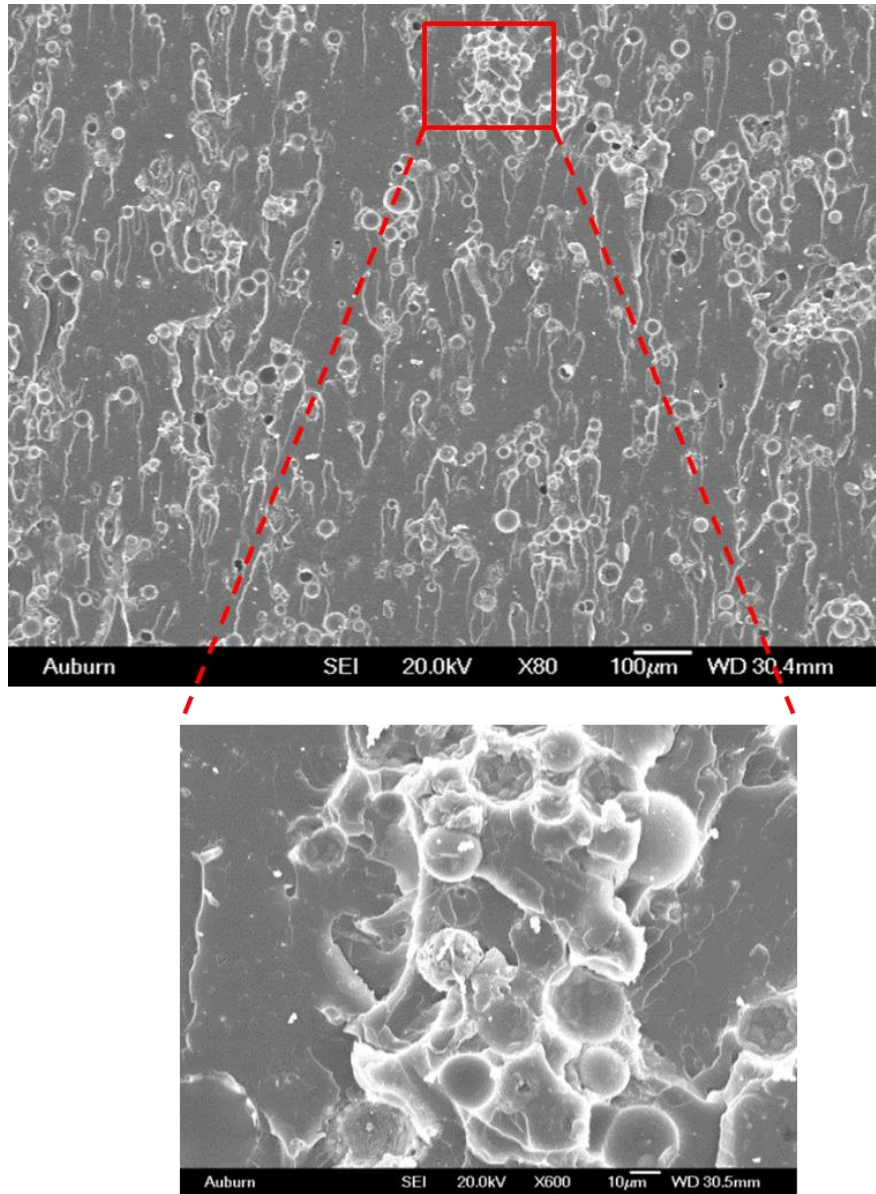


Figure 6.12: Fractograph of 15%  $V_f$  nano-syntactic foam showing agglomeration of CNT-grown microballoons

### 6.3.4 Carbon nanotube growth on spherical solid glass particles

The same poptube approach was employed to grow CNTs on solid glass particles (3000A solid glass spheres, Fiberglass Supply, USA). But the CNT coverage on the solid glass particles was significantly poorer when compared to hollow glass-microballoons. Also, due to the sudden

increase in temperature up to 1500°C during the CNT growth, solid glass spheres were melted and fused together and formed large unbreakable clumps as shown in Figure 6.13.

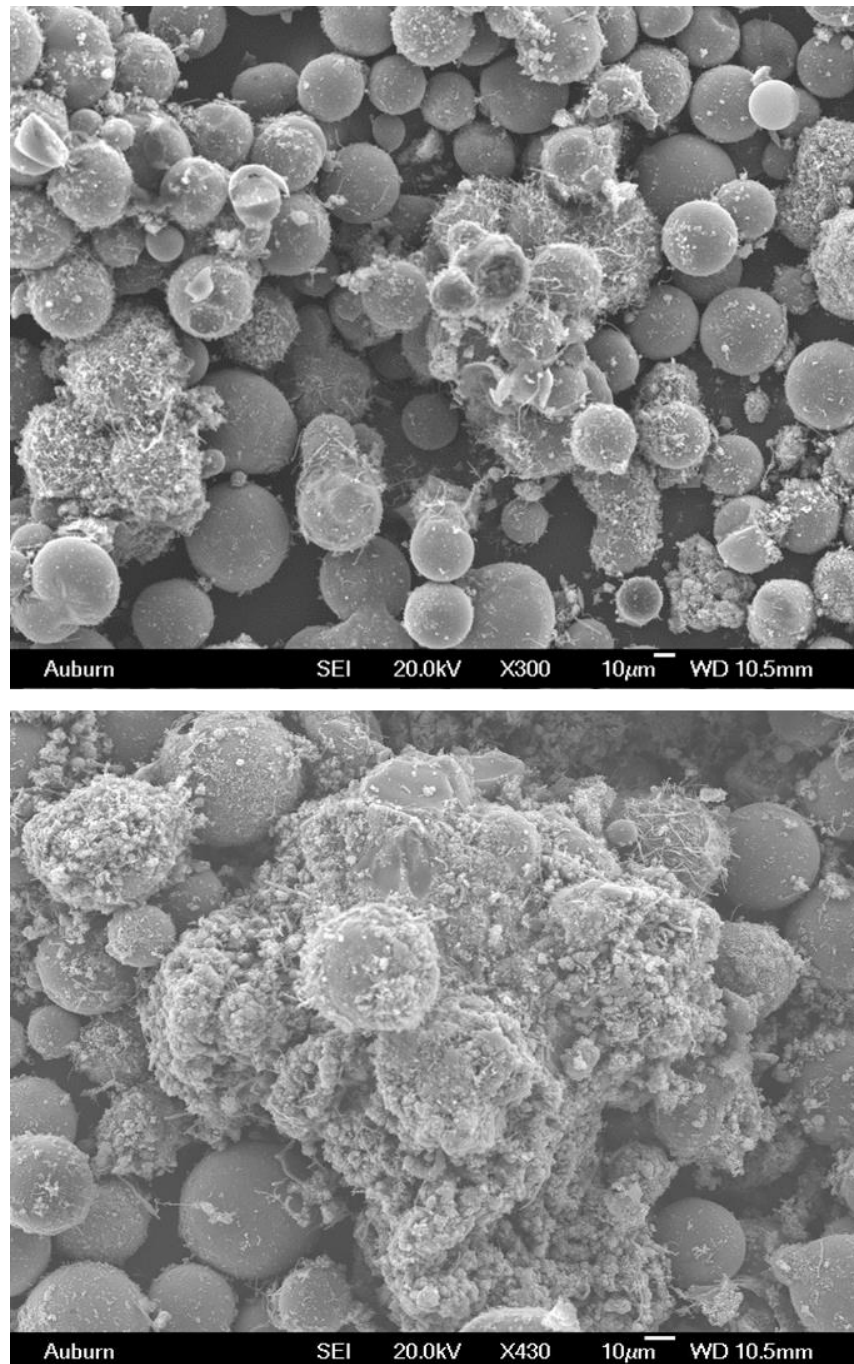


Figure 6.13: CNT Synthesis on solid spherical glass particles. The top micrograph shows the poor CNT coverage and the bottom shows the large fused clump of solid glass particles

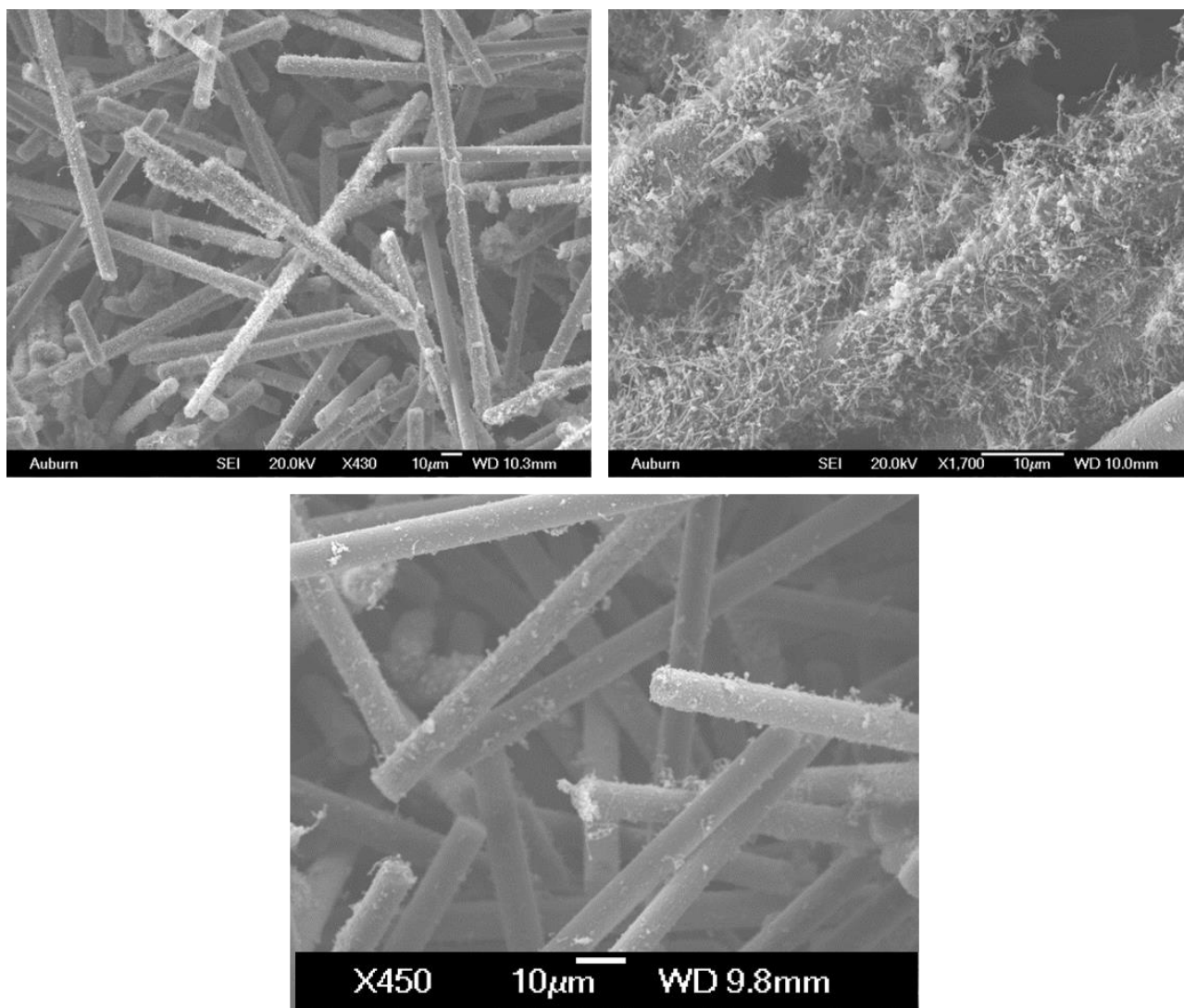


Figure 6.14: CNT growth on carbon fibers (top-left); excellent CNT coverage on a few carbon fibers (top-right); almost no CNT coverage on some carbon fibers (bottom)

### 6.3.5 Carbon nanotube growth on carbon fibers

The poptube approach was employed to grow CNTs on milled carbon fibers (60 µm in length and 8 µm in diameter, Toho Tenax America Inc, USA; density 1810 Kg/m<sup>3</sup>). Five grams of carbon fibers + 150 ml of HCl + 1 ml PPy + 1.15 gm APS were placed into a beaker and magnetically stirred for four hours. Then 200 mg of PPy-coated carbon fibers and 25 mg of ferrocene were placed in a cup and spun in a speed mixer at 3500 rpm for 5 minutes. PPy-coated

carbon fibers and the ferrocene mixture was placed in a glass vial and then microwaved for 15-20 seconds. The CNT growth on carbon fibers are shown in Figure 6.14. The SEM micrographs showed excellent CNT coverage for some fibers but for some other fibers there was almost no growth in the case of carbon fibers. Even after several trials still CNT coverage in the case of carbon fibers could not be improved to over 50%.

#### 6.3.5.1 Quasi-static fracture test

The carbon nanotube-grown carbon fibers were dispersed in a low-viscosity epoxy (Epo-Thin, from Beuhler Inc., USA; Bisphenol-A resin and Amine based hardener; densities 1130 kg/m<sup>3</sup> and 961 kg/m<sup>3</sup>, respectively) to make a hierarchical epoxy composite. To carry out the comparative static fracture study, carbon fibers modified epoxy (containing 5% carbon fibers by volume) and CNT grown carbon modified epoxy (containing equal amount of carbon nanotube grown carbon fibers as in the case of carbon fiber modified epoxy) sheets were cast separately and cured at room temperature for a week. Cured sheets were machined into test specimens of the dimensions 76 mm x 30 mm x 9 mm. An edge notch of nominal length of 6 mm was introduced at mid-span of each specimen using a high-speed diamond impregnated circular saw. The tip of the notch was sharpened using a razor blade.

The three-point bending tests (no. of tests = 3) on edge cracked samples were performed at room temperature using Instron 4465 testing machine, under displacement control mode and a cross head speed of 1.27 mm/min. The load-displacement behavior (Figure 6.15) remains linear until fracture, which suggests the failure to be brittle for carbon fiber modified as well as for CNT grown carbon fiber modified epoxy. The critical fracture toughness  $(K_{I})_{cr}$  at failure was computed using the critical load at fracture. The  $(K_{I})_{cr}$  values for carbon modified epoxy and CNT-grown

carbon modified epoxy are  $2.71 \pm 0.04 \text{ MPa}\sqrt{\text{m}}$  and  $2.32 \pm 0.06 \text{ MPa}\sqrt{\text{m}}$ , respectively, shown in Table 6.2. The introduction of CNT-grown carbon-fibers reduced the critical fracture toughness at fracture by  $\sim 15.0\%$  compared to carbon fiber modified epoxy. To assure the repeatability of experimental results, three specimens of each composite were tested under identical conditions.

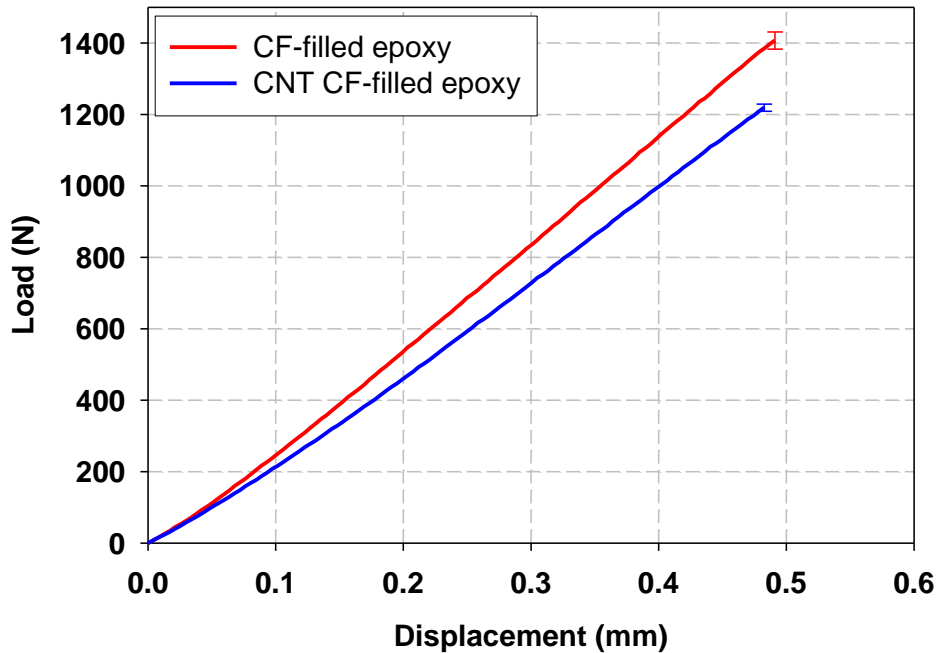


Figure 6.15: Load-displacement response for carbon fiber modified (CF modified) epoxy and CNT grown carbon fiber modified (CNT CF modified) epoxy

Fractographs of carbon fiber modified epoxy and CNT-grown carbon fiber modified epoxy test specimens are shown in Figure 6.16 and Figure 6.17, respectively. No agglomeration was found in case of carbon fiber modified epoxy composite case. In the case of CNT-grown carbon fiber modified hierarchical composite, substantial agglomerations were found throughout the fracture surface. These agglomerations acted like weak spots and during the crack propagation could not resist the crack growth and got pulled out (shown in Figure 6.17) which explains the deterioration in fracture toughness compared to carbon fiber modified epoxy.



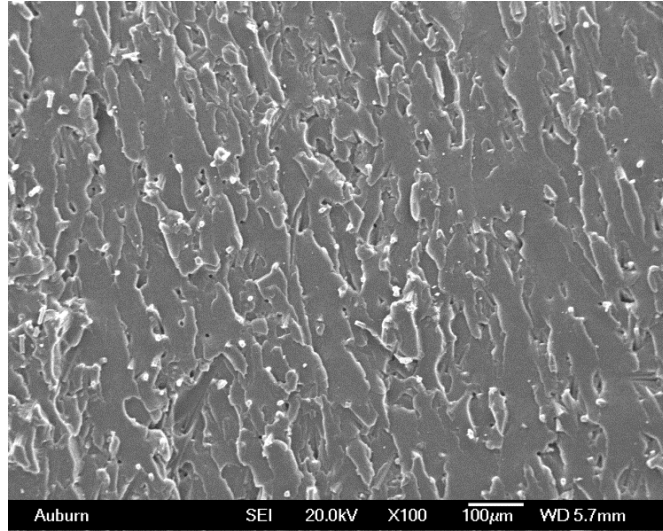


Figure 6.16: Fractograph of 5%  $V_f$  carbon fiber modified epoxy

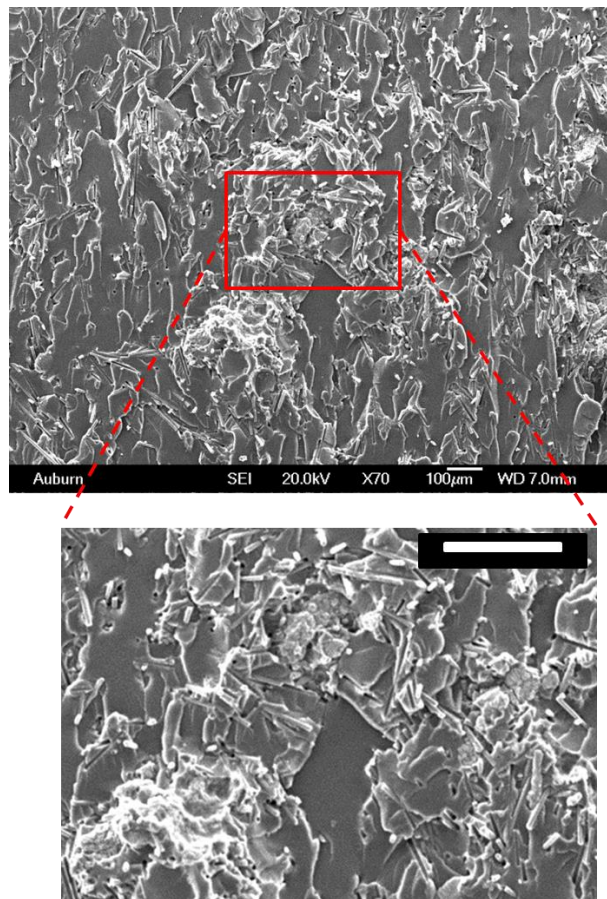


Figure 6.17: Fractograph of 5%  $V_f$  CNT grown carbon fiber modified epoxy (top), center spot at high resolution showing material pull out during crack propagation (bottom)

Table 6.2: Quasi-static fracture toughness and critical energy release rate comparison

	CF modified epoxy	CNT CF modified epoxy	Improvement
$(K_I)_{cr}$ (MPa $\sqrt{m}$ )	2.71 $\pm$ 0.04	2.32 $\pm$ 0.06	-15%
* $(G_I)_{cr}$ (kPa-m)	1.56 $\pm$ 0.05	1.13 $\pm$ 0.06	-28%

(\*for  $(G_I)_{cr}$  calculation  $E$  was measured using ultrasonic method described in chapter 3)

### 6.3.5.2 Dynamic mechanic analysis (DMA)

DMA analysis was performed to assess the storage modulus and  $\tan(\delta)$  characteristics of CF modified and CNT CF modified epoxy samples using RSA3 TA instruments in three-point bending configuration. Specimens were machined to 30 mm x 8 mm x 3 mm. The dynamic temperature ramp test was performed at 0.1% strain at a frequency of 1 Hz from 25°C to 100°C with a heating rate of 5°C/min. Storage modulus vs. temperature and  $\tan(\delta)$  plots are shown in Figure 6.18 and Figure 6.19, respectively. It was found that at room temperature CNT CF modified showed 35% lower storage modulus compared to CF modified epoxy. The storage modulus showed steep drop for CF modified and CNT CF modified epoxy as temperature reached to glass transition temperature ( $T_g$ ) as expected (because material enters into rubbery phase). The agglomerations acting like weak spots in CNT CF modified epoxy explained the deterioration in storage modulus compared to CF modified epoxy. The  $T_g$  was found to be about 62°C and 64°C for CNT CF modified and CF modified epoxy, respectively.



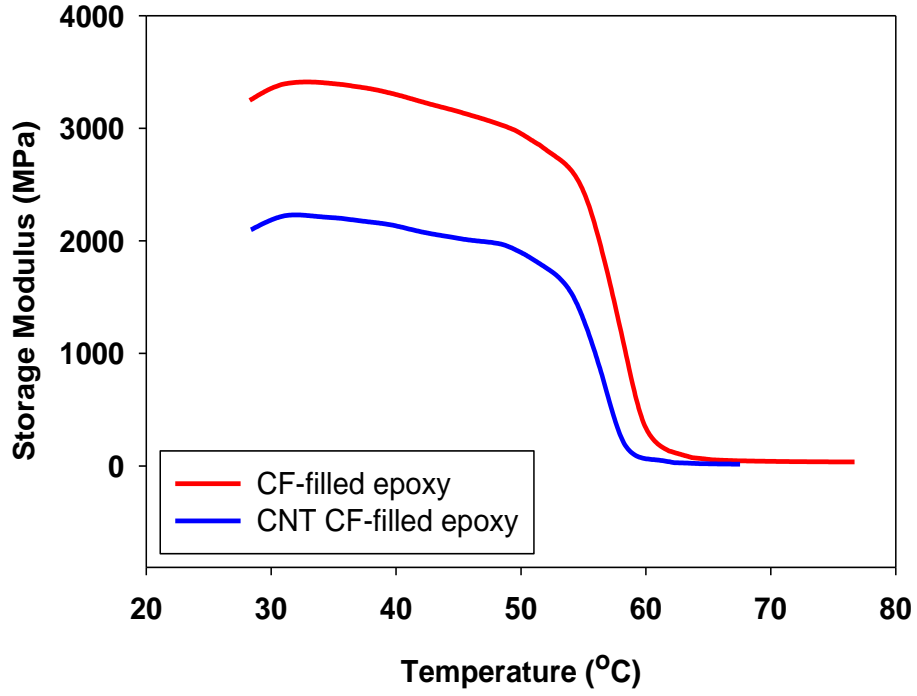


Figure 6.18: Storage modulus comparison between CF and CNT CF modified epoxy

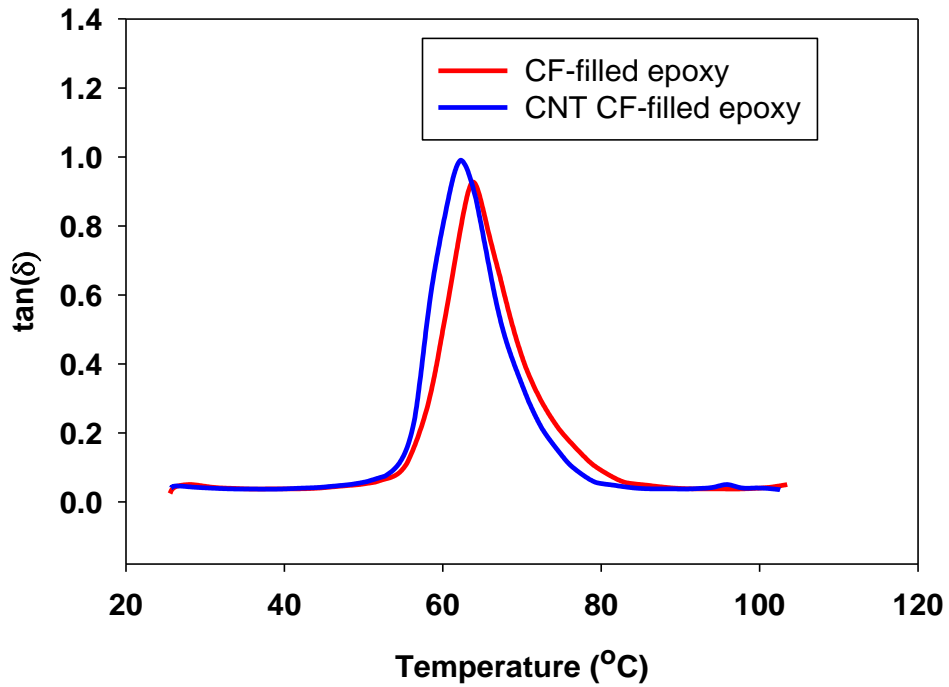


Figure 6.19:  $\tan(\delta)$  comparison between CF and CNT CF modified epoxy

## CHAPTER 7

### SUMMARY AND CONCLUSIONS

In this research, the effect of filler shape, volume fraction and loading rate on mode-I fracture behavior of glass-filled Particulate Polymer Composites (PPCs) were studied experimentally using 2D Digital Image Correlation (DIC) method and high-speed photography under impact loading condition. Subsequently the mixed-mode fracture behavior of a select subset of glass-filled particulate composites was also studied. Also to understand the stress-strain behavior of fiber modified epoxy composite, finite element modeling of carbon fiber modified epoxy composite was carried out in ABAQUS structural analysis software. In the last part of this research, a novel technique called the poptube approach was used to grow Carbon Nanotubes (CNTs) on micron-sized engineering substrates (such as hollow glass microballoons, solid glass spheres, solid glass fibers and carbon fibers) for use as filler and to develop micro-/nano-hierarchical epoxy based composites. To understand the fracture behavior of those hierarchical composites, quasi-static fracture experiments were carried out.

In the first part of this dissertation, the effects of filler shape, filler volume fraction and loading rate on fracture toughness were investigated. Three different micron size fillers - rods, flakes and spheres - dispersed at volume fractions ranging from 0-15% in epoxy matrix were studied. The filler shapes were characterized by the average aspect ratio (rod ~80, flake ~6, and sphere = 1). The DIC was used in conjunction with high-speed photography for determining dynamic fracture histories. The experiments were carried out on pre-notched glass-filled epoxy specimens

using a setup comprised of a long-bar impactor struck with a cylindrical striker launched by a gas-gun delivering one-point impact to an unconstrained specimen. The following major conclusions were drawn from this part of the work.

- For all three filler shapes – flakes, rods and spheres - crack initiation toughness increased significantly with filler volume fraction.
- For epoxy filled with spherical filler, 5%, 10% and 15%  $V_f$  cases showed 18%, 39% and 68% improvement, respectively; for those reinforced with flakes, 5%, 10% and 15%  $V_f$  cases showed 47%, 71% and 97% improvement, respectively; and for epoxy filled with rod-shaped fillers at 5%, 10% and 15%  $V_f$  showed 82%, 118% and 145% improvement, respectively, in terms of crack initiation fracture toughness when compared to neat epoxy.
- For all three different volume fractions considered, the rod-shaped fillers produced the highest crack initiation toughness as well as post-initiation Stress Intensity Factor (SIF) values followed by flakes and spheres, respectively.
- At 5%  $V_f$ , filled epoxy with rods, flakes and spheres showed 82%, 47% and 18% improvement, respectively; at 10%  $V_f$ , filled epoxy with rods, flakes and spheres showed 118%, 71% and 39% improvement, respectively; and at 15%  $V_f$ , filled epoxy with rods, flakes and spheres showed 145%, 97% and 68% improvement, respectively, in crack initiation fracture toughness compared to neat epoxy.
- The fractographic evaluation showed the different failure mechanisms associated with different filler shapes during dynamic fracture and their contribution towards enhancement of fracture toughness. Among all the observed failure modes, filler breakage was the most preferred one due to higher energy consumption derived from filler strength when compared to that for

neat epoxy. Even a few broken fillers could contribute significantly to a rather high apparent fracture toughness of the PPC.

- Three different loading rates (42.0/sec, 10.7/sec, and 3.7/sec) were achieved through the usage of different pulse shapers between the striker and the long-bar. As the loading rate increased, the PPC showed a stiffer response and produced higher crack initiation toughness.
- The crack initiated earlier in neat epoxy compared to 10%  $V_f$ , filled epoxy with rod-shaped filler for all the loading rates used. Also, the crack speed was higher in neat epoxy compared to 10%  $V_f$ , filled epoxy with rod-shaped filler for all the three loading cases used.
- At 10%  $V_f$ , filled epoxy with rod-shaped filler showed 113%, 118% and 50% increase in crack initiation toughness for the 3.7/sec, 10.7/sec, and 42/sec loading rate cases, respectively, compared to the neat epoxy of the respective loading rate case.

In the second part of this research, mixed-mode dynamic fracture behavior of glass-filled epoxy composite was studied using 2D DIC and high speed photography under impact loading conditions. The shape effect study showed that filled-epoxy with rod-shaped fillers produce the highest enhancement in crack initiation and post-initiation toughness among the three different filler shapes considered. Accordingly, the mixed-mode fracture behavior was studied for 10%  $V_f$  rod-shaped glass-filled epoxy relative to that for neat epoxy. The mixed-mode experiments were carried out on pre-notched specimens using a setup comprised of a long-bar impactor aided by a gas-gun delivering one-point impact to an unconstrained specimen. The mode-I experiments were repeated due to the unavailability of the epoxy system used in the shape effect study. In mode-I fracture experiments, the specimen having edge notch of 10 mm length ( $a = 10$  mm) was impacted at an eccentricity  $e = 0$  mm (or simply in-line loading). In mixed-mode experiments, however, the first two sets of experiments used epoxy and glass-filled samples with 10 mm long edge notches

( $a = 10$  mm) and were impacted at eccentricities  $e = 15$  and  $20$  mm. However, the mode-mixity at crack initiation in these configurations could not be increased due to geometric limitations that did not produce crack initiation when eccentricity was increased further. Hence, to achieve a higher mode-mixity at crack initiation a third set of samples was used. In these, edge notch length was increased to  $15$ ,  $20$  and  $25$  mm ( $a = 15$ ,  $20$  and  $25$  mm) and the eccentricity of  $e = 20$  mm was held fixed. The following major conclusions were drawn from this part of the work.

- In the select geometries studied, for neat epoxy, the mixed-mode crack initiation and crack propagation was found to occur dominantly in mode-I condition for ( $e = 15$ ,  $a = 10$ ), ( $e = 20$ ,  $a = 10$ ), and ( $e = 20$ ,  $a = 15$ ) and dominantly in mode-II condition for ( $e = 20$ ,  $a = 20$ ) and ( $e = 20$ ,  $a = 25$ ). Similarly, for glass-filled epoxy, the mixed-mode crack initiation and crack propagation was found to occur dominantly in mode-I condition for ( $e = 15$ ,  $a = 10$ ), ( $e = 20$ ,  $a = 10$ ), ( $e = 20$ ,  $a = 15$ ), and ( $e = 20$ ,  $a = 20$ ) and dominantly in mode-II condition for and ( $e = 20$ ,  $a = 25$ ).
- For both mode-I and mixed-mode loading, the  $K_I$  and  $K_{\text{eff}}$  (vectorial sum of  $K_I$  and  $K_{II}$ ) histories show a monotonic increase up to the crack initiation.
- For both neat and glass-filled epoxy cases, the effective crack initiation toughness was higher for the mode-I case when compared to its respective mixed-mode counterpart.
- In mode-I, the  $10\% V_f$  glass-filled epoxy produced  $\sim 128\%$  and  $\sim 288\%$  improvement in effective crack initiation fracture toughness and critical energy release rate, respectively, compared to neat epoxy.
- In the mixed-mode case, the  $10\% V_f$  glass-filled epoxy produced  $\sim 112\%$ ,  $\sim 117\%$ ,  $\sim 108\%$ ,  $119\%$  and  $98\%$  improvement in the effective crack initiation fracture toughness and  $\sim 236\%$ ,

~266%, ~225%, ~263% and ~194% improvement of the critical energy release rate, respectively, relative to its respective ( $e = 15, a = 10$ ), ( $e = 20, a = 10$ ), ( $e = 20, a = 15$ ), ( $e = 20, a = 20$ ) and ( $e = 20, a = 25$ ) neat epoxy cases.

- In the mode-I case, the crack being loaded symmetrically, the extracted values of  $K_{II}$  histories show a negligible value within the measurement errors. However, in the mixed-mode case, the mode-II histories showed a monotonic increase in magnitude of  $K_{II}$  up to crack initiation and then a drop due to elastic unloading near the crack-tip. However, no such noticeable drop is evident in  $K_I$  histories suggesting the tendency of the crack to grow under mode-I condition.
- A higher value of mode-mixity  $\psi$  was evident in the presence of a significant in-plane shear component at the crack tip all the way up to crack initiation. Once the crack initiated, mode-mixity  $\psi$  dropped and approached zero, again suggesting a preference for crack propagation under dominant mode-I conditions.
- Fracture envelopes were constructed using critical values of  $K_I$  and  $K_{II}$  measured in each case using Maximum Tangential Stress (MTS) criterion commonly used for brittle materials under quasi-static conditions. The measurements and the theory followed similar trends but deviations of up to 15% between the two were observed.
- Inspired by the empirical relations for cementitious and geomaterials reported in the literature, a modified fracture envelope was proposed by curve fitting critical values of stress intensity factors at different mode-mixities for both neat and glass-filled epoxy:

$$\left( \frac{K_I}{(K_I)_c} \right)^{1.4} + \left( \frac{K_{II}}{(K_{II})_c} \right)^{1.4} = 1 \text{ for neat epoxy}$$

$$\left( \frac{K_I}{(K_I)_c} \right)^{1.3} + \left( \frac{K_{II}}{(K_{II})_c} \right)^{1.3} = 1 \text{ for glass - filled epoxy}$$

where  $(K_I)_C$  and  $(K_{II})_C$  are the critical fracture toughness in pure mode-I and pure mode-II conditions, respectively. The reasonable prediction of  $(K_{II})_C$  using Maximum Tangential Stress (MTS) criterion is  $0.866(K_I)_C$ .

- MTS criterion predicted the crack propagation direction reasonably well (maximum error ~13%) compared to experimentally measured angles on fractured specimens for the geometries studied under mixed-mode loading configuration.

In the third part of this research, the Finite Element Method (FEM) was employed to model the stress-strain behavior of 5%  $V_f$  carbon fiber modified epoxy composite under uniaxial tension using ABAQUS. Also, the Extended FEM (or simply XFEM) was employed to model crack propagation in carbon fiber modified epoxy composites using ABAQUS. The following major conclusions were drawn from this study.

- The 2D finite element stress-strain responses from a representative area element of the composite were in agreement with measurements for 5%  $V_f$  carbon fiber modified epoxy composite subjected to uniaxial tension. The plane stress and strain results showed the lower and upper bounds, respectively.
- Both plane stress and plane strain cases match the experimental response up to the elastic limit. Beyond the elastic limit, at higher strain levels, experimental response deviates from plane strain and plane stress responses as 3D effects become significant.
- The agreement between computations and experiments up to the elastic limit is attributed to a perfect bonding between epoxy matrix and carbon fibers assumed in the simulations.

- Due to the Poisson effect the plane strain case produced a stiffer response than the plane stress case. In carbon fibers within the representative area element showed higher stress and lower strain magnitudes due to significantly higher stiffness compared to the matrix material.
- The XFEM results showed that in the perfectly bonded fiber case, the crack propagated through the fiber. However, in the weakly bonded fiber case, the crack path circumvented the fiber.
- The stress-strain response obtained from the 2D finite element analysis explained that the carbon fibers were strongly bonded with the epoxy matrix in carbon fiber modified epoxy composite, and the crack propagation analysis using XFEM showed that the crack propagates through the fibers in the perfectly bonded case. Thus, during crack propagation carbon fiber resisted the crack growth and eventually broke through causing higher energy dissipation and hence higher apparent fracture toughness of the composite.

In the last part of this work, a poptube approach was utilized to grow CNTs on various engineering substrates using a microwave within a few seconds. CNTs were successfully grown on hollow glass-microballoons, solid glass spheres, solid glass fibers and carbon fibers and then were used as filler material in the synthesis of micro-nano hierarchical composites. The quasi-static fracture behavior of these hierarchical composites was studied. The following are some of the conclusions drawn from this part of the work.

- The ultrafast poptube approach, which does not require sophisticated setup like the other existing conventional techniques, was utilized to grow CNTs on various micron sized glass/carbon substrates.



- Scanning electron micrographs showed that CNT coverage on micron filler surfaces was inconsistent. Part of the substrate surface was covered with CNTs uniformly whereas in other parts almost no growth was observed.
- The hierarchical epoxy composite made of CNT-grown microballoons called nano-syntactic foam enhanced the critical fracture toughness  $K_{IC}$  by ~17% relative to conventional syntactic foam in quasi-static fracture tests.
- The critical fracture toughness  $K_{IC}$  for CNT-grown carbon fiber modified epoxy compared to carbon fiber modified epoxy decreased by ~15% relative to carbon fiber modified epoxy composite in quasi-static fracture tests.
- Fractography revealed that improvements due to CNTs were compromised by agglomeration of micro-fillers among CNTs grown on them.

## 7.1 Future directions

The effect of filler shape (rod, flake and sphere shaped glass fillers) and filler volume fraction on the dynamic fracture behavior of particulate polymer composites has been studied. The rod shaped glass-filled epoxy composite produced the highest stress intensity factors in pre-and post-crack initiation regime among all three fillers used in this study. The rod shaped fillers were 800  $\mu\text{m}$  in length and 10  $\mu\text{m}$  in diameter (aspect ratio = 80). The effect of constant shape but varying aspect ratio of rod shaped fillers can be studied on the dynamic fracture toughness of glass-filled epoxy composite.

The mixed-mode fracture behavior of rod shaped glass-filled epoxy composite was studied using 2D DIC and high-speed photography under impact loading. Only a single loading rate was used during the mixed-mode study. The different loading rate can be employed as described in

Chapter 3 to study the effect of loading rate on mixed-mode dynamic fracture behavior of neat and glass-filled epoxy.

## REFERENCES

- [1] R. Jhavar. Compression response and modeling of interpenetrating phase composites and foam-filled honeycombs. Auburn University, 2009.
- [2] Jacob GC, Starbuck JM, Fellers JF, Simunovic S, Boeman RG. Fracture toughness in random-chopped fiber-reinforced composites and their strain rate dependence. *J Appl Polym Sci* 2006;100:695–701. doi:10.1002/app.23414.
- [3] Compston P, Jar P-YB, Burchill PJ, Takahashi K. The effect of matrix toughness and loading rate on the mode-II interlaminar fracture toughness of glass-fibre/vinyl-ester composites. *Composites Science and Technology* 2001;61:321–33. doi:10.1016/S0266-3538(00)00226-8.
- [4] Compston P, Jar P-YB, Davies P. Matrix effect on the static and dynamic interlaminar fracture toughness of glass-fibre marine composites. *Composites Part B: Engineering* 1998;29:505–16. doi:10.1016/S1359-8368(98)00004-3.
- [5] Kushvaha V, Tippur H. Effect of Filler Particle Shape on Dynamic Fracture Behavior of Glass-Filled Epoxy. In: Chalivendra V, Song B, Casem D, editors. *Dynamic Behavior of Materials, Volume 1*, Springer New York; 2013, p. 513–22.

- [6] Kushvaha V, Branch A, Tippur H. Effect of Loading Rate on Dynamic Fracture Behavior of Glass and Carbon Fiber Modified Epoxy. In: Song B, Casem D, Kimberley J, editors. *Dynamic Behavior of Materials, Volume 1*, Springer International Publishing; 2014, p. 169–76.
- [7] Kushvaha V, Tippur H. Effect of filler shape, volume fraction and loading rate on dynamic fracture behavior of glass-filled epoxy. *Composites Part B: Engineering* 2014;64:126–37. doi:10.1016/j.compositesb.2014.04.016.
- [8] Owens A. Development of a split hopkinson tension bar for testing stress-strain response of particulate composites under high rates of loading. AuburnUniversity, n.d.
- [9] Fu S-Y, Feng X-Q, Lauke B, Mai Y-W. Effects of particle size, particle/matrix interface adhesion and particle loading on mechanical properties of particulate–polymer composites. *Composites Part B: Engineering* 2008;39:933–61. doi:10.1016/j.compositesb.2008.01.002.
- [10] Koh S-W, Kim J-K, Mai Y-W. Fracture toughness and failure mechanisms in silica-filled epoxy resin composites: effects of temperature and loading rate. *Polymer* 1993;34:3446–55. doi:10.1016/0032-3861(93)90474-O.
- [11] Karger-Kocsis J, Friedrich K. Temperature and strain-rate effects on the fracture toughness of poly(ether ether ketone) and its short glass-fibre reinforced composite. *Polymer* 1986;27:1753–60. doi:10.1016/0032-3861(86)90272-7.
- [12] Nakamura Y, Okabe S, Iida T. Effects of particle shape, size and interfacial adhesion on the fracture strength of silica-filled epoxy resin. *Polymers & Polymer Composites* 1999;7:177–86.

- [13] Jajam KC, Tippur HV. Quasi-static and dynamic fracture behavior of particulate polymer composites: A study of nano- vs. micro-size filler and loading-rate effects. *Composites Part B: Engineering* 2012;43:3467–81. doi:10.1016/j.compositesb.2012.01.042.
- [14] Liu H-Y, Wang G-T, Mai Y-W, Zeng Y. On fracture toughness of nano-particle modified epoxy. *Composites Part B: Engineering* 2011;42:2170–5. doi:10.1016/j.compositesb.2011.05.014.
- [15] Liang J-Z. Reinforcement and quantitative description of inorganic particulate-filled polymer composites. *Composites Part B: Engineering* 2013;51:224–32. doi:10.1016/j.compositesb.2013.03.019.
- [16] Park BG, Crosky AG, Hellier AK. Fracture toughness of microsphere Al<sub>2</sub>O<sub>3</sub>–Al particulate metal matrix composites. *Composites Part B: Engineering* 2008;39:1270–9. doi:10.1016/j.compositesb.2008.01.005.
- [17] Song SG, Shi N, Iii GTG, Roberts JA. Reinforcement shape effects on the fracture behavior and ductility of particulate-reinforced 6061-Al matrix composites. *MMTA* 1996;27:3739–46. doi:10.1007/BF02595465.
- [18] Nakamura Y, Yamaguchi M, Okubo M, Matsumoto T. Effect of particle size on the fracture toughness of epoxy resin filled with spherical silica. *Polymer* 1992;33:3415–26. doi:10.1016/0032-3861(92)91099-N.
- [19] Wu TT. The effect of inclusion shape on the elastic moduli of a two-phase material. *International Journal of Solids and Structures* 1966;2:1–8. doi:10.1016/0020-7683(66)90002-3.

- [20] Spanoudakis J, Young RJ. Crack propagation in a glass particle-filled epoxy resin. *J Mater Sci* 1984;19:473–86. doi:10.1007/BF02403234.
- [21] Nakamura Y, Yamaguchi M, Okubo M, Matsumoto T. Effect of particle size on mechanical properties of epoxy resin filled with angular-shaped silica. *J Appl Polym Sci* 1992;44:151–8. doi:10.1002/app.1992.070440116.
- [22] Kitey R, Tippur HV. Role of particle size and filler–matrix adhesion on dynamic fracture of glass-filled epoxy. I. Macromolecular measurements. *Acta Materialia* 2005;53:1153–65. doi:10.1016/j.actamat.2004.11.012.
- [23] Kusaka T, Hojo M, Mai Y-W, Kurokawa T, Nojima T, Ochiai S. Rate dependence of mode I fracture behaviour in carbon-fibre/epoxy composite laminates. *Composites Science and Technology* 1998;58:591–602. doi:10.1016/S0266-3538(97)00176-0.
- [24] Lee D, Tippur H, Bogert P. Quasi-static and dynamic fracture of graphite/epoxy composites: An optical study of loading-rate effects. *Composites Part B: Engineering* 2010;41:462–74. doi:10.1016/j.compositesb.2010.05.007.
- [25] Iijima S. Helical microtubules of graphitic carbon. *Nature* 1991;354:56–8. doi:10.1038/354056a0.
- [26] Dresselhaus MS, Dresselhaus G, Avouris P, editors. *Carbon Nanotubes*. vol. 80. Berlin, Heidelberg: Springer Berlin Heidelberg; 2001.
- [27] Gojny FH, Wichmann MHG, Köpke U, Fiedler B, Schulte K. Carbon nanotube-reinforced epoxy-composites: enhanced stiffness and fracture toughness at low nanotube content. *Composites Science and Technology* 2004;64:2363–71. doi:10.1016/j.compscitech.2004.04.002.

- [28] Schadler LS, Giannaris SC, Ajayan PM. Load transfer in carbon nanotube epoxy composites. *Applied Physics Letters* 1998;73:3842–4. doi:10.1063/1.122911.
- [29] P Jindal, K. R. Sharma, P. Chandel, V. Mangla, S. Pandey. Modification of impact strength of polycarbonate composites with carbon nanotubes 2011.
- [30] K. L. Lu RML. Mechanical damage of carbon nanotubes by ultrasound. *Carbon* 1996;34:814–816. doi:10.1016/0008-6223(96)89470-X.
- [31] Hung KH, Kuo WS, Ko TH, Tzeng SS, Yan CF. Processing and tensile characterization of composites composed of carbon nanotube-grown carbon fibers. *Composites Part A: Applied Science and Manufacturing* 2009;40:1299–304. doi:10.1016/j.compositesa.2009.06.002.
- [32] Mathur RB, Chatterjee S, Singh BP. Growth of carbon nanotubes on carbon fibre substrates to produce hybrid/phenolic composites with improved mechanical properties. *Composites Science and Technology* 2008;68:1608–15. doi:10.1016/j.compscitech.2008.02.020.
- [33] Nguyen XH, Lee YB, Lee CH, Lim D-S. Synthesis of sea urchin-like particles of carbon nanotubes directly grown on stainless steel cores and their effect on the mechanical properties of polymer composites. *Carbon* 2010;48:2910–6. doi:10.1016/j.carbon.2010.04.027.
- [34] Zhan G-D, Kuntz JD, Garay JE, Mukherjee AK. Electrical properties of nanoceramics reinforced with ropes of single-walled carbon nanotubes. *Applied Physics Letters* 2003;83:1228–30.
- [35] Moiala A, Li Q, Kinloch IA, Windle AH. Thermal and electrical conductivity of single- and multi-walled carbon nanotube-epoxy composites. *Composites Science and Technology* 2006;66:1285–8. doi:10.1016/j.compscitech.2005.10.016.

- [36] Gojny FH, Schulte K. Functionalisation effect on the thermo-mechanical behaviour of multi-wall carbon nanotube/epoxy-composites. *Composites Science and Technology* 2004;64:2303–8. doi:10.1016/j.compscitech.2004.01.024.
- [37] Frew DJ, Forrestal MJ, Chen W. A split Hopkinson pressure bar technique to determine compressive stress-strain data for rock materials. *Experimental Mechanics* 2001;41:40–6. doi:10.1007/BF02323102.
- [38] Periasamy C. *Digital Gradient Sensing (DGS): A Full-Field Optical Technique to Measure Angular Deflections of Light Rays and Its Applications to Failure Mechanics* 2012.
- [39] Peters WH, Ranson WF. *Digital Imaging Techniques In Experimental Stress Analysis*. *Opt Eng* 1982;21:213427-213427-. doi:10.1117/12.7972925.
- [40] Bruck HA, McNeill SR, Sutton MA, Iii WHP. Digital image correlation using Newton-Raphson method of partial differential correction. *Experimental Mechanics* 1989;29:261–7. doi:10.1007/BF02321405.
- [41] Chu TC, Ranson WF, Sutton MA. Applications of digital-image-correlation techniques to. *Experimental Mechanics* 1985;25:232–44. doi:10.1007/BF02325092.
- [42] Dickinson AS, Taylor AC, Ozturk H, Browne M. Experimental validation of a finite element model of the proximal femur using digital image correlation and a composite bone model. *J Biomech Eng* 2011;133:14504. doi:10.1115/1.4003129.
- [43] Vinod Kushvaha, S. Javid, H. Giambini, S. McEligot, D. Dragomir-Daescu. Failure Characterization of Cadaveric Proximal Femora in a Sideways Fall on the Hip Configuration Using



Digital Image Correlation, in SEM XIII International Congress & Exposition on Experimental and Applied Mechanics, Springer New York; 2013.

- [44] Pan B, Qian K, Xie H, Asundi A. Two-dimensional digital image correlation for in-plane displacement and strain measurement: a review. *Meas Sci Technol* 2009;20:62001. doi:10.1088/0957-0233/20/6/062001.
- [45] H. V. Tippur. *Optical Methods In Mechanics* 2009.
- [46] Kitey R, Tippur HV. Dynamic Crack Growth Past a Stiff Inclusion: Optical Investigation of Inclusion Eccentricity and Inclusion-matrix Adhesion Strength. *Exp Mech* 2007;48:37–53. doi:10.1007/s11340-007-9050-z.
- [47] Bedsole R, Tippur HV. Dynamic Fracture Characterization of Small Specimens: A Study of Loading Rate Effects on Acrylic and Acrylic Bone Cement. *J Eng Mater Technol* 2013;135:031001–031001. doi:10.1115/1.4023405.
- [48] Dally JW, Riley WF, Kobayashi AS. Experimental Stress Analysis. *Journal of Applied Mechanics* 1978;45:968. doi:10.1115/1.3424473.
- [49] Nishioka T, Atluri SN. Path-independent integrals, energy release rates, and general solutions of near-tip fields in mixed-mode dynamic fracture mechanics. *Engineering Fracture Mechanics* 1983;18:1–22. doi:10.1016/0013-7944(83)90091-7.
- [50] Tippur HV, Krishnaswamy S, Rosakis AJ. Optical mapping of crack tip deformations using the methods of transmission and reflection coherent gradient sensing: a study of crack tip K-dominance. *Int J Fract* 1991;52:91–117. doi:10.1007/BF00032372.

- [51] M.A. Kaiser. *Advancements in the Split Hopkinson Bar Test*. Virginia Polytechnic Institute and State University: Blacksburg, Virginia, 1998.
- [52] Kirugulige MS, Tippur HV, Denney TS. Measurement of transient deformations using digital image correlation method and high-speed photography: application to dynamic fracture. *Applied Optics* 2007;46:5083. doi:10.1364/AO.46.005083.
- [53] Sharon E, Gross SP, Fineberg J. Energy Dissipation in Dynamic Fracture. *Phys Rev Lett* 1996;76:2117–20. doi:10.1103/PhysRevLett.76.2117.
- [54] M. Z. Janssen, Wanhill, R. *Fracture Mechanics*. CRC Press; 2004.
- [55] M.S. K. A study of mixed-mode dynamic fracture in advanced particulate composites by optical interferometry, digital image correlation and finite element methods, in *Mechanical Engineering*. Auburn University, 2007.
- [56] Qian J, Fatemi A. Mixed mode fatigue crack growth: A literature survey. *Engineering Fracture Mechanics* 1996;55:969–90. doi:10.1016/S0013-7944(96)00071-9.
- [57] Kirugulige M, Tippur HV. Mixed-Mode Dynamic Crack Growth in a Functionally Graded Particulate Composite: Experimental Measurements and Finite Element Simulations. *J Appl Mech* 2008;75:051102–051102. doi:10.1115/1.2932095.
- [58] Kirugulige MS, Tippur HV. Measurement of Fracture Parameters for a Mixed-Mode Crack Driven by Stress Waves using Image Correlation Technique and High-Speed Digital Photography. *Strain* 2009;45:108–22. doi:10.1111/j.1475-1305.2008.00449.x.

- [59] Singh D, Shetty DK. Fracture Toughness of Polycrystalline Ceramics in Combined Mode I and Mode II Loading. *Journal of the American Ceramic Society* 1989;72:78–84. doi:10.1111/j.1151-2916.1989.tb05957.x.
- [60] M. R. Ayatollahi MRMA. Fracture toughness study for a brittle rock subjected to mixed mode I/II loading. *International Journal of Rock Mechanics and Mining Sciences* 2007;617–24. doi:10.1016/j.ijrmms.2006.10.001.
- [61] Lim IL, Johnston IW, Choi SK, Boland JN. Fracture testing of a soft rock with semi-circular specimens under three-point bending. Part 2—mixed-mode. *International Journal of Rock Mechanics and Mining Sciences & Geomechanics Abstracts* 1994;31:199–212. doi:10.1016/0148-9062(94)90464-2.
- [62] Hibbeler RC. *Mechanics of Materials*. 8th edition. Boston: Prentice Hall; 2010.
- [63] Abaqus User's Manual 2013.
- [64] Mier JGM van. Microstructural Effects on Fracture Scaling in Concrete, Rock and Ice. In: Dempsey JP, Shen HH, editors. *IUTAM Symposium on Scaling Laws in Ice Mechanics and Ice Dynamics*, Springer Netherlands; 2001, p. 171–82.
- [65] Martinez WL, Martinez AR. *Computational Statistics Handbook with MATLAB*, Second Edition. CRC Press; 2007.
- [66] Zhu HX, Hobdell JR, Windle AH. Effects of cell irregularity on the elastic properties of open-cell foams. *Acta Materialia* 2000;48:4893–900. doi:10.1016/S1359-6454(00)00282-2.
- [67] Sotomayor O. *Numerical Modeling of Random 2D and 3D Structural Foams Using Voronoi Diagrams: A Study of Cell Regularity and Compression Response*. thesis. 2013.

- [68] Belytschko T, Black T. Elastic crack growth in finite elements with minimal remeshing. *Int J Numer Meth Engng* 1999;45:601–20. doi:10.1002/(SICI)1097-0207(19990620)45:5<601::AID-NME598>3.0.CO;2-S.
- [69] Zamani A, Eslami MR. Implementation of the extended finite element method for dynamic thermoelastic fracture initiation. *International Journal of Solids and Structures* 2010;47:1392–404. doi:10.1016/j.ijsolstr.2010.01.024.
- [70] Belytschko T, Chen H, Xu J, Zi G. Dynamic crack propagation based on loss of hyperbolicity and a new discontinuous enrichment. *Int J Numer Meth Engng* 2003;58:1873–905. doi:10.1002/nme.941.
- [71] Dolbow J, Moës N, Belytschko T. An extended finite element method for modeling crack growth with frictional contact. *Computer Methods in Applied Mechanics and Engineering* 2001;190:6825–46. doi:10.1016/S0045-7825(01)00260-2.
- [72] Moës N, Dolbow J, Belytschko T. A finite element method for crack growth without remeshing. *Int J Numer Meth Engng* 1999;46:131–50. doi:10.1002/(SICI)1097-0207(19990910)46:1<131::AID-NME726>3.0.CO;2-J.
- [73] Pommier S, Gravouil A, Combescure A, Moës N, Pommier S, Gravouil A, et al. Extended Finite Element Method X-FEM. *Extended Finite Element Method for Crack Propagation*, John Wiley & Sons, Inc.; 2013, p. 69–108.
- [74] Wong DC, Sung JC. Dynamic response of an inclusion with compliant interface in an elastic medium due to a plane shear wave. *Applied Mathematical Modelling* 1994;18:3–13. doi:10.1016/0307-904X(94)90177-5.

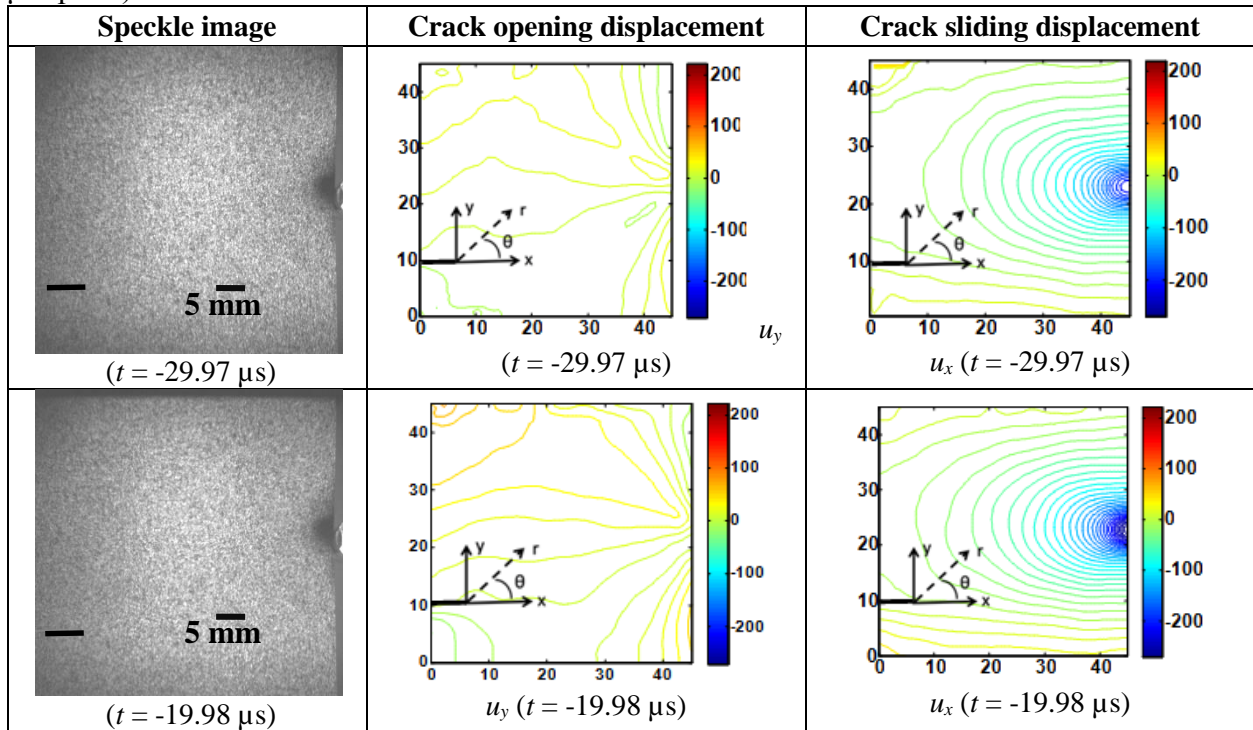
- [75] Y. K, Y I, S O. Direct Measurement on Fracture Toughness of Carbon Fiber, 2013.
- [76] Alan B Dalton SC. Super-tough carbon-nanotube fibres. *Nature* 2003;423:703. doi:10.1038/423703a.
- [77] Rakesh L, Howell BA, Chai M, Mueller A, Kujawski M, Fan D, et al. Computer-aided applications of nanoscale smart materials for biomedical applications. *Nanomedicine (Lond)* 2008;3:719–39. doi:10.2217/17435889.3.5.719.
- [78] Kong J, Franklin NR, Zhou C, Chapline MG, Peng S, Cho K, et al. Nanotube Molecular Wires as Chemical Sensors. *Science* 2000;287:622–5. doi:10.1126/science.287.5453.622.
- [79] Baughman RH, Zakhidov AA, de Heer WA. Carbon nanotubes--the route toward applications. *Science* 2002;297:787–92. doi:10.1126/science.1060928.
- [80] Rinzler AG. Materials processing: Sorting out carbon nanotube electronics. *Nat Nano* 2006;1:17–8. doi:10.1038/nnano.2006.76.
- [81] Journet C, Maser WK, Bernier P, Loiseau A, de la Chapelle ML, Lefrant S, et al. Large-scale production of single-walled carbon nanotubes by the electric-arc technique. *Nature* 1997;388:756–8. doi:10.1038/41972.
- [82] Fischer JE, Dai H, Thess A, Lee R, Hanjani NM, Dehaas DL, et al. Metallic resistivity in crystalline ropes of single-wall carbon nanotubes. *Phys Rev B* 1997;55:R4921–4. doi:10.1103/PhysRevB.55.R4921.
- [83] Baykal B, Ibrahimova V, Er G, Bengü E, Tuncel D. Dispersion of multi-walled carbon nanotubes in an aqueous medium by water-dispersible conjugated polymer nanoparticles. *Chem Commun* 2010;46:6762–4. doi:10.1039/C0CC00510J.

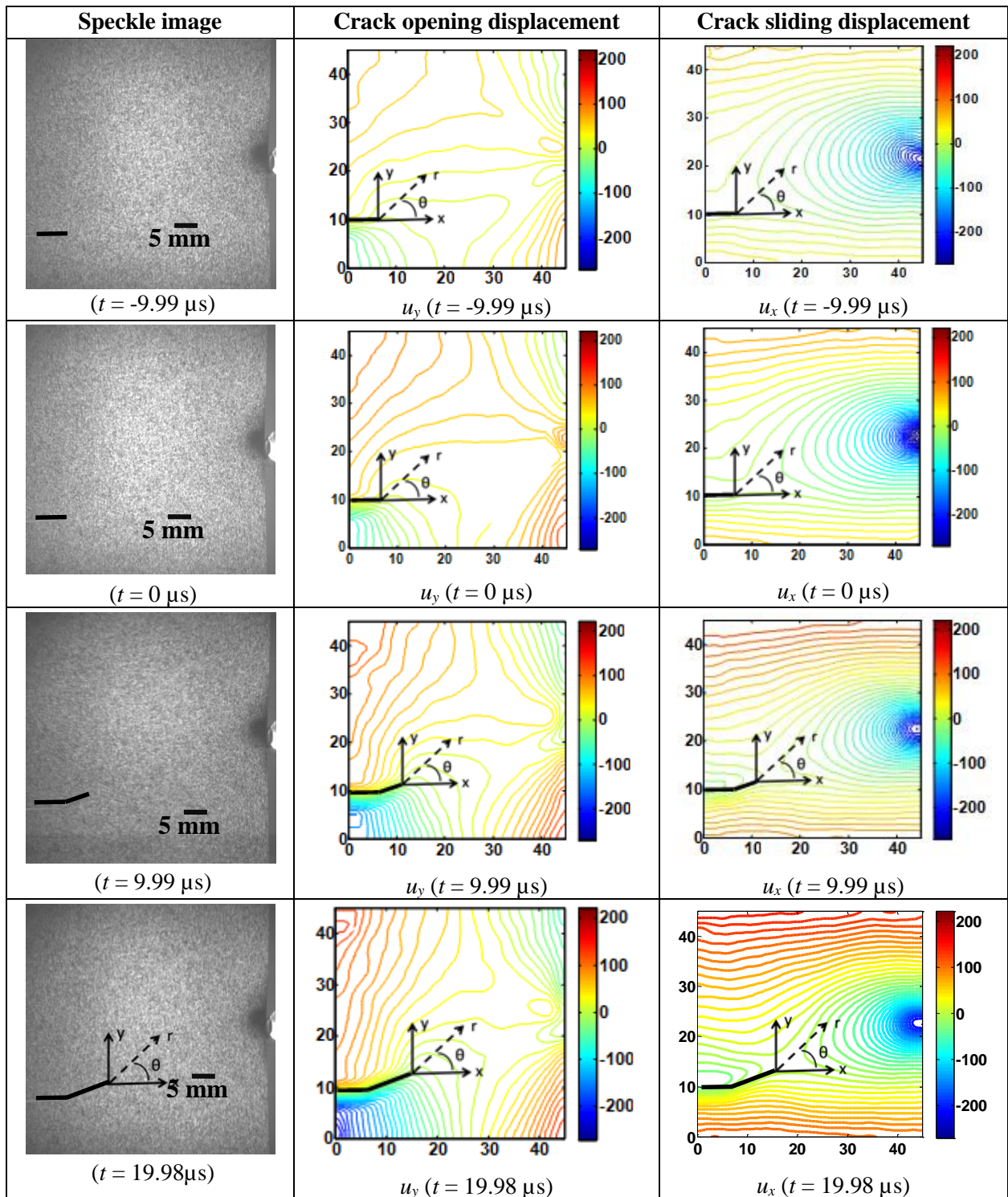
- [84] Abusch-Magder D, Someya T, Wang J, Laskowski E, Dodabalapur A, Bao Z, et al. Measurements of Gated Conjugated Polymer with Electrode Spacing Down to Several Nanometers. arXiv:cond-mat/0210332 2002.
- [85] Fraczek-Szczypta A, Bogun M, Blazewicz S. Carbon fibers modified with carbon nanotubes. *J Mater Sci* 2009;44:4721–7. doi:10.1007/s10853-009-3730-2.
- [86] Zhao J, Liu L, Guo Q, Shi J, Zhai G, Song J, et al. Growth of carbon nanotubes on the surface of carbon fibers. *Carbon* 2008;46:380–3.
- [87] Zhang X, Manohar SK. Microwave synthesis of nanocarbons from conducting polymers. *Chem Commun* 2006:2477–9. doi:10.1039/B603925A.
- [88] O’Connell MJ. *Carbon Nanotubes: Properties and Applications*. CRC Press; 2006.
- [89] Liu Z, Wang J, Kushvaha V, Poyraz S, Tippur H, Park S, et al. Poptube approach for ultrafast carbon nanotube growth. *Chem Commun* 2011;47:9912–4. doi:10.1039/C1CC13359D.
- [90] Liu Z, Zhang L, Poyraz S, Smith J, Kushvaha V, Tippur H, et al. An ultrafast microwave approach towards multi-component and multi-dimensional nanomaterials. *RSC Adv* 2014;4:9308–13. doi:10.1039/C3RA47086E.
- [91] Kushvaha V, Tippur HV, Zhang X. *Novel Syntactic Foam: Synthesis, Processing and Fracture Characterization*, Auburn, AL: Auburn University; 2013.

## Appendix A

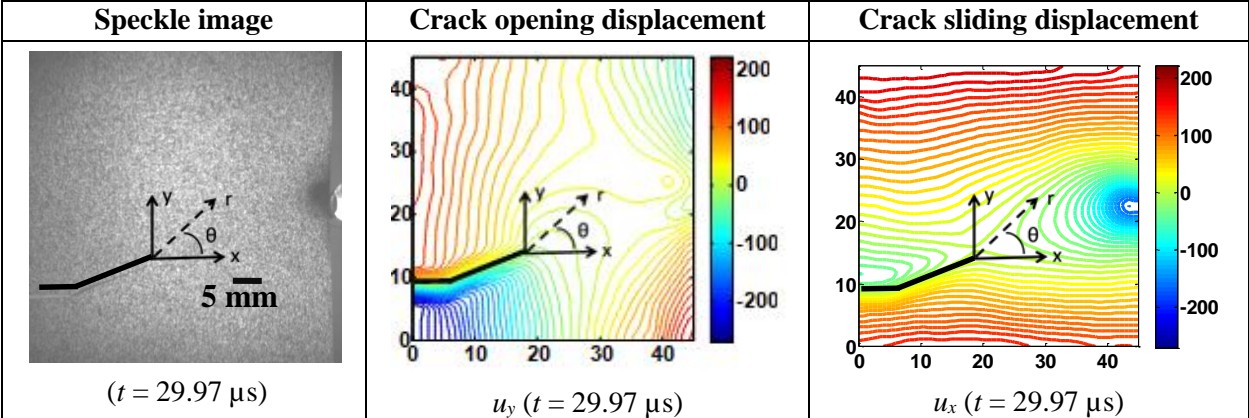
This appendix contains the acquired speckle images, crack opening ( $u_y$ ) and crack sliding ( $u_x$ ) displacement contours for glass-filled epoxy at time instants  $t = -29.97, -19.98, -9.99, 0, 9.99, 19.98, 29.97 \mu\text{s}$ , respectively. The time  $t = -29.97, -19.98, -9.99 \mu\text{s}$  corresponds to pre-crack initiation. The time  $t = 0$  is at crack initiation and time  $t = 9.99, 19.98, 29.97 \mu\text{s}$  corresponds to post-crack initiation. The transformed crack opening ( $u_y'$ ) and transformed crack sliding ( $u_x'$ ) displacements are also plotted for post-crack initiation instants ( $t = 9.99, 19.98, 29.97 \mu\text{s}$ ). The units are in mm on the displacement contours on  $x$ - and  $y$ -axis and the contours are in steps of  $10 \mu\text{m}$ .

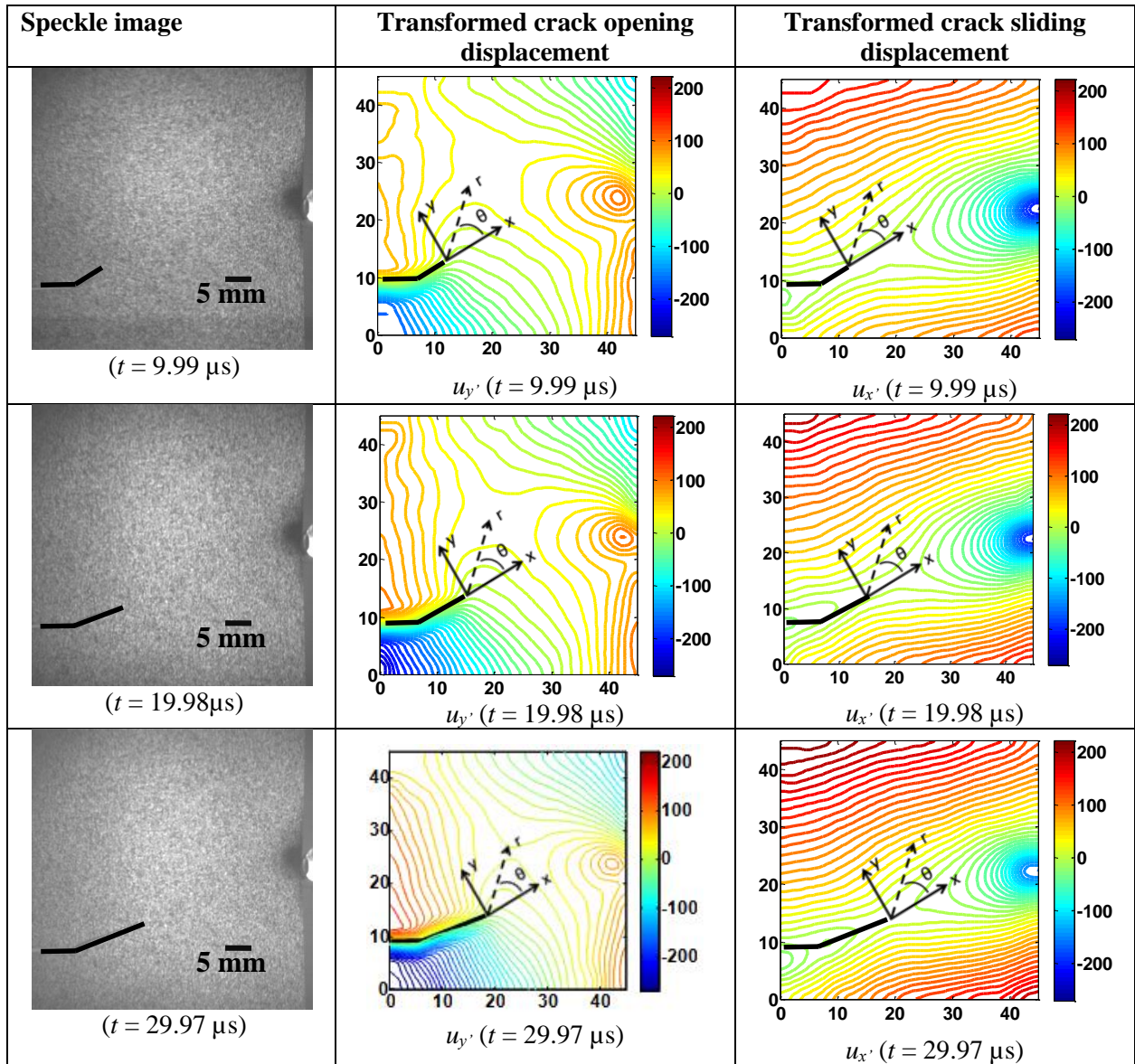
**A1.** 10%  $V_f$  glass-filled epoxy ( $e = 15, a = 10$ ) (Facet size: 15x15; Overlap:0x0, Scale factor: 48  $\mu\text{m}/\text{pixel}$ )



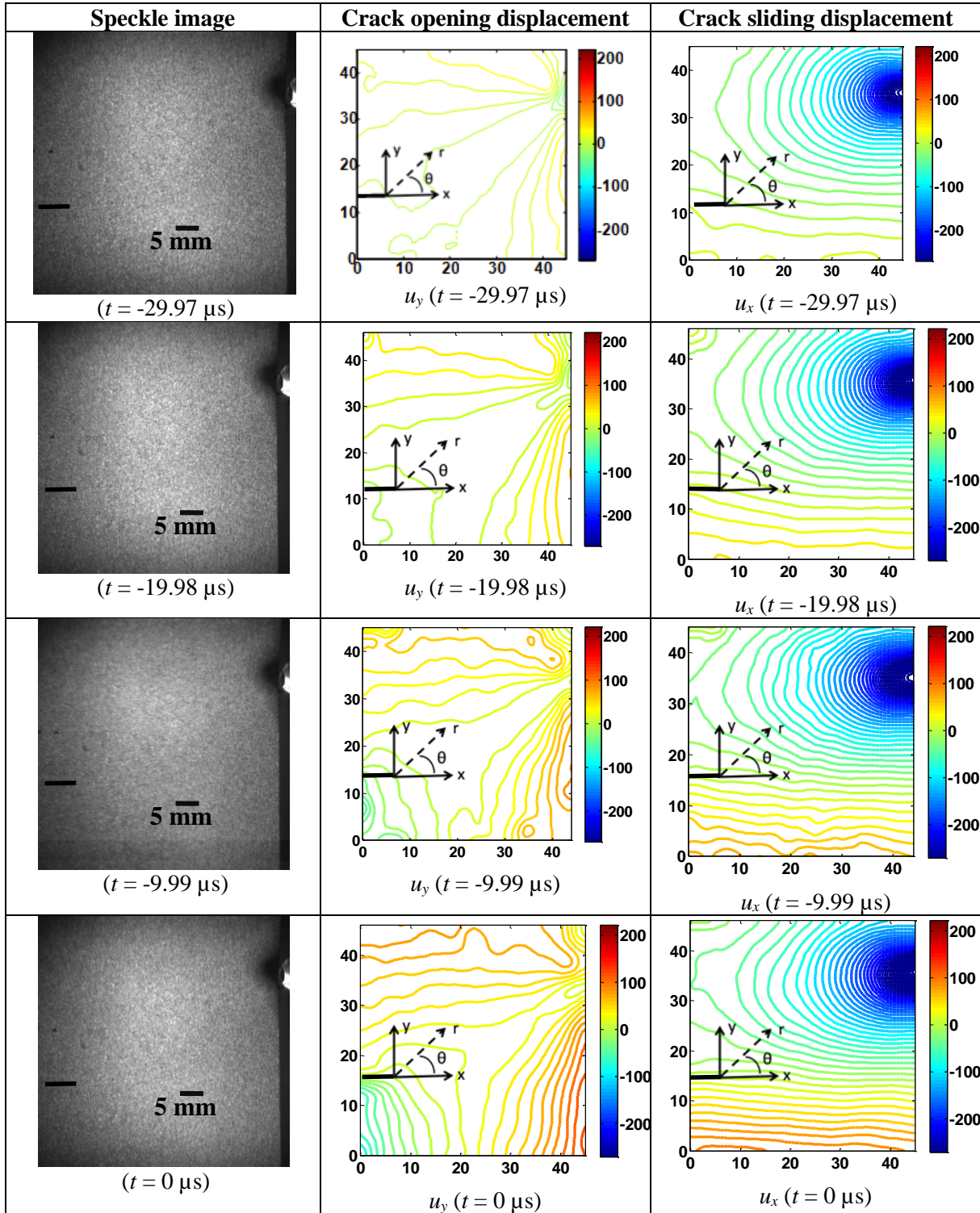


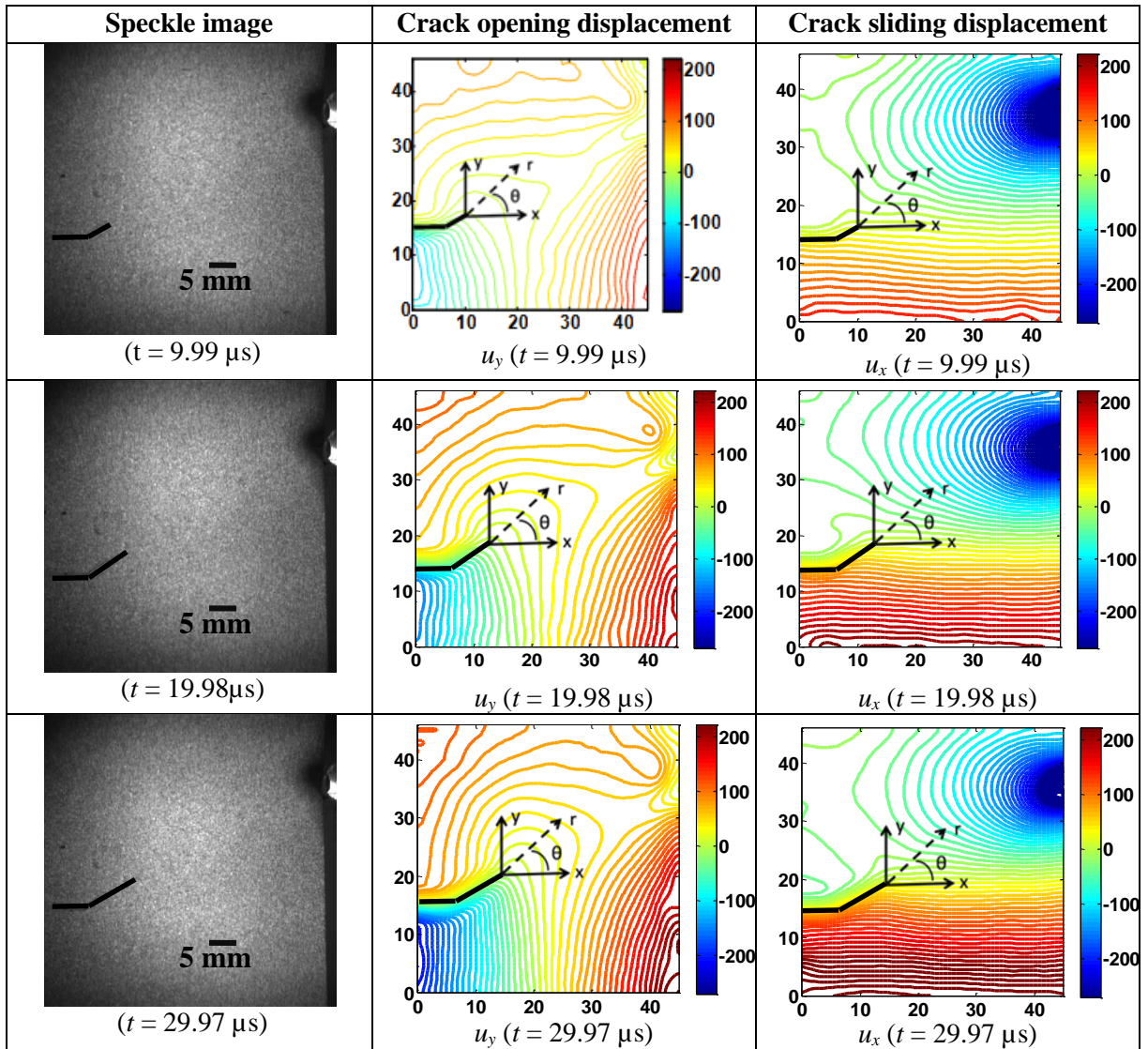




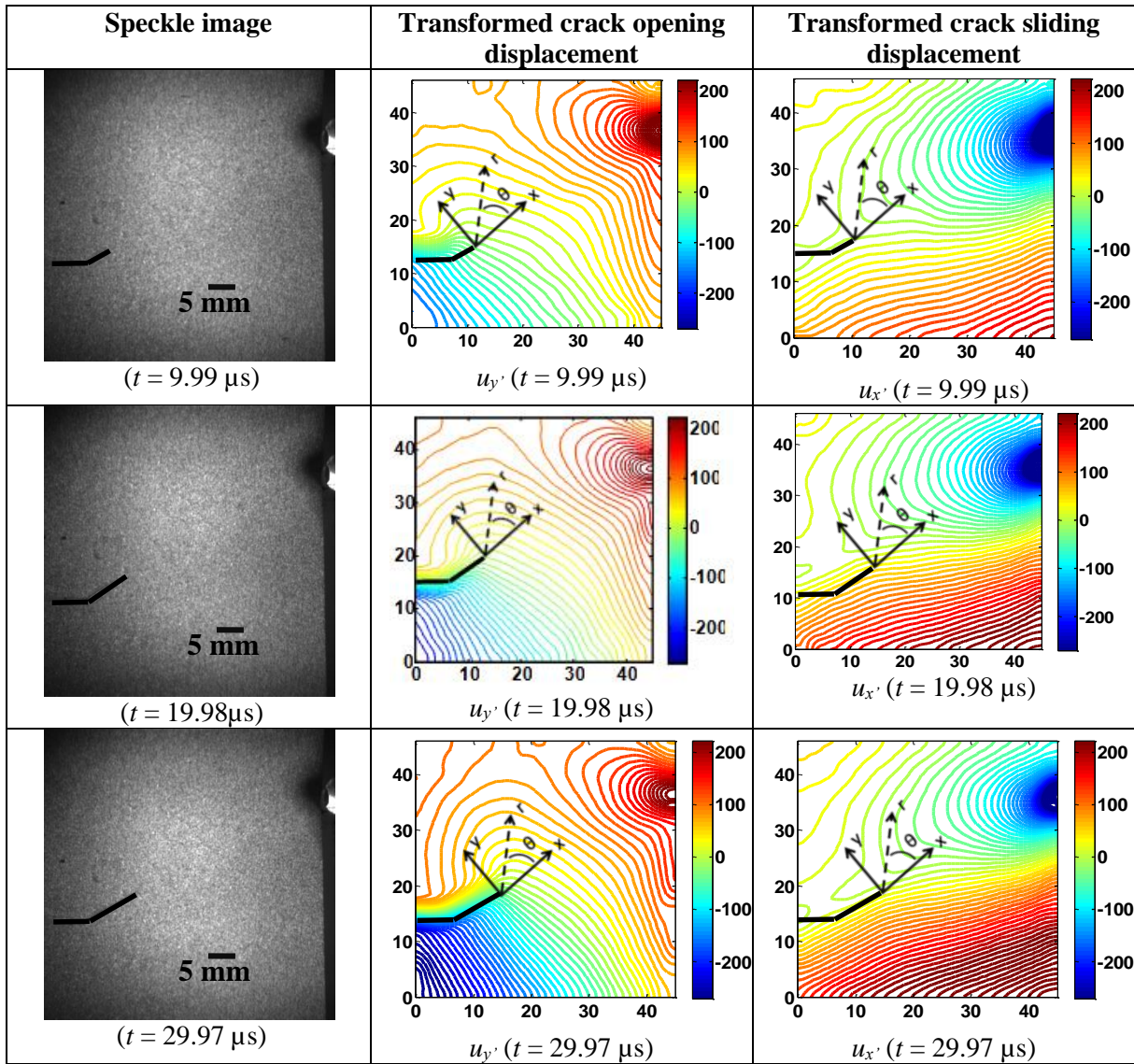


A2. 10%  $V_f$  glass-filled epoxy ( $e = 20$ ,  $a = 10$ ) (Facet size: 15x15; Overlap:0x0, Scale factor: 49  $\mu\text{m}/\text{pixel}$ )

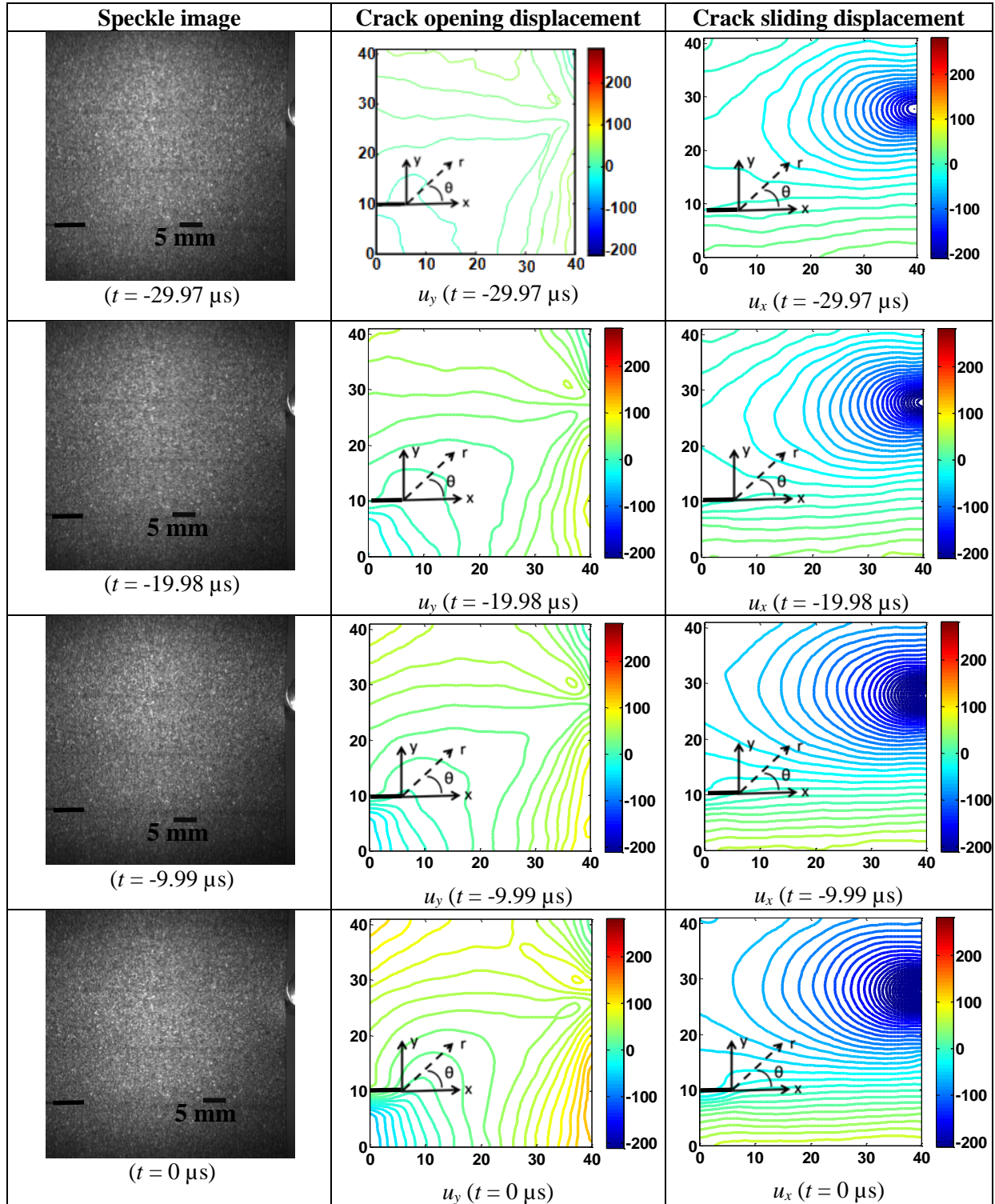


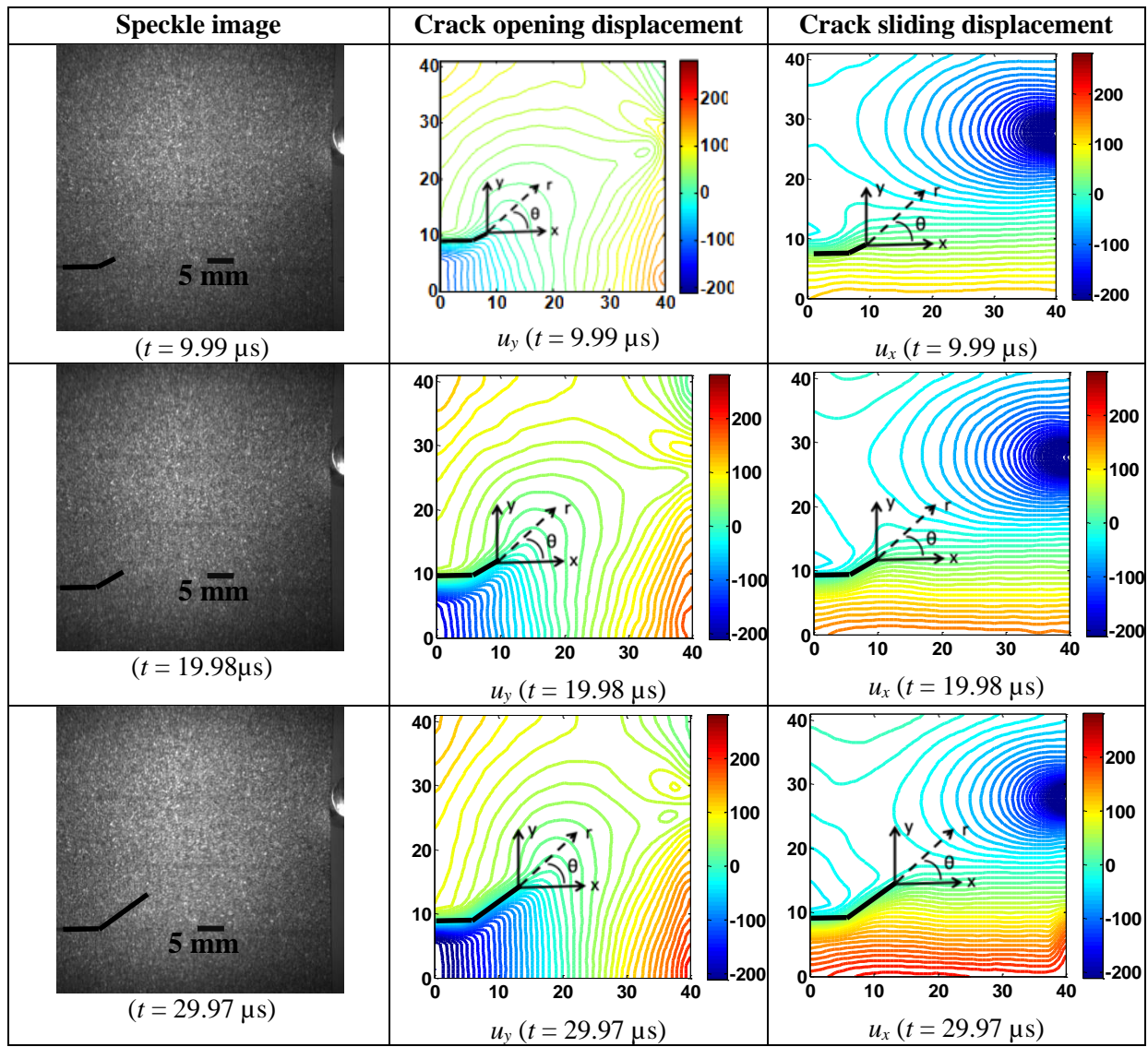




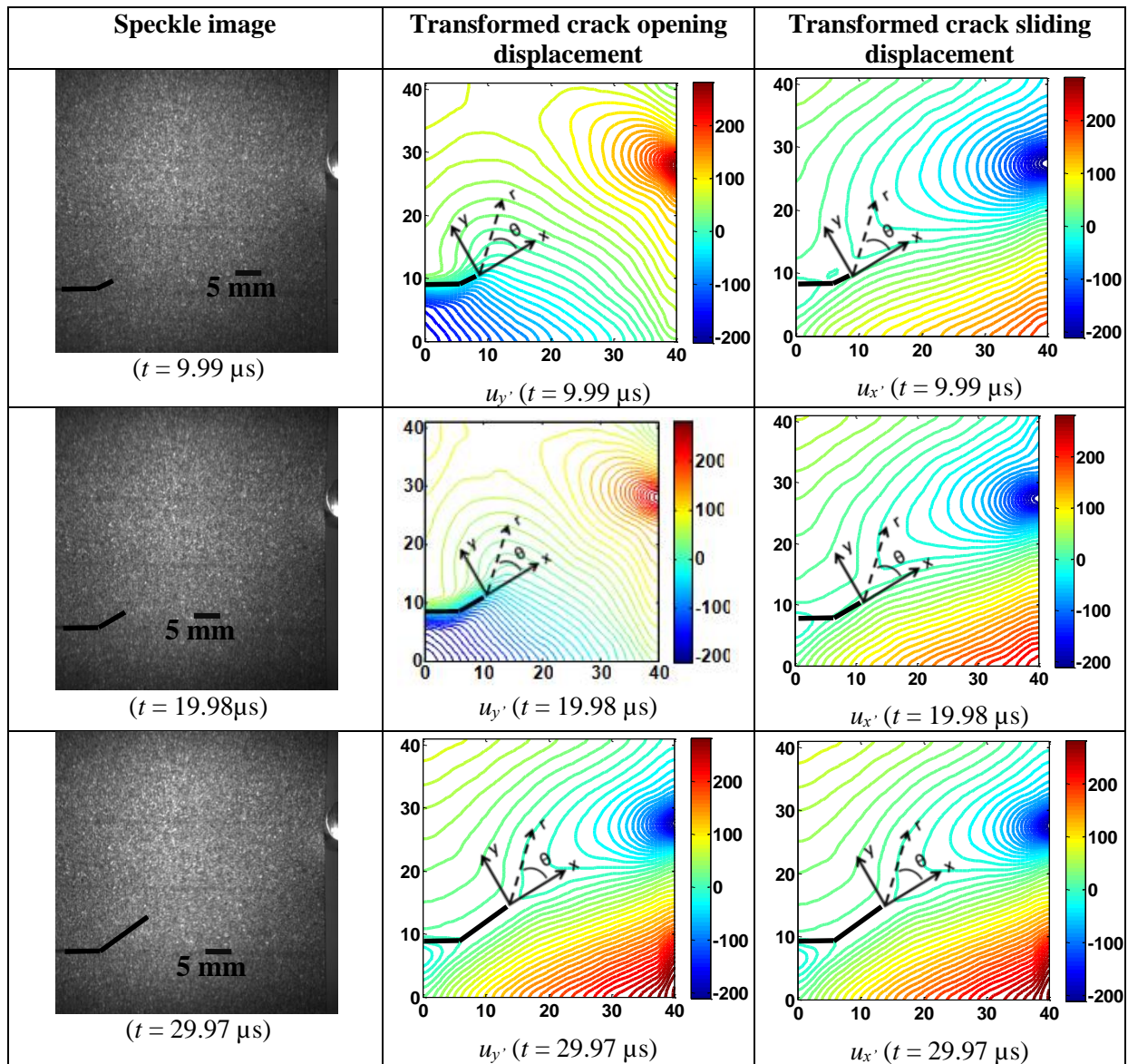


**A3.** 10%  $V_f$  glass-filled epoxy ( $e = 20$ ,  $a = 15$ ) (Facet size: 15x15; Overlap:0x0, Scale factor: 43  $\mu\text{m}/\text{pixel}$ )



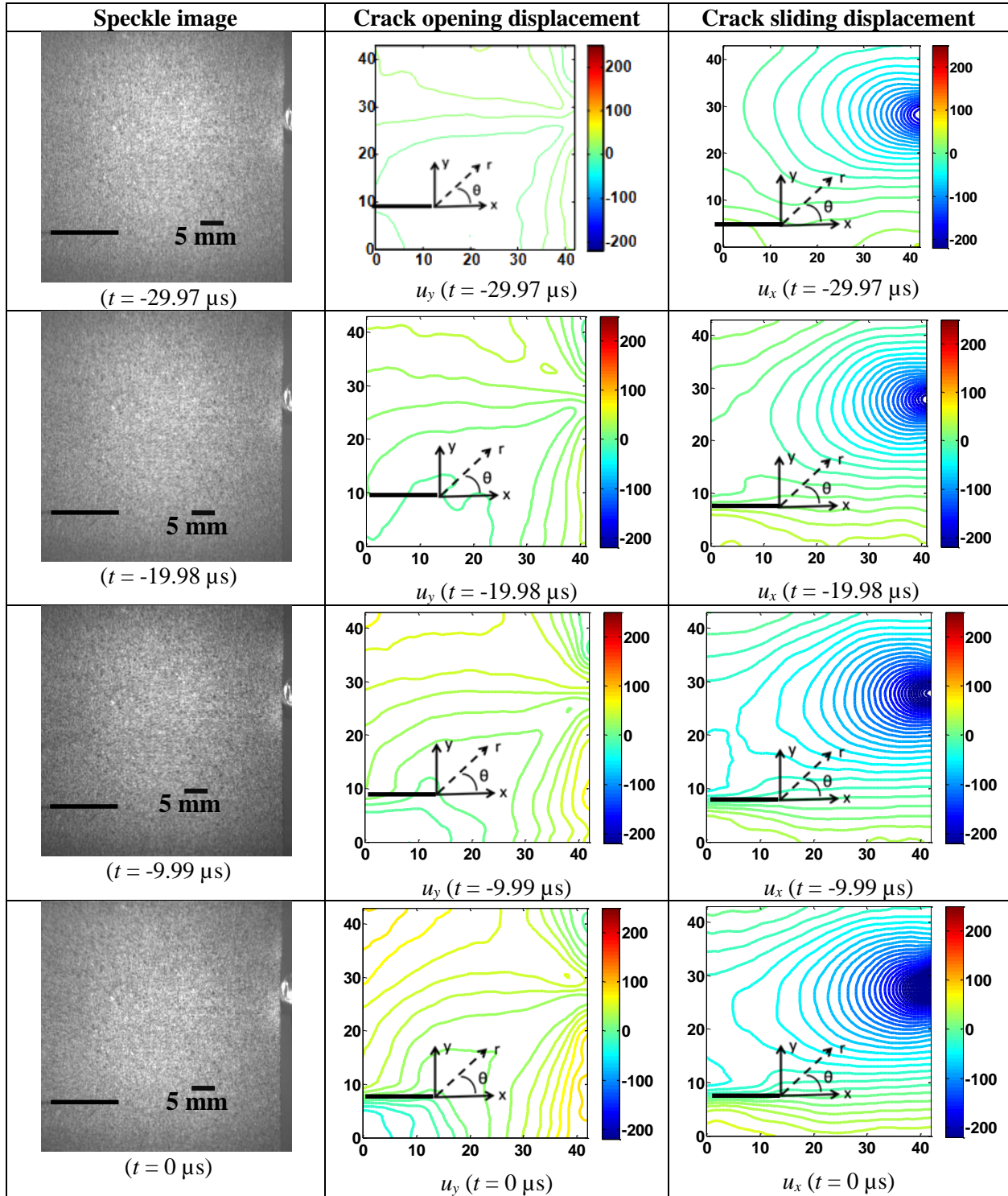


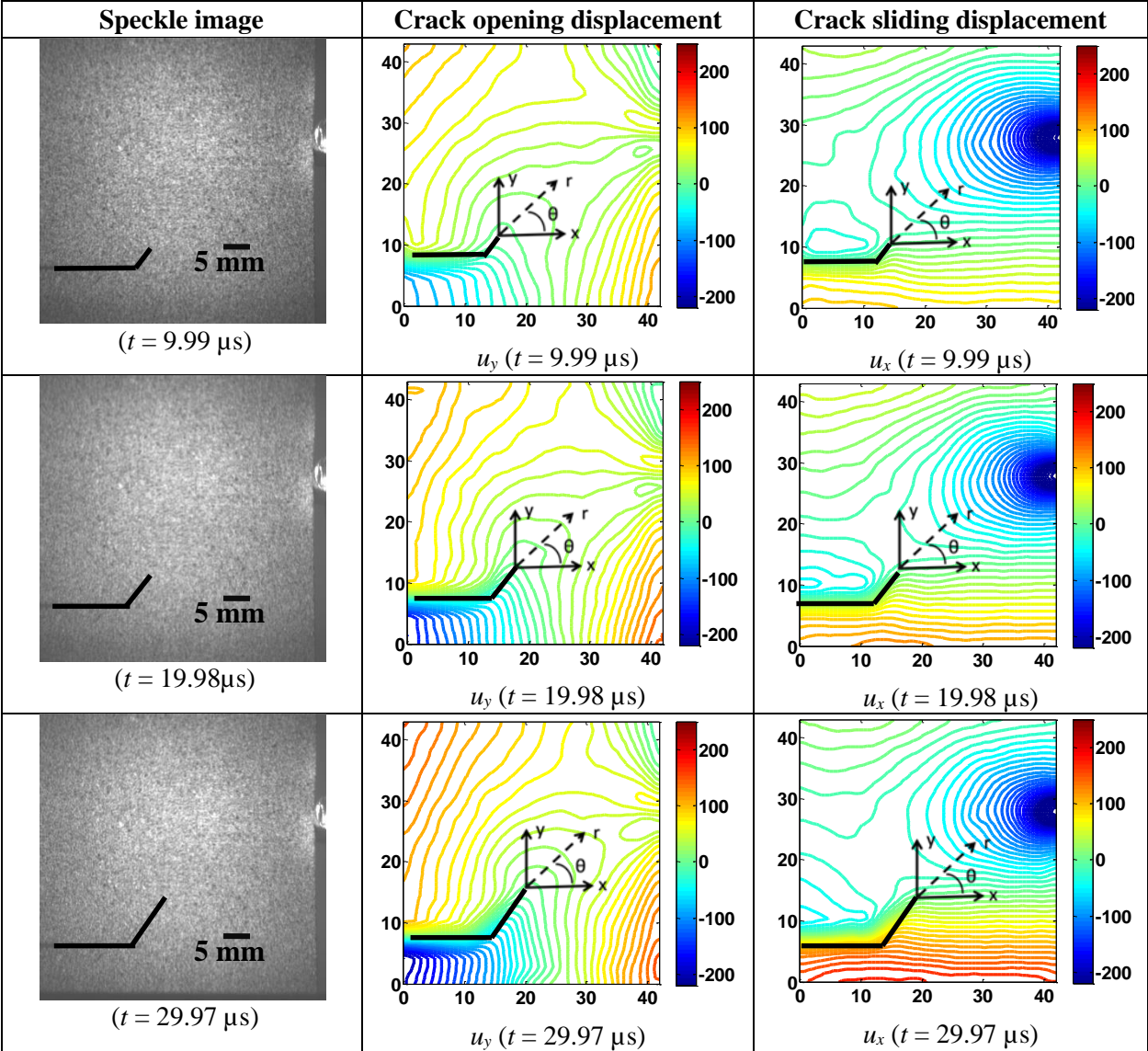


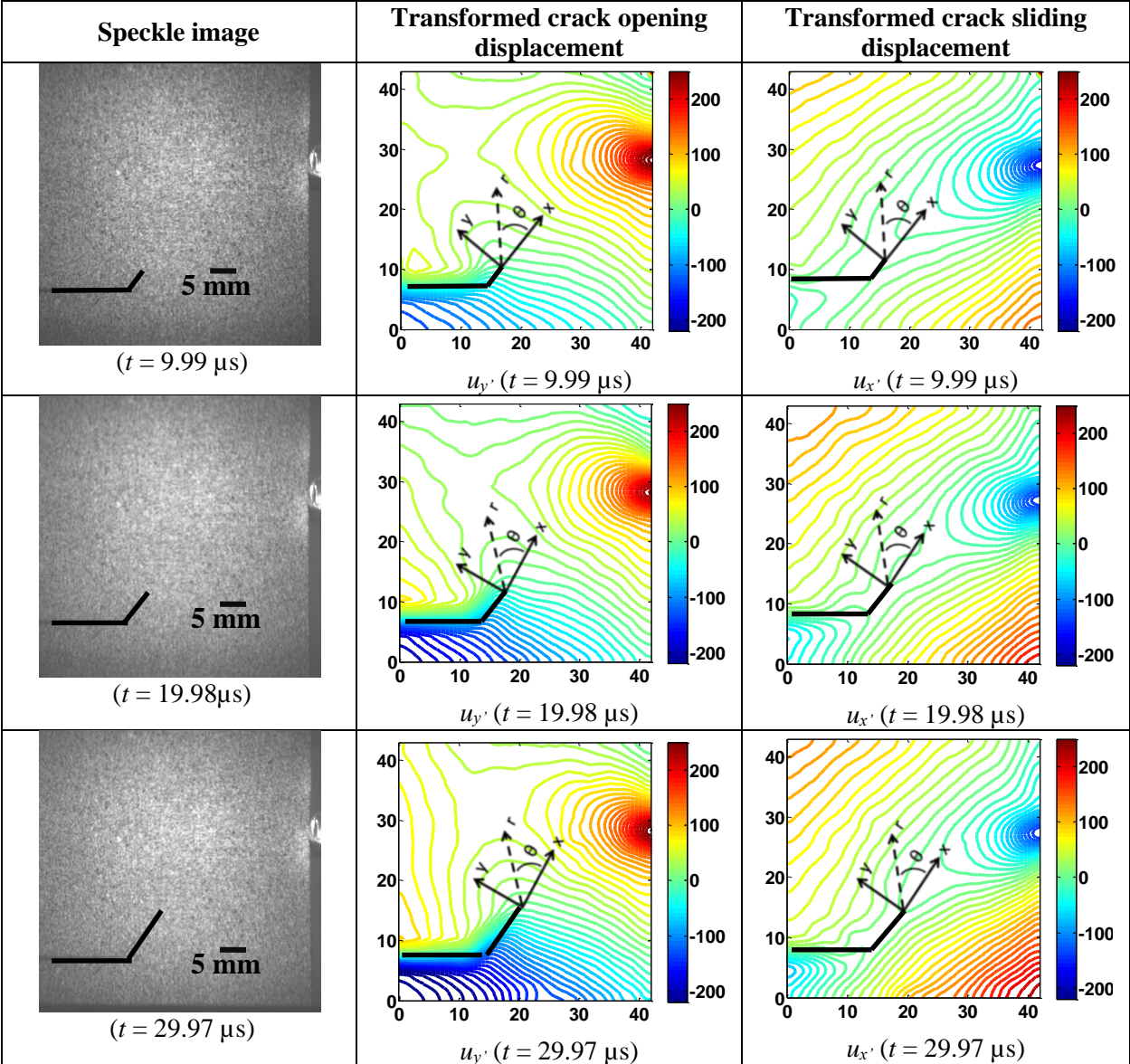




**A4.** 10%  $V_f$  glass-filled epoxy ( $e = 20$ ,  $a = 20$ ) (Facet size: 15x15; Overlap:0x0, Scale factor: 45  $\mu\text{m}/\text{pixel}$ )









**A5.** 10%  $V_f$  glass-filled epoxy ( $e = 20$ ,  $a = 25$ ) (Facet size: 15x15; Overlap:0x0, Scale factor: 35  $\mu\text{m}/\text{pixel}$ )

